3)

Impedance Matching and Energy Shunting Control for Nonpositive Real Structures

by

Carl Blaurock

B.S. Massachusetts Institute of Technology (1991)

SUBMITTED TO THE DEPARTMENT OF
AERONAUTICS AND ASTRONAUTICS
IN PARTIAL FULFILLMENT OF THE REQUIREMENTS
FOR THE DEGREE OF
S.M.
at the
Massachusetts Institute of Technology
February, 1994

Signature of Author _____
Department of Aeronautics and Astronautics
January 20, 1994

Certified by _____
David W. Miller
Thesis Advisor, Principal Research Scientist, Department of Aeronautics and Astronautics

Accepted by _____
Professor Harold Y. Wachman
Chairman, Department Graduate Committee

Impedance Matching and Energy Shunting Control for Nonpositive Real Structures

by

Carl Blaurock

SUBMITTED TO THE DEPARTMENT OF AERONAUTICS AND ASTRONAUTICS
ON JANUARY 20, 1994, IN PARTIAL FULFILLMENT OF THE
REQUIREMENTS FOR THE DEGREE OF
S.M.

The objective of this thesis is to examine the implementation issues of local structural control. Local control is used to alter those dynamic properties of a structure which can be completely defined at a particular structural cross-section: transmission and reflection coefficients. Local control includes impedance matching, which absorbs power from the system, and energy shunting, which minimizes the transmission of power in specified directions. Any local controller can be shown to implement some proportion of both impedance matching and energy shunting, and offer high stability robustness due to its positive real nature.

Time delays and sensor/actuator noncollocation are two common effects which cause loss of positivity. Time delay can be accommodated by modifying the local model. Impedance matching and energy shunting control are investigated on testbeds incorporating time delay. Noncollocation invalidates the assumptions used to create the local model, requiring a global model. Global design techniques which capture the characteristics of the local controllers are assembled.

Three of these techniques are implemented on the AMASS solar array simulator, which exhibits both time delay and noncollocation. Modal frequency shifts in the AMASS flight experiment place high requirements on stability and performance robustness. A reduced order, multimodel compensator is designed which provides acceptable damping and robustness. An alpha shifted compensator enforces closed loop damping. Damping is high, however, the controller is analytically found to be comparatively unrobust. A modified feedthrough controller increases the modal observability of the structure. Analytical robustness is high, and predicted damping is nearly equal to the alpha shifted compensator. However, the measured damping is lower than predicted, possibly due to nonlinearities in the piezoelectric actuator.

Thesis Supervisor: Dr. David W. Miller
Principal Research Scientist, Aeronautics and Astronautics

Acknowledgments

I would like to thank Dr. Dave Miller for supporting me through this work, especially for the opportunity to visit TRW to implement the AMASS controllers.

I would also like to thank Ted Nye for constant advice, encouragement and support, and the chance to work under him at TRW.

I have to also thank Bob Kraml, Bob Betros, and Oscar Alvarez at TRW for many ideas and interesting conversations. Many others at TRW also contributed in vital ways to the work presented here. Thanks especially to John Innes and Nick Steffen for repeatedly fixing what I blew up.

Here at MIT, I want to acknowlege my officemates and compatriots, Simon, Roger, Charissa, Brett, Aaron, Greg, Mark, Leonard, et al. (not least for sharing what I went through). And, of course, Becky, the "Boondoggle Queen", for looking out for me.

I also want to say thank you to Sonia, for getting me away from the lab occasionally.

Of course, Mom.

Finally, I want to thank Cindy Gregory, the MIT volleyball coach and PE instructor, for giving me a way to blow off steam.

Contents

1 Introduction **17**

2 Positive real systems **21**
2.1 Impedance matching 22
2.1.1 Local Modeling 22
2.1.2 Impedance Matching control design 39
2.1.3 Brass Beam Impedance Matching Experiments 51
2.2 Energy Shunting 66
2.2.1 Shunting model 67
2.2.2 Shunting control derivation 68
2.2.3 Truss Energy Shunting Experiments 78
2.3 Combinations of Impedance Matching and Shunting 88
2.3.1 RMS optimal compensator for a BE beam 91
2.3.2 Global Characteristics of the Impedance Match and Energy Shunt 97
2.3.3 $\mathcal{H}_2$ Minimization 101

3 Nonpositive Real Systems **117**
3.1 Systems with time delay 118
3.1.1 Stability in the presence of time delay 118
3.1.2 Performance in the presence of time delay 125
3.2 Noncollocation 127

4 AMASS Active Materials Testbed **129**
4.1 AMASS Flight Experiment 129
4.2 AMASS Ground Testbed 132
4.2.1 Modeling 133
4.2.2 Control Objectives 139
4.2.3 $\mathcal{H}_2$ Control Design Procedure 140
4.3 AMASS Control Designs 144
4.3.1 LQG 145
4.3.2 Alpha-shifted LQG 145
4.3.3 Modified Feedthrough Compensator 149
4.4 Analytical Evaluation of AMASS Controllers 153
4.4.1 Analytical Tools for Assessing Stability and Performance using Data 154

4.4.2 LQG analysis 156
4.4.3 Alpha shifted LQG analysis 161
4.4.4 Modified Feedthrough Controller analysis 166
4.5 Experimental Evaluation of AMASS Controllers 171
4.5.1 Measured Compensator Frequency Response 171
4.5.2 Measured Closed Loop Frequency Response 176
4.5.3 Measured Closed Loop Impact Tests 179
4.6 AMASS Ground Testbed Conclusions 182

5 Conclusions **187**

References **191**

A Global Wave Model **195**

B Reduction and $\mathcal{H}_2$ Tuning **199**

C Controller Implementation **203**

List of Figures

2.1 Generalized structural junction: The wave model describes transmission of energy along the members. 24
2.2 Complex wave number k: for passive systems, k must lie in the second or fourth quadrants. 25
2.3 Rod example 28
2.4 Rod example: global wave modes 29
2.5 Rod example: Junction 2 boundary conditions 31
2.6 Generic wave junction 34
2.7 Arbitrary structure 34
2.8 Rod example: Differentiated direct field vs critically damped and log averaged approximations, for end force to end velocity. 38
2.9 Rod example: Differentiated direct field vs critically damped and log averaged approximations, for x_2 force to velocity. 38
2.10 Open and closed loop transfer functions from q to collocated velocity at the left end. 50
2.11 The Brass Beam testbed at SERC. Disturbance energy is introduced at the left end using a torque actuator. The left end is controlled using a force actuator and collocated displacement sensor. 50
2.12 The real-time control computer and supporting amplifiers and filters. 52
2.13 Performance is evaluated by measuring the pinned-end frequency response. 53
2.14 Non-causal impedance match and experimentally implemented approximations. 58
2.15 Predicted junction power flow for the experimentally implemented compensators. The conservative junction has zero net power in open loop, while incoming alone has -1. 61
2.16 Measured brass beam frequency response from torque to rotation, with the rational approximation implemented on the right end of the beam. 63
2.17 Measured brass beam frequency response from torque to rotation, with the phase-matching approximation implemented on the right end of the beam. 64
2.18 Measured brass beam frequency response from torque to rotation, with rate feedback implemented on the far end of the beam. 65
2.19 General control junction in the transmission path between a disturbance d and output z 68

2.20 Rod example: energy shunting at junction 2 to minimize transmission from disturbance to performance. 71
2.21 Equivalent junction boundary condition produced by the shunting feedforward. 73
2.22 Another shunting objective can be posed as minimizing the RMS of z, when disturbances act on both sides of the control. 74
2.23 The directional shunt: energy is allowed to flow in only one direction. 76
2.24 The 20-bay single leg truss testbed, and supporting equipment. 78
2.25 The dereverberated model of the truss testbed. 79
2.26 The closed loop performance of the impedance-matching compensator on the Finite Element model. 82
2.27 The high gain shunting compensator on the truss Finite Element model. 82
2.28 Mode shapes of the FE model: Open loop mode shapes of the first six modes show beam-like deformations. 84
2.29 Mode shapes of the FE model: Shunting compensator is actively removing the control strut at bay 6. 85
2.30 Measured transfer functions of the shunting (solid) and the impedance matching (dashed) compensators. 86
2.31 The measured performance transfer functions in open loop (dotted), using the shunting (solid), and using the impedance matching (dashed) compensator. 87
2.32 The analytical high gain open loop (dashed) plotted against the measured open bay truss (solid). 87
2.33 Local control options: For a controlled structure with a single disturbance path, shunting can be used when the sensitive portions of the structure are concentrated to one side of the control Q (right). On the left, energy shunting would reflect energy back to the performance, thus the impedance match will be used. 89
2.34 The general local control problem: a subset of the disturbance paths are controlled. The remaining paths are characterized as a structural transmissibility $T(s)$. 90
2.35 The BE beam simulation: the control $K(s)$ is optimized for each location from 0 to L. 91
2.36 The gain α which minimizes $E\{z^T z\}$ as a function of location. 93
2.37 The RMS cost $E\{z^T z\}$ as a function of control location, for the RMS optimal compensator, the impedance match, the high gain shunt, and the open loop. 94
2.38 Power absorption of the RMS optimal compensator, as a function of location. 95
2.39 Accuracy of the impedance matching approximation: the approximation can be made an exact match to the noncausal impedance match (solid) at a discrete set of modal frequencies (dashed) or an inaccurate match across a broad frequency range (dashed) by the choice of input spectrum. 99

2.40 Modified feedthrough design model: The design model includes the desired feedthrough D_2 (left). When the control is implemented on the true plant, the feedthrough is folded into the compensator (right). 110
2.41 Design model with time delay: When the measurement is a filtered version of y (for example through a time delay), the plant D term cannot be canceled directly (dashed line). Instead, it must be canceled with a signal composed of u filtered by a model of the time delay, $\hat{F}$. 111
2.42 The design plant consists of the true plant (including $F(s)$) augmented with the dynamic approximation $\hat{F}$. On implementation, the compensator is augmented. 114

3.1 Rolloff for a structural loop. 119
3.2 Loop magnitude for a structural system: if the envelope determined by the log average $g(j\omega)$ and the reverberant mode height $h(\zeta)$ is rolled off, the loop will be gain stable. 120
3.3 The reverberant mode height $h(\zeta_i)$ can be approximated using the residue expansion of $G(s)$. 120
3.4 The loop phase for a structural system: the plant perturbation phase, ϕ_p, is the difference between the backbone phase, $90°n$, and the lowest plant phase. 122
3.5 The control design with time delay. The inverse of the time delay is added to the model, creating a "pseudo-positive real" plant. 125

4.1 The AMASS testbed. 130
4.2 ADCE positions on the active yoke. The ADCEs operate independently on embedded piezo actuators and sensors. 133
4.3 G_{11}: Measured response from ADCE 1 drive amp to S_{nc_1}. 135
4.4 G_{22}: Measured response from ADCE 2 drive amp to S_{nc_2}. 135
4.5 G_{33}: Measured response from ADCE 3 drive amp to S_{nc_3}. 136
4.6 G_{44}: Measured response from ADCE 4 drive amp to S_{nc_4}. 136
4.7 G_{11}: measured (solid) and state-space fit (dashed). 137
4.8 G_{14}: measured (solid) and state-space fit (dashed). 137
4.9 G_{44}: measured (solid) and state-space fit (dashed). 138
4.10 G_{41}: measured (solid) and state-space fit (dashed). 138
4.11 The general control design procedure for the AMASS ground testbed. 140
4.12 Reduced-order LQG control design process. 144
4.13 The alpha shifted LQG control design process. The design plant is iteratively chosen, then the controller is iteratively reduced and optimized. 146
4.14 The MF compensator control design process. The plant model is modified to increase the observability of plant modes to the controller. . . 148
4.15 Effect of varying feedthrough: The zeros of the plant shift as the D term is varied. 149
4.16 The G_{11} transfer function at the chosen design value of D_2, showing the improved modal observability. 150

4.17 AMASS compensator designs: reduced order LQG (solid), alpha-shifted (dashed) and MF (dash-dot), plotted with the open-loop plant response G_{11} (dotted). 152
4.18 Nichols plot of the LQG compensator: The plot must pass below the critical points, marked by "x"s. 157
4.19 LQG compensator sensitivity singular values, calculated from the data (solid) and the model (dashed). 158
4.20 The closed loop response for the LQG controller: obtained from data (solid) and the state space model (dashed). The open loop data is also plotted (dotted). 159
4.21 The covariance of the output of the ADCE 1 sensor, as modes 1, 2 and 3 are varied. The nominal frequencies are marked by the vertical dotted lines. 160
4.22 Nichols plot of the alpha shifted LQG compensator: The plot must pass below the critical points, marked by "x"s. 162
4.23 alpha shifted LQG compensator sensitivity singular values, calculated from the data (solid) and the model (dashed). 163
4.24 The closed loop response for the LQG controller, calculated from data (solid) and the state space model (dashed). The open loop data is also plotted (dotted). 164
4.25 The covariance of the output of the ADCE 1 sensor, as modes 1, 2 and 3 are varied. The nominal frequencies are marked by the vertical dotted lines. 165
4.26 Nichols plot of the modified D term compensator: The plot must pass below the critical points, marked by "x"s. 167
4.27 MF compensator sensitivity singular values, calculated from the data (solid) and the model (dashed). 168
4.28 The closed loop response for the modified D term controller, calculated from data (solid) and the state space model (dashed). The open loop data is also plotted (dotted). 169
4.29 The covariance of the output of the ADCE 1 sensor, as modes 1, 2 and 3 are varied. The nominal frequencies are marked by the vertical dotted lines. 170
4.30 Discrete LQG compensator measured through the ADCE (solid), plotted against the continuous compensator with predicted time delay (dashed). 173
4.31 Discrete alpha shifted LQG compensator measured through the ADCE (solid), plotted against the continuous compensator with predicted time delay (dashed). 174
4.32 Discrete modified feedthrough compensator measured through the ADCE (solid), plotted against the continuous compensator with predicted time delay (dashed). 175
4.33 Closed loop frequency response through ADCE 1, measured (solid) and modeled (dashed), with the LQG controller closed at ADCEs 1 and 4. 176

4.34 Closed loop frequency response through ADCE 1, measured (solid) and modeled (dashed), with the α-shifted LQG controller closed at ADCEs 1 and 4. 177
4.35 Closed loop frequency response through ADCE 1, measured (solid) and modeled (dashed), with the modified feedthrough controller closed at ADCEs 1 and 4. 178
4.36 The impact locations on the AMASS array: (1) first bending mode , (2) first torsion mode, (3) second bending. 180
4.37 FFTs of the tome domain data. A) 1^{st} mode excitation, averaged sensors. B) 2^{nd} mode excitation, differenced sensors. Shown is the postprocessed, filtered data (solid) against the unfiltered (dashed). C) 3^{rd} mode excitation, averaged sensors. 181
4.38 LQG compensator: measured ringdown for first, second, and third mode excitations, in closed loop (solid) and open loop (dotted). Second mode has been postprocessed. 183
4.39 alpha shifted LQG compensator: measured ringdown for first, second, and third mode excitations, in closed loop (solid) and open loop (dotted). Second mode has been postprocessed. 184
4.40 MF compensator: measured ringdown for first mode excitation, in closed loop (solid) and open loop (dotted). Second mode has been postprocessed. 185

A.1 Truss structure 196

List of Tables

2.1 BE beam testbed parameters 52

4.1 Identified Modes of the AMASS ground testbed. 132
4.2 Design control and sensor noise weights. 142
4.3 Alpha shifts for modes 1, 2, and 3. 147
4.4 Multimodel homotopy steps taken to stabilize the α-shifted controllers to $+10\%/-2\%$ shifts in mode frequency. 148
4.5 Closed loop poles for the final designs. 153
4.6 Continuous and discrete pole frequencies for the compensator poles, showing the effects of compensator discretization and roundoff error. . 172

Chapter 1

Introduction

Active control has been investigated in numerous contexts. Feedforward control [1], classical feedback control [2], and modern or optimal feedback control [3] have received a great deal of attention. This work has examined issues of nominal stability and performance, as well as robust stability and robust performance [4] and implementation [5] of feedback control. These concepts have been applied to the control of servo systems, and more recently, flexible structures [6, 7].

The advantages of active control include the ability to more precisely hold a desired attitude or pointing angle, reject disturbances introduced by a basebody, minimize disturbances induced into a basebody, or decrease structural mass. These advantages are gained at the expense of increased engineering effort, cost, power requirements, system complexity and attendant potential for failure. For feedback systems, closed loop instability can lead to damage or loss of the hardware. The advantages of active control may only outweigh the costs and risks for structures whose development or deployment costs are already exceptionally high, or when passive methods are simply not sufficient to achieve the required performance.

Space applications are an area in which costs are sufficient to justify the expense of an active control system. Per-kilogram launch costs drive the mass of a spacecraft downwards. The mass reduction enabled by an actively controlled system may be sufficient to recoup the expense of the design. Satellite sizes and masses are being driven down by advances in system miniaturization, the desire to lower the risk inherent in

launch and deployment, and by dividing payloads among smaller launch vehicles. This trend decreases the mass budget for passive isolation. At the same time, the requirements for isolation are increasing. As payload mass fraction increases, the effects of on-board disturbances on the spacecraft and on other instruments increase.

Requirements on disturbance rejection and attitude control will only become tighter. More precise line-of-sight instruments, tighter communications links, including the development of laser communications, and the potential for biological and industrial processes designed to take advantage of a microgravity environment, all will tighten the spacecraft design tolerances. Passive systems may be unable to provide the necessary performance. Active control becomes an enabling technology.

Minimizing Solar Panel Induced Jitter. A specific example of conflict between spacecraft mass and performance is the necessity of providing power. Solar arrays are generally used. Since the spacecraft often maintains a certain orientation with respect to the Earth, the arrays are moved to track the sun. When the array mass is small compared to the satellite bus, the jitter induced is negligible. However, while spacecraft mass can decrease, a fixed solar panel area is required to provide power. Flexibility in the panels will eventually limit the pointing accuracy.

In order for active control to be a viable technology for control of flexible spacecraft, the stability performance of the active system must be guaranteed to a high degree of confidence. Many approaches may be taken. A particularly promising approach is the use of a local controller, which is designed from a local model. A local model throws out all information about the parts of the structure spatially removed from the control actuator and sensor. The part which remains, the local response, can often be characterized accurately, even when little is known about global structure.

Further, if the control hardware is designed properly, the control can be designed to take advantage of certain stability guarantees. The performance may degrade due to mismodeling, however, the closed loop system will be stable. These guarantees follow from the *duality* of the sensor and actuator. The important characteristic of duality is the phase-boundedness of the frequency response from the actuator to the

sensor [8].

Previous Approaches to Local Control. Some of the original work on local controllers concerned bridge feedback designs which were designed based on impedance matching ideas from electrical engineering [9]. The impedance of a structural system was defined and used to design an optimal damping controller. The approach was combined with other methods in a layered control architecture which used the damping controller to enhance stability margins in a series of progressively higher authority control loops [10].

Another approach to structural impedance matching was presented by Miller [11]. Structural motion was decomposed into component wave modes, explicitly representing the directional nature of energy flow. The wave model is derived from an explicit Partial Differential Equation description of the plant. Minimizing the flow of power away from the control location creates a controller which absorbs power. While the control is generally not physically implementable, various methods for arriving at an implementable approximation are shown.

Yet another local control methodology was presented by MacMartin [12]. Approaching the problem from the context of Statistical Energy Analysis (SEA), the structural response is considered to be uncertain, highly resonant (i.e.. lightly damped) and modally dense [13]. The "known" portion of the response is the logarithmic mean of the resonant response, which is equivalent in some sense to a local model. A combined $\mathcal{H}_2/\mathcal{H}_\infty$ cost is defined, and the minimization of the cost is shown to be equivalent to minimizing power.

Spangler approaches the local control design from the context of state space, $\mathcal{H}_2$ optimization [14]. The issues in creating a perfectly collocated sensor and actuator are investigated. The approach is to measure the impedance of the actuator, in order to back out the structural motion. The results thereby tie into previous impedance matching work. The connection is strengthened, through the real-pole constrained form of the $\mathcal{H}_2$ optimal controller, by the fact that the MacMartin local model and $\mathcal{H}_2/\mathcal{H}_\infty$ optimal controller are both parameterized as real-pole entities.

Topics of Investigation. The current work seeks to build upon the last three citations. The thrust will be towards addressing implementation issues. The results of the local modeling and local control design are reviewed in Chapter 2. Impedance matching implementation is discussed. A second power flow local control objective, energy shunting, is introduced, and the relationship of the two is investigated. Based on the statement that any local controller can be described in terms of the mixture of impedance matching and energy shunting, an investigation of the globally $\mathcal{H}_2$ optimal local controller is presented.

Secondly, the effects of non-idealities on the implementation of impedance matching and energy shunting are explored in Chapter 3. Many effects can be posed in the local framework. However, some non-idealities do not fit into the local framework. The objectives of the local design are reflected into the global design framework. A number of approaches to meeting these objectives are presented.

Finally, implementation of the local controllers is presented for a representative structure in Chapter 4. The AMASS testbed is the ground prototype of a Controlled Structures Interaction (CSI) flight experiment. The experiment examines the ability of passive and active components to reduce spacecraft jitter due to appendage flexibility. Analytical and experimental results are presented and assessed in terms of the design goals.

Chapter 2

Positive real systems

Stability and performance robustness are of primary importance to active control of space systems. Many techniques have been investigated for increasing the robustness of active controllers to uncertain or time-varying plant parameters. The greatest degree of stability robustness can be attained when both the plant and the controller are *positive real* (PR) [8]. A system is positive real when the real part of the frequency response of the system is positive. This characteristic requires that the phase of the response is bounded by $\pm 90°$.

The attribute of positive realness must be designed into the plant. One way to create a positive real plant is to choose the sensor and actuator to be collocated and *dual*. Dualness in turn refers to the property that the product of the sensed and actuated quantities is power. Given a positive real plant, a controller which is also positive real is guaranteed to produce a stable system when interconnected using negative feedback. Termed *hyperstability* [8], such a guarantee is a powerful way to robustify against any plant uncertainty. The collocated nature of the sensor and actuator gives rise to the term *local control*. Local control requires a knowledge of the response of the structure at the control location. A *local model*, which captures the desired response, is required.

Performance robustness is also a desired attribute of any compensator. Using a dual sensor and actuator, the designer can control the closed loop power flow. By controlling the power flow at the control location, the designer can effect the desired

performance improvement. Closed loop power is a function of the plant response at the control location, termed the local response. Since the local system is likely to be characterized better than the global structure, the performance will also be robust to changes in the structure as a whole.

The local model can be used to describe the power at the control. Depending on the topology of the structure to be controlled, the designer may re-direct energy or absorb energy. The latter technique has been termed *impedance matching*, since the controller has a specific relationship to the impedance of the structure as seen through the control hardware.

2.1 Impedance matching

The structural impedance match is derived by minimizing the closed loop power flow away from the control location. A local model is used to describe the power flow. In the global system, motion at the control location produces, and is produced by, motion in other regions of the structure. By using a local model, knowledge of the global response of the structure is removed from the problem. That is, incoming disturbances are no longer correlated with outgoing energy. The control only has one opportunity to affect the power before it departs into the rest of the structure. As a result, the controller minimizes the local power by absorbing the greatest possible proportion of the incoming power.The first step, in deriving the impedance match is to obtain a local model of the structure.

2.1.1 Local Modeling

The measured, reverberant response arises from the interaction of energy arriving from other parts of the structure with energy introduced by the actuator. The desired local model captures the *direct field* response, the motion due solely to the energy imparted by the control. Local models have been obtained analytically, using a wave model. The wave modeling approach is suitable for structures composed of an assemblage of one-dimensional waveguide-like members, for example trusses. It

was developed by von Flotow [15]. From a wave perspective, the local model consists of reflection and transmission (scattering) coefficients of the controlled structural cross-section. Since such a description is not always applicable, approximations to the direct field can be derived from measurement data, or from more conventional modeling techniques such as Finite Element modeling. These approximations were suggested by MacMartin [16].

Wave Model

The wave model is a technique for describing the motion of a system in terms of wave modes which propagate around the structure. It can be used to describe structures which can be modeled as an assemblage of one-dimensional waveguides (Figure 2.1). The structure is composed of a number of linear members which allow energy to propagate primarily along their longitudinal axis. Members intersect at junctions, which reflect and scatter energy. In the wave concept, motion arises from the combined response of independent wave modes which travel along each member. Wave modes arise from control and disturbance forces.

In steady state, wave modes travel around the structure and return to their point of origin to interfere with themselves. The relative phasing determines whether such interference is constructive, as at a modal frequency, or destructive, as at a zero. The analysis is conducted in the frequency domain and describes steady-state behavior of the structure. The following chapter is a summary of [11], to which the reader is referred for further information. The results will be used for control derivations presented in succeeding chapters.

The basis for the wave model is a transformation from wave mode amplitudes, w, to physical variables, $y = \begin{bmatrix} u \\ f \end{bmatrix}$, where u and f are the strains and stresses in a member. The physical deformation u at a particular cross-section of a given member can be expressed as the sum of independent wave modes passing the cross-section:

$$u(x,t) = w_{left}e^{ik_{left}x+i\omega t} + w_{right}e^{-ik_{right}x+i\omega t} \tag{2.1}$$

The wave mode amplitudes w_{left} and w_{right} are subscripted according to the direction

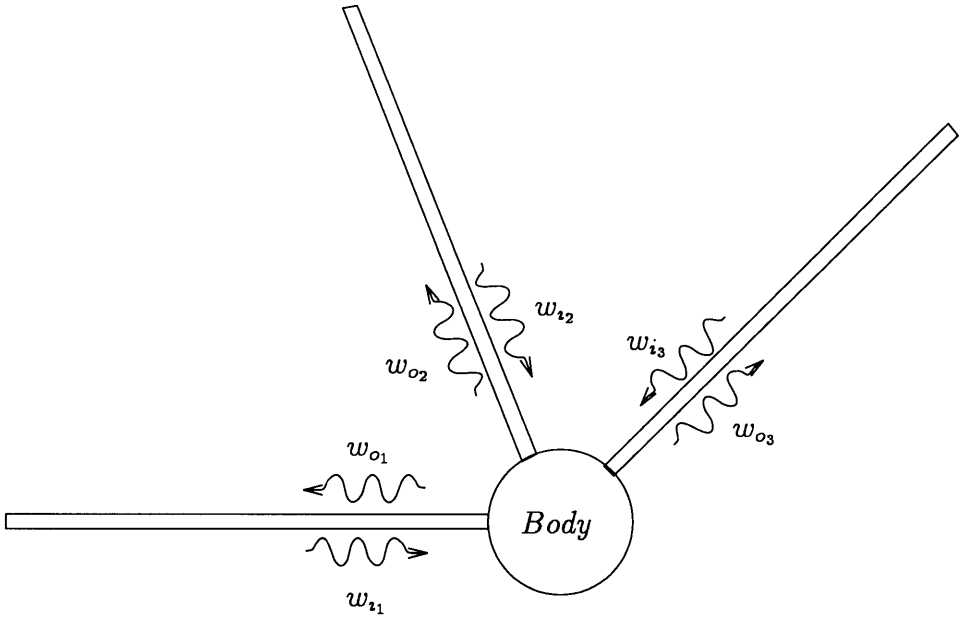

Figure 2.1: Generalized structural junction: The wave model describes transmission of energy along the members.

of their origination. Leftward waves w_{left} originate to the right of the cross-section. If they are propagating waves, they travel leftward. Rightward waves w_{right} similarly originate towards the left, and if they are traveling waves, travel rightward.

The wave number, k, relates the wavelength to the frequency of the wave. The wave number is obtained from the partial differential equation (PDE) of the member. The PDE is Fourier-transformed in the temporal domain, and placed into a state-space form:

$$\frac{\partial}{\partial x}\begin{bmatrix} u \\ f \end{bmatrix} = A(\omega)\begin{bmatrix} u_m \\ f_m \end{bmatrix} = A(\omega)y(\omega) \tag{2.2}$$

$A(\omega)$ is the frequency-dependent state-space matrix of the medium. The characteristic equation

$$\det\left[\, kI - A(\omega) \,\right] = 0 \tag{2.3}$$

is the dispersion relation. The solutions to Equation 2.3 are the wave numbers k whose inverses give the wavelengths which the medium supports at a particular frequency. Real wave numbers correspond to unattenuated propagating waves (Figure 2.2). Imaginary wave numbers correspond to evanescent waves, that is, waves

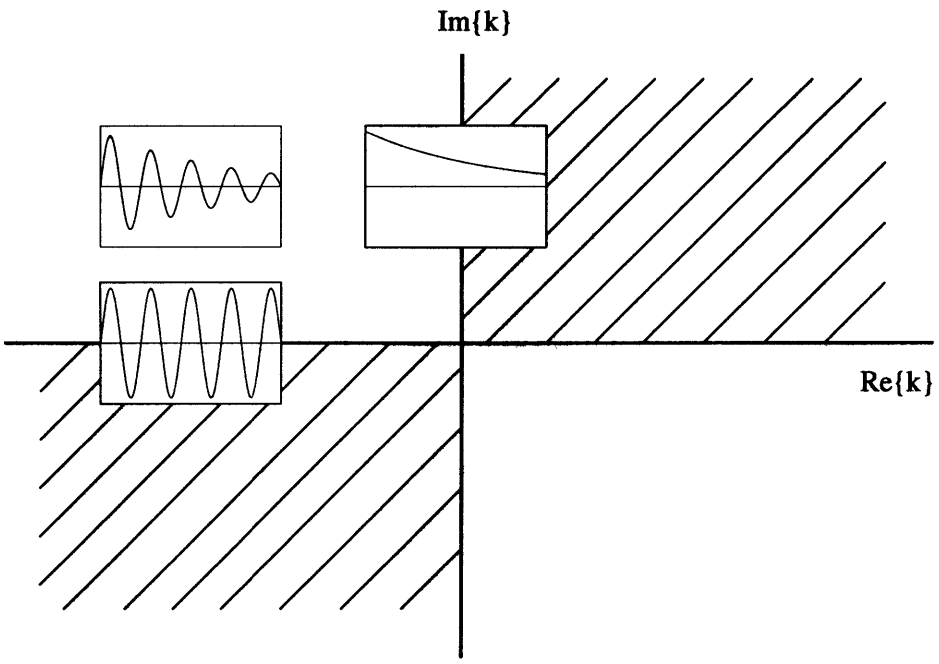

Figure 2.2: Complex wave number k: for passive systems, k must lie in the second or fourth quadrants.

whose spatial distribution is exponential rather than sinusoidal. Complex wave numbers indicate propagating waves whose amplitude attenuates or amplifies. For passive structural systems the waves must attenuate, hence complex wave numbers must lie in the second or fourth quadrant of the complex plane.

Given the wave number k, a transformation matrix $Y(\omega)$ can be defined, which maps wave mode amplitudes $w = \begin{bmatrix} w_{left} \\ w_{right} \end{bmatrix}$ into physical variables $y = \begin{bmatrix} u_m \\ f_m \end{bmatrix}$ in the member at each frequency ω:

$$y(\omega) = Y(\omega)w(\omega) \tag{2.4}$$

The transformation Y is square, reflecting the fact that the number of independent wave modes equals the number of cross-sectional variables.

The wave transformation Y is the basis for the description of junctions in the wave model. Junctions can be physical discontinuities in the structure, such as the intersection of two or more members. Junctions can also be defined at arbitrary locations, such as at disturbance or control force inputs, or at locations where the

structural response is desired. The general form of the junction boundary condition is

$$\begin{bmatrix} B_u & B_f \end{bmatrix} \begin{bmatrix} u_m \\ f_m \end{bmatrix} = Q \tag{2.5}$$

where non-zero elements in the matrices B_u and B_f pick out the combinations of member forces and deflections which are specified at the junction. The vector Q describes the imposed forces and displacements, and can include both actuator forces as well as geometric and natural boundary conditions.

The wave transformation Y can be used to transform the boundary condition (Equation 2.5) into wave coordinates:

$$\begin{bmatrix} B_u & B_f \end{bmatrix} \begin{bmatrix} u_m \\ f_m \end{bmatrix} = \begin{bmatrix} B_u & B_f \end{bmatrix} Yw = Q \tag{2.6}$$

The wave modes w can be grouped into modes which originate at the junction (*outgoing* waves w_o) and those which originate elsewhere (*incoming* waves w_i), so that $w = \begin{bmatrix} w_i \\ w_o \end{bmatrix}$. If the columns of the wave transformation Y are ordered correspondingly, the boundary condition in wave coordinates, Equation 2.6, can be arranged as follows:

$$\begin{bmatrix} B_u & B_f \end{bmatrix} \begin{bmatrix} Y_{ui} & Y_{uo} \\ Y_{fi} & Y_{fo} \end{bmatrix} \begin{bmatrix} w_i \\ w_o \end{bmatrix} = Q \tag{2.7}$$

The subscripts $(.)_{ui}$, $(.)_{uo}$, $(.)_{fi}$, $(.)_{fo}$, denote those elements of Y which relate the internal deflections u to the incoming and outgoing waves, and the internal forces f to the incoming and outgoing waves, respectively.

It is useful to re-arrange this equation so that the outgoing waves w_o are a linear combination of the incoming waves w_i and the junction forces Q:

$$w_o(\omega) = S(\omega)w_i(\omega) + \Psi(\omega)Q(\omega) \tag{2.8}$$

where

$$S = -\begin{bmatrix} B_u Y_{uo} + B_f Y_{fo} \end{bmatrix}^{-1} \begin{bmatrix} B_u Y_{ui} + B_f Y_{fi} \end{bmatrix} \tag{2.9}$$

$$\Psi = \begin{bmatrix} B_u Y_{uo} + B_f Y_{fo} \end{bmatrix}^{-1} \tag{2.10}$$

Equation 2.8 is the junction description in wave coordinates, and is fundamental to wave-based local control. S is the *scattering matrix*, which describes how incoming wave modes mix and scatter. The *generation matrix* Ψ describes how externally imposed forces and displacements generate outgoing waves.

To model a structure composed of multiple junctions, a description of wave propagation between junctions is needed. Wave propagation along members is described by the *transmission matrix* ξ. The transmission matrix $\xi(x_1, x_2, \omega)$ describes how waves w_2 at a location x_2 along a member are related to waves w_1 at another location x_1:

$$w_2(\omega) = w(x_2, \omega) = \xi(x_2, x_1, \omega) w(x_1, \omega) = \xi_{2-1} w(x_1, \omega) = \xi_{2-1} w_1(\omega) \tag{2.11}$$

where x_1 can be thought of as "upstream" of x_2, that is, waves travel from x_1 towards x_2. There will be another $\xi(x_2, x_1, \omega) = \xi_{2-1}$ which describes how waves at x_2 relate to waves at x_1. For a passive, reciprocal member, ξ_{1-2} and ξ_{2-1} will be identical, indicating that the member can support two sets of wave modes, traveling in opposite directions. The ξs are used in the global model, to relate waves departing one junction to the waves incoming at other junctions. The junction matrices, S and Ψ, and transmission matrix, ξ, are the basic elements of the wave model.

Appendix A discusses the assembly of the wave model elements into a global model. Reference [11] discusses in detail the assembly of more complicated elements from various types of members (such as beams and torsion members) in more extensive combinations such as truss structures. The derivation of local control does not require such complicated models. However, global wave models will be derived for use in simulating the global behavior of at structure under the influence of local controllers.

The key to the use of the wave model in local control is that the generation matrix Ψ is exactly the local model desired. If the incoming wave modes w_i are zero, the response at a junction is due only to the outgoing waves generated by the control force through Ψ. Thus Ψ is the exact direct field response. If the control force Q is considered as feedforward of incoming waves, $Q = Fw_i$, junction control can be described as modification of the scattering matrix:

$$w_o = (S + \Psi F) w_i = S_{cl} w_i \tag{2.12}$$

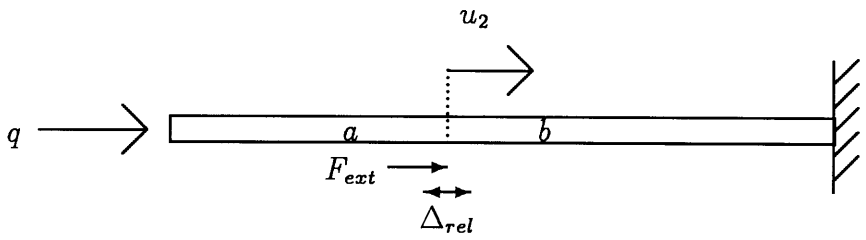

Figure 2.3: Rod example

Control can be posed as explicitly specifying entries in S_{cl}. Alternatively another metric such as power flow can be minimized. Using the transformation matrix Y, feedforward of wave modes can be posed as feedback of physical variables.

Example 1: Wave Model of a Rod Figure 2.3 shows a simple structural system, consisting of a rod supporting axial motion. The left end is free, and supports an external force q. The right end is rigidly attached to an inertial base. A wave model of the rod will be constructed. In wave terminology, the rod is composed of 5 elements. The two ends and the location x_2 are junctions, and the segments a and b of the rod are members.

The rod is uniform with cross-sectional properties EA and ρA, where E is Young's modulus, ρ is mass density, and A is cross-sectional area. The junctions are the left end, the response location x_2, and the right end. These are numbered in Figure 2.4 as junctions 1, 2, and 3 respectively. The global wave modes given by

$$W = \begin{bmatrix} W_i \\ W_o \end{bmatrix} = \begin{bmatrix} w_{i_1} \\ w_{i_{2_{left}}} \\ w_{i_{2_{right}}} \\ w_{i_3} \\ w_{o_1} \\ w_{o_{2_{left}}} \\ w_{o_{2_{right}}} \\ w_{o_3} \end{bmatrix} \tag{2.13}$$

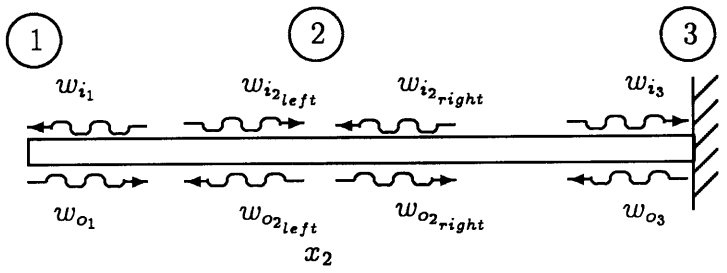

Figure 2.4: Rod example: global wave modes

To find the wave model S, Ψ, and ξ matrices, the junction transformation Y is found from the PDE.

The PDE of a rod is given by

$$EA\frac{\partial^2 u(x,t)}{\partial x^2} - \rho A\frac{\partial^2 u(x,t)}{\partial t^2} = 0 \tag{2.14}$$

Fourier transforming 2.14, the PDE in the frequency domain is

$$EA\frac{\partial^2 u(x,\omega)}{\partial x^2} - \rho A\omega^2 u(x,\omega) = 0 \tag{2.15}$$

The PDE is placed in state space form:

$$\frac{\partial}{\partial x}\begin{bmatrix} u \\ EA\frac{\partial u}{\partial x} \end{bmatrix} = \begin{bmatrix} 0 & \frac{1}{EA} \\ \rho A\omega^2 & 0 \end{bmatrix}\begin{bmatrix} u \\ EA\frac{\partial u}{\partial x} \end{bmatrix} = A(\omega)y(\omega) \tag{2.16}$$

The dispersion relation, Equation 2.3, can be solved for the wave numbers:

$$k = \pm\sqrt{\frac{\rho}{E}}\omega \tag{2.17}$$

The two wave numbers for the rod are real and of opposite sign. Thus two independent, unattenuated traveling wave modes are supported, one in each direction: $w = \begin{bmatrix} w_{left} \\ w_{right} \end{bmatrix}$. The waves are unattenuated. The physical displacement $u(x,t)$ is the sum of the displacements caused by each wave:

$$u(x,t) = w_{left}e^{ikx+i\omega t} + w_{right}e^{-ikx+i\omega t} \tag{2.18}$$

Using the relation of strain to internal force:

$$f = EA\frac{\partial u}{\partial x} \tag{2.19}$$

the cross-sectional variable state can be expressed in terms of wave mode amplitudes:

$$\begin{bmatrix} u \\ EA\frac{\partial u}{\partial x} \end{bmatrix} = \begin{bmatrix} 1 & 1 \\ ikEA & -ikEA \end{bmatrix} \begin{bmatrix} w_{left} \\ w_{right} \end{bmatrix} \tag{2.20}$$

which has the form of the junction transformation matrix.

Since at junction 1, w_i are leftward-traveling waves and w_o are rightward-traveling waves, the junction transformation matrix Y_1 is the same as Equation 2.20. The boundary condition at junction 1 is given by

$$-EA\frac{\partial u_1}{\partial x} = q \tag{2.21}$$

Equation 2.21 can be written in terms of the cross-sectional state vector y:

$$\begin{bmatrix} 0 & -1 \end{bmatrix} \begin{bmatrix} u \\ EA\frac{\partial u}{\partial x} \end{bmatrix} = \begin{bmatrix} B_u & B_f \end{bmatrix} \begin{bmatrix} u \\ EA\frac{\partial u}{\partial x} \end{bmatrix} = q \tag{2.22}$$

This is the junction description, Equation 2.8. The scattering matrix S_1 and generation matrix Ψ_1 can be found from Equation 2.9 and Equation 2.10, respectively:

$$\begin{aligned} S_1 &= -\begin{bmatrix} B_u Y_{uo_1} + B_f Y_{fo_1} \end{bmatrix}^{-1} \begin{bmatrix} B_u Y_{ui_1} + B_f Y_{fi_1} \end{bmatrix} \\ &= -\begin{bmatrix} 0*1 + -1*-ikEA \end{bmatrix}^{-1} \begin{bmatrix} 0*1 + -1*ikEA \end{bmatrix} \\ &= 1 \end{aligned} \tag{2.23}$$

$$\begin{aligned} \Psi_1 &= \begin{bmatrix} B_u Y_{uo_1} + B_f Y_{fo_1} \end{bmatrix}^{-1} \\ &= \begin{bmatrix} 0*1 + -1*-ikEA \end{bmatrix}^{-1} \\ &= \frac{1}{ikEA} \end{aligned} \tag{2.24}$$

The right end, constrained boundary condition (junction 3) is given by

$$\begin{bmatrix} B_u & B_f \end{bmatrix} \begin{bmatrix} u \\ \frac{\partial u}{\partial x} \end{bmatrix} = \begin{bmatrix} 1 & 0 \end{bmatrix} \begin{bmatrix} u \\ \frac{\partial u}{\partial x} \end{bmatrix} = 0 \tag{2.25}$$

giving the scattering and generation matrices, S_3 and Ψ_3, as

$$S_3 = -1 \tag{2.26}$$

$$\Psi_3 = 1 \tag{2.27}$$

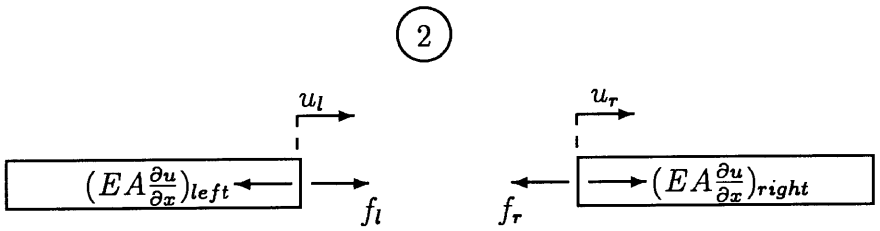

Figure 2.5: Rod example: Junction 2 boundary conditions

The implication of Ψ_3 is that if the boundary were given a commanded displacement, Δ_c, waves would be generated in the rod.

The treatment of the response location x_2 is instructive. If there are no forces acting at x_2, any arriving waves will pass unchanged through the junction: $w_o = w_i$. It will be useful to derive the full junction model of the form of Equation 2.8. Figure 2.5 shows the boundary conditions that must be satisfied. At the response location, there are four independent cross-sectional variables: u_l and u_r, the deflection of the left and right elements, and $(EA\frac{\partial u}{\partial x})_l$ and $(EA\frac{\partial u}{\partial x})_r$, the internal stresses. The subscript $(.)_{left}$ will denote properties of the left side of the cross-section, and $(.)_{right}$, of the right side.

The junction 2 transformation matrix Y_2 is given by Equation 2.28, with leftward and rightward waves ordered into incoming and outgoing waves:

$$\begin{bmatrix} u_l \\ u_r \\ (EA\frac{\partial u}{\partial x})_l \\ (EA\frac{\partial u}{\partial x})_r \end{bmatrix} = \begin{bmatrix} 1 & 0 & 1 & 0 \\ 0 & 1 & 0 & 1 \\ -ikEA & 0 & ikEA & 0 \\ 0 & ikEA & 0 & -ikEA \end{bmatrix} \begin{bmatrix} w_{i_{2_{left}}} \\ w_{i_{2_{right}}} \\ w_{o_{2_{left}}} \\ w_{o_{2_{right}}} \end{bmatrix} \tag{2.28}$$

Equilibrium requires that $u_r - u_l = 0$, and that $(EA\frac{\partial u}{\partial x})_r - (EA\frac{\partial u}{\partial x})_l = 0$. This can be stated more generally as:

$$\begin{bmatrix} -1 & 1 & 0 & 0 \\ 0 & 0 & -1 & 1 \end{bmatrix} \begin{bmatrix} u_l \\ u_r \\ (EA\frac{\partial u}{\partial x})_l \\ (EA\frac{\partial u}{\partial x})_r \end{bmatrix} = \begin{bmatrix} \Delta_{rel} \\ F_{ext} \end{bmatrix} \tag{2.29}$$

where Δ_{rel} is a commanded gap and F_{ext} is an external force applied at that cross-section. The commanded gap Δ_{rel} might arise for example from a strain actuator such as a piezoelectric wafer bonded to the beam.

Partitioning the transformation matrix into quadrants, the junction scattering matrix and generation matrix can be found from Equations 2.9 and 2.10, respectively:

$$S_2 = \left[B_u Y_{uo_2} + B_f Y_{fo_2} \right]^{-1} \left[B_u Y_{ui_2} + B_f Y_{fi_2} \right] = \begin{bmatrix} 0 & 1 \\ 1 & 0 \end{bmatrix} \tag{2.30}$$

$$\Psi_2 = \left[B_u Y_{uo_2} + B_f Y_{fo_2} \right]^{-1} = \frac{1}{2ikEA} \begin{bmatrix} -ikEA & -1 \\ ikEA & -1 \end{bmatrix} \tag{2.31}$$

As expected, the open loop scattering behavior of the junction does not change waves passing through it. Note, however, that in order to completely control all wave modes traversing the junction, it is necessary to have both elements of $Q_2 = \begin{bmatrix} \Delta_{rel} \\ F_{ext} \end{bmatrix}$ as actuators. This is equivalent to stating that, in order to completely specify the deflection of a cross-section, there must be as many independent actuators as physical degrees of freedom. In the current example, the actuator will be external force: $Q_2 = \begin{bmatrix} 0 \\ 1 \end{bmatrix} F_{ext}$.

The final elements of the model are the transmission matrices ξ for the left and right segments. The lengths of the segments are denoted as l_1 and l_2, respectively. Across the left member, waves travel a distance l_1 and undergo a phase change of kl_1, hence $\xi_1 = e^{ikl_1}$. Waves traversing the right member undergo a phase change of kl_2, hence $\xi_2 = e^{ikl_2}$. The complete transmission matrix is thus given by

$$W_i = \begin{bmatrix} w_{i_1} \\ w_{i_{2_{left}}} \\ w_{i_{2_{right}}} \\ w_{i_3} \end{bmatrix} = \begin{bmatrix} 0 & e^{ikl_1} & 0 & 0 \\ e^{ikl_1} & 0 & 0 & 0 \\ 0 & 0 & 0 & e^{ikl_2} \\ 0 & 0 & e^{ikl_2} & 0 \end{bmatrix} \begin{bmatrix} w_{o_1} \\ w_{o_{2_{left}}} \\ w_{o_{2_{right}}} \\ w_{o_3} \end{bmatrix} = \xi_{glob} W_o \tag{2.32}$$

From Equation A.4, the wave model is:

$$\begin{bmatrix} w_{i_1} \\ w_{i_{2_{left}}} \\ w_{i_{2_{right}}} \\ w_{i_3} \\ w_{o_1} \\ w_{o_{2_{left}}} \\ w_{o_{2_{right}}} \\ w_{o_3} \end{bmatrix} = \left(I + \begin{bmatrix} 0 & 0 & 0 & 0 & 0 & e^{ikl_1} & 0 & 0 \\ 0 & 0 & 0 & 0 & e^{ikl_1} & 0 & 0 & 0 \\ 0 & 0 & 0 & 0 & 0 & 0 & 0 & e^{ikl_2} \\ 0 & 0 & 0 & 0 & 0 & 0 & e^{ikl_2} & 0 \\ 1 & 0 & 0 & 0 & 0 & 0 & 0 & 0 \\ 0 & 0 & 1 & 0 & 0 & 0 & 0 & 0 \\ 0 & 1 & 0 & 0 & 0 & 0 & 0 & 0 \\ 0 & 0 & 0 & -1 & 0 & 0 & 0 & 0 \end{bmatrix} \right)^{-1} \begin{bmatrix} 0 & 0 \\ 0 & 0 \\ 0 & 0 \\ 0 & 0 \\ \frac{-1}{ikEA} & 0 \\ 0 & \frac{-1}{2ikEA} \\ 0 & \frac{-1}{2ikEA} \\ 0 & 0 \end{bmatrix} \begin{bmatrix} q \\ F_{ext} \end{bmatrix} \tag{2.33}$$

Equation 2.33 can be solved at a set of discrete frequencies $\{\omega\}$ for a set of wave mode amplitudes $\{W\}$. Using the global transformation matrix, the wave amplitudes at each frequency can be transformed into physical stresses and deformations:

$$y_{glob} = Y_{glob} W \tag{2.34}$$

resulting in a transfer function from input force $q(\omega)$ to any desired physical variable.

General local modeling

The wave description derived above has been applied to a relatively limited number of plants. The use of wave-based local models for larger structures such as trusses is problematical. It is not clear where the local structure ends, that is, how much of the structure contributes to the direct field response. For example, one approach to creating simplified models of trusses has been to use Timoshenko beams to represent straight truss members [17]. The Timoshenko model captures the gross response characteristics of the truss, but not behaviors of the individual members. The wave model can be used to create an exact representation of the Timoshenko model [11], from which the direct field can be found. However, such an approach has not been found to yield good compensator designs when implemented on trusses, because the direct field response of the Timoshenko beam is not the same as the truss. As a result, the compensator derived from the local model is in error.

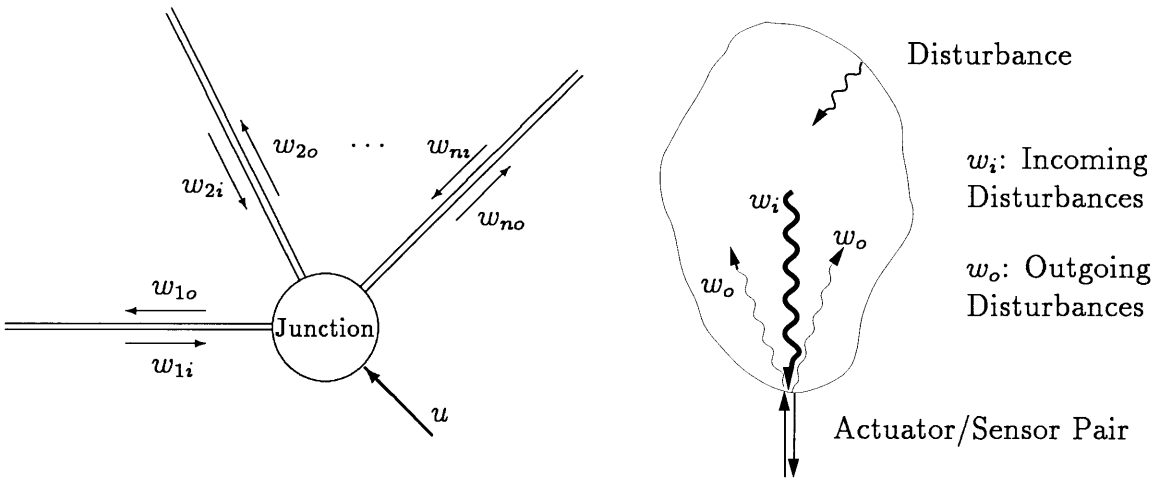

Figure 2.6: Generic wave junction

Figure 2.7: Arbitrary structure

The truss has the necessary waveguide-like characteristics to fit well into the wave model framework. More complicated structures such as plates also have a PDE description, now in two spatial dimensions. Theoretically it is possible to formulate a two-dimensional wave description for the purposes of control design, but this has not been done. Even more complicated structures, with more intricate geometries, will compound the difficulty.

Critical damping MacMartin uses an alternative method for generalizing the wave-based local model [16]. The structure is represented as an arbitrary body subject to a control force f and with a collocated, dual measurement u.

Control action produces a disturbance wave which travels out into the structure. When it reaches a boundary, it reflects. Some of the energy reflects back towards the control location, to become an incoming wave. It scatters again, mixing with other waves at that location to produce the physical motion. In steady state, the relative phasing of the incoming and outgoing waves w_i and w_o determines whether constructive or destructive interference occurs. The concept is identical to the wave model, however, there is no mathematical way to model the directional behavior of the waves. Instead, the local behavior is approximated by characterizing the response as the combination of the direct field G_d and a reverberant field, which carries the

information about the rest of the structure:

$$u = G_d f + d \tag{2.35}$$

The sensed output u and control force f are dual. The disturbance d is composed of energy reflected from the rest of the structure, combined with energy due to other forces acting elsewhere in the structure. The reverberant portion of the structural response is included in d.

One can derive an approximation to the direct field by creating a full-order model, with all of the poles critically damped. By damping the global poles, the amount of reflected energy returning to the measurement u is reduced, thus the response approaches the direct field response. A local model derived from a reverberant model is termed a *dereverberated model*, and is only an approximation to the direct field.

Log averaged local model The critically damped approximation to the direct field is justified using energy arguments. The effect is to average the logarithm of the response [18, 13]. A second approximation to the direct field can be found by explicitly averaging the logarithm of the frequency response. The goal is a model which captures the "backbone" of the reverberant transfer function from a measurement of the reverberant data. Typically the model is parameterized as a low order set of poles and zeros, for example 3-4 real poles. A cost is formed, composed of the logarithmic error between the reverberant transfer function and the direct field approximation, integrated over frequency:

$$J = \int_{\omega_1}^{\omega_2} \left(\log G(\jmath\omega) - \log G_{fit}(\jmath\omega)\right)^2 \mathrm{d}\omega \tag{2.36}$$

where

$$G_{fit}(\jmath\omega) = \left| k \frac{\sum_i (s - z_i)}{\sum_j (s - p_j)} \right|_{s=\jmath\omega} \tag{2.37}$$

The cost J is minimized using a numerical search procedure.

The log averaged model will capture the same behavior as the critically damped model. The computational cost is considerably smaller, and the resulting model will

be low order relative to the plant. In contrast, the critically damped fit requires a full-order model, which is computer-intensive to generate. If only measurement data is available, the model must be obtained via a curve-fitting routine. Further, the resulting model will be high-order relative to the log averaged model.

Example 2: Rod direct field approximation. The two dereverberated modeling techniques will be demonstrated on the rod example of the previous section. The exact direct field will be obtained from the wave model. A critically damped dereverberated model, and a real-pole log averaged model will be obtained. Two input/output locations will be used. In the first case, the dereverberated response from left end force q to collocated displacement is found. Second, the dereverberated response of external force at junction 2 to collocated displacement is modeled.

Exact Direct Field. At the left, free end, the exact direct field response is given by Ψ_1, Equation 2.25:

$$\Psi_1 = \frac{1}{ikEA} \tag{2.38}$$

By Equation 2.17, the direct field response as a function of frequency is

$$\Psi_1(\omega) = \frac{1}{A\sqrt{\rho E}} \frac{1}{i\omega} = \frac{1}{A\sqrt{\rho E}} \frac{1}{s} \tag{2.39}$$

At junction 2, the direct field due to force actuation is given by Ψ_2 as

$$\Psi_{2_f} = \frac{1}{2ikEA} \begin{bmatrix} -ikEA & -1 \\ ikEA & -1 \end{bmatrix} \begin{bmatrix} 0 \\ 1 \end{bmatrix} = \begin{bmatrix} \frac{-1}{2ikEA} \\ \frac{-1}{2ikEA} \end{bmatrix} \tag{2.40}$$

since $Q_2 = \begin{bmatrix} 0 \\ 1 \end{bmatrix} F_{ext}$. Equation 2.40 gives the response from F_{ext} to $u = \begin{bmatrix} u_{2_l} \\ u_{2_r} \end{bmatrix}$. The measurement is dual to the actuation, so the direct field is in terms of inertial (or *absolute*) displacement:

$$\Delta_{abs} = u_{2_r} + u_{2_l} = \frac{1}{2} \begin{bmatrix} 1 & 1 \end{bmatrix} \begin{bmatrix} u_{2_l} \\ u_{2_r} \end{bmatrix} \tag{2.41}$$

so that the exact direct field from external force to displacement at junction 2 is

$$\begin{bmatrix} 1 & 1 \end{bmatrix} \begin{bmatrix} \frac{-1}{2ikEA} \\ \frac{-1}{2ikEA} \end{bmatrix} = \frac{-1}{ikEA} = \frac{1}{A\sqrt{\rho E}} \frac{1}{i\omega} = \frac{1}{A\sqrt{\rho E}} \frac{1}{s} \tag{2.42}$$

which is the same as the free end case.

Dereverberated Models. The critically damped and real pole approximations are generated from reverberant data from a wave model. The full order model is a 40-state fit to the reverberant transfer function from 0.1 to 10 Hz. The poles are then critically damped, giving a 40^{th}-order dereverberated model. The log average fit is a 2-real-pole fit to the reverberant transfer function.

Comparison of Dereverberated Models with Direct Field. The transfer functions of the resulting models are plotted against the reverberant transfer function in Figures 2.8 and 2.9. Figure 2.8 shows the behavior when the input is at the left end of the rod, junction 1. Notice that the zeros of the reverberant data are evenly spaced with frequency. The exact direct field lies along the backbone of the reverberant response. Figure 2.9 shows the behavior when the input is located in the midsection of the rod. The reverberant zeros have shifted in frequency, relative to the end force case. The critically damped and log averaged models approximate the reverberate field, so they vary as the reverberant zeros change. That is, they vary depend on the input location. The exact direct field, on the other hand, is the same at any cross-section.

The exact direct field for the rod, when plotted on a log-log axis, is a line with slope -1. Both measurement approximations are in error at the lower and higher frequencies. Below the first mode, the reverberant data deviates from the exact direct field. Any approximation will not be valid below the first mode. The log average model captures the high frequency behavior well. The critically damped model shows more high-frequency error, due to truncation effects. The poles and zeros of the 40-state model occur in complex pairs. The relative degree of the full-

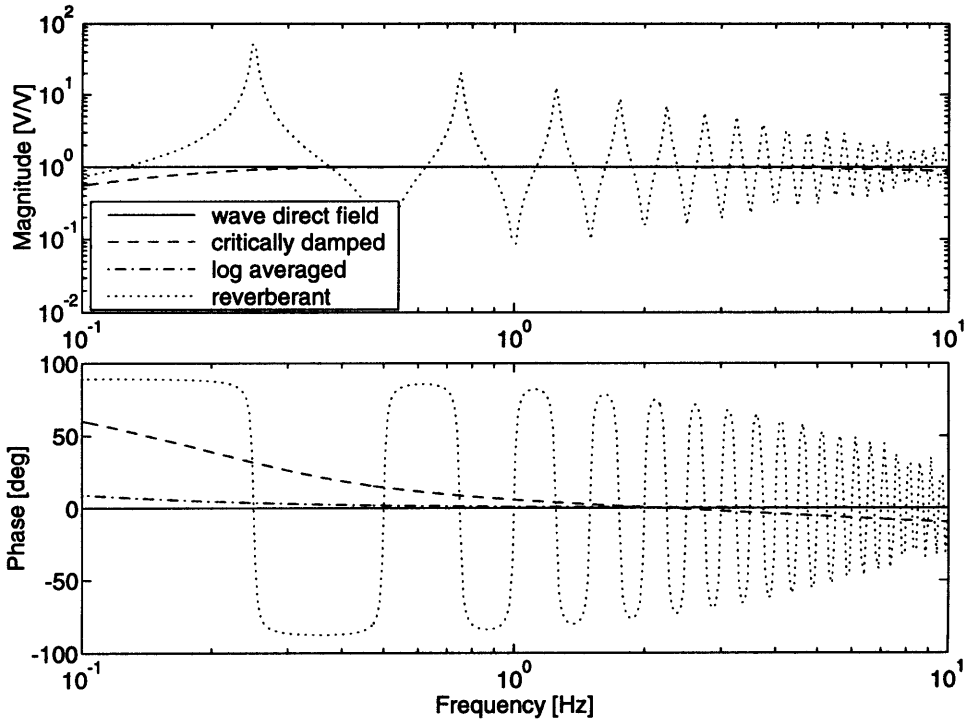

Figure 2.8: Rod example: Differentiated direct field vs critically damped and log averaged approximations, for end force to end velocity.

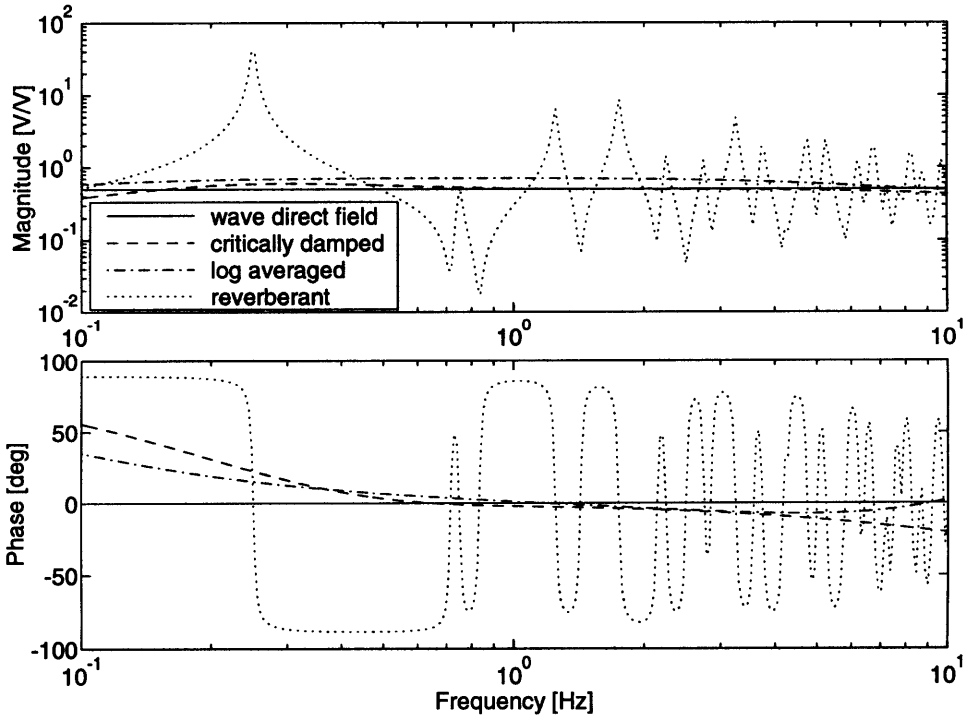

Figure 2.9: Rod example: Differentiated direct field vs critically damped and log averaged approximations, for x_2 force to velocity.

order model must therefore be $2n$, where n is an integer. So at high frequencies the critically damped approximation cannot capture the -1 slope of the exact direct field.

It should be noted that both reverberant transfer functions were derived from wave models, which are exact solutions of the rod equations of motion. Reverberant data from finite element models will have errors due to discretization, which will add additional error. Some structures such as the rod are amenable to approximation techniques such as log averaging, due in part to the fact that there are only two reflection points in the structure. In general, a complex structure can have many discontinuities and partial discontinuities which will affect the local response. The error inherent in the approximations is an unavoidable result.

As a final note, it is important to realize that the log averaging technique is valid in regions of high modal density, when the modal spacing is on the order of the half power bandwidth of the modes. It is not intended, and is of questionable validity, when the modal spacing is large. For many physical systems, the modal spacing may not be enough to justify the use of a log averaged model. The log averaging technique may be the only route available to a local model suitable for impedance matching local control.

2.1.2 Impedance Matching control design

The optimal control problem is posed as the minimization of some cost by proper choice of a dynamic compensator $K(s)$. The cost is often stated as some global objective , such as keeping one point motionless or keeping two or more points aligned. When the structural model has been reduced to a local model, it is not possible to explicitly state a global objective. The global cost must be stated via a local objective. Additionally, the controller must be stable when applied to the global system.

An example of a local objective is the maximization of power absorption by the control, or equivalently, the minimization of total power. Such a power objective can be thought of as maximizing damping, which always improves performance. Pure damping is the globally optimal control strategy in two cases: 1) when the dynamics of the plant are uncertain or modally dense [12], and 2) when the disturbance and/or

the performance cannot be characterized well. The stability of the closed loop system can be guaranteed in the power framework by requiring that no power be put into the structure at any frequency. For a conservative system, the amount of power returning to the control location will always be less than or equal to the amount generated by the control. Thus if power is always attenuated, the closed loop system will be stable. The following chapter is a summary of the work of Miller [11]. The reader is referred to that reference for further information.

The unconstrained power-minimizing compensator will in general be *non-causal*. That is, the control requires future information about the disturbance. Such a non-causal control cannot be implemented in real time. Thus additional constraints must be placed in the problem to achieve a causal, implementable compensator. Two equivalent power formulations are presented. First, the impedance match is derived in closed-form in the wave domain. Second, the general local model of Section 2.1.1 is used to derive the impedance match for the general structure.

Unconstrained Wave Impedance Match

The wave impedance match is found by describing the power at the control junction as a function of incoming and outgoing waves. Parameterizing the control as feedforward of incoming waves, the total junction power as a function of the feedforward matrix is minimized. The unconstrained impedance match is determined by choosing the feedforward matrix to minimize power at all frequencies, without regard for causality.

The instantaneous power at a cross-section can be written as the product of internal stresses f and deflections u:

$$P = \frac{\partial u(x,t)^T}{\partial t} f(x,t) \tag{2.43}$$

where u and f are vectors whose components are of like type - linear velocity and force, rotational velocity and moment. By averaging Equation 2.43 over all time, the expected value of junction power can be described:

$$P_{avg} = \lim_{T\to\infty} \frac{1}{2T} \int_{-T}^{T} \frac{\partial u(x,t)^T}{\partial t} f(x,t) \mathrm{d}t \tag{2.44}$$

The time averaged power flow P_{avg} can then be transformed into the frequency domain using the Power Theorem , a variation of Parseval's Theorem:

$$P_{avg} = \frac{1}{2\pi}\int_{-\infty}^{\infty} i\omega u(x,\omega)^H f(x,\omega)\mathrm{d}\omega \tag{2.45}$$

The integrand of Equation 2.45 describes the steady-state power as a function of frequency. Using the wave transformation Y, the steady state power flow can be written in terms of wave modes w:

$$\begin{aligned}
P_{avg} &= Re\left\{\imath\omega\, u^H f\right\} && (2.46)\\
&= Re\left\{\imath\omega \begin{bmatrix} w_i^H & w_o^H \end{bmatrix} \begin{bmatrix} Y_{ui}^H \\ Y_{uo}^H \end{bmatrix} \begin{bmatrix} Y_{fi} & Y_{fo} \end{bmatrix} \begin{bmatrix} w_i \\ w_o \end{bmatrix}\right\} && (2.47)\\
&= Re\left\{\imath\omega \begin{bmatrix} w_i^H & w_o^H \end{bmatrix} \begin{bmatrix} Y_{ui}^H Y_{fi} & Y_{ui}^H Y_{fo} \\ Y_{uo}^H Y_{fi} & Y_{uo}^H Y_{fo} \end{bmatrix} \begin{bmatrix} w_i \\ w_o \end{bmatrix}\right\} && (2.48)\\
&= \frac{\imath\omega}{2} \begin{bmatrix} w_i^H & w_o^H \end{bmatrix} \left(\begin{bmatrix} Y_{ui}^H Y_{fi} & Y_{ui}^H Y_{fo} \\ Y_{uo}^H Y_{fi} & Y_{uo}^H Y_{fo} \end{bmatrix} - \begin{bmatrix} Y_{fi}^H Y_{ui} & Y_{fo}^H Y_{ui} \\ Y_{fi}^H Y_{uo} & Y_{fo}^H Y_{uo} \end{bmatrix} \right) \begin{bmatrix} w_i \\ w_o \end{bmatrix} && (2.49)\\
&= \frac{1}{2} w^H P w && (2.50)
\end{aligned}$$

where the power matrix P is

$$P = \imath\omega \left(\begin{bmatrix} Y_{ui}^H Y_{fi} & Y_{ui}^H Y_{fo} \\ Y_{uo}^H Y_{fi} & Y_{uo}^H Y_{fo} \end{bmatrix} - \begin{bmatrix} Y_{fi}^H Y_{ui} & Y_{fo}^H Y_{ui} \\ Y_{fi}^H Y_{uo} & Y_{fo}^H Y_{uo} \end{bmatrix} \right) \tag{2.51}$$

Since P is hermitian , P_{avg} is always real.

The power matrix, Equation 2.50, describes the steady-state power flow through the junction in terms of incoming waves w_i and outgoing waves w_o. Power is carried by incoming waves, by outgoing waves, and by the interaction of incoming and outgoing waves. Incoming power is defined to be negative power. Outgoing power is positive. If the junction is non-dissipative, the outgoing power will equal the incoming power and the net power will be zero. If the junction is dissipative, for example due to control forces adding damping, the net power P_{avg} becomes negative. The control objective can be stated as minimizing the net power.

A cost J is defined, composed of junction power and control effort:

$$\begin{aligned} J &= \frac{1}{2}E\left[\int_{-\infty}^{\infty}\left(w^H P w + Q^H R Q\right)\,\mathrm{d}\omega\right] \\ &= \frac{1}{2}E\left[\int_{-\infty}^{\infty}\left(\begin{bmatrix} w_i^H & w_o^H \end{bmatrix} P \begin{bmatrix} w_i \\ w_o \end{bmatrix} + Q^H R Q\right)\,\mathrm{d}\omega\right] \end{aligned} \tag{2.52}$$

The control penalty R is needed to ensure finite control effort.

Using the junction relation, Equation 2.8 , the control can be expressed as feedforward of incoming wave modes, $Q = Fw_i$, so that the closed loop scattering matrix is given by

$$S_{cl} = S + \Psi F$$

The cost J can be written in terms of the incoming waves w_i and the feedforward matrix F:

$$\begin{aligned} J &= \frac{1}{2}E\int_{-\infty}^{\infty}\left\{w_i^H\begin{bmatrix} I & S^H + F^H\Psi^H \end{bmatrix} P \begin{bmatrix} I \\ S+\Psi F \end{bmatrix} w_i + w_i^H F^H R F w_i\right\}\,\mathrm{d}\omega \\ &= \frac{1}{2}tr\left(E\left[\int_{-\infty}^{\infty}\left(\begin{bmatrix} I & S^H + F^H\Psi^H \end{bmatrix} P \begin{bmatrix} I \\ S+\Psi F \end{bmatrix} + F^H R F\right) w_i w_i^H\,\mathrm{d}\omega\right]\right) \\ &= \frac{1}{2}tr\left(\int_{-\infty}^{\infty}\left(\begin{bmatrix} I & S^H + F^H\Psi^H \end{bmatrix} P \begin{bmatrix} I \\ S+\Psi F \end{bmatrix} + F^H R F\right)\Phi_{w_i w_i}\,\mathrm{d}\omega\right) \end{aligned} \tag{2.53}$$

where the cost is expressed in terms of the expected value of the incoming wave modes: $\Phi_{w_i w_i} = E\left[w_i\, w_i^H\right]$.

Partitioning the power matrix P:

$$P = \begin{bmatrix} P_{ii} & P_{io} \\ P_{oi} & P_{oo} \end{bmatrix} \tag{2.54}$$

the cost is given by

$$\begin{aligned} J = \frac{1}{2}\int_{-\infty}^{\infty} tr\Big(\Big[&P_{ii} + (S^H + F^H\Psi^H)P_{oi} + P_{io}(S+\Psi F) + \\ &(S^H + F^H\Psi^H)P_{oo}(S+\Psi F)\Big]\,\Phi_{w_i w_i}\Big)\,\mathrm{d}\omega \end{aligned} \tag{2.55}$$

Allowing any feedforward matrix F, the cost of Equation 2.55 can be set to zero

frequency-by-frequency, independent of $\Phi_{w_i w_i}$. The feedforward matrix F which accomplishes this is given by ([11]):

$$F = -\left[\Psi^H P_{oo} \Psi + R \right]^{-1} \Psi^H \left[P_{oi} + P_{oo} S \right] \tag{2.56}$$

The control weighting R is needed when $\Psi^H P_{oo} \Psi$ is singular, and can be set to zero otherwise. Equation 2.56 can be transformed to feedback of physical variables u using the transformation matrix Y.

The cross-sectional variables have the form $y = \begin{bmatrix} u \\ f \end{bmatrix}$ where $u^T f$ is power. The actuation Q can be any linear combination of internal deflection rates u and stresses f. Given Q, one can define a set of sensed variables U_s as a combination of u and f, where $U_s^T Q$ is power. In other words, the sensed variables U_s are the duals of the actuated variables Q. If there are $2n$ independent cross-sectional variables, there are n independent actuators, i.e. Q is an $n \times 1$ vector. If a subset Q is used, i.e. m actuators, with $m < n$, Q can be written as $e\tilde{Q}$. The $n \times m$ matrix e is a matrix of ones and zeros.

Using the junction transformation Y, the new control variables can be related to the controlled junction wave modes:

$$\begin{bmatrix} U_s \\ Q \end{bmatrix} = T \begin{bmatrix} u \\ f \end{bmatrix} = TY \begin{bmatrix} w_i \\ w_o \end{bmatrix} \tag{2.57}$$

Inverting and partitioning Equation 2.57 gives

$$\begin{bmatrix} w_i \\ w_o \end{bmatrix} = (TY)^{-1} \begin{bmatrix} U_s \\ Q \end{bmatrix} = \begin{bmatrix} (TY)^{-1}_{11} & (TY)^{-1}_{12} \\ (TY)^{-1}_{21} & (TY)^{-1}_{22} \end{bmatrix} \begin{bmatrix} U_s \\ Q \end{bmatrix} \tag{2.58}$$

where the incoming waves can be described in terms of the actuated and sensed variables:

$$w_i = (TY)^{-1}_{11} U_s + (TY)^{-1}_{12} Q = (TY)^{-1}_{11} U_s + (TY)^{-1}_{12} e\tilde{Q} \tag{2.59}$$

Using the feedforward matrix F, the control can be expressed in terms of feedback of physical variables:

$$\tilde{Q} = F w_i$$

$$
\begin{aligned}
&= F(TY)_{11}^{-1} U_s + F(TY)_{12}^{-1} e\tilde{Q} \\
&= \left[I - F(TY)_{12}^{-1} e\right]^{-1} F(TY)_{11}^{-1} U_s \\
&= GU_s
\end{aligned} \tag{2.60}
$$

where G is the desired feedback matrix.

Unconstrained General Impedance Match

MacMartin extended the structural impedance matching results to general systems [16]. The following is a summary and discussion of that work. The dereverberated model G_d is the log averaged or critically damped model of Section 2.1.1. It captures the portion of the response due to the actuation f. Since u and f are dual, the control problem can be stated as a SISO formulation. G_d is a therefore a scalar. All information about the global structure is lumped into the disturbance d and is treated as uncorrelated with the actuation.

The cost is the average power flow at the control location, as in Equation 2.44, which can again be expressed as a function of frequency through Parseval's Theorem:

$$
P_{avg} = \lim_{T\to\infty} \frac{1}{2T} \int_{-T}^{T} \frac{\partial u(x,t)^T}{\partial t} f(x,t) \mathrm{d}t = \frac{1}{2\pi} \int_{-\infty}^{\infty} i\omega u(x,\omega)^H f(x,\omega) \mathrm{d}\omega \tag{2.61}
$$

In the wave power minimization, the power is expressed in terms of wave modes w_i and w_o. For the general structure, the cost can be expressed in terms of the dereverberated model, $G_d(s)$, the compensator, $K(s)$, and the disturbance $d(s)$.

The control force f is expressed as a feedback of the measurement u:

$$
f(s) = -K(s)u(s) = -K(s)G_d(s)f(s) - K(s)d(s) \tag{2.62}
$$

so that

$$
\begin{aligned}
f(s) &= -(1 + K(s)G_d(s))^{-1} K d(s) \\
&= H(s)d(s)
\end{aligned} \tag{2.63}
$$

The measurement is

$$
u(s) = (1 + G_d(s)H(s))d(s) \tag{2.64}
$$

The expressions for u and f above can be substituted into Equation 2.61.

The integrand of Equation 2.61, as a function of the Laplace variable s, is then

$$J = d^* \left(H^*(1 + G_d H) + (1 + G_d H)^* H \right) d \tag{2.65}$$

where the notation $(.)^*$ is the extension of the Hermitian operator to the complex plane, i.e. $G_d^*(s) = G_d(-s)^T$. The cost in Equation 2.65 can be expressed in terms of its trace:

$$\begin{aligned} J &= E\left\{ tr\left(dd^* \left(H^*(1 + G_d H) + (1 + G_d H)^* H \right) \right) \right\} \\ &= tr\left(\left(H^*(1 + G_d H) + (1 + G_d H)^* H \right) \Phi_{dd} \right) \end{aligned} \tag{2.66}$$

where $\Phi_d d = E\left\{ dd^* \right\}$ is the spectrum of the incoming power.

Using the symmetry of Equation 2.66, $H^* = H$ at the optimum, so that the derivative with respect to H can be calculated:

$$\frac{\partial J}{\partial H} = 2\Phi_{dd} + \Phi_{dd} H (G_d + G_d^*) + (G_d + G_d^*) H \Phi_{dd} \tag{2.67}$$

Setting Equation 2.67 equal to zero, the H which minimizes Equation 2.66 frequency-by-frequency can be found:

$$H_{opt} = -(G_d + G_d^*)^{-1} \tag{2.68}$$

Solving for the feedback compensator $K(s)$ from Equation 2.63:

$$\begin{aligned} K_{opt} &= -H_{opt}(1 + G_d H)^{-1} \\ &= \frac{1}{G_d^*} \end{aligned} \tag{2.69}$$

Equation 2.69 explicitly shows the non-causal nature of the impedance match. Only if G_d is constant with frequency will the compensator $K(s)$ be causal, and in fact the optimal compensator will be constant gain feedback.

In general the compensator will be a function of $(-s)$. Left half-plane (LHP) dynamics are characteristics of both unstable systems and *non-causal* systems. A non-causal system is stable in negative time. Information about the future response is required to determine the current control. Such a control cannot be implemented

in real time. It is therefore necessary to minimize the cost functionals Equation 2.55 and Equation 2.66 subject to a restriction on the causality of the compensator K(s).

The resulting causal compensator is an approximation of the exact impedance match. The fidelity of the match will vary with the degree of non-causality of the impedance match, and the frequency range over which power absorption is desired. Hence, while the unrestricted compensator minimizes the cost independent of the disturbance spectrum, the causal approximation must be a function of the incoming disturbance spectrum. The approximation will more closely match the noncausal compensator at frequencies where the disturbance energy is higher.

The sensor and actuator need only be dual to within a temporal integral or derivative. Strictly speaking, the only true dual pair is force and displacement rate. Structural impedance is defined as rate over force. The transfer function from force to rate is a *mobility*. The mobility $G(s)$ can be found by measuring the response from force actuation to a rate sensor, or from integrated force to displacement. That is,

$$G(S) = \frac{sx}{F} = \frac{x}{\frac{1}{s}F} \tag{2.70}$$

The designer has some freedom in choosing the sensor and actuator pair.

Furthermore, the temporal integration, or derivative in Equation 2.70, can be included in the compensator. For example, the response of the dual pair of force and rate is equivalent to filtering the response of force to displacement through a differentiator. Thus, for a control pair consisting of force and displacement, the necessary dynamics to create an impedance can be included in the compensator.

Example 3: Rod power minimization The impedance-matching compensator for a rod can be derived using the wave model in Section 2.1.1. The power absorbing abilities of the impedance match will be examined when both actuators are available, as well as when only external force is used.

For the controlled, midsection junction, the scattering and generation matrices are:

$$S_2 = \begin{bmatrix} 0 & 1 \\ 1 & 0 \end{bmatrix}$$

$$\Psi_2 = \begin{bmatrix} \frac{-1}{2} & \frac{-1}{2ikEA} \\ \frac{1}{2} & \frac{-1}{2ikEA} \end{bmatrix}$$

The matrices P_{oi}, P_{oo} are the partitions of the power matrix P, Equation 2.51. With the elements of Y_2 as defined in Equation 2.28,

$$P_{oo} = 2kEA\omega \begin{bmatrix} -1 & 0 \\ 0 & 1 \end{bmatrix} \tag{2.71}$$

$$P_{oi} = \begin{bmatrix} 0 & 0 \\ 0 & 0 \end{bmatrix} \tag{2.72}$$

The signs on the diagonal elements of P_{oo} indicate that leftward-traveling waves carry positive power. The signs of both diagonal elements of P_{oo} can be made positive, redefining power flow outward as positive, without loss of validity.

When both Δ_{rel} and F_{ext} are available as actuators, the optimal feedforward is

$$F_1 = \begin{bmatrix} -1 & 1 \\ ikEA & ikEA \end{bmatrix} \tag{2.73}$$

The physical feedback relation G is given by Equation 2.60, which requires that the matrix TY be known. The transformation T gives the transformation from independent cross-sectional variables to actuated and sensed variables:

$$\begin{bmatrix} \Delta_{abs} \\ F_{rel} \\ \Delta_{rel} \\ F_{abs} \end{bmatrix} = \begin{bmatrix} 1 & 1 & 0 & 0 \\ 0 & 0 & 1 & 1 \\ -1 & 1 & 0 & 0 \\ 0 & 0 & -1 & 0 \end{bmatrix} \begin{bmatrix} u_l \\ u_r \\ (EA\frac{\partial u}{\partial x})_l \\ (EA\frac{\partial u}{\partial x})_r \end{bmatrix} \tag{2.74}$$

Note that the lower two rows of T are the boundary condition for junction 2. The junction transformation Y_2 is given in Equation 2.28. Equation 2.73 can then be expressed as feedback: of $U_s = \begin{bmatrix} \Delta_{abs} \\ F_{rel} \end{bmatrix}$:

$$G_2 = \begin{bmatrix} 0 & \frac{1}{ikEA} \\ ikEA & 0 \end{bmatrix} \tag{2.75}$$

where $Q = G_2 U_s$. Using the expression for the wave number, $k = \sqrt{\frac{\rho}{E}}\omega$ (Equation 2.17), the control can be expressed as a function of frequency:

$$G_1 = \begin{bmatrix} 0 & \frac{-1}{A\sqrt{\rho E}i\omega} \\ -A\sqrt{\rho E}i\omega & 0 \end{bmatrix} \tag{2.76}$$

Since $Q = \begin{bmatrix} \Delta_{rel} \\ F_{ext} \end{bmatrix}$ and $U_s = \begin{bmatrix} F_{rel} \\ \Delta_{abs} \end{bmatrix}$, the feedback given by Equation 2.76 is uncoupled feedback through dual variables:

$$\begin{aligned} \Delta_{rel} &= \frac{-1}{A\sqrt{\rho A}i\omega} F_{rel} \\ F_{ext} &= -A\sqrt{\rho A}i\omega \Delta_{abs} \end{aligned} \tag{2.77}$$

The closed loop scattering matrix can be found from Equation 2.12:

$$S_{cl_1} = \begin{bmatrix} 0 & 0 \\ 0 & 0 \end{bmatrix} \tag{2.78}$$

The ability to zero all the elements in the closed loop scattering matrix is due in part to having a sufficient number of independent actuators at the cross-section. In general, the closed loop scattering matrix cannot be the zeroed. The following example demonstrates a case in which the number of actuators at the junction is not sufficient to zero the closed loop scattering matrix. The impedance match then controls those combinations of cross-sectional variables which carry the greatest portion of the power.

The closed loop power flow in the rod is a function of the eigenvalues of the closed loop power matrix:

$$P_1 = 2EAk\omega \begin{bmatrix} -1 & 0 \\ 0 & -1 \end{bmatrix} \tag{2.79}$$

which has 2 eigenvalues of $-2EAk\omega$. Since the eigenvalues are always negative, the compensator never produces power, and the closed loop system will be stable.

If the actuator is limited to F_{ext}, that is, $\tilde{Q} = Q \begin{bmatrix} 0 \\ 1 \end{bmatrix}$, the feedforward compensator which minimizes junction power is

$$F_2 = \begin{bmatrix} ikEA & ikEA \end{bmatrix} \tag{2.80}$$

The feedback matrix is

$$G_2 = \begin{bmatrix} A\sqrt{\rho E}i\omega & 0 \end{bmatrix} \tag{2.81}$$

which is collocated feedback of rate to force. Rate feedback is the typical active damping compensator. For the rod, rate feedback at this specific gain gives the most damping possible. In this case the optimal damping compensator is causal.

The closed-loop scattering matrix is

$$S_{cl_2} = \begin{bmatrix} -\frac{1}{2} & \frac{1}{2} \\ \frac{1}{2} & -\frac{1}{2} \end{bmatrix} \tag{2.82}$$

The closed loop power matrix is

$$P_2 = 2EAk\omega \begin{bmatrix} -\frac{1}{2} & -\frac{1}{2} \\ -\frac{1}{2} & -\frac{1}{2} \end{bmatrix} \tag{2.83}$$

which has eigenvalues of 0 and $-2EAk\omega$. Again the closed loop system never produces power. However, the junction cannot remove all the power arriving from the disturbance (as was the case when both Δ_{rel} and F_{ext} were actuated). In fact, certain wave mode combinations pass through the controlled junction without dissipation.

Figure 2.10 shows the transfer function from disturbance force q to collocated velocity in open loop and in closed loop. When both actuators are available, the compensator removes all the power arriving at the junction, and the global modes are completely damped. When force is the only actuator, the compensator cannot remove all the power crossing the junction. As a result, the damping in the closed loop poles is not as high. The single actuator cannot remove all the disturbance energy because it travels both through a combination of absolute force with inertial displacement, and through relative force and relative displacement. When only a subset of those variables are controlled, energy has an uncontrolled path through which to travel.

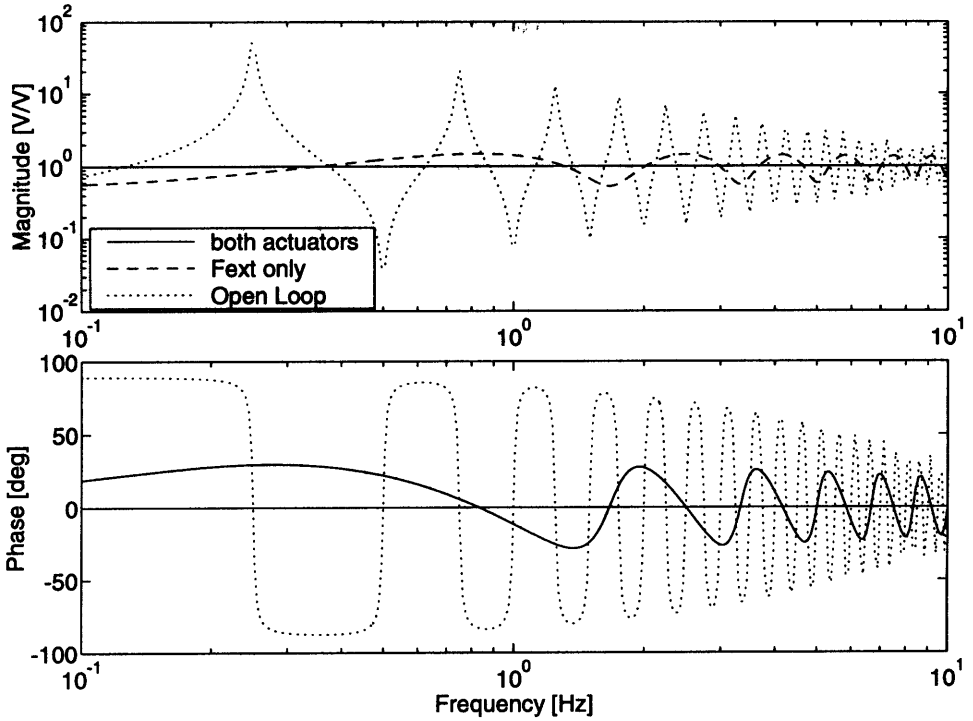

Figure 2.10: Open and closed loop transfer functions from q to collocated velocity at the left end.

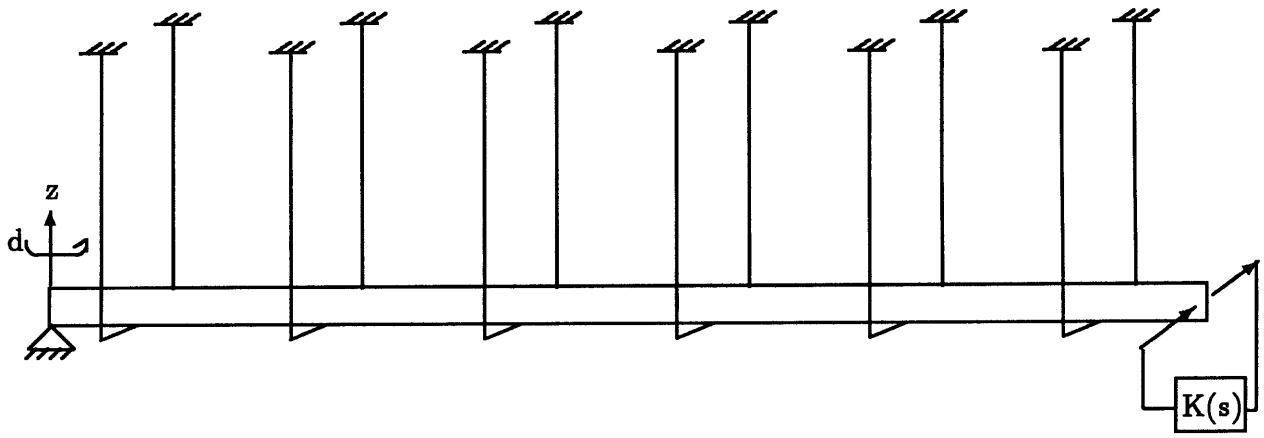

Figure 2.11: The Brass Beam testbed at SERC. Disturbance energy is introduced at the left end using a torque actuator. The left end is controlled using a force actuator and collocated displacement sensor.

2.1.3 Brass Beam Impedance Matching Experiments

The impedance matching concept was validated on a brass beam testbed (Figure 2.11). The beam is controlled at the free end, through a force actuator and a collocated displacement sensor. At the pinned end, a torque motor acts to introduce a disturbance torque. A collocated angle sensor allows a transfer function measurement to be made. The first mode frequency is roughly 0.5 Hz, and the modal density is high. A high authority control technique such as LQG would be high order, due to the number of plant modes. Implementation would be difficult. Stability of the closed loop system would be difficult to guarantee, because of the difficulty in accurately characterizing the frequencies and damping ratios of the beam modes. However, the geometry of the beam is such that a Bernoulli-Euler (BE) wave model captures the horizontal-plane dynamics. Using the results of the last section, impedance matching compensators can be designed around the controlled junction at the free end.

Three compensators are implemented. Two are approximations to the impedance match. The third is rate feedback, the standard damping compensator. Predicted damping performance based on local power dissipation is compared among the three compensators. Experimental transfer functions are measured to confirm the predictions. The two compensators based on the impedance match are found to add more damping in a selected frequency range than rate feedback.

Hardware. The Brass Beam testbed consists of a 7.3 meter brass beam. The height to width ratio makes shear deformation negligible, leading to the use of a Bernoulli-Euler (BE) model. A wire suspension with six attachment points allows freedom of movement in the horizontal plane. The suspension is configured to suppress vertical bending and torsion. The beam properties are listed in Table 2.1. The boundary conditions are pinned-free.

A non-contacting sensor and actuator pair acts at the free, controlled end. The control force is created using a magnetic actuator, forcing against a small permanent magnet attached to the beam. Displacement is measured using an eddy-current non-contacting linear displacement sensor. The steel sensor target is located on the

Table 2.1: *BE* beam testbed parameters

width	10.2	cm
thickness	0.3175	cm
L	7.32	m
ρ A	2.85	$\frac{kg}{m}$
EI	31.1	Nm^2

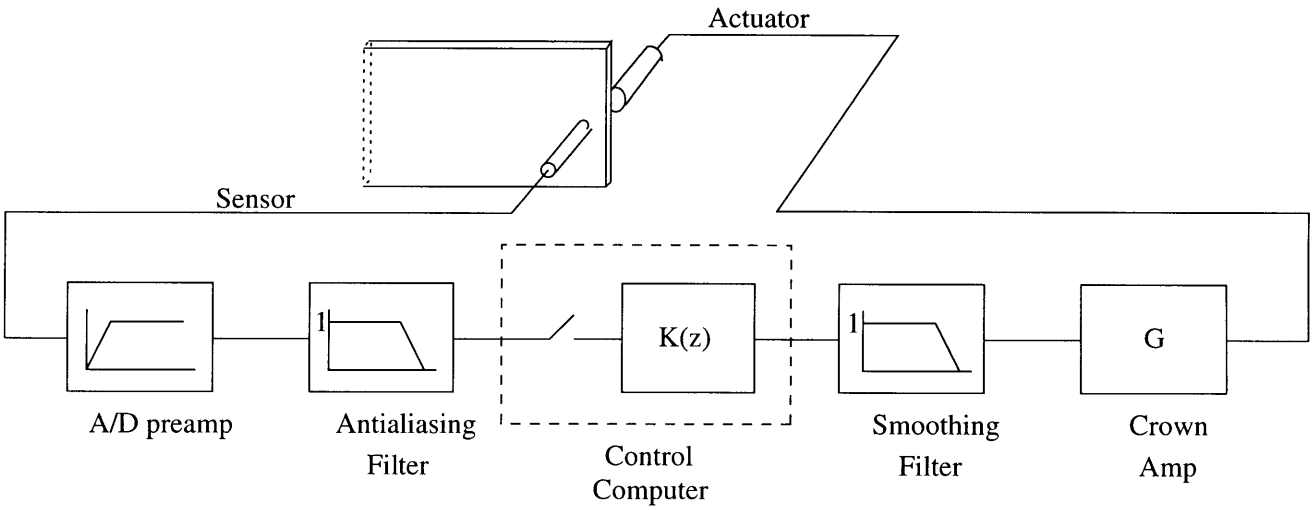

Figure 2.12: The real-time control computer and supporting amplifiers and filters.

opposite side of the beam from the permanent magnet, producing a collocated measurement. The use of the non-contacting sensors minimizes the mass loading at the beam tip.

The control is implemented using a digital control computer (Figure 2.12). The computer is a 68030-based processor running at 33 mHz, with a floating point SuperCard vector coprocessor. Controllers can be designed in a Matlab environment, discretized using standard Matlab commands, and run automatically at 6 kHz. The control loop includes a variable-gain A/D preamplifier with a high-pass filter, a 4 pole anti-aliasing Bessel filter, and a Crown amplifier driving the magnetic actuator.

The performance is evaluated by looking at the frequency response at the left end (see Figure 2.11). The fixed motor axis creates a pinned end condition, about which a torque proportional to voltage is applied. Collocated rotation is measured using a

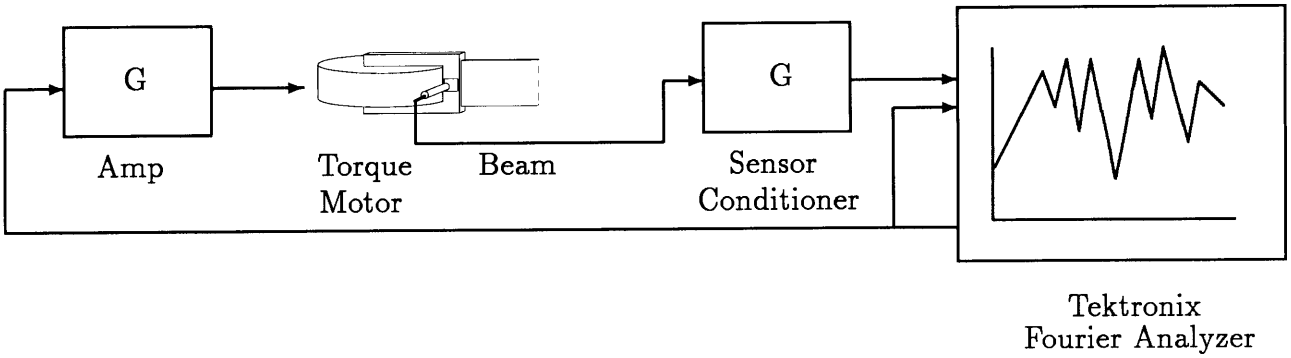

Figure 2.13: Performance is evaluated by measuring the pinned-end frequency response.

non-contacting linear displacement sensor which measures the motion of the torque motor bracket. Since the bracket is effectively rigid, and the angles induced are small, the measurement is proportional to beam tip rotation. Signal acquisition and transfer function estimation is performed using a Tektronics 2641 Fourier analyzer. Matlab.

Control Design. The modal density of the brass beam testbed is such that a full-state controller based on a global model will be extremely high order. The low open loop damping will make the performance sensitive to mismodeling. In contrast, a local controller, for example the impedance match of the last section, is designed using a local model. In this case the model will capture the behavior of the free end. As a result, sensitivity to mismodeling of the global system is low, and performance robustness is high.

Impedance Match. The impedance match can be found from the junction description of the right, controlled end. The PDE which describes the beam is

$$EI\frac{\partial^4 v}{\partial x^4} + \rho A\frac{\partial^2 v}{\partial t^2} = 0 \tag{2.84}$$

where E is Young's Modulus, I is the area moment of inertia, ρ is mass density, and A is cross-sectional area. Denoting the partial with respect to x as $(.)'$, the PDE in

state space form is

$$\frac{\partial}{\partial x}\begin{bmatrix} v \\ v' \\ -EIv''' \\ EIv'' \end{bmatrix} = \begin{bmatrix} 0 & 1 & 0 & 0 \\ 0 & 0 & 0 & \frac{1}{EI} \\ -\rho A\omega^2 & 0 & 0 & 0 \\ 0 & 0 & -1 & 0 \end{bmatrix}\begin{bmatrix} v \\ v' \\ -EIv''' \\ EIv'' \end{bmatrix} \tag{2.85}$$

where v is transverse displacement, v' is cross-section rotation, $-EIk^3v'''$ is internal shear stress, and EIv'' is internal moment. The dispersion relation is

$$k^4 - \frac{\rho A}{EI}\omega^2 = 0 \tag{2.86}$$

with solutions $\pm i\sqrt[4]{\frac{\rho A}{EI}}\sqrt{\omega}, \pm\sqrt[4]{\frac{\rho A}{EI}}\sqrt{\omega}$. The wave number k is therefore $\sqrt[4]{\frac{\rho A}{EI}}\sqrt{\omega}$. Four wave modes are supported:

$$v(x,t) = w_{rp}e^{-ikx+i\omega t} + w_{re}e^{-kx+i\omega t} + w_{lp}e^{ikx+i\omega t} + w_{le}e^{kx+i\omega t} \tag{2.87}$$

where the notation $(.)_{rp}, (.)_{lp}$ refers to propagating waves, and $(.)_{re}, (.)_{le}$ refers to evanescent waves. Evanescent waves have an exponentially decaying, rather than sinusoidal, spatial shape.

Differentiating Equation 2.87, the transformation matrix Y is found:

$$\begin{bmatrix} v \\ v' \\ -EIv''' \\ EIv'' \end{bmatrix} = \begin{bmatrix} 1 & 1 & 1 & 1 \\ -ik & -k & ik & k \\ -iEIk^3 & EIk^3 & iEIk^3 & -EIk^3 \\ -EIk^2 & EIk^2 & -EIk^2 & EIk^2 \end{bmatrix}\begin{bmatrix} w_{rp} \\ w_{re} \\ w_{lp} \\ w_{le} \end{bmatrix} \tag{2.88}$$

At the right end, $w_i = \begin{bmatrix} w_{rp} \\ w_{re} \end{bmatrix}$ and $w_o = \begin{bmatrix} w_{lp} \\ w_{le} \end{bmatrix}$. The right end boundary condition is

$$\begin{bmatrix} 0 & 0 & 1 & 0 \\ 0 & 0 & 0 & 1 \end{bmatrix}\begin{bmatrix} v \\ v' \\ -EIv''' \\ EIv'' \end{bmatrix} = \begin{bmatrix} q_F \\ q_M \end{bmatrix} \tag{2.89}$$

where q_F, q_M are externally imposed force and moment, respectively.

Using the correct submatrices from Equation 2.88 (i.e., *in* = *right* , *out* = *left*), the junction scattering and generation matrices are:

$$S = \begin{bmatrix} -i & 1+i \\ 1-i & i \end{bmatrix} \tag{2.90}$$

$$\Psi = \frac{1+i}{2EIk^3} \begin{bmatrix} -1 & -k \\ -1 & -ik \end{bmatrix} \tag{2.91}$$

The impedance matching compensator is also a function of the partitions of the power matrix P. For the beam, the matrices P_{oi}, P_{oo} are:

$$P_{oo} = 4EIk^3\omega \begin{bmatrix} 1 & 0 \\ 0 & 0 \end{bmatrix} \tag{2.92}$$

$$P_{oi} = 4EIk^3\omega \begin{bmatrix} 0 & 0 \\ 0 & -i \end{bmatrix} \tag{2.93}$$

Note that in contrast to the rod, the matrix P_{oi} is not the zero matrix. P_{oi} describes the power generated by the interaction of incoming and outgoing waves. The non-zero entry indicates that power is propagated by the interaction of incoming and outgoing evanescent waves.

The actuator is external force only: $Q = \begin{bmatrix} 1 \\ 0 \end{bmatrix} q_F = eq_F$. The impedance match feedforward matrix, F_{BE}, is

$$F_{BE} = EIk^3 \begin{bmatrix} -1-i & 1-i \end{bmatrix} \tag{2.94}$$

This can be transformed into physical variables using Equation 2.60. Since the actuator and sensor quantities Q and U_s are the cross-sectional variables $-EIv'''$ and v, T is the identity matrix. The actuator $\tilde{Q}$ is q_F. Therefore

$$q_F = \frac{EIk^3}{2}(1+i) \begin{bmatrix} 1 & 0 \end{bmatrix} \begin{bmatrix} v \\ v' \end{bmatrix} \tag{2.95}$$

Equation 2.95 shows that the impedance match uses collocated feedback through dual variables q_F and v. Using the expression for the wave number, $k = \sqrt[4]{\frac{\rho A}{EI}}\sqrt{\omega}$, the

feedback can be expressed as a function of ω.

$$\begin{aligned} q_F &= (\rho A)^{3/4}(EI)^{1/4}\frac{1+i}{2}\omega^{3/2}v \\ &= \frac{1}{\sqrt{2}}(\rho A)^{3/4}(EI)^{1/4}(-i\omega)^{3/2}v \\ &= \frac{1}{\sqrt{2}}(\rho A)^{3/4}(EI)^{1/4}(-s)^{3/2}v \end{aligned} \tag{2.96}$$

where s is the Laplace variable. Equation 2.96 shows that the impedance match for the BE beam is irrational and non-causal. Note that the impedance match would be the same at the free end of any BE beam with the same height, width and material properties, regardless of differences in the structure away from the control location (including its length).

The impedance match is proportional to $(-s)^{3/2}$, which is noncausal (due to the dependence on a fractional power of $-s$) and cannot be implemented in real time. Causal approximations must be created. The non-causal impedance match removes all the power in the controlled variables, at all frequencies. The causal approximations can only match the non-causal over a limited bandwidth, so the bandwidth to be damped must be known. The brass beam compensators will be designed to damp in a 1-10 Hz window. Three impedance matching approximations will be designed and implemented, and compared to rate feedback, the standard damping compensator.

Gain-Matching Approximation. The frequency dependence of this compensator is chosen to be $s^{3/2}$ and the gain is chosen to minimize Equation 2.55 (for $\Phi_{w_i w_i}=I$, i.e. unit disturbance power at all frequencies) . The optimal compensator is (from [11])

$$-\frac{1}{\sqrt{2}}(\rho A)^{3/4}(EI)^{1/4}s^{3/2} \tag{2.97}$$

The causal, irrational function $s^{3/2}$ can be approximated to arbitrary accuracy using a rational transfer function [19].

This causal approximation has the same magnitude at all frequencies as the optimal compensator of Equation 2.96. The phase deviation from the non-causal is a constant 90 degrees. The compensator never removes as much power as the optimal impedance match, but it removes the same amount of power at all frequencies. In

fact, Equation 2.97 can be shown to be the solution to the $\mathcal{H}_\infty$minimization of power flow for the BE beam [16].

The technique of matching the gain of the non-causal compensator, while allowing the phase to deviate, will be referred to as *gain-matching*. Note that the gain-matching compensator has not been shown to be the $\mathcal{H}_\infty$ power-minimizing compensator in all cases. A six-pole rational approximation to Equation 2.97 was created. However, the compensator could not be rolled off due to time delay caused by the digital implementation, and closed loop results cannot be presented.

Phase-Matching Approximation. The gain-matching compensator has a *phase-matching* counterpart. The phase of the non-causal compensator is 45 degrees. The causal function $s^{1/2}$ has the same phase as the impedance match at all frequencies. However, the logarithmic slope is $\frac{1}{2}$ decade per decade, rather than $\frac{3}{2}$. Thus the gain of the phase-matching compensator can only match the gain of the non-causal compensator at one frequency. At that frequency, the compensator will extract all the power in the beam. At higher and lower frequencies, the gain will deviate. To achieve damping in the 1-10 Hz window, the compensator gain is chosen so that the magnitude match occurs at 3Hz, the center of the (logarithmic) frequency range. A six-pole rational implementation is created.

Rational Approximation. The gain-matching and phase-matching compensators can be thought of as the extrema of a spectrum of approximations to the non-causal impedance match. The gain-matching compensator removes equal power at all frequencies. Thus it gives the best possible broadband performance. The phase-matching compensator gives perfect power absorption at one frequency, thus is in some sense a narrow-band compensator.

Compensators can be designed which allow phase and gain deviations to be traded off against one another. The design can be carried out by explicitly minimizing the closed loop power, Equation 2.55, where the spectrum of the disturbance power $\Phi_{w_i w_i}$ is band-limited. Alternatively, a set of poles and zeros can be fit to the magnitude

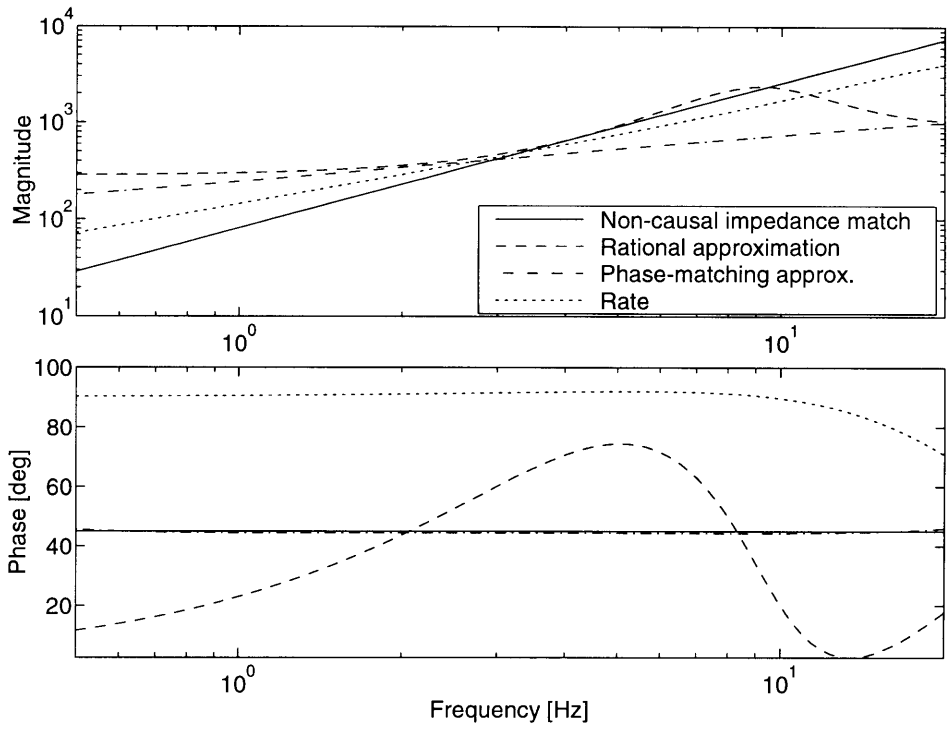

Figure 2.14: Non-causal impedance match and experimentally implemented approximations.

and phase of the non-causal impedance match. A frequency weighting can be used to determine the bandwidth of the fit. The smaller the bandwidth, the more accurate the fit. If a match at a single frequency is specified, the match will be exact.

For the brass beam experiments, a compensator was designed using the curve-fitting technique, with a boxcar weighting from 1 to 10 Hz.

Rate Feedback. Rate feedback is the standard damping compensator for a force actuator and a displacement sensor. As a comparison, a rate feedback compensator is implemented. The gain is chosen so that the magnitude of the rate compensator intersects the impedance match at 3 Hz.

Compensator Evaluation. The damping performance of the compensators can be predicted based on the deviation in magnitude and phase from the noncausal impedance match. Figure 2.14 shows the frequency response of the impedance match-

ing approximations, plotted against the non-causal impedance match. The solid line represents the impedance match.

The dashed curve is the rational approximation, arrived at by a 1-10 Hz curve fit to the non-causal solution. Notice that the magnitude matches the non-causal closely from 3 to above 9 Hz. The phase deviates in this range by a maximum of about 35 degrees, intersecting the non-causal at 2 and 8.5 Hz. Where the gain match is good, the phase match is worsened, and vice versa.

The phase-matching approximation matches the gain of the non-causal in the center of the 1-10 Hz window. At 3 Hz, the compensator has the correct gain and phase to remove all incident power. At higher and lower frequencies, the gain deviates from the non-causal.

The rate feedback gain is chosen such that the maximum damping occurs at 3Hz. The phase is never near the non-causal phase, so the rate compensator cannot achieve the damping of the impedance match at any frequency. Note, however, that the rate feedback gain remains close to the impedance match for a wide range. Thus damping can be expected to be more broadband than either of the impedance approximations. The gain matching compensator is not plotted because the time delay of the digital implementation caused instability in the closed loop.

Stability of the Impedance Matching Approximations. The non-causal impedance match removes all the power in the controlled cross-sectional variables at all frequencies. The stability of the system arises because power is never generated. The causal compensators were selected for their ability to mimic the gain and phase of the optimal non-causal impedance match. Stability, a global attribute, must be determined for each. However, using the fact that the plant is positive real, it follows from positive realness theory (see for example Reference [8]) that the closed loop system will be stable if the compensator is positive real, without recourse to a global model. All of the compensators were positive real.

Of course, no physical system is truly positive real. For the brass beam implementation, time delay causes the system phase to become unbounded. Since the control

computer was run at 6kHz, and the frequency range to be damped was from 1-10 Hz, time delay was ignored in the impedance matching approximations above, and did not affect performance. However, the delay was enough to cause instability in the gain-matching approximation. Design of impedance matching compensators in the presence of time delay will be treated in Chapter 3. For the present, note that the gain matching compensator has the highest slope of the compensators designed. The rolloff requirements are therefore impossible to accommodate using the given hardware.

Performance of the Impedance Matching Approximations. The objective is to introduce damping into the closed loop system. Modal damping, like stability, is a global characteristic. Rather than relying on a global model to predict performance, one still wants to judge the local compensators using a local model. Damping is accomplished by removing power from the system. By analytically determining the amount of power removed by the impedance matching approximations, the performance of the compensators can be compared.

The closed loop power matrix can be found from Equation 2.55. The closed loop power is a function of the feedforward gain matrix F:

$$P_{cl} = tr\left(\left[P_{ii} + S_{cl}^H P_{oi} + P_{io} S_{cl} + S_{cl}^H P_{oo} S_{cl}\right] \Phi_{w_i w_i}\right) \tag{2.98}$$

The controllers are implemented as a feedback of physical variables, G, from a single input to a single output. Writing the junction feedback as Gee^T, where e is the vector which determines the actuators used, the closed loop scattering matrix can be written in terms of the feedback:

$$S_{cl} = \left(I - \Psi G e e^T Y_{uo}\right)^{-1} \left(S + \Psi G e e^T Y_{ui}\right) \tag{2.99}$$

By assuming a disturbance spectrum $\Phi_{w_i w_i}$, Equation 2.98 can be solved at each frequency for the closed loop junction power.

Figure 2.15 shows the analytical junction power flow for the three implemented compensators (Equation 2.98), compared to the non-causal impedance match. The disturbance input spectrum has been frequency-shaped to have unit power at all

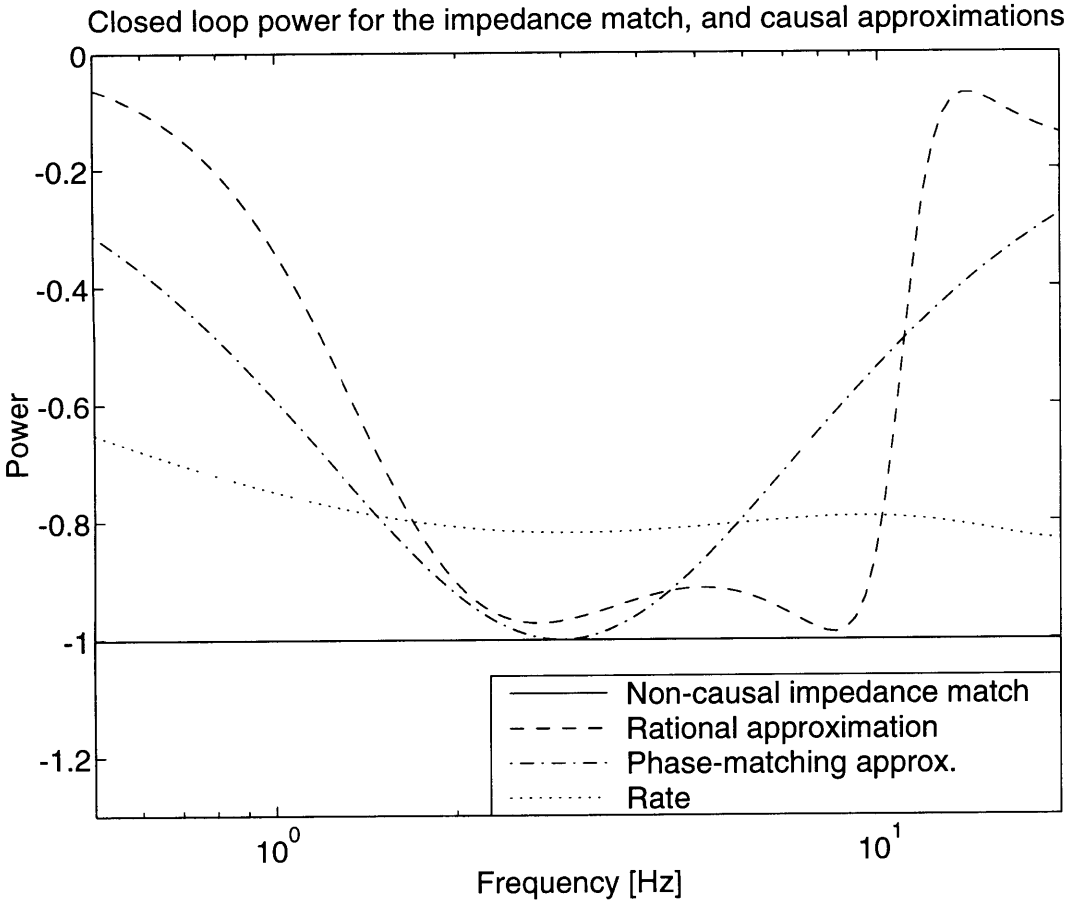

Figure 2.15: Predicted junction power flow for the experimentally implemented compensators. The conservative junction has zero net power in open loop, while incoming alone has -1.

frequencies. Incoming power is defined to be negative, and outgoing power is positive. The open loop junction is conservative, so net power flow is zero. If the junction is dissipative, net power is negative. The impedance match absorbs all the power arriving.

Nowhere does the rational approximation remove as much power as the non-causal compensator, but over the 1-10 Hz bandwidth, the power absorption is good. The phase-matching compensator removes all of the power at 3 Hz. As noted above, 3 Hz is the frequency at which the compensator gain and phase both exactly match the non-causal compensator. The power absorption drops off at higher and lower frequencies, where the magnitude of the approximation deviates from the noncausal

magnitude. The rate feedback implementation has the worst power absorption over the bandwidth of interest. However, it absorbs power over a significantly broader band than the other causal compensators.

The analysis shows that the power absorption of the impedance matching approximations is related to the deviation, in magnitude and phase, from the non-causal impedance match. Since global damping is introduced by dissipating energy at the junction, the damping introduced in the global modes will be higher at those frequencies where more power is dissipated. In the next section, the impedance matching approximations will be implemented. The global damping will be assessed from measurement data and correlated with the analytical results above.

Closed loop results. The three impedance matching approximations were implemented on the brass beam. To measure the performance of each, a white noise disturbance was put into the beam using the torque motor, and the rotation of the pinned end was measured. The closed loop performance frequency responses are shown in Figures 2.16 through 2.18, plotted against the open loop.

The rational approximation has the best damping in the 1 to 10 Hz bandwidth. The damping is fairly evenly distributed throughout this frequency range, except below 2 Hz where modal damping seems to be decreasing. The predicted power absorption also decreases below 2 Hz (see Figure 2.15 above), confirming that the compensator is less effective at the lower end of the range. The reason can be found in the logarithmic error curve fit used in the rational approximation approach. The function to be fit (the impedance match) has a positive slope on a log-log scale, which tends to emphasize the higher frequencies. The effect could be alleviated by including a frequency weight with the opposite slope.

The performance of the phase-matching compensator is shown in Figure 2.17. As predicted, the controller introduces the greatest amount of damping at around 3 Hz. Away from 3 Hz, the amount of damping decreases, as predicted by the junction power absorption. The damping is quite narrowband, but all the power at that one frequency is removed. Such a design could be useful if the disturbance energy is at a

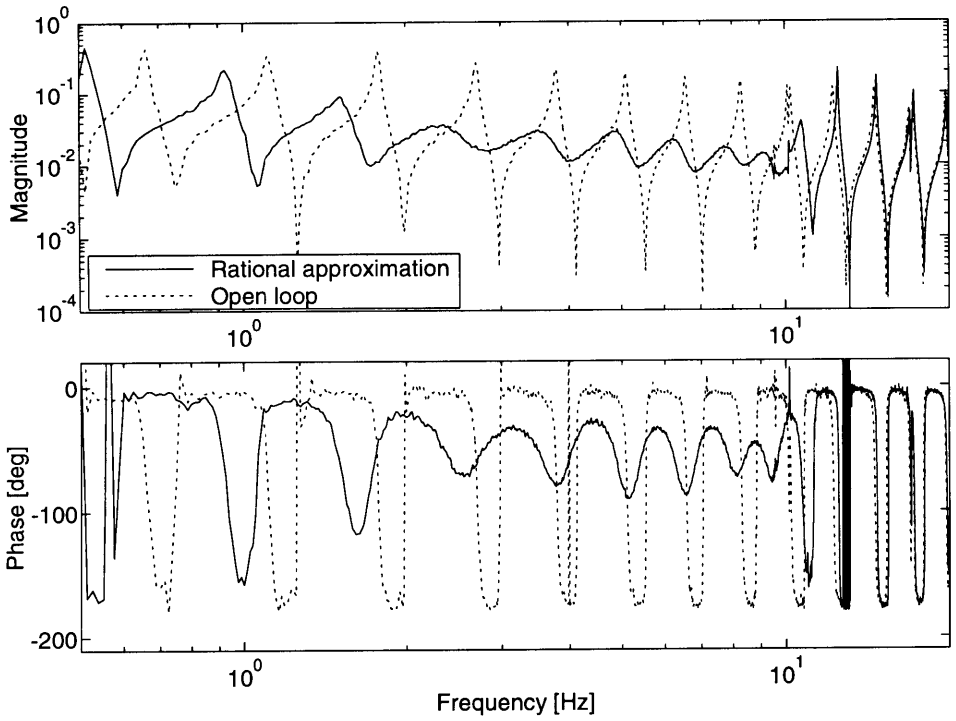

Figure 2.16: Measured brass beam frequency response from torque to rotation, with the rational approximation implemented on the right end of the beam.

single frequency.

It should be noted that the phase-matching compensator which was implemented is not the only compensator which would achieve the same level of damping at that frequency. Any compensator which similarly matches the magnitude and phase of the noncausal compensator at that frequency would damp as well.

The rate feedback performance is shown in Figure 2.18. Damping is broadband, relative to the impedance matching approximations implemented. However, the damping introduced in the region of interest is never as good as any of the impedance matching approximations. Note that, as predicted, the performance is best near 3 Hz, where the gain and phase most closely approach the impedance match.

Conclusions. The brass beam experiment demonstrated the impedance matching approach applied to a physical system. The control was designed using a wave-based local model. The optimal impedance match was found to be non-causal. Two

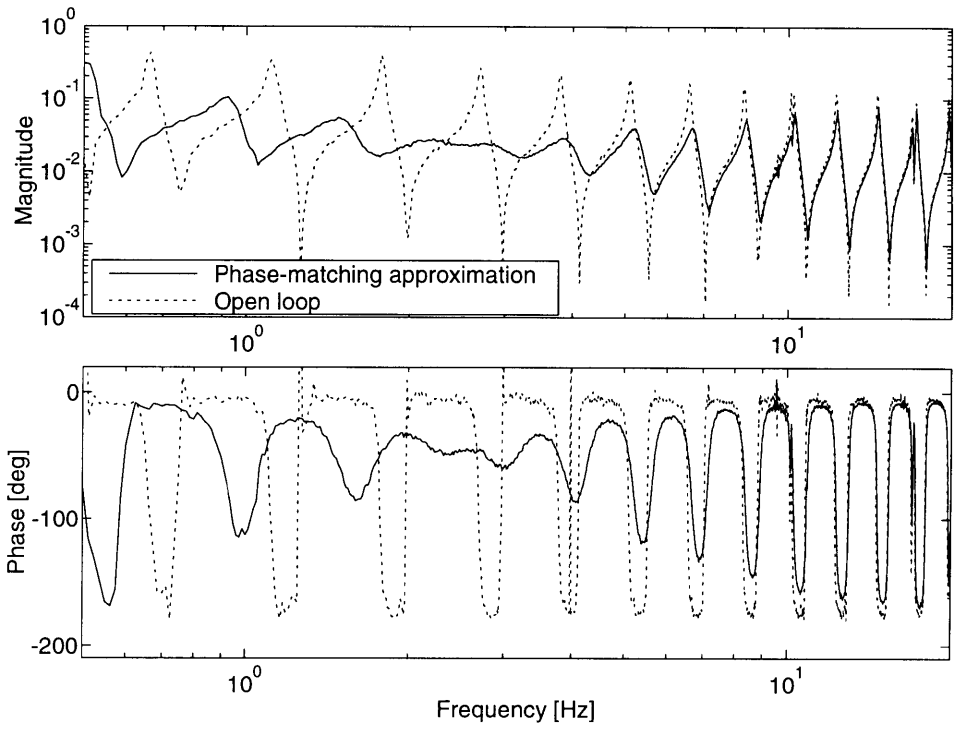

Figure 2.17: Measured brass beam frequency response from torque to rotation, with the phase-matching approximation implemented on the right end of the beam.

causal compensators were derived by approximating the phase and magnitude of the impedance match. Global stability and performance were inferred from the local junction model. Based on the local power dissipation, the closed loop damping as a function of frequency was predicted. The experimentally measured closed loop damping was found to be higher where the predicted power absorption of each of the compensators was greater. The results indicate that the impedance match is the optimal compensator for damping the global modes.

The impedance matching approximations were derived using fairly unsophisticated techniques. Particularly, the ability of the curve fitting technique to match the noncausal compensator at specific frequencies could be examined further. If the modal spacing of the plant were known to be significant (half a decade or a decade), the weights could be sharp spikes at the expected modal frequencies. The causal compensator would intersect the impedance match at those frequencies, in order to damp the modes. At intermediate frequencies, where less power flows in the beam,

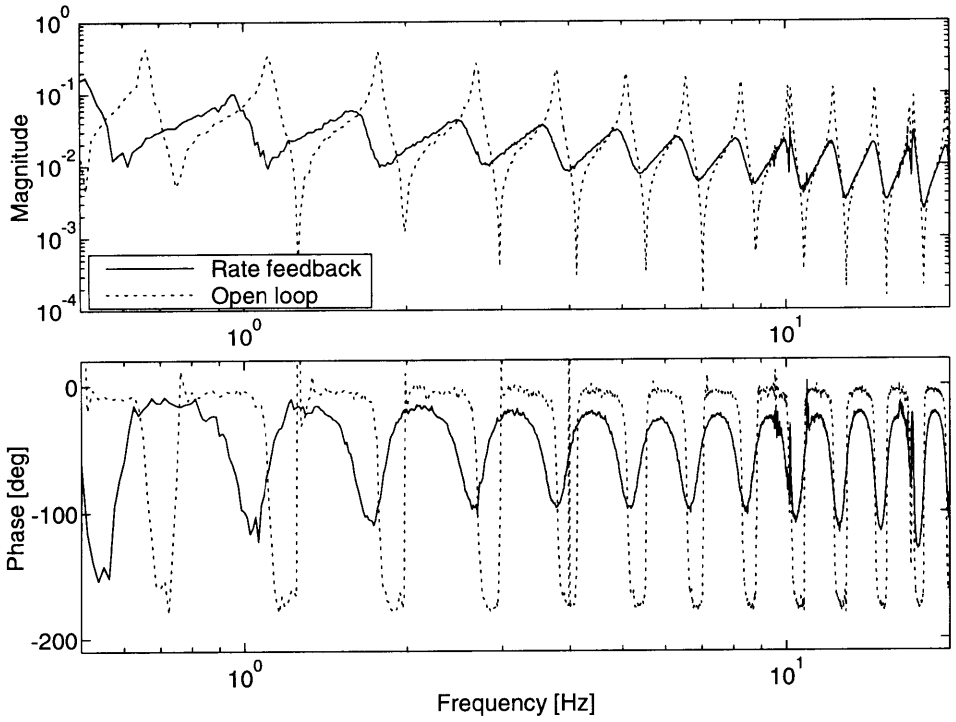

Figure 2.18: Measured brass beam frequency response from torque to rotation, with rate feedback implemented on the far end of the beam.

the compensator can deviate from the impedance match. Provided the compensator is positive real, the closed loop system will be stable. However, some performance robustness will be sacrificed.

The same design techniques could be applied to a general structure. Using the real-pole approximation to the direct field, given in Section 2.1.1, and the resulting non-causal impedance match, Equation 2.69, an approximation could be designed by fitting a causal compensator using frequency weights. Note that two levels of approximation, of the local model and of the impedance match for that model, are introduced. Thus two stages where significant error could arise form part of the design procedure. Alternatively, MacMartin looked at $\mathcal{H}_\infty$[16] and mixed $\mathcal{H}_2$- $\mathcal{H}_\infty$design [12], for the case when uncertainty in modal frequencies drives the control design.

Loss of positive realness, due to time delay, was responsible for the instability of the gain-matching approximation. Time delays will exist in any system, and could be a driving factor in digitally controlled systems. The time delay in the brass beam

experiments did not introduce significant phase loss in the bandwidth of interest. The accuracy of the wave model was not compromised in that range, so the performance of the compensators on the testbed was predicted well by the model. However, it was significant enough that the controller could not be rolled off successfully. In Chapter 3, the effect of time delays on rolloff, as well as time delay within the bandwidth of interest, will be addressed.

The brass beam testbed possessed a number of attributes which made it particularly suitable for an impedance matching control design. The control was located at the end of the beam, and only external force was available for control. No moment could be applied, and no power could exist in the moment/rotation pair. All the power at the beam tip is in the form of force interacting with displacement, hence it can all be seen and absorbed by the control. The situation in which power flows past the control in an uncontrolled set of variables is avoided.

An additional consequence of the beam topology is that damping is the best strategy available. The disturbance input and performance output are collocated and separated from the control. The control can only change the amount of disturbance energy which reaches the performance by preventing energy from reflecting back to the performance. If the control hardware were located on a transmission path between the disturbance and performance, the control could prevent transmission from one to the other.

The concept of reflecting energy away from certain locations is termed *energy shunting*. The following section investigates the uses of the shunting concept, and demonstrates that some of the difficulties of the impedance match can be avoided by using a shunting approach. The stability and performance robustness of the impedance match can be shown to hold.

2.2 Energy Shunting

The impedance matching controller is a powerful way to guarantee robust performance and stability. However, as seen in the last section, there are fundamental limitations to

performance for certain control locations and actuators. Power flows in combinations of the cross-sectional components of displacement and force. When the control can affect only a subset of the combinations, a portion of the power can cross the junction unaffected.

A different power cost can be used to minimize the power transmission across the junction. Such a strategy is termed *energy shunting*. Shunting can be achieved through a constrained minimization of a subset of the junction power. Shunting is applicable at a transmission junction, that is, when the control is located between the disturbance and the performance. The closed form solution is not known in general. Rather, the desired energy transmission is minimized, and the resulting closed loop junction power flow is analyzed. As with the impedance match, causality of the compensator is not guaranteed, and a causal approximation may be required.

2.2.1 Shunting model

Energy shunting minimizes the transmission of energy through the cross-section. Consider Figure 2.19, which shows a general control junction in the middle of a member. A disturbance force acts on the structure, to the left of the junction, producing incoming waves w_{i_1}. The homogeneous behavior of the junction allows the waves to traverse the junction to arrive at the performance z. That is, the open loop behavior is purely transmissive:

$$\begin{bmatrix} w_{o_1} \\ w_{o_2} \end{bmatrix} = \begin{bmatrix} 0 & I \\ I & 0 \end{bmatrix} \begin{bmatrix} w_{i_1} \\ w_{i_2} \end{bmatrix} \tag{2.100}$$

The waves which arrive at z create motion. $E\{z^T z\}$ could represent the RMS motion of a pointing payload on a spacecraft. The control objective is to minimize the amount of energy which reaches z.

An applicable control strategy is the impedance match. However, as shown by Equation 2.69, the required control could be non-causal, and therefore a suboptimal approximation can be necessary. Even if the optimal impedance match is causal, it will not remove all the power from the member unless all cross-sectional variables are controlled, as shown in Section 2.1.2. An alternative strategy is to cause the closed

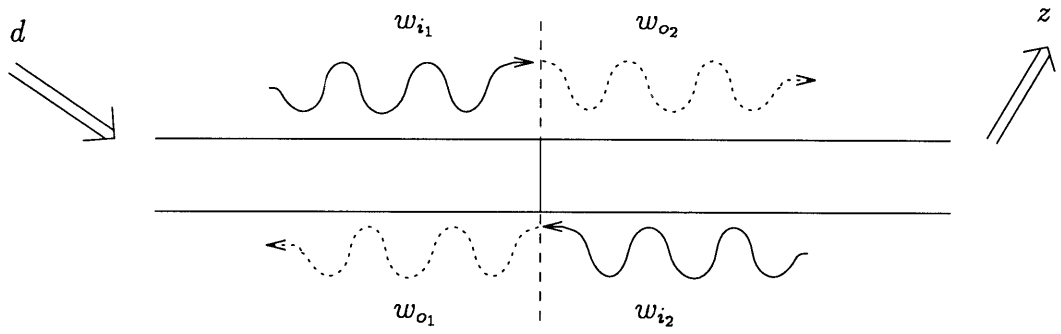

Figure 2.19: General control junction in the transmission path between a disturbance d and output z

loop junction to be reflective:

$$S_{cl_1} = \begin{bmatrix} I & 0 \\ 0 & I \end{bmatrix} \tag{2.101}$$

The energy in w_{o_2}, due to w_{i_1}, and the energy in w_{o_1}, due to w_{i_2}, are minimized. Thus any energy which approaches from the left is reflected away, and the performance is isolated from the disturbance.

Shunting is a competing strategy with the impedance match. The shunting compensator removes no power. Power is simply re-directed. Hence, shunting a portion of the incoming energy necessarily means that it is not damped. Zero power absorption can be shown to be a constraint on the shunting control derivation, although no closed form solution for the constrained problem has been found.

2.2.2 Shunting control derivation

The feedforward matrix for accomplishing the shunting objective can be found by specifying the closed loop scattering matrix (S_{cl_d}). Then, the feedforward control is given by:

$$F = \Psi^{-1}\left(S_{cl_d} - S\right) \tag{2.102}$$

where all actuators are available. The desired scattering matrix can be realized exactly when the rank of the left-hand side of Equation 2.102 is equal to the rank of F, that is, to the number of available actuators. However, when the number of actuators is

not sufficient, the desired closed loop scattering matrix S_{cl_d} is no longer attainable. The problem is then to minimize the combination of waves which carry the greatest proportion of power along the desired directions. This motivates the formulation of a power minimization problem.

Partitioning the waves into those in the left member, denoted $()_1$, and those in the right member, denoted $()_2$, from Equation 2.55, the junction power matrix is

$$\begin{aligned} P_{cl} = & \\ & \begin{bmatrix} w_{i_1}^H & w_{i_2}^H \end{bmatrix} \begin{bmatrix} P_{ii_{11}} & P_{ii_{12}} \\ P_{ii_{21}} & P_{ii_{22}} \end{bmatrix} \begin{bmatrix} w_{i_1} \\ w_{i_2} \end{bmatrix} + \begin{bmatrix} w_{i_1}^H & w_{i_2}^H \end{bmatrix} \begin{bmatrix} P_{io_{11}} & P_{io_{12}} \\ P_{io_{21}} & P_{io_{22}} \end{bmatrix} \begin{bmatrix} w_{o_1} \\ w_{o_2} \end{bmatrix} \\ & + \begin{bmatrix} w_{o_1}^H & w_{o_2}^H \end{bmatrix} \begin{bmatrix} P_{oi_{11}} & P_{oi_{12}} \\ P_{oi_{21}} & P_{oi_{22}} \end{bmatrix} \begin{bmatrix} w_{i_1} \\ w_{i_2} \end{bmatrix} + \begin{bmatrix} w_{o_1}^H & w_{o_2}^H \end{bmatrix} \begin{bmatrix} P_{oo_{11}} & P_{oo_{12}} \\ P_{oo_{21}} & P_{oo_{22}} \end{bmatrix} \begin{bmatrix} w_{o_1} \\ w_{o_2} \end{bmatrix} \end{aligned} \quad (2.103)$$

Using the closed loop scattering matrix, w_o can be found in terms of w_i, for substitution into Equation 2.103:

$$\begin{aligned} \begin{bmatrix} w_{o_1} \\ w_{o_2} \end{bmatrix} &= \left(\begin{bmatrix} S_{11} & S_{12} \\ S_{21} & S_{22} \end{bmatrix} + \begin{bmatrix} \Psi_1 \\ \Psi_2 \end{bmatrix} \begin{bmatrix} F_1 & F_2 \end{bmatrix} \right) \begin{bmatrix} w_{i_1} \\ w_{i_2} \end{bmatrix} \\ &= \begin{bmatrix} S_{11} + \Psi_1 F_1 & S_{12} + \Psi_1 F_2 \\ S_{21} + \Psi_2 F_1 & S_{22} + \Psi_2 F_2 \end{bmatrix} \begin{bmatrix} w_{i_1} \\ w_{i_2} \end{bmatrix} \end{aligned} \quad (2.104)$$

The junction power is then

$$\begin{aligned} P_{cl} = & \begin{bmatrix} w_{i_1}^H & w_{i_2}^H \end{bmatrix} \left(\begin{bmatrix} P_{ii_{11}} & P_{ii_{12}} \\ P_{ii_{21}} & P_{ii_{22}} \end{bmatrix} \right. \\ & + \begin{bmatrix} P_{io_{11}} & P_{io_{12}} \\ P_{io_{21}} & P_{io_{22}} \end{bmatrix} \begin{bmatrix} S_{11} + \Psi_1 F_1 & S_{12} + \Psi_1 F_2 \\ S_{21} + \Psi_2 F_1 & S_{22} + \Psi_2 F_2 \end{bmatrix} \\ & + \begin{bmatrix} S_{11}^H + F_1^H \Psi_1^H & S_{12}^H + F_2^H \Psi_1^H \\ S_{21}^H + F_1^H \Psi_2^H & S_{22}^H + F_2^H \Psi_2^H \end{bmatrix} \begin{bmatrix} P_{oi_{11}} & P_{oi_{12}} \\ P_{oi_{21}} & P_{oi_{22}} \end{bmatrix} \\ & \left. + \begin{bmatrix} S_{11}^H + F_1^H \Psi_1^H & S_{12}^H + F_2^H \Psi_1^H \\ S_{21}^H + F_1^H \Psi_2^H & S_{22}^H + F_2^H \Psi_2^H \end{bmatrix} \begin{bmatrix} P_{oo_{11}} & P_{oo_{12}} \\ P_{oo_{21}} & P_{oo_{22}} \end{bmatrix} \begin{bmatrix} S_{11} + \Psi_1 F_1 & S_{12} + \Psi_1 F_2 \\ S_{21} + \Psi_2 F_1 & S_{22} + \Psi_2 F_2 \end{bmatrix} \right) \begin{bmatrix} w_{i_1} \\ w_{i_2} \end{bmatrix} \end{aligned} \quad (2.105)$$

The control objective is to minimize w_{o_2} due to w_{i_1}, and w_{o_1} due to w_{i_1}. The steady-state power in the pair $[w_{i_1}, w_{o_2}]$ is a function of the partitions of Equa-

tion 2.105 which relate those two wave modes. Denoting the partition of P_{cl} which relates w_{i_1} to w_{o_2} as $P_{cl_{12}}$,

$$\begin{aligned} P_{cl_{12}} &= w_{i_1}^H P_{ii_{11}} w_{i_1} + w_{i_1}^H P_{io_{12}} w_{o_2} + w_{o_2}^H P_{oi_{21}} w_{i_1} + w_{o_2}^H P_{oo_{22}} w_{o_2} \\ &= w_{i_1}^H \left[P_{ii_{11}} + P_{io_{12}} \left(S_{21} + \Psi_2 F_1 \right) + \left(S_{21}^H + F_1^H \Psi_2^H \right) P_{oi_{21}} + \right. \\ &\quad \left. \left(S_{21}^H + F_1^H \Psi_2^H \right) P_{oo_{22}} \left(S_{21} + \Psi_2 F_1 \right) \right] w_{i_1} \end{aligned} \tag{2.106}$$

Similarly for $[w_{i_2}, w_{o_1}]$:

$$\begin{aligned} P_{cl_{21}} &= w_{i_2}^H \left[P_{ii_{22}} + P_{io_{21}} \left(S_{12} + \Psi_1 F_2 \right) + \left(S_{12}^H + F_2^H \Psi_1^H \right) P_{oi_{12}} + \right. \\ &\quad \left. \left(S_{12}^H + F_2^H \Psi_1^H \right) P_{oo_{11}} \left(S_{12} + \Psi_1 F_2 \right) \right] w_{i_2} \end{aligned} \tag{2.107}$$

The minimizing solution can be found using the same techniques as the impedance match. By comparison with Equation 2.55, the power minimizing feedforward is

$$\begin{aligned} F_1 &= -\left(\Psi_2^H P_{oo_{22}} \Psi_2 + R \right)^{-1} \Psi_2^H \left(P_{oi_{21}} + P_{oo_{22}} S_{21} \right) \\ F_2 &= -\left(\Psi_1^H P_{oo_{11}} \Psi_1 + R \right)^{-1} \Psi_1^H \left(P_{oi_{12}} + P_{oo_{11}} S_{12} \right) \end{aligned}$$

F_1 is the feedforward of waves w_{i_1} to control force Q, and F_2 is feedforward of w_{i_2}. Again the matrix R can be set to zero if the appropriate inverse exists. The complete feedforward matrix is

$$F = \begin{bmatrix} F_1 & F_2 \end{bmatrix} \tag{2.108}$$

Note that the derivation does not constrain the closed loop power to equal the open loop power, as desired. The open loop junction power matrix P, and closed loop power matrix P_{cl}, are

$$P = w_i^H \left[P_{ii} + P_{io} S + S^H P_{oi} + S^H P_{oo} S \right] w_i \tag{2.109}$$

$$\begin{aligned} P_{cl} &= w_i^H \left[P_{ii} + P_{io} \left(S + \Psi F \right) + \left(S^H + F^H \Psi^H \right) P_{oi} + \right. \\ &\quad \left. \left(S^H + F^H \Psi^H \right) P_{oo} \left(S + \Psi F \right) \right] w_i \end{aligned} \tag{2.110}$$

In order that $P_{cl} = P$, the terms in F must sum to zero:

$$\left(P_{io} \Psi + S^H P_{oo} \Psi \right) F + F^H \left(\Psi^H P_{oi} + \Psi^H P_{oo} S \right) + F^H \Psi^H P_{oo} \Psi F = 0 \tag{2.111}$$

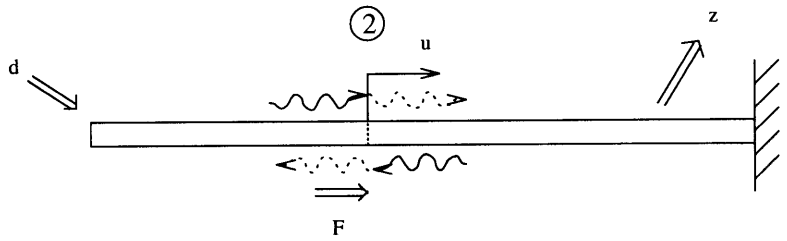

Figure 2.20: Rod example: energy shunting at junction 2 to minimize transmission from disturbance to performance.

or

$$AF + F^H A^H + F^H B F = 0 \tag{2.112}$$

The shunting compensator minimizes Equations 2.106 and 2.107 subject to Equation 2.112. The closed form solution has not been found. Rather, the appropriate controller can be found from Equation 2.108, and the dissipation characteristics analyzed by solving for the eigenvalues of the closed loop power matrix. If the open loop junction is conservative, the closed loop power matrix is identically Equation 2.112.

Example 4: Rod shunting The rod example offers a useful means to evaluate the performance of the shunting strategy, as compared to the impedance match of Section 2.1.2. The shunting compensator will be derived for the midsection junction when only external force is available as an actuator (Figure 2.20). The objective will be to minimize the transmission of power across the junction. The junction relations are

$$S = \begin{bmatrix} 0 & 1 \\ 1 & 0 \end{bmatrix}$$

$$\begin{bmatrix} \Psi_1 \\ \Psi_2 \end{bmatrix} = \begin{bmatrix} \frac{-1}{2iEAk} \\ \frac{-1}{2iEAk} \end{bmatrix}$$

$$P_{oo} = 2EAk\omega \begin{bmatrix} 1 & 0 \\ 0 & 1 \end{bmatrix}$$

$$P_{oi} = \begin{bmatrix} 0 & 0 \\ 0 & 0 \end{bmatrix}$$

Using the shunting result derived above,

$$\begin{aligned} F_1 &= -\left(\frac{1}{2iEAk}2EAk\omega\frac{-1}{2iEAk}\right)^{-1}(0+1*2EAk\omega) \\ &= 2iEAk \end{aligned} \tag{2.113}$$

Similarly,

$$F_2 = 2iEAk \tag{2.114}$$

The feedforward compensator which minimizes transmission is thus

$$F = 2iEAk\begin{bmatrix} 1 & 1 \end{bmatrix} \tag{2.115}$$

Compare the rod shunting compensator with the impedance match of Equation 2.80. The feedforward is almost identical, except for a factor of two.

The closed loop scattering matrix is found to be

$$S_{cl} = \begin{bmatrix} 0 & 1 \\ 1 & 0 \end{bmatrix} + \begin{bmatrix} \frac{-1}{2iEAk} \\ \frac{-1}{2iEAk} \end{bmatrix}\begin{bmatrix} 2iEAk & 2iEAk \end{bmatrix} = \begin{bmatrix} -1 & 0 \\ 0 & -1 \end{bmatrix} \tag{2.116}$$

The relevant submatrices, $S_{cl_{12}}$ and $S_{cl_{21}}$ have been zeroed. For the rod example, the number of actuators is not sufficient to control all the elements of S_{cl}, but can control all the entries which correspond to transmission across the junction. Thus, the disturbance to performance transmissibility is zero and the performance is perfectly isolated. The same actuator, acting alone, was not able to zero transmission when the impedance match was attempted.

The power absorption characteristics of the junction are given by the eigenvalues of the closed loop power matrix (Equation 2.110):

$$\begin{aligned} P_{cl} &= \begin{bmatrix} -2EAk\omega & 0 \\ 0 & -2EAk\omega \end{bmatrix} + \begin{bmatrix} 0 & -1 \\ -1 & 0 \end{bmatrix}\begin{bmatrix} 2EAk\omega & 0 \\ 0 & 2EAk\omega \end{bmatrix}\begin{bmatrix} 0 & -1 \\ -1 & 0 \end{bmatrix} \\ &= \begin{bmatrix} 0 & 0 \\ 0 & 0 \end{bmatrix} \end{aligned} \tag{2.117}$$

There are two eigenvalues, both zero. Thus the closed loop junction is conservative. The open loop junction is also conservative, so the energy flowing through the junction

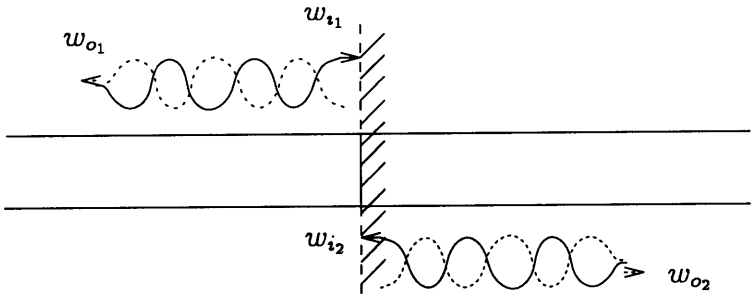

Figure 2.21: Equivalent junction boundary condition produced by the shunting feedforward.

has not changed. Only the direction of propagation is different. While the junction scattering matrix prevents energy from traveling across the junction, it does not remove any energy. Energy shunting therefore improves the performance based on the relative location of the disturbance and performance. Note that the conservative property is a characteristic of the particular problem. In general, the closed loop junction will not be conservative.

Compare the entries of S_{cl} with the fixed end scattering matrix of the rod, given by Equation 2.27. The shunting junction is mimicking a fixed boundary condition in the center of the rod (See Figure 2.21).

The physical variable feedback matrix can be found from Equation 2.60. The feedforward compensator will be derived using a factor ϵ times the feedforward matrix F. When $\epsilon \to 1$, the compensator approaches the shunting compensator. The reason will become apparent. The actuator is $\begin{bmatrix} 0 \\ 1 \end{bmatrix} F_{ext}$ and the sensor is $U_s = \begin{bmatrix} \Delta_{abs} \\ F_{rel} \end{bmatrix}$. With $(TY)^{-1}$ defined as in Section 2.1.2, the feedback is

$$\begin{aligned} G &= \left(I - F\,(TY)_{12}^{-1}\,e\right)^{-1} F\,(TY)_{11}^{-1} \\ &= \left(1 - \epsilon \begin{bmatrix} 2iEAk & 2iEAk \end{bmatrix} \begin{bmatrix} \frac{1}{4ikEA} \\ \frac{1}{4ikEA} \end{bmatrix}\right)^{-1} \epsilon \begin{bmatrix} 2iEAk & 2iEAk \end{bmatrix} \begin{bmatrix} \frac{1}{4} & \frac{-1}{4iEAk} \\ \frac{1}{4} & \frac{1}{4iEAk} \end{bmatrix} \\ &= \frac{\epsilon}{1-\epsilon} \begin{bmatrix} iEAk & 0 \end{bmatrix} \\ &= \frac{\epsilon}{1-\epsilon} \begin{bmatrix} A\sqrt{\rho E}i\omega & 0 \end{bmatrix} \end{aligned} \tag{2.118}$$

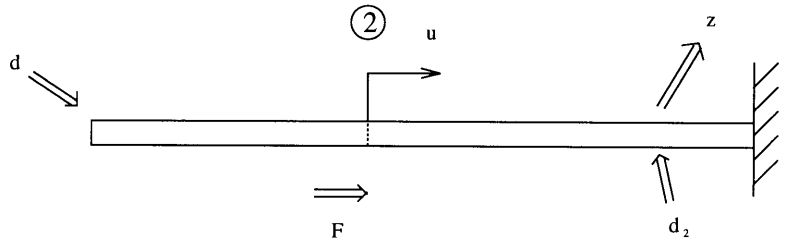

Figure 2.22: Another shunting objective can be posed as minimizing the RMS of z, when disturbances act on both sides of the control.

which is high gain, collocated rate feedback from displacement to external force. In fact the optimal shunting gain is infinite as $\epsilon \to 1$. Physically, the control imposes zero displacement at the control location. The conservative nature of the junction can be readily explained using this information.

Power flows in the rod through the mixture of internal stress and strain. At the junction, the displacement is zeroed. The internal stress in the rod is exactly matched by the external force, so no force is transmitted across the junction. Hence the incoming power cannot create stress and strain in the opposite side of the junction. In broad terms, energy exists in the product of a generalized force with a generalized displacement. If either force or displacement goes to zero, no energy can propagate. This is the fundamental property of the energy shunting compensator.

Other shunting objectives. The compensator in the previous example was derived to minimize transmission across the junction. Other shunting objectives can be posed. Consider the rod in Figure 2.22, which is identical to the previous example, except that an additional disturbance d_2 acts at the right side of the junction. In this case, the junction derived above would reflect all of the energy input by d_2 towards the performance z. Another local performance objective can be defined: minimize the power in $[w_{i_1}, w_{o_2}]$, as before, and in $[w_{i_2}, w_{o_2}]$. That is, minimize the power carried into the right half of the rod. The feedforward which accomplishes the first objective is F_1 as given in Equation 2.113. The submatrix of P_{cl} which captures the second objective is

$$P_{cl_{22}} = w_{i_2}^H \left[P_{ii_{22}} + P_{io_{22}} \left(S_{22} + \Psi_2 F_2 \right) + \left(S_{22}^H + F_2^H \Psi_2^H \right) P_{oi_{22}} + \right.$$

$$\left(S_{22}^H + F_2^H \Psi_2^H\right) P_{oo_{22}} \left(S_{22} + \Psi_2 F_2\right)\Big] w_{i_2} \tag{2.119}$$

The feedforward matrix F_2 which minimizes Equation 2.119 is

$$\begin{aligned} F_2 &= -\left(\Psi_2^H P_{oo_{22}} \Psi_2\right)^{-1} \Psi_2^H \left(P_{oi_{22}} + P_{oo_{22}} S_{22}\right) \\ &= -\left(\frac{1}{2iEAk} 2EAk\omega \frac{-1}{2iEAk}\right)^{-1} (0 + 0 * 2EAk\omega) \\ &= 0 \end{aligned} \tag{2.120}$$

The total feedforward matrix is

$$F = \begin{bmatrix} 2iEAk & 0 \end{bmatrix} \tag{2.121}$$

The feedback matrix is

$$G = \begin{bmatrix} iEAk & -1 \end{bmatrix} \tag{2.122}$$

or

$$F_{ext} = A\sqrt{\rho E}(i\omega)\Delta_{abs} - F_{rel} \tag{2.123}$$

The feedback is finite gain, but both sensors are required. The closed loop scattering matrix is

$$S_{cl} = S + \Psi F = \begin{bmatrix} 0 & 1 \\ 1 & 0 \end{bmatrix} + \begin{bmatrix} \frac{-1}{2iEAk} \\ \frac{-1}{2iEAk} \end{bmatrix} \begin{bmatrix} 2iEAk & 0 \end{bmatrix} = \begin{bmatrix} -1 & 1 \\ 0 & 0 \end{bmatrix} \tag{2.124}$$

Note that the control has zeroed the outgoing wave into the right member (Figure 2.23). The closed loop junction is a one-way energy path, termed a *directional shunt.* In addition to isolating a noisy payload from a disturbance source, as in the present example, the directional shunt might be used to bottle up energy in an unimportant portion of the structure. For example, a number of directional shunts might surround a passive or active damping element.

The closed loop power matrix is

$$\begin{aligned} P_{cl} &= \begin{bmatrix} 2EAk\omega & 0 \\ 0 & 2EAk\omega \end{bmatrix} + \begin{bmatrix} -1 & 0 \\ 1 & 0 \end{bmatrix} \begin{bmatrix} 22EAk\omega & 0 \\ 0 & 22EAk\omega \end{bmatrix} \begin{bmatrix} -1 & 1 \\ 0 & 0 \end{bmatrix} \\ &= \begin{bmatrix} 0 & 2EAk\omega \\ 2EAk\omega & 0 \end{bmatrix} \end{aligned} \tag{2.125}$$

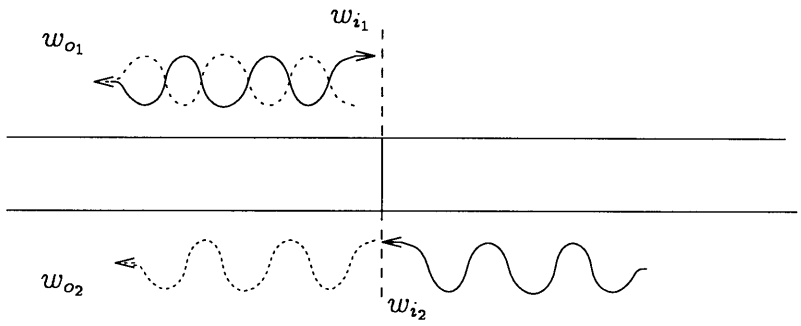

Figure 2.23: The directional shunt: energy is allowed to flow in only one direction.

Since the power matrix is non-zero, the junction is no longer conservative. The eigenvalues of P_{cl} are $\pm 2EAk\omega$, indicating that power is produced for certain combinations of incoming power.

The closed loop power $\mathcal{P}$ is

$$\mathcal{P} = tr\left\{ \begin{bmatrix} \Phi_{w_{i_1} w_{i_1}} & \Phi_{w_{i_1} w_{i_2}} \\ \Phi_{w_{i_2} w_{i_1}} & \Phi_{w_{i_2} w_{i_2}} \end{bmatrix} P_{cl} \right\} \tag{2.126}$$

where $\Phi_{w_{i_1} w_{i_1}}, \Phi_{w_{i_2} w_{i_2}}$ are the variances of the incoming disturbance waves, and $\Phi_{w_{i_1} w_{i_2}}$, $\Phi_{w_{i_2} w_{i_1}}$ are the covariances. The net junction power flow will be zero if the left and right waves are uncorrelated. For a finite system, incoming waves are in part due to outgoing waves which reflect from distant points on the structure. For a closed system, the left and right waves can be correlated. Thus the power $\mathcal{P}$ can be non-zero. $\mathcal{P}$ cannot be determined to be negative or positive without a global model. The global closed loop system is not necessarily unstable. Since stability is a function of global parameters, stability robustness becomes a factor. This illustrates the importance of knowledge of the junction power, and the utility of constraining the closed loop junction to be dissipative.

Note that the causality of the rod shunting compensators is a fortunate outcome. Causality for the rod is not a surprise in light of the fact that the impedance match was causal. The shunting solution is not constrained to be causal. As with the impedance match, a causal approximation can be necessary. However, the shunting feedforward matrix has been found to transform to high gain collocated feedback,

for many problems. At high gain, the phase of the approximation tends to be less important. Thus high gain feedback through a causal compensator can effectively mimic the shunting solution.

The ability of the compensator to zero transmission is particular to the rod. The rod only supports linear displacement, so power will flow as a combination of linear displacement and force. Any possible actuator will control either force or displacement, so the only available energy path is controlled. In general, when the number of actuators is not sufficient to zero all the relevant entries in the closed loop scattering matrix, the shunting compensator will control those elements which, alone or in combination, carry the greatest portion of energy across the junction. Such partial shunting will be examined in the next section.

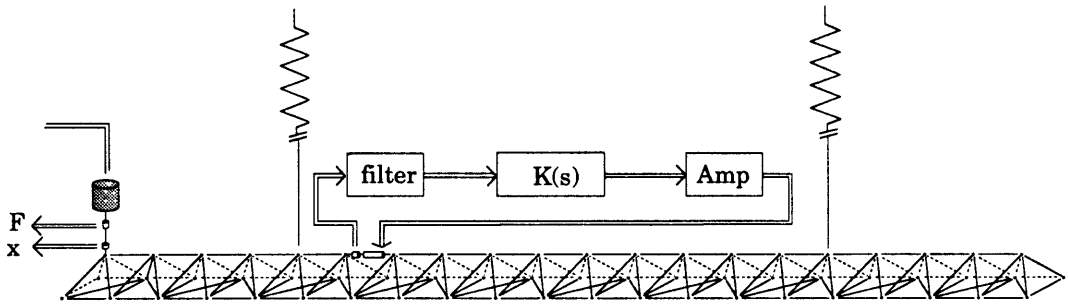

Figure 2.24: The 20-bay single leg truss testbed, and supporting equipment.

2.2.3 Truss Energy Shunting Experiments

An experiment is performed to investigate the performance of energy shunting compensators, compared to impedance matching approximations. The experiment testbed is a 20-bay free-free truss (Figure 2.24). The truss is constructed of aluminum struts with aluminum nodes. Each bay is 0.25m long, for a total length of 5m. The cross-section is triangular. The truss is suspended on 0.5m springs attached at the 1/4 and 3/4 length locations. Suspension modes are a decade below the 22.5 Hz first bending mode. As a result the dynamic boundary conditions are free-free. A vertical disturbance force is input at the left end by a Bruel and Kjaer shaker. The input force is measured with a PCB 208B load cell, and together with a collocated Kistler accelerometer provides a measure of the input impedance.

Control is implemented using a Physik Instruments P-843 piezoelectric active strut located at bay 6. The active strut is significantly stiffer than the truss, hence it acts to enforce displacement. A PCB load cell in series measures collocated relative force. By the argument made in Section 2.1.2, collocated displacement and force can be made a power pair by appropriate choice of the compensator. The compensator is implemented on a VME-based 68030 digital processor.

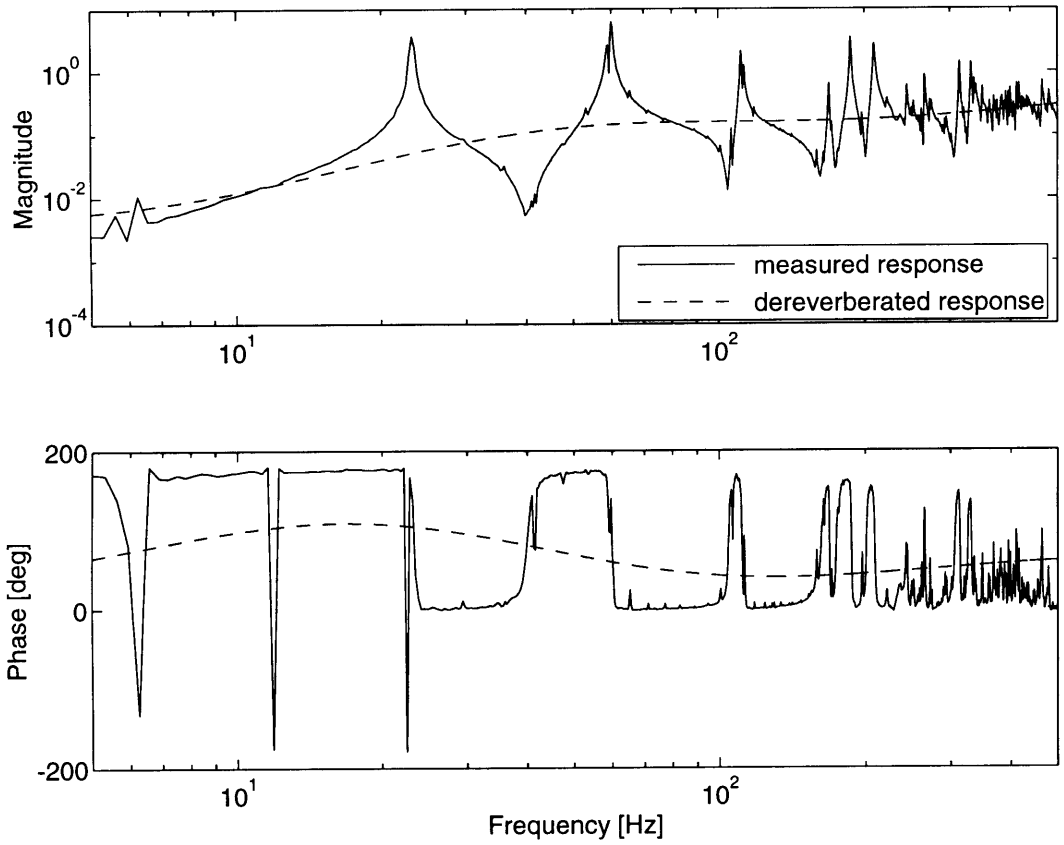

Figure 2.25: The dereverberated model of the truss testbed.

Modeling. Two models are needed: one local model for local control design, and one global model for evaluation of the global performance. The local model is a log averaged model, as derived in Section 2.1.1. The global model is a 2-dimensional finite element model composed of rod elements. The 2D model captures most of the relevant dynamics of the truss, except for torsional modes. The applicability of a Timoshenko model is also discussed.

The local model must capture the response of the truss through the control hardware, from piezo voltage to load cell voltage. A log averaged model is created. The log averaged model is a 7 pole curve fit to the frequency response of the control hardware. The log averaged model is shown in Figure 2.25, plotted against the measured reverberant response. The truss exhibits good pole/zero spacing to about 200 Hz.

After 200 Hz, the local modes of the individual struts begin to dominate.

A global wave model was attempted, using a Timoshenko beam model. The use of Timoshenko beam models to capture the behavior of beam-like trusses has been suggested elsewhere[17]. The open bay structure of a truss can allow large shear deformations, which can be represented by a Timoshenko model. In the wave model derivation, Miller presented a wave model treatment of the Timoshenko beam element [11]. With such a wave model, the exact direct field local model could be found, similar to the previous BE experiment. Using the exact direct field, a suitable impedance matching approximation could be found.

A Timoshenko wave model was created by choosing the beam parameters so that the beam modes matched the modes of the truss. Subsequent control designs based on the Timoshenko model showed poor performance. The poor results are explained by the fact that the physics of the structural motion determine the direct field. While the truss may show approximately the same global mode frequencies and shapes as a continuous beam, the pattern of stresses and strains underlying the response is considerably different.

Control design. The global performance of the two local control objectives, the impedance matching (damping) technique, and the energy shunting objective, are to be compared. The impedance matching compensator can be found from Equation 2.69:

$$H_{nc} = \frac{1}{G_d^*} \tag{2.127}$$

where $G_d(s)$ is the dereverberated model derived above. The optimal compensator is non-causal, so a causal approximation must be found. The techniques in the last section are applicable. However, the error in the dereverberated model G_d is potentially large. Any approximation which matches Equation 2.127 at specific frequencies is performance limited by that error. It is therefore unwise to attempt to target specific frequencies. The impedance match is implemented as a gain matching approximation:

$$H_c = \frac{1}{G_d} \tag{2.128}$$

which is the conjugate of the noncausal impedance match. The magnitude will be approximately correct over a broad frequency band. However, the phase will be in error.

The shunting compensator can best be designed using a wave model with the power minimization as presented above. However, by generalizing the wave result that the shunting compensator is typically high gain feedback through dual variables, the shunting compensator is chosen to be high gain negative feedback of force to displacement. Energy shunting is designed to alter the scattering behavior at the junction without changing the power dissipation characteristics.

If the actuator is external force, in open loop, the force is zero. There is motion, but power, the product of force and rate, is zero. For high gain feedback from displacement to force, the control will zero displacement. Again power is zero, however, where in open loop the force is zero, in closed loop displacement is zero. The energy scattering behavior of the control location has necessarily been changed.

Truss experiment: Control Evaluation The Finite Element model offers a useful comparison of the shunting and impedance matching techniques. The shunting compensator will be bandlimited on the truss testbed due to time delays, sensor/actuator dynamics, and so on. The Finite Element model can be used to compare the ideal performance of the compensators.

The closed loop performance of the impedance match is shown in Figure 2.26. There is only moderate damping in the first three modes. This could be due to a lack of fidelity in the Finite Element model, or to errors in the impedance matching approximation. Note that performance degrades in the fourth and fifth modes. The performance transfer function is taken from the end of the truss, so all modes are observable in the performance. However, the control is situated in the interior of the truss, so there will be near pole-zero cancellation of some modes. The control will have less authority over these modes.

The performance of the high gain shunting compensator is shown in Figure 2.27. Note that the response at the first three open loop modal frequencies is almost flat.

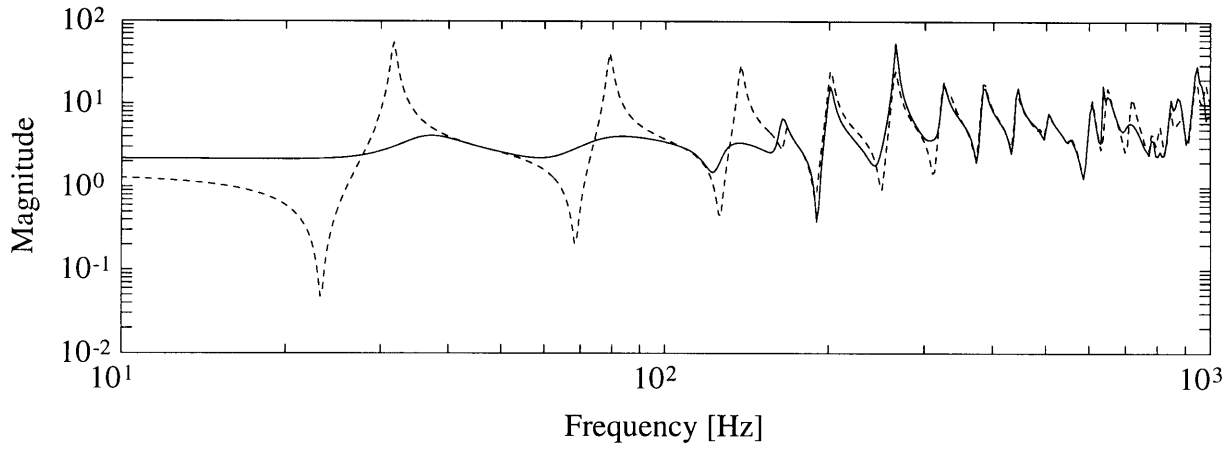

Figure 2.26: The closed loop performance of the impedance-matching compensator on the Finite Element model.

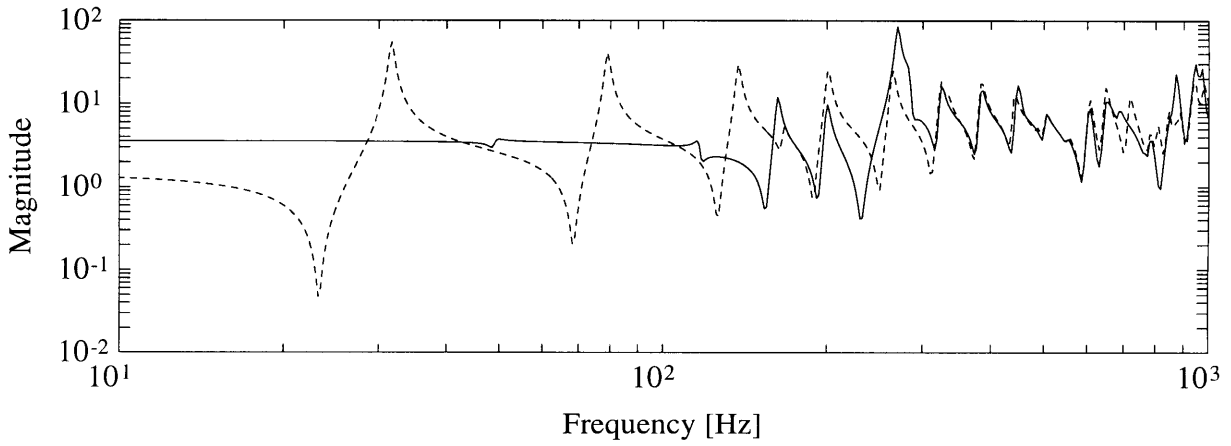

Figure 2.27: The high gain shunting compensator on the truss Finite Element model.

The first modes do not appear in the closed loop transfer function until nearly 200 Hz. The amplitudes of most modes have been decreased. An exception is the mode at 280 Hz which has become more prominent.

A fundamental difference exists in the impedance matching compensator and the energy shunt. The impedance match damps the closed loop modes. The shunt adds no damping, because no power is removed. In the closed loop system with the shunting compensator applied, the first three modes have not been damped. They have in

fact been removed. In a wave sense, modes result from constructive interference of waves which travel along the truss. Those waves have been broken up by the shunting junction. The shunting compensator is in effect an active impedance mismatch. The waves have been prevented from crossing the controlled cross-section. Waves originating at the disturbance cannot reach the performance. In particular, the control commands that no force be transmitted by the strut.

The Finite Element model offers a useful way to visualize the closed loop response of the shunting compensator. The first six mode shapes of the open and closed loop structures are shown in Figures 2.28 and 2.29. The command zeros the force carried through the strut, thereby actively removing the controlled strut from the structure. The bending moment in the strut is zeroed. Bending moment is a major component of the first few modes.

Closed loop results. The impedance matching and shunting compensators are implemented on a digital control computer running at 6 kHz. Since the truss supports its own weight, through the two suspension points, zeroing the force carried by the strut at DC would allow the truss to sag.Therefore, the compensators were rolled off at DC.

Since the shunting compensator cannot be truly infinite gain, the gain was chosen to minimize the RMS of the performance output from the first to the third mode (22 Hz to 110Hz). Neither of the compensators were stable at the design gain. The shunting compensator was implemented at 0.8 of the design gain, and the impedance match at 0.9 of the design gain.

Figure 2.30 shows the frequency response of the compensators (at the implemented gains). The shunting compensator has a higher gain through the bandwidth of interest. The phase of the impedance match is lower than the shunting compensator, causing the impedance match to be unstable at a lower gain than the shunting compensator.

The performance transfer functions for the impedance matching and shunting compensators are shown in Figure 2.31, plotted against the open loop. The shunting

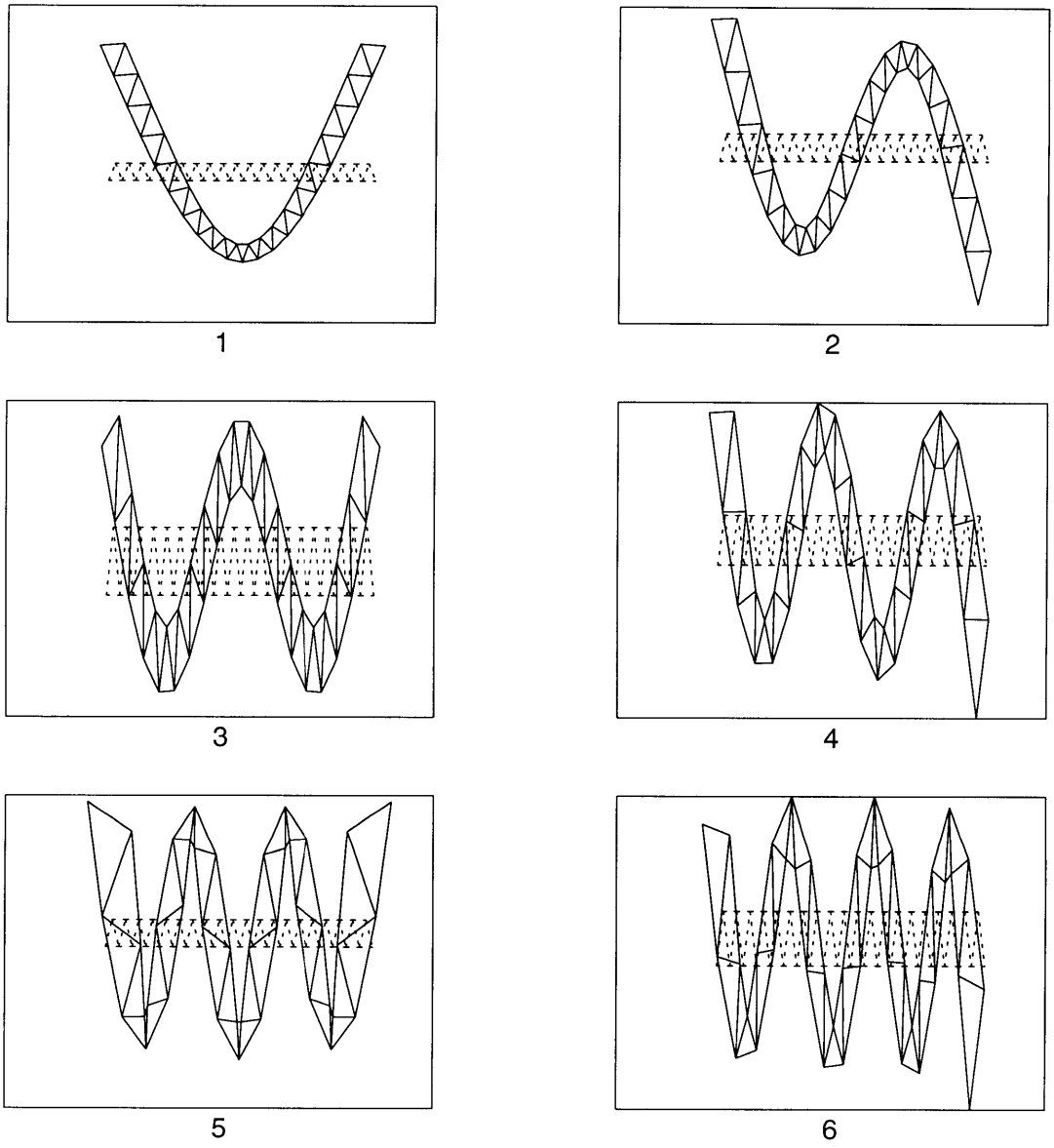

Figure 2.28: Mode shapes of the FE model: Open loop mode shapes of the first six modes show beam-like deformations.

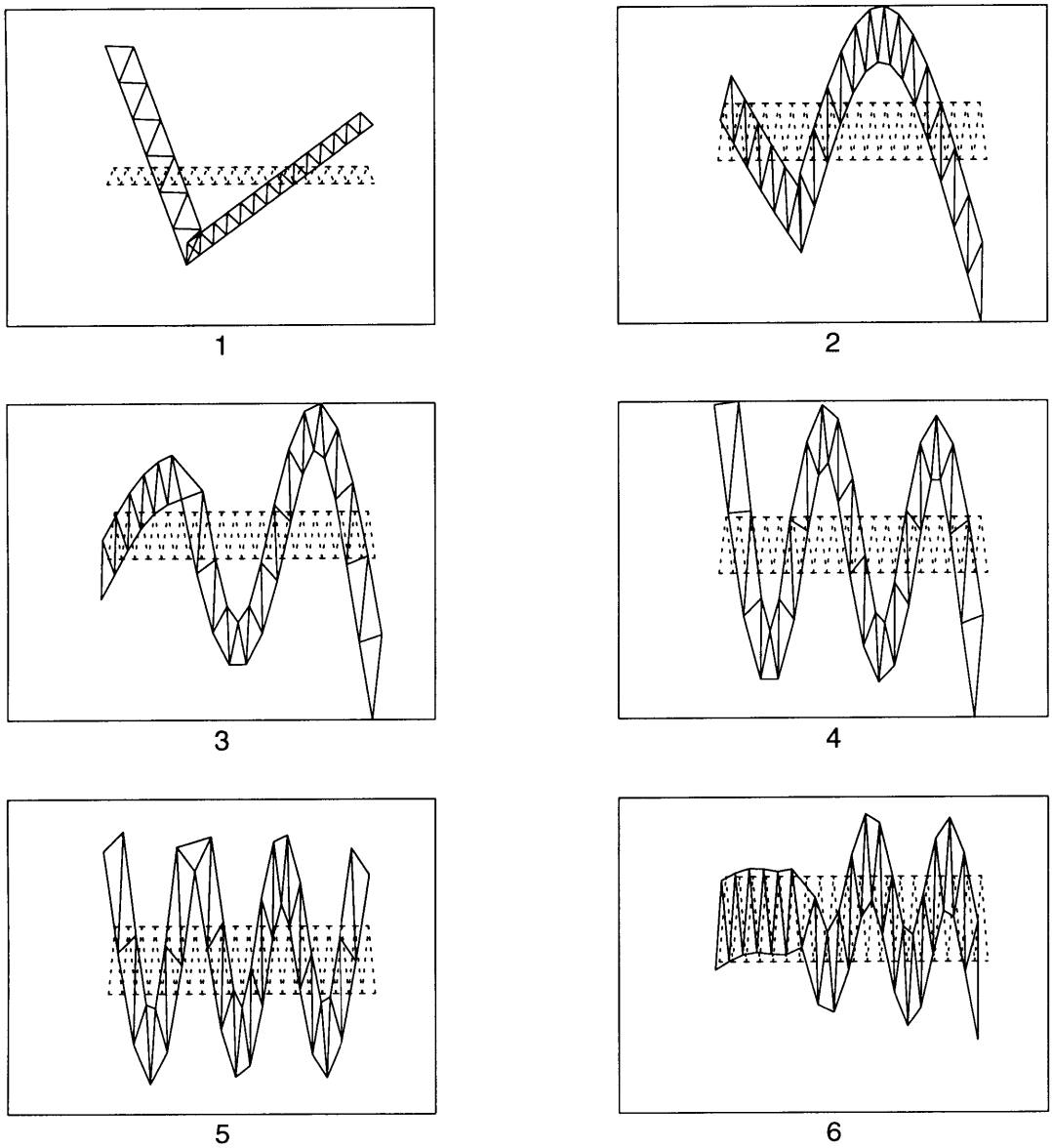

Figure 2.29: Mode shapes of the FE model: Shunting compensator is actively removing the control strut at bay 6.

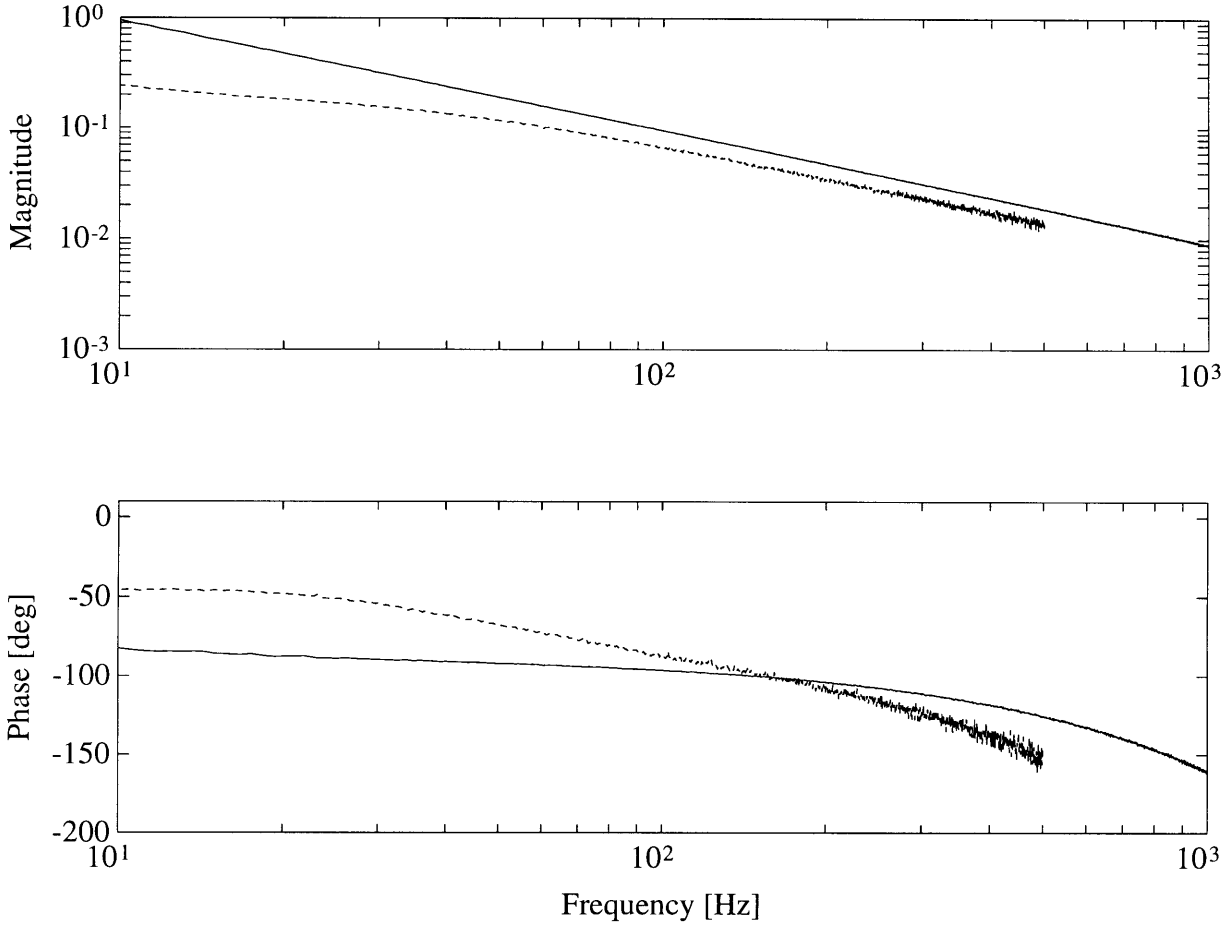

Figure 2.30: Measured transfer functions of the shunting (solid) and the impedance matching (dashed) compensators.

compensator lowers the magnitudes of all the modes in the 20-110 Hz bandwidth. The impedance match does not achieve the same reduction in response over the same bandwidth. At 82 Hz there is a closed loop mode which has a significant resonance. This is likely the mode which limited the gain of the impedance match.

The Finite Element model results showed that the performance of the shunting compensator was due to the fact that the modal resonances were removed. The closed loop modes of the truss were not damped, but changed significantly. The experimental results do not show the same degree of improvement because the experimental gain is limited. However, it is possible to analytically close the high gain feedback loop on data. The resulting analytical frequency response can be compared to the measured

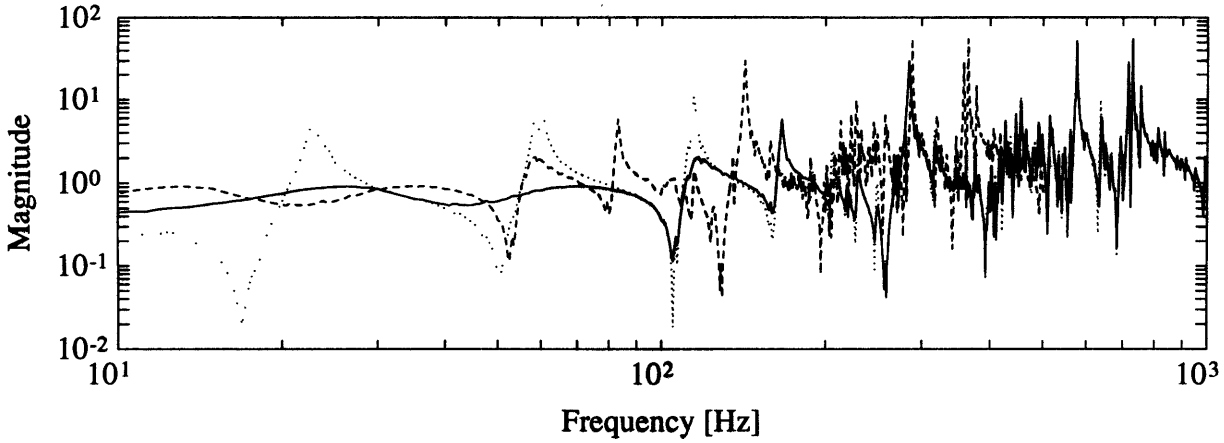

Figure 2.31: The measured performance transfer functions in open loop (dotted), using the shunting (solid), and using the impedance matching (dashed) compensator.

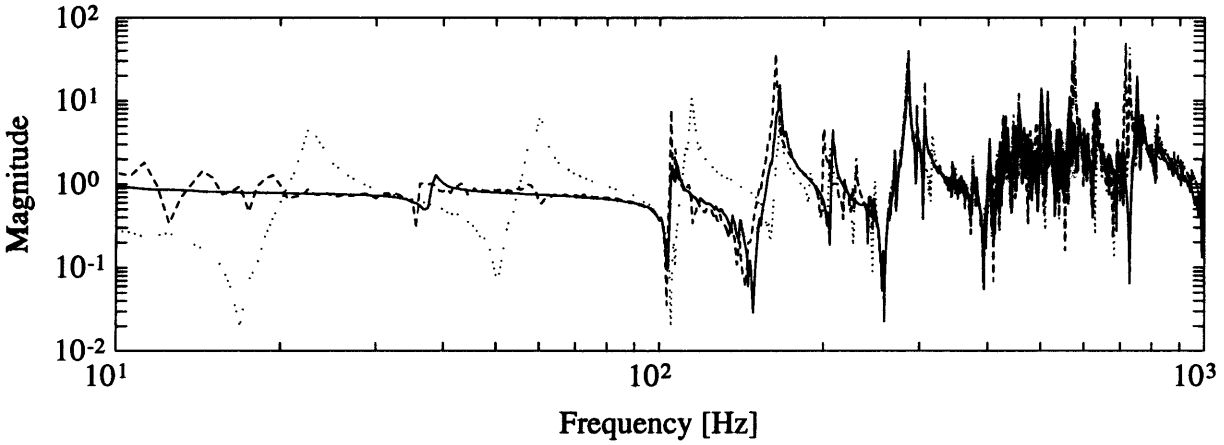

Figure 2.32: The analytical high gain open loop (dashed) plotted against the measured open bay truss (solid).

response of the truss with no strut in bay 6. If the shunting compensator is indeed actively removing the strut, the analytical high gain transfer function should overlay the measured open-bay transfer function. As shown in Figure 2.32, the analytical and measured transfer functions almost exactly overlay. It is therefore possible to extend the conclusion made for the Finite Element truss, that the shunting compensator actively removes the strut from the structure.

Conclusions. The energy shunting compensator is designed to address a shortcoming of the impedance matching formulation. Specifically, the impedance match cannot minimize the power transmission across a control junction. By controlling transmission, using the shunting formulation, two advantages are realized. First, the impedance match can only zero transmission when all cross-sectional variables can be actuated. The shunting compensator requires fewer actuators to zero transmission. Therefore, if the global objective can be stated as minimizing a transmissibility, the shunting strategy is inherently suited. Secondly, the impedance match will never zero the response at the control location, since zero motion implies that no power is being removed. A number of situations have been presented in which the desired global cost will be lower for zero motion than for maximum energy absorption. These situations arise when the disturbance input is separated from the performance output by the control junction.

The impedance matching and energy shunting examples presented above have all been one-dimensional, open topologies. In more complicated controlled structure geometries, the compensator which minimizes the global cost can perform a mix of energy shunting and energy absorption. The combination of the two strategies will be investigated in the following section.

2.3 Combinations of Impedance Matching and Shunting

The local control techniques derived above are intended to reduce the power carried in the controlled cross-sectional variables. The global cost is not the minimized quantity. For example, the impedance match cannot zero the velocity at a sensitive location. This would result in zero power dissipation. If the control is collocated with the disturbance or the performance, zeroing the velocity is optimal in an RMS sense. The shunting compensator was formulated to address this need. However, the shunting compensator is still designed to minimize a local objective, specifically the power crossing the junction, not the global objective.

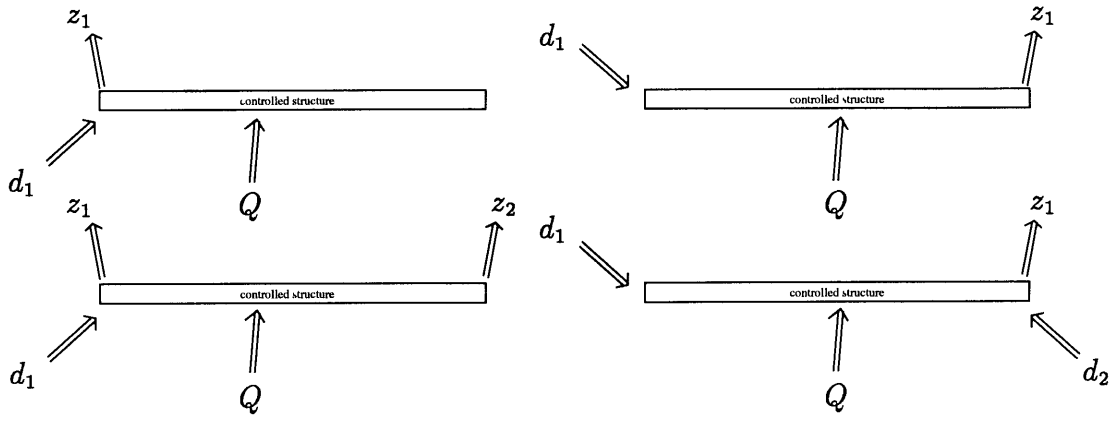

Figure 2.33: Local control options: For a controlled structure with a single disturbance path, shunting can be used when the sensitive portions of the structure are concentrated to one side of the control Q (right). On the left, energy shunting would reflect energy back to the performance, thus the impedance match will be used.

The choice between the impedance match and the energy shunt is made, broadly speaking, based on the locations of the disturbance and performance relative to the control. A controlled structure with a single energy path is illustrated in Figure 2.33. A controlled force Q, acting in the middle of the structure, is used to minimize the energy from disturbances d_1, d_2 which reach the performance represented by z_1, z_2. On the left, situations calling for the impedance match are represented. A disturbance d_1 acts on the system, and the disturbability of performance outputs z_1, or z_1 and z_2, is to be minimized. When there is a component of the performance near the disturbance, shunting disturbance energy back towards d_1 will increase the energy reaching that component. On the right of the figure are situations in which shunting would be beneficial. The performance output(s) are located the far side of the coontrol. Now the shunting compensator can drain energy away from the output(s).

The above analysis applies when the control has authority over all the power introduced by d_1 and d_2. The situation becomes more complicated when alternate energy flow paths exist around the control. Such alternate paths can be physical, such as exist in a closed structure. For example, an active element in a truss is surrounded by alternate paths, through the surrounding struts. The brass beam experiment

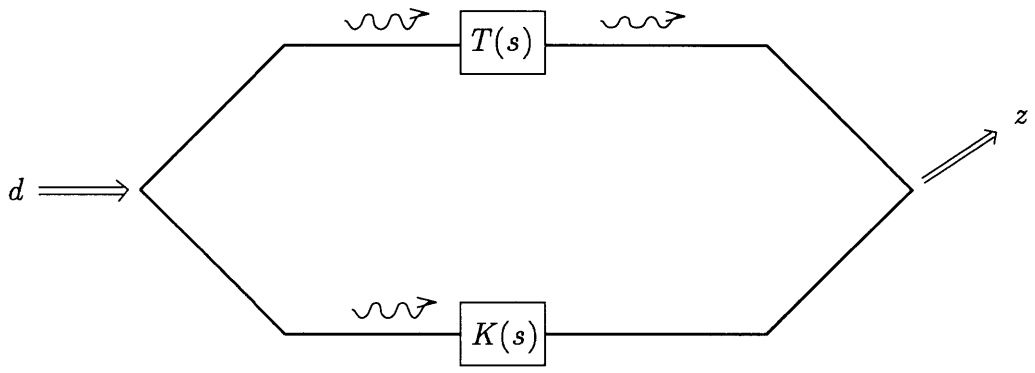

Figure 2.34: The general local control problem: a subset of the disturbance paths are controlled. The remaining paths are characterized as a structural transmissibility $T(s)$.

(Section 2.1.3) showed that alternate paths also consist of uncontrolled cross-sectional variables. For the BE beam, power can flow as a combination of shear force and shear rate, and as bending moment and curvature rate. If only force actuation is available, some power will cross the junction uncontrolled in the moment/rotation pair. When uncontrolled paths exist, the RMS optimal control, which minimizes the disturbability of the performance, may be a combination of shunting with impedance matching. The combination is a function of the number of controlled paths versus the total number of paths.

The global objective of minimizing disturbability, when controlling a subset of energy paths, is represented in Figure 2.34. A disturbance d enters the structure where it splits. A portion travels through the compensator $K(s)$, and the remainder travels through the uncontrolled path which is represented by $T(s)$. $T(s)$ is a generalized structural transmissibility which can range from purely transmissive ($T = 1$) through absorptive ($T = 0$) to purely reflective ($T = -1$). The objective is to design $K(s)$ to minimize $E\{z^T z\}$. If the uncontrolled path absorbs or reflects all energy ($T = 0, -1$), the optimal compensator is the energy shunt. The output z will then be completely isolated from d. If the structure is transmissive ($T = 1$), $K(s)$ must be purely absorptive. Any energy which is shunted will travel unattenuated through the uncontrolled path. Hence the impedance match is the RMS optimal compensator,

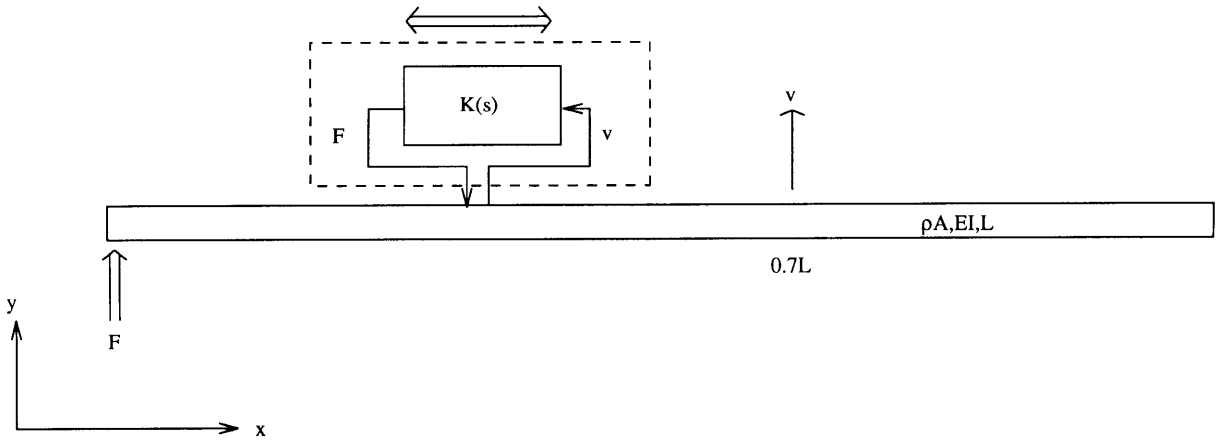

Figure 2.35: The BE beam simulation: the control $K(s)$ is optimized for each location from 0 to L.

provided a global model does not exist. For any T which is partially transmissive ($0 < T < 1$), the RMS optimal compensator will be a combination of the energy shunt and the impedance match.

2.3.1 RMS optimal compensator for a BE beam

The ability of local controllers to minimize a global $\mathcal{H}_2$ performance metric is investigated using a simulation of a free-free BE beam. The beam is represented in Figure 2.35. Mass per unit area ρA, stiffness EI, and length L are used to characterize the beam. A disturbance d enters at the left end, as transverse force. Transverse displacement at the $0.7L$ location along the beam is the measure of performance. Control is implemented through transverse force to displacement. As noted above, a portion of the power flows as moment/rotation, and is uncontrollable. The proportion varies with the location along the beam. A small amount of open loop damping, approximately 1% modal damping, is incorporated in the model.

To investigate how placement affects the RMS optimal control, the control hardware can be swept along the beam. When the control is between 0 and $0.7L$, the situation is similar to that shown in the right side of Figure 2.33. The disturbance and performance are separated by the control. Thus the compensator can shunt energy away from z. When the control is to the right of $0.7L$, the situation is captured

by that shown in the top left of Figure 2.33.

The true RMS-optimal compensator for these cases is the Linear Quadratic Gaussian (LQG) compensator [3], when a complete and accurate global model is available. However, the compensator that will be used has the form of the non-causal impedance match. From Equation 2.96, the impedance match for transverse force to displacement for a BE beam is

$$H_{nc} = \frac{1}{\sqrt{2}}(\rho A)^{3/4}(EI)^{1/4}(-s)^{3/2} \tag{2.129}$$

H_{nc} is the same at any location in the beam. The analysis is designed to investigate the relative merits of shunting and damping, hence the (non)implementability of H_{nc} is not a concern. The design compensator will be H_{nc} with a multiplicative gain α:

$$H = \alpha H_{nc} \tag{2.130}$$

That is, for $\alpha = 1$, $H = H_{nc}$. The gain will be varied to minimize $E\{z^T z\}$ at each control location as the control is swept from 0 to L. For $\alpha > 1$, less power is being absorbed, which can be interpreted as partial shunting. The closed loop power absorption can be found from Equation 2.66. Since the RMS optimal compensator H is a function of the optimal impedance matching compensator H_{nc}, which is in turn a function of the direct field response G_d, the closed loop power absorption reduces to a scalar function of α:

$$\mathcal{P}_{cl} = -\frac{2\alpha}{1+\alpha^2} \tag{2.131}$$

Note that as $\alpha \to \infty$, the compensator is approaching a high gain shunting compensator. Since only one set of cross-sectional variables is actuated, the shunt will not be complete.

The gain α was optimized at 334 locations. The RMS-optimal gain α is shown in Figure 2.36, plotted as a function of location. As stated, $\alpha = 1$ is the impedance match. Note that only when the control is at the far right of the beam does the RMS gain go to the impedance gain. As expected when controlling at $x = L$, shunting only reflects power towards z, so absorbing power is the only way to prevent it from appearing at z. The gain goes to ∞ at two locations: when the control is collocated

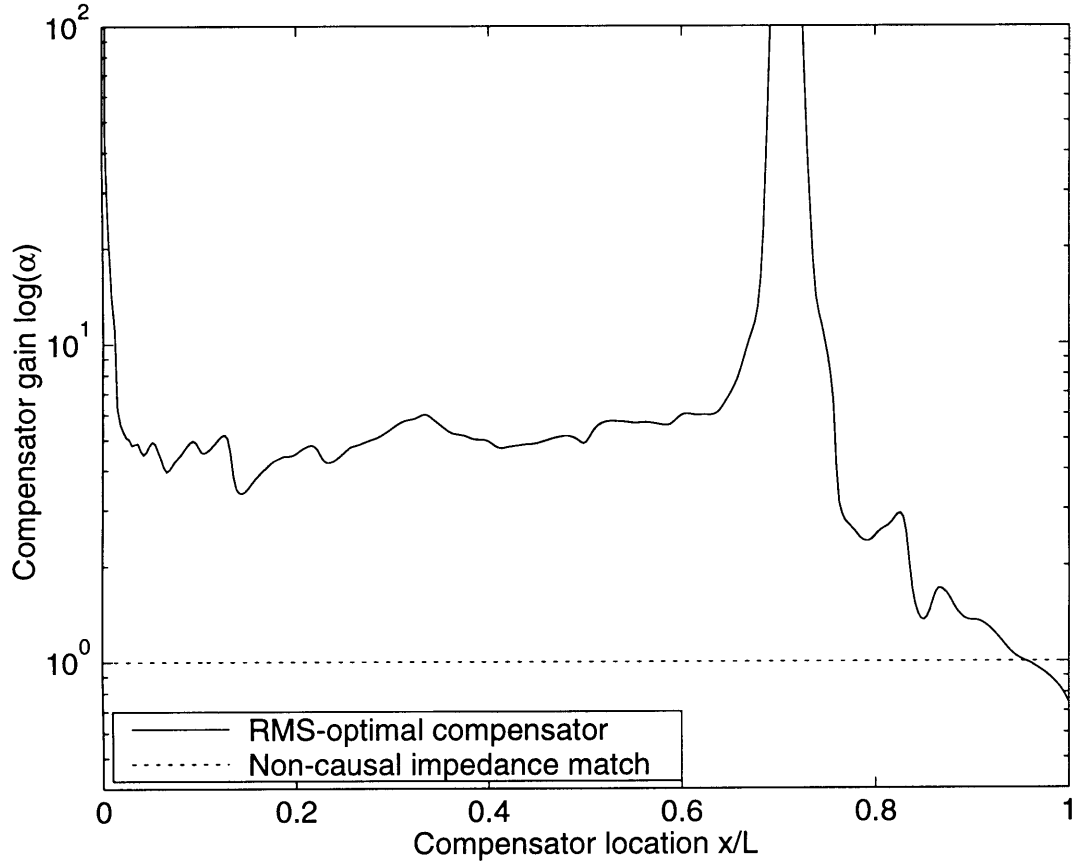

Figure 2.36: The gain α which minimizes $E\{z^T z\}$ as a function of location.

with d and with z. In the former case, high gain zeros the disturbance input power by clamping the beam. In the latter case, the control clamps the performance location. When the control is at an intermediate location, between 0 and $0.7L$, the gain is approximately 5 times the impedance gain. Thus some fraction of the power seen by the control is shunted, rather than absorbed, and the compensator is using a mixed shunting/matching strategy.

The RMS cost, given by $E\{z^T z\}$ as a function of location, is plotted for four cases in Figure 2.37. The RMS-optimal compensator zeros the RMS output at two locations, which correspond to collocation of the control with the disturbance and with the performance. For control beyond $0.7L$, the RMS optimal compensator has about the same RMS as the impedance match. In other words, the impedance match

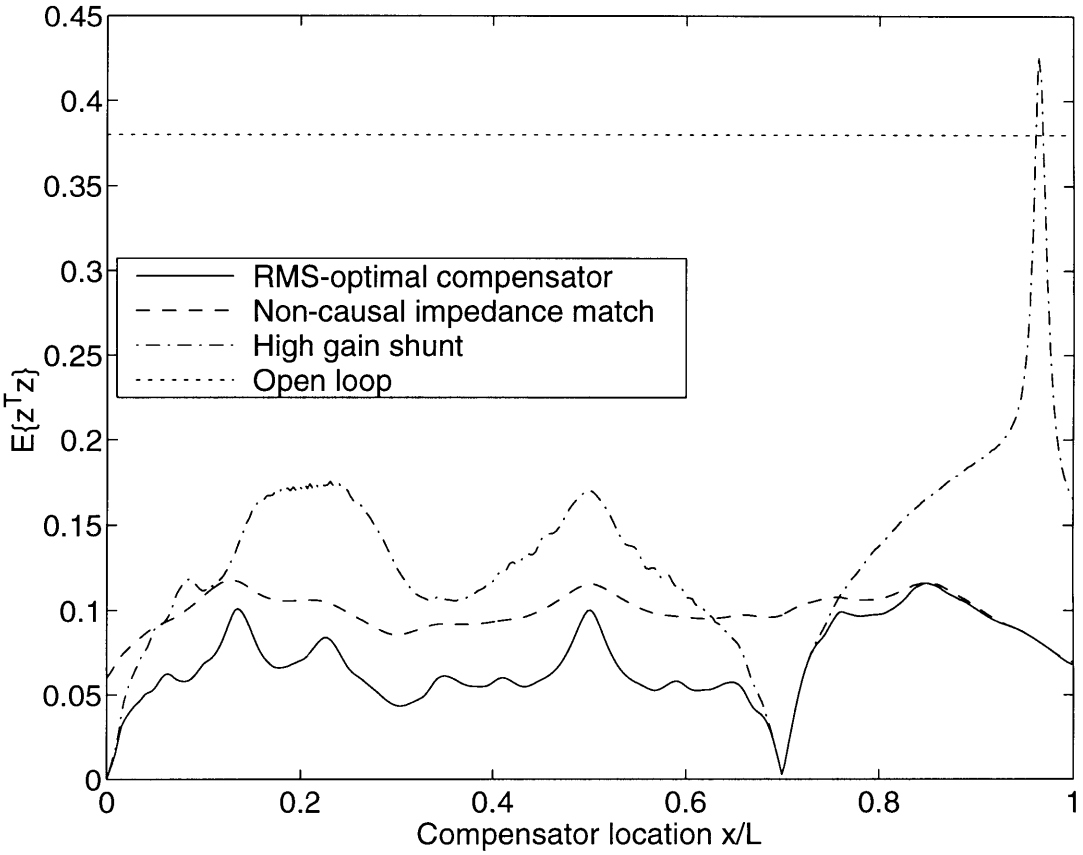

Figure 2.37: The RMS cost $E\{z^T z\}$ as a function of control location, for the RMS optimal compensator, the impedance match, the high gain shunt, and the open loop.

is the RMS optimal compensator when the control is not between the disturbance and the performance. When the control is located between d and z, the impedance match does not achieve the best RMS. Since the gain in this region is higher, some energy is necessarily being shunted away from z. Since the compensator cannot control all cross-sectional variables, some combinations of wave modes are not reflected. Thus not all power can be shunted. If all variables were controlled, the compensator could zero z from anywhere in the 0 to $0.7L$ range.

The RMS of the impedance match is interesting. One of the desirable attributes of the impedance match is its insensitivity to global variations. The location of the control along the beam changes the observability of the global modes to the

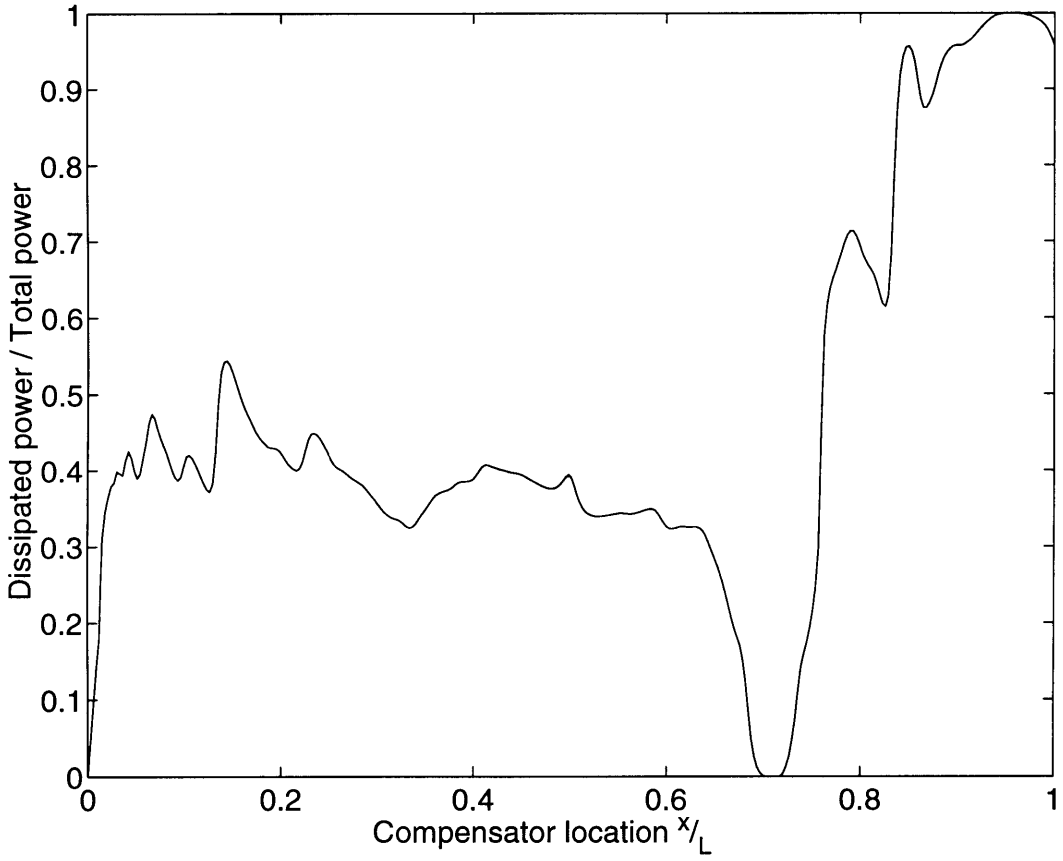

Figure 2.38: Power absorption of the RMS optimal compensator, as a function of location.

compensator. However, the RMS of the output changes minimally as the location of the impedance match varies. This is both a disadvantage and an advantage. The RMS performance is often not as good as it can be, however, the sensitivity to location is very low. The performance achieved by minimizing a global metric will be more sensitive to global plant uncertainties, possibly reducing the achieved performance. Thus the increased performance of the RMS optimal design has been achieved with a sacrifice in performance robustness. Also note that in order to achieve reduced motion at $0.7L$, the RMS optimal controller has most likely increased motion elsewhere. If the objective is to minimize a distributed RMS motion, for example the motion of the surface of a mirror, the RMS optimal controller might be closer to the impedance match.

The normalized power absorption of the RMS-optimal solution is plotted in Figure 2.38. The quantity plotted is the power absorbed by the RMS optimal controller, αH_{nc}, divided by the power absorbed by the impedance match. The power which flows in the moment/rotation combination is not accounted for. Three regions are evident, corresponding to three control strategies: total power absorption, zero power absorption, and partial absorption. At 0 and $0.7L$, no power is absorbed, since the control can zero input power or the output z. For the control location to the right of $0.7L$, the RMS optimal control absorbs about the same amount of power as the impedance match, which attempts to remove all power. When the control is located between the disturbance and performance, a combination of shunting and impedance matching is used. Power absorption is around 40 percent. Sixty percent of the energy is being shunted away from the output.

The performance of the RMS optimized compensator has been interpreted in terms of power absorption and shunting. Obviously, the control also has a modal interpretation. The high gain shunt is effectively pinning the control location. Rotation can occur, but no displacement. When the disturbance input is pinned, no power can enter the beam. The disturbance does not create any moment, so the beam does not rotate around the control. When the performance output is pinned, the beam will rotate around the output location, but the output will not be sensitive to this motion. At other locations, the performance of the beam is simply dependent on the modal observability and controllability of the beam in that configuration. The combined shunt and impedance match is essentially trying to hold the beam as still as possible. The rapid transition from zero power absorption to nearly unity between $0.7L$ and $0.8L$ is a region in which the increasing flexibility of the beam is decreasing the ability to hold z fixed.

The impedance matching and energy shunting controllers were derived to use minimal information about the plant. The objective was to desensitize the resulting local controller to changes in the plant at distant locations, robustifying performance. However, the typical control objective is a global one. A compensator explicitly designed to meet that objective is going to have nominal performance at least as

good as the local controller. In most cases the performance will be better. The tradeoff is a loss in performance robustness. The extent of the tradeoff must be investigated. To do so, it is desirable to state the objectives of the local control in a global framework. Additional advantages for a global design are the tools which are available. For example, many linear algebra tools exist to solve state space problem formulations. Also, in the course of implementation of the local controllers, non-idealities arise which cannot be treated in a local framework. These non-idealities are treated in Chapter 3.

2.3.2 Global Characteristics of the Impedance Match and Energy Shunt

$\mathcal{H}_2$ optimization has been examined in a number of frameworks. The unconstrained $\mathcal{H}_2$ optimal controller for the beam example presented above is known to be the Linear Quadratic Gaussian (LQG) controller. It is desirable to constrain the LQG problem in such a manner that the LQG solution is the impedance match, or the energy shunt, or some recognizable mixture. The formulation of the impedance matching and energy shunting problems in the state space domain is not presently known. The difficulty is in removing the global character of the response, that is, the knowledge that outgoing energy eventually returns. In lieu of an explicit state space formulation, the global characteristics of the local controllers will be examined. A number of state space $\mathcal{H}_2$ formulations which capture the same behavior will be presented.

The global $\mathcal{H}_2$ control design problem can be stated as minimizing the disturbability of some performance output z from a disturbance w, using a compensator which feeds back a measurement y to an input u. The global system can be represented as

$$\begin{bmatrix} z \\ y \end{bmatrix} = \begin{bmatrix} G_{zw}(s) & G_{zu}(s) \\ G_{yw}(s) & G_{yu}(s) \end{bmatrix} \begin{bmatrix} w \\ u \end{bmatrix} \tag{2.132}$$

where the transfer functions $G_{zw}(s), G_{zu}(s), G_{yw}(s), G_{yu}(s)$ relate the output signals z, y to the inputs w, u. They are global quantities which capture the reverberant nature of the structure.

The local control techniques offer high stability and performance robustness because they do not rely on information from $G_{zw}(s), G_{zu}(s), G_{yw}(s)$, and only extract the local portion of $G_{yu}(s)$. Stability can be guaranteed when G_{yu} is positive real [8]. Guarantees of performance robustness are more difficult to quantify, and will be approached as two separate issues. First, the control transfer function G_{yu} may be inaccurate. Second, the disturbance w and its effect on the performance, given by G_{zw}, may be known inaccurately, or not at all.

The impedance match is designed using the dereverberated portion of G_{yu}. The dereverberated model $G_d(s)$ is either a smoothed version of G_{yu}, from a log average, or a transcendental function of s from a wave model. In either case it is a "smooth" function of s, that is, the magnitude and phase change relatively slowly with frequency. For a lightly damped plant pole, the magnitude and phase can change dramatically (1 decade magnitude shifts and 180° phase shifts) in a few Hertz. If the plant pole is slightly shifted in frequency, the magnitude and phase of the compensator are nearly the same at the new modal frequency, hence the amount of damping is almost unchanged.

The optimal impedance match is generally noncausal. A causal approximation is required, which will only be able to approach the noncausal solution at certain frequencies. The approximation can be chosen to trade off nominal performance with robustness.

Consider w to be a white noise disturbance. The open loop disturbance which reaches the control is a colored noise y with a spectrum determined by the plant:

$$y = G_{yw} w \tag{2.133}$$

Assuming the plant is lightly damped, the colored disturbance will be relatively large at the plant modal frequencies. The optimal impedance matching approximation will attempt to match the noncausal solution exactly at the modal frequencies. A near match may be possible using lightly damped poles. The response of the causal compensator then deviates greatly from the noncausal between the modal frequencies (for example the dashed curve in Figure 2.39). If the modal frequencies are in actuality

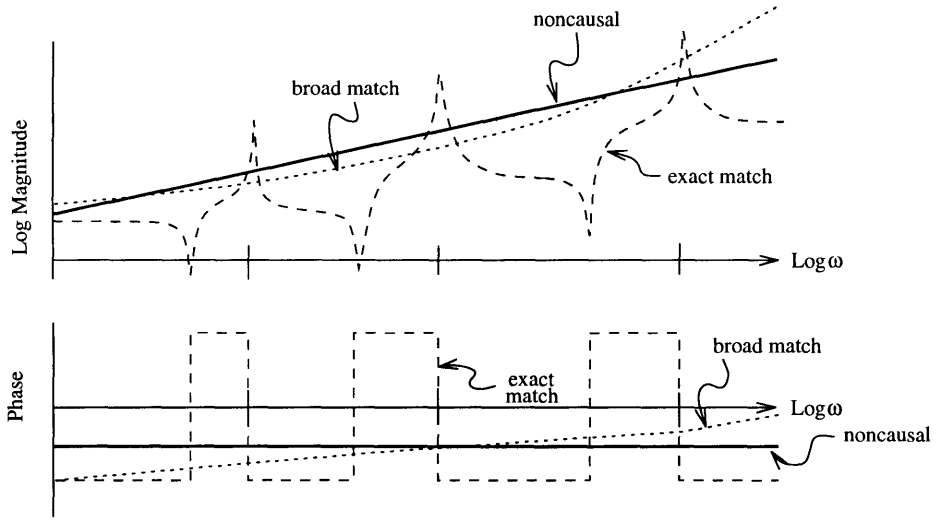

Figure 2.39: Accuracy of the impedance matching approximation: the approximation can be made an exact match to the noncausal impedance match (solid) at a discrete set of modal frequencies (dashed) or an inaccurate match across a broad frequency range (dashed) by the choice of input spectrum.

slightly shifted, the compensator gain and phase can be greatly in error at the new frequency. If, however, the compensator were designed to match over a broader range, it would not be able to match exactly at any frequency, but instead would attempt to match in an average sense (the dotted curve in Figure 2.39). The performance sensitivity is a function of how quickly the gain and phase of the approximation vary with respect to the noncausal optimal compensator. Thus the smoothness of the impedance match is one key to its performance robustness. The energy shunt is similarly smooth. The same arguments made above can be applied.

The second issue in performance robustness is the degree of knowledge of the effect of the disturbance w on the performance z. When the $\mathcal{H}_2$optimal compensator has knowledge of the G_{zw} transfer function, it can make a mode uncontrollable from the disturbance. This can be more efficient than damping the mode. The mode is made undisturbable by placing a zero in the G_{zw} transfer function. However,

zeros are properties of the input/output structure of a system, and thus depend on the disturbance location. If another disturbance acts elsewhere, the mode will be undamped.

The impedance match, on the other hand, attempts to remove energy from the system. The result is added damping in the closed loop modes. Since the modes are characteristics of the system, and not of the input/output behavior, the performance from any unmodeled or mismodeled input disturbance will be improved. The energy shunt attempts to prevent energy from reaching z. As discussed in Section 2.2, the required knowledge is the relative physical location of z and w.

The robustness properties of the impedance match and shunting compensators can be stated in global terms as follows. Stability is guaranteed because the local controllers are positive real, and are implemented on a PR plant. The $\mathcal{H}_2$ compensator can be constrained to be PR. Performance robustness to mismodeling follows from the smoothness of the compensator. Performance robustness to unknown disturbances follows by guaranteeing damping in the closed loop modes.

It is desired to state the $\mathcal{H}_2$ problem so that its solution mimics the impedance match and energy shunt as far as possible. Stability robustness for a positive real plant can be guaranteed by a positive real compensator. For a non-positive real plant, the guarantee no longer holds, regardless of the positive realness of the compensator. Stability becomes a global design issue. Techniques such as multimodel design [20] can be used to guarantee stability in the face of known plant parameter changes.

Performance robustness of the first type can be added by creating a smoothed compensator, for example using a reduced order compensator which must achieve broadband control of a large number of plant modes using relatively few compensator modes. Alternatively, the controller can be constrained to consist of real dynamics only. Performance robustness of the second type can be increased by forcing the compensator to damp system poles rather than canceling them. The real pole constraint will leave the compensator unable to cancel complex modes. Alpha shifting [21], which shifts the design plant model poles into the right half plane, can be used. Rather than perform an unstable pole zero cancellation, the compensator must shift

the closed loop pole leftward. These techniques will be presented in the following section.

2.3.3 $\mathcal{H}_2$ Minimization

A large body of theory and experience has been accumulated for linear control design. Minimization of an $\mathcal{H}_2$ performance objective, in the framework of linear, state space control has been widely investigated. It is the purpose of this chapter to examine various state space control techniques for the characteristics which were enumerated above. Formulations of the $\mathcal{H}_2$ problem will be presented which achieve the same objectives as the impedance matching and energy shunting controllers. The chapter is intended to be an outline only. For an in-depth analysis of these techniques and others, a good source is Grocott [22].

Unconstrained $\mathcal{H}_2$ Optimal Controller

The $\mathcal{H}_2$ optimal controller takes the form of the Linear Quadratic Gaussian (LQG) compensator. The n^{th} order global system, Equation 2.132, can be represented in state space as

$$\begin{aligned} \dot{x} &= Ax + B_w w + B_u u \\ z &= C_z x + D_{zu} u \\ y &= C_y x + D_{yw} w + D_{yu} u \end{aligned} \tag{2.134}$$

A dynamic compensator of order n_c of the form

$$\begin{aligned} \dot{x}_c &= A_c x_c + B_c y \\ u &= C_c x_c \end{aligned} \tag{2.135}$$

is desired to minimize the quadratic cost

$$J = E\left\{ \lim_{T\to\infty} \frac{1}{T} \int_0^T \left(z^T z + \rho u^T u \right) \, \mathrm{d}t \right\} \tag{2.136}$$

The $\mathcal{H}_2$ optimal, LQG compensator is given by

$$A_c = A - B_u K - H C_y + B_u D_{yu} C_y$$

$$B_c = H$$
$$C_c = K \tag{2.137}$$

where the matrices H, K are the solutions of

$$K = \frac{1}{\rho} B_u^T P \tag{2.138}$$

$$PA + A^T P + C_z^T C_z - \frac{1}{\rho} P B_u B_u^T P = 0 \tag{2.139}$$

$$H = \frac{1}{\mu} Q C_y \tag{2.140}$$

$$AQ + QA^T + B_w B_w^T - \frac{1}{\mu} C_y Q = 0 \tag{2.141}$$

The LQG controller is the same order as the plant ($n_c = n$). The above result is well known and can be found in any optimal control text, for example Reference [3]. A short discussion of its features will be given.

The LQG controller assumes perfect knowledge of the plant. No uncertainty in the plant model given by Equation 2.134 is taken into account. Thus the LQG controller can be undesirably sensitive to variations in plant parameters, and modifications to the problem presented above must be included to desensitize the controller to mismodeling. In addition, the controller assumes knowledge of the disturbance w. Since the problem formulation minimizes control cost as well as state cost $E\{z^T z\}$, the LQG controller often finds it more efficient to cancel closed loop poles with zeros, rather than damping the poles.

Reduced Order Control Design

A compensator of the form of Equation 2.135 which minimizes the cost Equation 2.136 is designed. However, the compensator is of order less than the plant, i.e. $n_c < n$. The order may be dictated, for example, by a limitation in controller size which can be implemented, or by the number of plant poles which appear in the performance. If a plant mode does not greatly affect the cost in Equation 2.136, computational overhead can be reduced by leaving it uncontrolled. The Separation Principle which allows the decoupling of the optimal LQG problem into two separate Riccati equations, no

longer applies. Instead, the cost is modified and the gradients with respect to the compensator matrices are found. The cost is then minimized numerically using a numerical gradient search.

The closed loop system created by impinging the reduced order controller on the plant is

$$\begin{bmatrix} \dot{x} \\ \dot{x}_c \end{bmatrix} = \begin{bmatrix} A & B_u C_c \\ B_c C_y & A_c + B_c D_{yu} C_c \end{bmatrix} \begin{bmatrix} x \\ x_c \end{bmatrix} + \begin{bmatrix} B_w \\ 0 \end{bmatrix} w$$
$$z = \begin{bmatrix} C_z & 0 \end{bmatrix} \begin{bmatrix} x \\ x_c \end{bmatrix} \tag{2.142}$$

Defining the closed loop states $\tilde{x} = \begin{bmatrix} x \\ x_c \end{bmatrix}$, the closed loop system in Equation 2.142 is

$$\begin{aligned} \dot{\tilde{x}} &= \tilde{A}\tilde{x} + \tilde{B}w \\ z &= \tilde{C}\tilde{x} \end{aligned} \tag{2.143}$$

The cost is

$$J = tr\left\{\tilde{C}^T \tilde{C} Q\right\} \tag{2.144}$$

where Q is the closed loop state covariance matrix found as the solution to:

$$\tilde{A}Q + Q\tilde{A}^T + \tilde{B}\tilde{B}^T = 0 \tag{2.145}$$

At the optimum,

$$P\tilde{A} + \tilde{A}^T P + \tilde{C}^T \tilde{C} = 0 \tag{2.146}$$

Adjoining Equation 2.145 to the cost with the Lagrange multiplier P,

$$J = tr\left\{\tilde{C}^T \tilde{C} Q + P\left(\tilde{A}Q + Q\tilde{A}^T + \tilde{B}\tilde{B}^T\right)\right\} \tag{2.147}$$

The gradient of the augmented cost Equation 2.147 can be found, with respect to the compensator. Partitioning P,Q and the product (PQ) into $n \times n$,$n \times n_c$,$n_c \times n$, and $n_c \times n_c$ elements,

$$P = \begin{bmatrix} P_{11} & P_{12} \\ P_{21} & P_{22} \end{bmatrix}, Q = \begin{bmatrix} Q_{11} & Q_{12} \\ Q_{21} & Q_{22} \end{bmatrix} \tag{2.148}$$

The gradients are:

$$\frac{\partial J}{\partial A_c} = 2(PQ)_{22} \tag{2.149}$$

$$\frac{\partial J}{\partial B_c} = 2\left((PQ)_{21}C_y^T + (PQ)_{22}C_c^T D_{yu}^T + P_{21}B_w D12^T\right) \tag{2.150}$$

$$\frac{\partial J}{\partial C_c} = 2\left(B_u^T(PQ)_{12} + D_{yu}^T B_c^T (PQ)_{22} + P_{12}^T C_z Q_{12} + D_{zu}^T D_{zu} C_c Q_{22}\right) \tag{2.151}$$

$$\tag{2.152}$$

$(PQ)_{22}$,$(PQ)_{21}$, and $(PQ)_{12}$ are the $n_c \times n_c$, $n_c \times n$, and $n \times n_c$ blocks of the matrix product PQ. These equations cannot be solved in closed form. In practice, a numerical gradient search is implemented. For an overview of numerical search algorithms and a discussion of the practical issues involved, see [23].

For this work, a modified BFGS search procedure [23] is used to minimize the cost in Equation 2.147. The solution terminates when the gradients Equation 2.149-Equation 2.151 are smaller than a selected tolerance. The problem is not guaranteed to be convex, so local minima exist. A good initial guess is critical. Additionally, the closed loop system under the initial guess must be stable. The gradients are functions of the covariance of the closed loop system. Since the covariance of an unstable system is infinite, the gradients are not well-defined, and the algorithm cannot stabilize an unstable closed loop system.

Typically, the LQG is used to create an initial guess, which is then truncated down to the desired order. To minimize the number of free parameters in the search, the compensator form is constrained. However, constraining the form can introduce additional local minima. For example, in the path from the initial compensator to the $\mathcal{H}_2$optimal compensator, complex poles may coalesce to form real modes. The constrained form should capture this behavior. A tridiagonal form for A_c has been found to yield good convergence results:

$$A_c = \begin{bmatrix} \alpha_{11} & \alpha_{12} & 0 & 0 & \cdots \\ \alpha_{21} & \alpha_{22} & \alpha_{23} & 0 & \\ 0 & \alpha_{32} & \alpha_{33} & \alpha_{34} & \\ \vdots & & & & \end{bmatrix} \tag{2.153}$$

The parameterization reduces the number of search parameters for A_c from n^2 to $3n-2$.

The purpose of the reduced order control design in an impedance matching and energy shunting sense is to prevent pole/zero cancellation. By designing the compensator order to be much less than the optimal LQG order, $n_c \ll n$, it is desired to force the compensator to reproduce the average response of the LQG controller, that is, to smooth it.

Positive Real Constraint

Given a positive real plant, the closed loop system will be stable for any positive real controller (Note that if the plant is not positive real, the guarantee is destroyed, regardless of the compensator). MacMartin investigated a Riccati cost functional which guarantees a positive real compensator [24]. Alternatively, Spangler constrains the compensator form to search over positive real compensators [14]. The state space controller has the form

$$\begin{aligned} \dot{x_c} &= A_c x_x + B_c y \\ u &= B_c^T x_c \\ A_c &= A_c^T \end{aligned} \tag{2.154}$$

Again the compensator cannot be solved for in closed form. The augmented cost can be defined, in an identical manner to Equation 2.147:

$$J = tr\left\{\tilde{C}^T\tilde{C}Q + P\left(\tilde{A}Q + Q\tilde{A}^T + \tilde{B}\tilde{B}^T\right)\right\} \tag{2.155}$$

The gradients of the cost with respect to the controller are

$$\frac{\partial J}{\partial A_c} = 2(PQ)_{22} \tag{2.156}$$

$$\frac{\partial J}{\partial B_c} = 2\left(B_u^T(PQ)_{12} + D_{yu}^T B_c^T (PQ)_{22} + D_{zu}^T C_z Q_{12} + D_{zu}^T D_{zu} C_c Q_3\right) \tag{2.157}$$

$$\tag{2.158}$$

The symmetry constraint on A_c can be implemented by searching over the upper triangular elements of A_c, and constraining the lower elements to be the transpose.

A tridiagonal form can be implemented for the positive real controller, similar to the reduced-order controller:

$$A_c = \begin{bmatrix} \alpha_{11} & \alpha_{12} & 0 & 0 & \cdots \\ \alpha_{12} & \alpha_{22} & \alpha_{23} & 0 & \\ 0 & \alpha_{23} & \alpha_{33} & \alpha_{34} & \\ \vdots & & & & \end{bmatrix} \tag{2.159}$$

The search parameters x are

$$x = \begin{bmatrix} \alpha_{11} \\ \alpha_{12} \\ \alpha_{22} \\ \alpha_{23} \\ \vdots \end{bmatrix} \tag{2.160}$$

in addition to the elements of B_c. Typically the controller will be both reduced order and positive real. Since the procedure is a numerical search, like the reduced order control design, local minima will exist and the initial guess must be good. Finding an initial guess is more difficult than in the reduced order design since the initial guess must be positive real. For $n_c \ll n$, it is generally possible to begin with a low order compensator, adding states until the performance does not improve noticeably.

Real-Axis Compensator Poles

The purpose of the reduced-order controller is to force the compensator to control several plant modes with a single compensator mode. The desired effect is to smooth the compensator response. A similar smoothing can be achieved by constraining the compensator poles to lie on the real axis. If the compensator is diagonal, all of its eigenvalues will be real:

$$A_c = \begin{bmatrix} \alpha_{11} & 0 & 0 & 0 & \cdots \\ 0 & \alpha_{22} & 0 & 0 & \\ 0 & 0 & \alpha_{33} & 0 & \\ \vdots & & & & \end{bmatrix} \tag{2.161}$$

Again a numerical search algorithm is used. The cost and gradients are identical to the reduced-order compensator, Equation 2.147 and Equations 2.149-2.151.

The similarity can be drawn between the real-pole constrained $\mathcal{H}_2$ compensator and the log averaged model of Section 2.1.1. The log averaged model is an attempt to derive a smoothed model of the plant, from which a smooth compensator will be obtained. The errors inherent in the log averaged model limit the performance of the general impedance match. The real-pole constrained $\mathcal{H}_2$ compensator sidesteps these errors. Since it cannot cancel lightly damped poles, it is forced to damp them. Additionally, by incorporating the global performance, the high gain energy shunting strategy is included in the control design process.

α-Shifting

In contrast to the previous $\mathcal{H}_2$ design techniques, alpha-shifting [21] changes the design plant model, rather than constraining the compensator. Alpha-shifting relies on the stabilizing property of the LQG compensator. As the control weighting is increased in the LQG cost (Equation 2.136), the stable open loop plant poles remain in the same location in closed loop. Open-loop unstable poles are reflected across the imaginary axis. Alpha-shifting changes the design plant model A, by adding a constant, positive real part to the plant poles:

$$A_\alpha = A + \alpha I \tag{2.162}$$

When the compensator is moved to the true plant A, the closed loop poles are shifted left, increasing their damping. If the true plant model is parameterized in modal form, the α-shifts of each mode can be tailored individually:

$$A_\alpha = \begin{bmatrix} \sigma_1 & \omega_1 & 0 & 0 & \cdots \\ -\omega_1 & \sigma_1 & 0 & 0 & \\ 0 & 0 & \sigma_2 & \omega_2 & \\ 0 & 0 & -\omega_2 & \sigma_2 & \\ \vdots & & & & \end{bmatrix} + \begin{bmatrix} \alpha_1 & & & & \\ & \alpha_1 & & & \\ & & \alpha_2 & & \\ & & & \alpha_2 & \\ & & & & \end{bmatrix} \tag{2.163}$$

where σ_i, ω_i are the real and imaginary parts of each plant mode, and α_i are the desired mode shifts. The parameters α_1, α_2, etc. are chosen to give the highest damping possible in the closed loop modes.

A secondary benefit to the α-shift is that the resulting compensators tend to be smoother, relative to the LQG controller for the same plant. This is because the necessity of stabilizing the α-shifted modes overrides the necessity of minimizing control effort. Pole/zero cancellations are prevented, as desired.

Multi-Model Control Design

The multimodel (MM) technique is another method which changes the design plant model. For further information see [25]. The MM objective is to robustify the compensator to plant changes. To this end, the compensator is applied to several different plant models, and a weighted sum of the LQG costs for each is minimized.

$$J = \sum_i a_i tr \left\{ \tilde{C}_i^T \tilde{C}_i Q_i + P_i \left(\tilde{A}_i Q_i + Q_i \tilde{A}_i^T + \tilde{B}_i \tilde{B}_i^T \right) \right\} \tag{2.164}$$

where the models are $A_i = A + \delta A_i$, and the scalar weight a_i sets the relative importance of each model in the cost. The perturbations δA_i capture the physical uncertainties in the plant models. For example, an uncertain modal frequency, known to an accuracy of 5%, can be accommodated by designing a MM compensator based on the nominal model, and two additional models with the uncertain mode shifted by $\pm 5\%$. The relative weights a_i can be chosen merely to assure stability to a 5% shift, in which case the weights of the perturbed models are small. Since the closed loop stability is only known for the design models used, no guarantee is made that the closed loop system will be stable for all models in between the nominal and the perturbed models. Alternatively, some nominal performance is lost, but approximately equal performance can be reached on all models, if the weights are equal. It is not the purpose of this thesis to examine the nominal performance versus performance robustness trades which can be made. The reader is referred to [22] for an in-depth examination.

For the impedance matching and energy shunting objectives, a smooth compen-

sator is desired. That is, rapid shifts in compensator magnitude and phase are to be avoided. The MM design technique can produce a compensator with these characteristics, if the proper perturbations δA_i and performance weights a_i are chosen.

Nondual Sensor and Actuator

The local control formulations derived above are dependent on the use of power dual sensors and actuators, for example, rate and force. The sensors and actuators available to the control designer will not always be power duals. For example, embedded piezos can be used as both sensors and actuators for structural systems [26]. However, piezos act as strain devices, hence the actuated and sensed quantities are the same. If the piezos are collocated, the feedthrough from the command to the measurement will be high. Since the command is known, the feedthrough implies that only a portion of the measurement is useful information for control.

The high feedthrough will cause the transfer function from actuator to sensor to resemble a constant, with numerous near pole/zero cancellations superimposed. These near cancellations indicate that little structural motion is being measured.

The feedthrough of command to measurement appears as a D term in the state space model (Equation 2.134). A large D term corresponds to high feedthrough. Altering the D term causes the zeros of the model to shift. If a different D term, D_2, could be chosen, the zeros of the system could be moved away from the poles, making the latter more observable. Because the poles are more observable, greater control authority can be exerted over them.

The feedforward in the model can be altered by choosing a new measurement, which has the desired feedthrough:

$$y_d = Cx + D_2 u \tag{2.165}$$

The difference between the desired measurement y_d and the actual measurement y is denoted by $\tilde{y}$:

$$\tilde{y} = y_d - y = (D_2 - D)u \tag{2.166}$$

The signal $\tilde{y}$ is in some sense an error. It is known (since u is known), and can be

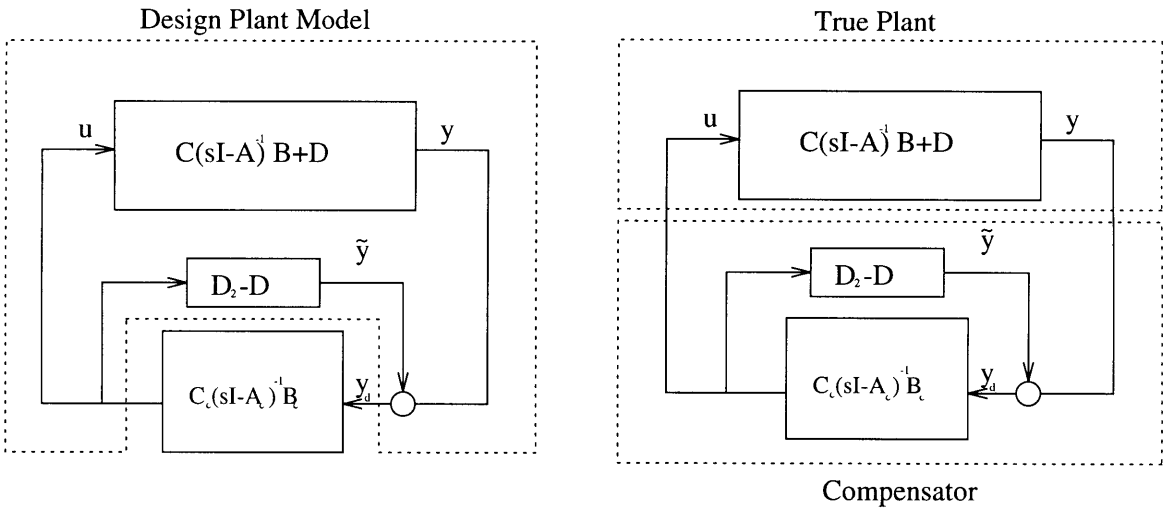

Figure 2.40: Modified feedthrough design model: The design model includes the desired feedthrough D_2 (left). When the control is implemented on the true plant, the feedthrough is folded into the compensator (right).

added to the actual measurement y to create a signal with the desired feedthrough:

$$y_d = y + \tilde{y} = Cx + D_2 u \tag{2.167}$$

The design system is now

$$\begin{aligned} \dot{x} &= Ax + Bu \\ y_d &= Cx + D_2 u \end{aligned} \tag{2.168}$$

The desired control technique ($\mathcal{H}_2$ or any applicable technique) can then be used to create a controller.

The resulting controller is

$$\begin{aligned} \dot{x}_c &= A_c x_c + B_c y_d \\ u &= C_c x_c \end{aligned} \tag{2.169}$$

where the controller is driven by the desired measurement y_d. The compensator is implemented on the true plant, Equation 2.134, whose output is y (see Figure 2.40). The component of y_d in Equation 2.169 which is due to u can be folded into the

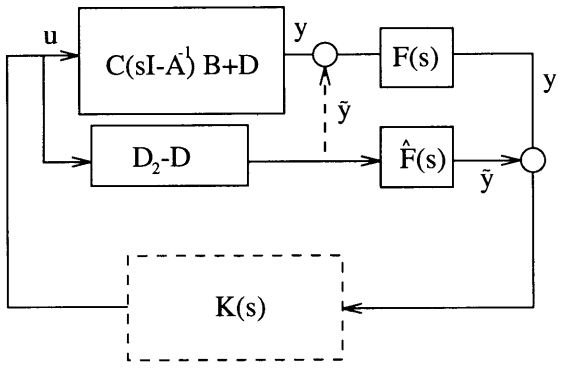

Figure 2.41: Design model with time delay: When the measurement is a filtered version of y (for example through a time delay), the plant D term cannot be canceled directly (dashed line). Instead, it must be canceled with a signal composed of u filtered by a model of the time delay, $\hat{F}$.

compensator matrix A_c. The controller dynamics are

$$\begin{aligned}
\dot{x_c} &= A_c x_c + B_c y_d \\
&= A_c x_c + B_c y + B_c(D_2 - D)u \\
&= A_c x_c + B_c y + B_c(D_2 - D)C_c x_c \\
&= \left[A_c + B_c(D_2 - D)C_c\right] x_c + B_c y
\end{aligned} \tag{2.170}$$

The command is, as before,

$$u = C_c x_c \tag{2.171}$$

Since the controller operates on the unaltered measurement y, the argument that the feedthrough modification alters the modal observability is somewhat misleading. It may be more accurate to state that the method alters the modal observability to the control design. The technique is motivated as an attempt to capture the good pole/zero spacing of a true power dual input/output pair. The connection to sensor/actuator duality has not, however, been fully explored.

The analysis presented above is correct when there is no time delay in the loop. If time delay exists, then $y + \tilde{y}$ will no longer be the desired measurement. The measurement y is delayed, while $\tilde{y}$ is not. Consider the time delay as a filter in

series with the plant (Figure 2.41), represented by a transfer function $F(s)$ (other dynamics in the loop, such as antialiasing filters, can be included in $F(s)$). The plant measurement (seen by the compensator) is now a filtered version of the plant output y:

$$\begin{aligned} y_f &= F(s)y \\ &= F(s)C(sI-A)^{-1}Bu + F(s)Du \end{aligned} \tag{2.172}$$

$$\tag{2.173}$$

The desired measurement y_d *at the plant output* is (as above)

$$y_d = Cx + D_2u \tag{2.174}$$

Now the compensator does not directly see the plant output. It sees a filtered version:

$$y_{d_f} = F(s)C(sI-A)^{-1}Bu + F(s)D_2u \tag{2.175}$$

The difference between the desired and actual output, $\tilde{y}$, is thus

$$\tilde{y} = F(s)(D_2 - D)u \tag{2.176}$$

In order to create the desired measurement, $\tilde{y}$ must be added to the actual measurement. However, $F(s)$ consists of a time delay, which is irrational, possibly in addition to high-order filters. It must therefore be approximated using a finite order system, for example a Pade approximation.

An approximation, denoted as $\hat{F}(s)$, can be realized in state space form as

$$\begin{aligned} \dot{x_f} &= A_f x_f + B_f u \\ y_f &= C_f x_f + D_f u \end{aligned} \tag{2.177}$$

The measurement "error" $\tilde{y}$ can then be approximated by filtering the correct proportion of the command feedthrough through $\hat{F}(s)$:

$$\tilde{y}_f = \hat{F}(s)(D_2 - D)u \tag{2.178}$$

The filtered desired measurement, y_{d_f}, is now equal to the filtered plant output y_f added to $\tilde{y}_f$.

$$\begin{aligned} y_{d_f} &= y_f + \tilde{y}_f \\ &= F(s)C(sI - A)^{-1}Bu + F(s)Du + \hat{F}(s)(D_2 - S)u \\ &\approx F(s)C(sI - A)^{-1}Bu + \hat{F}(s)D_2u \end{aligned} \tag{2.179}$$

The approximation is good over the bandwidth in which $\hat{F}(s) \approx F(s)$. Note that since y_{d_f} is proportional to u, it rolls off at the same rate as the compensator does. The filter $\hat{F}(s)$ need only be a good approximation to $F(s)$ over the bandwidth of the controller.

The design plant is created by augmenting the true plant dynamics, Equation 2.134, with the dynamics of the time delay $F(s)$. This can be accomplished by fitting the response of the plant from u to y_f. That is, the data used to create the plant includes the time delay. This creates a model which has the filter $F(s)$ included. The dynamics of the augmented design model can be written as

$$\begin{aligned} \dot{x}_d &= A_dx_d + B_du \\ y &= C_dx_d + D_du \end{aligned} \tag{2.180}$$

The design model is created by augmenting the filtered plant, Equation 2.180 (which represents the true plant with time delay), with the realization of $\hat{F}$. The systems are driven in parallel, and their outputs subtracted (See Figure 2.42):

$$\begin{aligned} \begin{bmatrix} \dot{x} \\ \dot{x_f} \end{bmatrix} &= \begin{bmatrix} A & 0 \\ 0 & A_f \end{bmatrix} \begin{bmatrix} x \\ x_f \end{bmatrix} + \begin{bmatrix} B \\ B_f \end{bmatrix} u \\ y_{d_f} &= \begin{bmatrix} C & (D_2 - D)C_f \end{bmatrix} \begin{bmatrix} x \\ x_f \end{bmatrix} + \begin{bmatrix} D \\ (D_2 - D)D_f \end{bmatrix} u \end{aligned} \tag{2.181}$$

The compensator is created using the design model. To implement it on the true plant, Equation 2.180, the filter approximation is augmented with the compensator:

$$\begin{bmatrix} \dot{x_c} \\ \dot{x_f} \end{bmatrix} = \begin{bmatrix} A_c + B_cD_f(D_2 - D)Cc & B_cCf \\ B_f(D_2 - D)Cc & A_f \end{bmatrix} \begin{bmatrix} x_c \\ x_f \end{bmatrix} + \begin{bmatrix} B_c \\ 0 \end{bmatrix} u$$

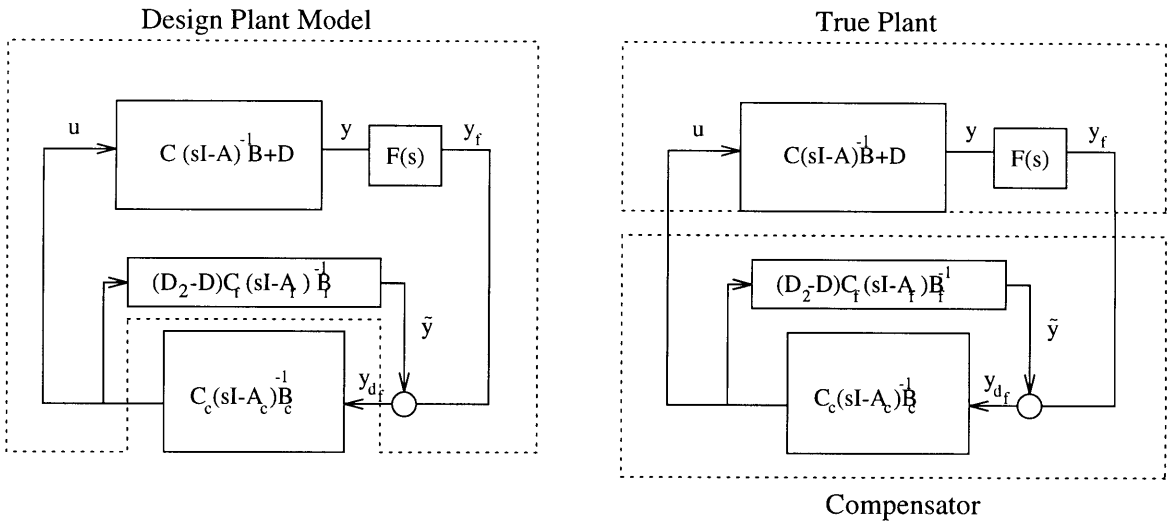

Figure 2.42: The design plant consists of the true plant (including $F(s)$) augmented with the dynamic approximation $\hat{F}$. On implementation, the compensator is augmented.

$$u = \begin{bmatrix} C_c & 0 \end{bmatrix} \begin{bmatrix} x_c \\ x_f \end{bmatrix} \tag{2.182}$$

The resulting controller will be referred to as the Modified Feedthrough (MF) controller.

Note that since the filter approximation $\hat{F}(s)$ is augmented to the compensator, its order must be taken into account if there is a constraint on the size of the compensator. Second, the bandwidth of the approximation need be no greater than the bandwidth of the control. Errors in the approximation will not be destabilizing. Only the ability to accurately cancel the D term will be affected. Finally, it is assumed that the feedthrough of the plant is high, necessitating this technique. For high feedthrough, the zero locations in the compensator measurement, y_{d_f}, can be highly sensitive to the D_2 term. The robustness of the compensator to zero locations must be assured. The local control techniques in the previous chapters tend to be quite insensitive. However, a high authority LQG-type compensator, which relies on pole/zero cancellation, can be quite sensitive.

The applicability of the modified feedthrough formulation as presented is limited by nonlinearities in the response of the piezoelectric actuator. Specifically, the piezo

voltage to strain coupling term (for a piezo wafer, the d_{31} term) is amplitude dependent. This will appear as a nonlinear gain in the control loop. The effect of the nonlinearity is small if the dynamic range of the command voltage is limited. Thus the MF design is applicable if the control commands are expected to be small (they remain in the linear range of the piezo). The modified feedthrough results could be extended through a software modification, or a hardware modification.

The software modification would take the form of a model of the piezo nonlinearity. The commanded strain would be passed through the inverse of the piezo nonlinearity before being output through the D/As. When the voltage creates a nonlinear strain in the piezo, nonlinearities would cancel, creating a strain proportional to the desired command. The software has two main drawbacks. Additional computational time is required, and the command to counteract the nonlinearity is created open-loop, creating the need for a good nonlinear model.

A second modification would entail feeding back actuator strain to enforce the desired actuation. The feedback would be done using analog circuitry. The advantages to enforcing strain actuation include removing other piezo nonlinearities such as hysteresis, as well as removing the additional computational burden of the software modification.

Chapter 3

Nonpositive Real Systems

The local control techniques derived above depend on a dual sensor and actuator. Control is then posed as influencing the power at the control location. The stability of the closed loop is guaranteed at the same time. It follows from duality that the transfer function through the control hardware is positive real. The controllers are constrained to be positive real (this is equivalent to a constraint that the closed loop junction never produces power). It follows from absolute stability theory [8] that the closed loop system will be stable.

In order to permit implementation of the impedance matching and shunting compensators on a wider class of physical systems, the implications of a nonpositive real plant need to be addressed. Control design for any real system will encounter time delays, model truncation, sensor/actuator dynamics, and possibly sensor/actuator noncollocation, which will destroy the positive real nature of the plant transfer function.

The effects of such non-idealities can occur within the control bandwidth, or beyond it. Loss of positivity beyond the control bandwidth can be dealt with by constraining the rolloff of the loop transfer function. If the effects are significant within the control bandwidth, performance (as well as stability robustness) will suffer. The design plant model can be modified by creating a "pseudo positive real" model. Alternatively, a global model incorporating the non-idealities can be created. The design then proceeds using a global technique which captures the features of the local con-

trollers (for example the techniques presented in the last chapter). Note that in all cases, the stability guarantee is no longer absolute, although stability and performance robustness may be extremely high.

Two types of non-idealities are treated in the following section, time delay and sensor/actuator noncollocation. Time delay will exist in any physical system, and may be a driving factor in control design for digital implementations. Sensor/actuator noncollocation can result in missing or nonminimum phase zeros [27].

3.1 Systems with time delay

Any real system will have time delays. For analog systems, time delays may be negligible. For digital control implementations, time delay can be significant, degrading both the performance and stability margins. The effects of time delay on the rolloff are first considered. Second, the impedance match is modified to account for time delay in the control bandwidth which degrades damping performance.

3.1.1 Stability in the presence of time delay

The impedance match and energy shunt of the previous section could in theory control energy over an infinite bandwidth. In practice, the control will be targeted at a specific bandwidth. For example, the system could be subject to a bandlimited disturbance. Alternatively, the control could be designed to damp in the rolloff region of a higher authority (perhaps MIMO) controller, increasing robustness [28]. Beyond the control bandwidth, the local controller is rolled off. The rolloff is begun at a frequency w_i. By frequency w_f the loop must be rolled off, with a gain margin of g_m (Figure 3.1). First, rolloff for an ideal system, with no time delay, is investigated.

The loop must be phase-stable within the rolloff range, and gain stabilized at the end of the range. The difficulty in rolling off a structural loop is that the response is difficult to model exactly: modes are often lightly damped, and mode frequencies are not well known. It is desirable to parameterize the rolloff in terms of quantities which

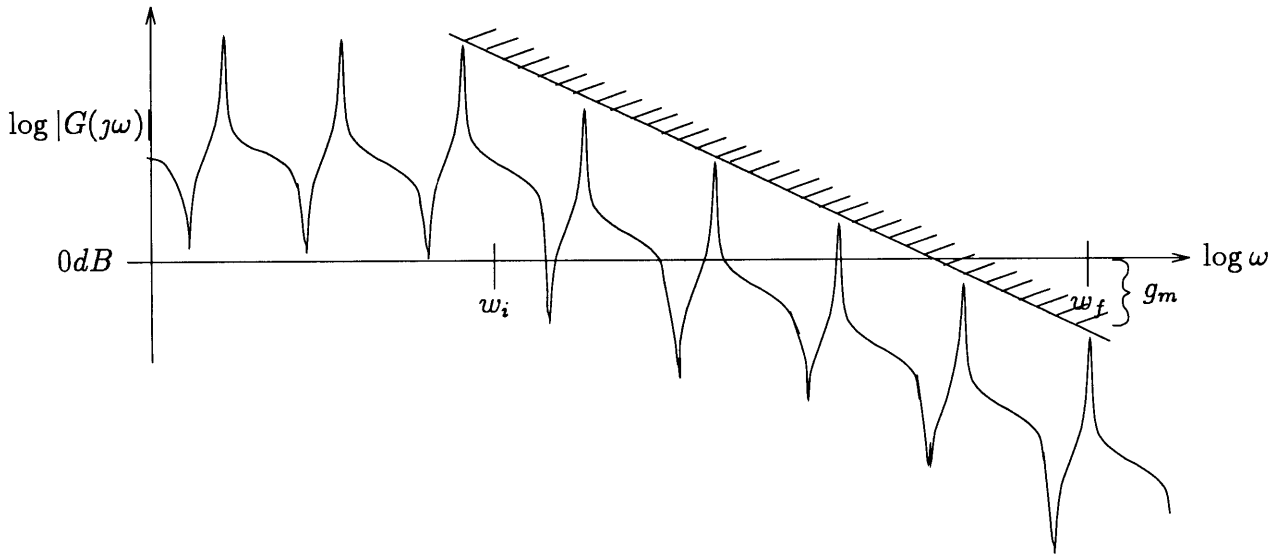

Figure 3.1: Rolloff for a structural loop.

may be known more accurately, such as the maximum magnitudes of resonances, and the minimum phase attained by the response.

In general, the modes in the rolloff range might not be known accurately. For example, finite element models suffer a loss of fidelity at higher frequencies. However, the modes are know to lie on the "backbone" response, which can be more reliably modeled, for example by a log average. The reverberant poles and zeros are perturbations to the backbone, with a certain height h. The height h establishes an envelope around the backbone. In order to gain stabilize the loop (ignoring the gain margin g_m for now), the envelope must be below the 0dB line by w_f(Figure 3.2). In other words, rolloff of the loop transfer function is guaranteed by rolling off the envelope determined by the log average $g(j\omega)$ and the reverberant mode height $h(\zeta)$.

The perturbation height for mode i, h_i, is a function of the modal damping ζ_i. The height h_i may be estimated from ζ_i by approximating mode i as a second order resonator. The reverberant system can be put in pole-residue form:

$$G(s) = \sum_i \frac{r_{1_i} s + r_{0_i}}{s^2 + 2\zeta_i \omega_i s + \omega_i^2} \tag{3.1}$$

where ζ_i,ω_i are the mode i damping and frequency, and r_{1_i}, r_{0_i} are the residues. Each of the terms in Equation 3.1 is a second order oscillator (Figure 3.3). The

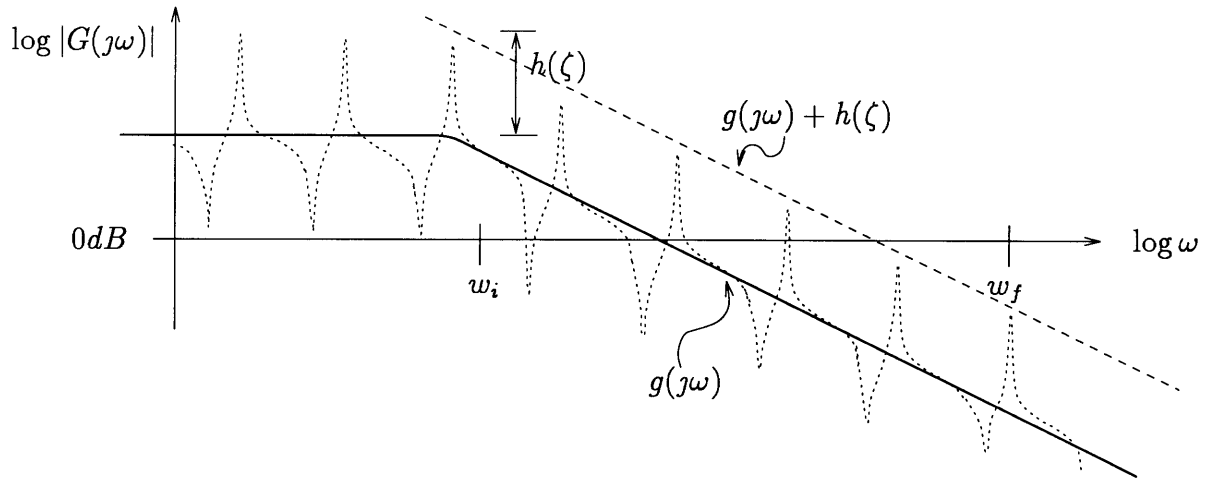

Figure 3.2: Loop magnitude for a structural system: if the envelope determined by the log average $g(j\omega)$ and the reverberant mode height $h(\zeta)$ is rolled off, the loop will be gain stable.

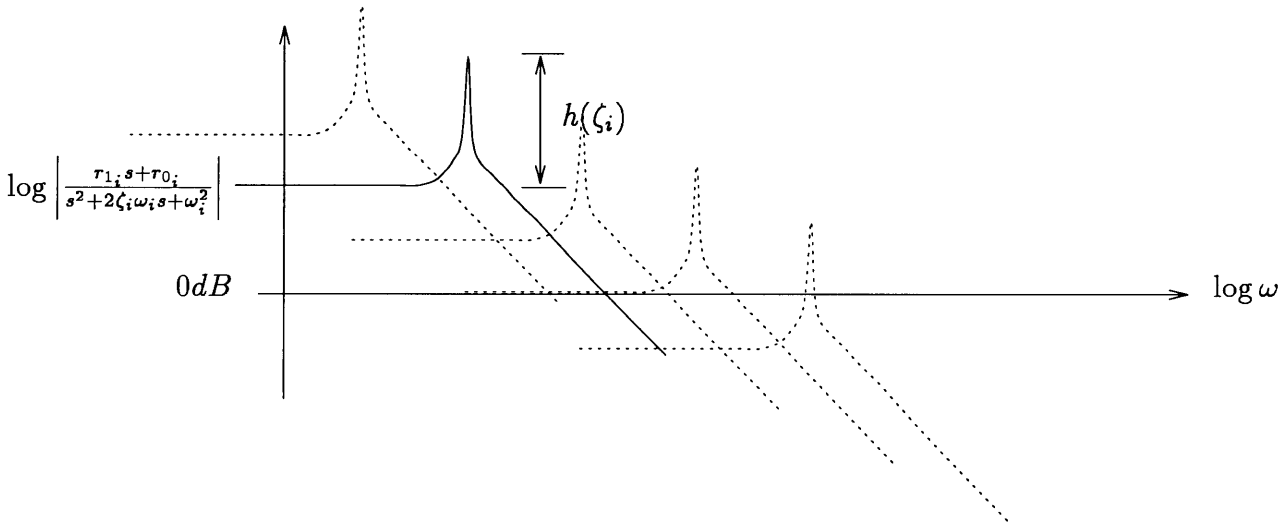

Figure 3.3: The reverberant mode height $h(\zeta_i)$ can be approximated using the residue expansion of $G(s)$.

log magnitude of the backbone is approximately the DC magnitude of the 2^{nd} order system. The height h_i is approximately the difference between the log magnitude of the resonant system at the damped pole frequency, $\omega_{d_i} = \omega_i\sqrt{1-\zeta^2}$, and the log magnitude at DC.

$$h_i \approx \log \frac{\left|\frac{r_{1_i}s+r_{0_i}}{s^2+2\zeta_i\omega_i s+\omega_i^2}\right|_{s=j\omega_d}}{\left|\frac{r_{1_i}s+r_{0_i}}{s^2+2\zeta_i\omega_i s+\omega_i^2}\right|_{s=0}} \tag{3.2}$$

For lightly damped systems, $\omega_d \approx \omega_i$, and $r_{1_i} \approx 0$. The height is then

$$\begin{aligned} h_i &\approx \log \frac{\left|\frac{r_{0_i}}{-\omega_i^2+2\zeta_i\omega_i^2 j+\omega_i^2}\right|}{\left|\frac{r_{0_i}}{\omega_i^2}\right|} \\ &\approx \log \frac{1}{2\zeta_i} \end{aligned} \tag{3.3}$$

Assuming approximately constant modal damping, $h(\zeta_i) \approx h(\zeta)$.

If the magnitude of the backbone is represented by $g(\jmath\omega)$, the log magnitude of the reverberant transfer function can be bounded:

$$\log|G(\jmath\omega)| \leq g(\jmath\omega) + h(\zeta) \tag{3.4}$$

The loop must be below $0dB$ at w_f to be gain stable. This is guaranteed if the envelope is below $0dB$.

$$\log|G(\jmath\omega_f)| \leq g(\jmath\omega_f) + h(\zeta) < 0 \tag{3.5}$$

For a constant rolloff slope $n = \frac{\partial g(\jmath\omega)}{\partial \log\omega}$, the magnitude of the backbone at w_f is related to the magnitude at w_i by

$$g(\jmath\omega_f) = g(\jmath\omega_i) + n\left(\log\omega_f - \log\omega_i\right) \tag{3.6}$$

Therefore, the loop envelope is gain-stable at ω_f if

$$g(\jmath\omega_i) + n\left(\log\omega_f - \log\omega_i\right) + h(\zeta) < 0 \tag{3.7}$$

Equation 3.7 can be satisfied by requiring

$$n < \frac{-\left(g(\jmath\omega_i) + h(\zeta)\right)}{\log\omega_f/\omega_i} \tag{3.8}$$

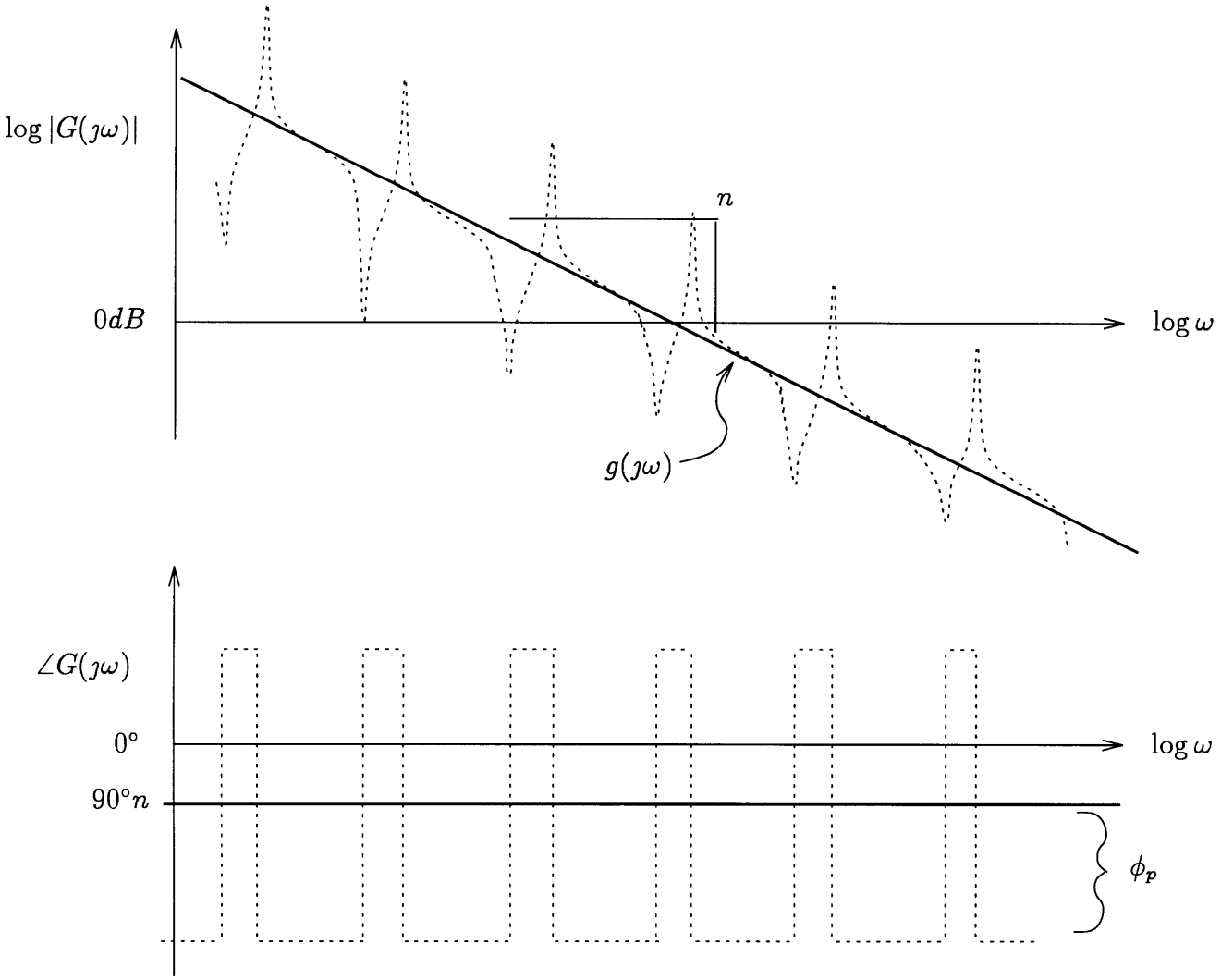

Figure 3.4: The loop phase for a structural system: the plant perturbation phase, ϕ_p, is the difference between the backbone phase, $90°n$, and the lowest plant phase.

Thus a gain margin constrains the loop to roll off faster than a certain rate. If a gain margin g_m is desired,

$$n < \frac{-g_m - (g(j\omega_i) + h(\zeta))}{\log \omega_f/\omega_i} \tag{3.9}$$

In other words, in order to be gain-stable by ω_f, a certain slope is required.

A phase margin ϕ_m constrains the slope to be greater than a certain value. A function with a slope n on a log magnitude vs log frequency axis, i.e. $f(s) \propto s^n$, has a phase of $90°n$ (Figure 3.4). The loop phase is the backbone slope, n, plus the

additional amount, ϕ_p, due to plant resonances. The phase margin is the difference between $-180°$ and the loop phase:

$$\phi_m = (90°n + \phi_p) - (-180°) \tag{3.10}$$

For a specified phase margin,

$$\begin{aligned} 90°n + \phi_p + 180 &\geq \phi_m \\ n &\geq \frac{1}{90°}\phi_m - \frac{1}{90°}\phi_p - 2 \end{aligned} \tag{3.11}$$

Thus, a faster rolloff necessitates a smaller phase margin. The gain requirement Equation 3.9 and phase margin Equation 3.11 cannot necessarily be satisfied at the same time. The maximum frequency w_f may need to be increased, to give a wider rolloff frequency range. Note that the gain margin must account for uncertainty in the knowledge of the damping, through $h(\zeta)$. Damping is difficult to predict, hence the choice of $h(\zeta)$ may potentially be very conservative.

The above analysis does not include time delay. Time delay will be present in any physical system, and may be a significant factor in a digital implementation. The presence of time delay in the loop is investigated. Time delay adds a linear phase lag. For a time delay T, the phase loss is

$$\phi_{TD} = -\frac{180°}{\pi}\omega T \tag{3.12}$$

The loop phase is now

$$90°n + \phi_p - \frac{180}{\pi}\omega T \tag{3.13}$$

which is a function of frequency. With no rolloff ($n = 0$), the loop phase will cross $-180°$ eventually. Thus the bandwidth of the loop (w_f) will have to be below a certain frequency, and the designer cannot arbitrarily choose w_f. For a specified phase margin, at the rolloff frequency w_f, the slope must be

$$n \geq \frac{1}{90°}\phi_m - \frac{1}{90°}\phi_p + \frac{180}{\pi}\omega_f T \tag{3.14}$$

However, the gain margin still requires that

$$n < \frac{-g_m - (g(j\omega_i) + h(\zeta))}{\log \omega_f/\omega_i} \tag{3.15}$$

With no time delay, the rolloff bandwidth can be increased to accommodate both the gain and the phase margin. Here, the system must be gain stable before the time delay causes phase instability. For zero phase margin and zero slope, the frequency at which the loop phase crosses $-180°$ is $\frac{\pi(180°+\phi_p)}{180°T}$ rad/sec. The loop *must* be gain-stable by this frequency, so w_f must be a lower frequency.

Certain assumptions made above can be relaxed. For example, the rolloff slope need not be constant. A faster rolloff can be accommodated at lower frequencies, at which the phase lag of the time delay is less significant. However, if the rolloff cannot be accomplished, the initiation of rolloff, at w_i, must be made at a lower frequency, decreasing performance.

The results above show that the plant perturbation phase ϕ_p is very important. ϕ_p is a result of the sensor and actuator used for control, thus a good choice of sensor and actuator is fundamental to robust implementation of either the impedance match or the energy shunting compensator. A useful example is the BE beam of Section 2.1.3. The controlled end is free to translate and rotate, thus either force or moment actuation can be used. The dual sensors are linear rate and rotational rate, respectively. The transfer functions through both sets of hardware are positive real, that is, the phase is bounded between $+90°$ and $-90°$. As defined above, ϕ_p is the difference between the lowest plant phase, $-90°$, and the phase of the backbone.

The backbone response of the beam is given by the direct field, which in turn is found from the generation matrix Ψ, Equation 2.91:

$$\Psi_F = \frac{1+i}{2EIk^3}\begin{bmatrix} -1 \\ -1 \end{bmatrix} \tag{3.16}$$

$$\Psi_M = \frac{1+i}{2EIk^2}\begin{bmatrix} -1 \\ -i \end{bmatrix} \tag{3.17}$$

The generation matrix Ψ describes how wave modes are formed by F and M. Using the wave transformation Y, the wave modes can be transformed into physical coordinates, and the correct displacements (displacement and rotation, respectively) found. The wave number k can be expressed as a function of frequency. Differentiating the

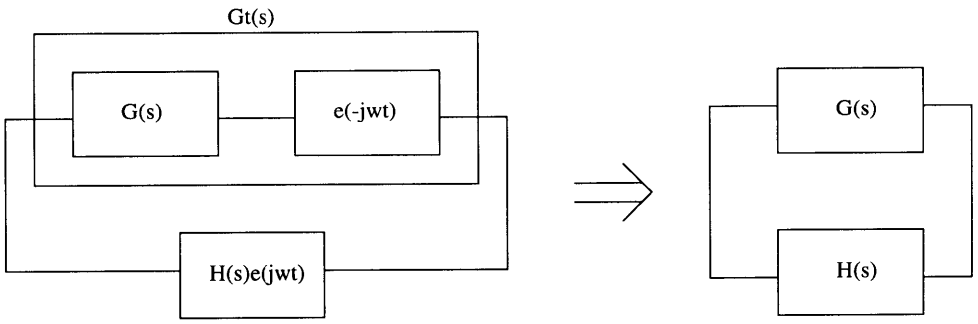

Figure 3.5: The control design with time delay. The inverse of the time delay is added to the model, creating a "pseudo-positive real" plant.

results, the direct fields are

$$g_F(s) = \frac{2\sqrt{2}}{(\rho A)^{\frac{3}{4}}(EI)^{\frac{1}{4}}} s^{-\frac{1}{2}} \tag{3.18}$$

$$g_M(s) = -\frac{2\sqrt{2}}{(\rho A)^{\frac{1}{4}}(EI)^{\frac{3}{4}}} s^{\frac{1}{2}} \tag{3.19}$$

which have phases of $-45°$ and $45°$. The plant perturbation phases are therefore $45°$ and $135°$. The force to linear rate pair has an additional $90°$ of phase margin.

3.1.2 Performance in the presence of time delay

Significant time delay can add phase to the loop in the control bandwidth. If the compensator is designed for the nominal plant, without time delay, the loop phase will be in error, and the performance will degrade. The difficulty will be greatest in the impedance matching compensator, because of the requirement of matching the noncausal phase. The energy shunting compensator is generally insensitive to phase errors which do not create instabilities, because of the high gain approximation normally used. Hence the performance discussion will be centered on the impedance matching approximation.

Consider Figure 3.5, in which the actual plant $\tilde{G}(s)$ is represented by a positive real component, $G(s)$, and a nonpositive real part, consisting of a time delay of T seconds. The objective is to design $K(s)$ using impedance matching techniques which are developed for positive real systems. They cannot be used on the actual plant $\tilde{G}(s)$ since it is not positive real. However, they can be used to find the (assumed noncausal)

impedance match for the positive real part $G(s)$. Rather than approximating that compensator, denoted as $H_{nc}(s)$, a causal approximation is found for $e^{\jmath\omega T}H_{nc}$. The loop phase for the impedance match with phase lead, when implemented on the actual plant $\tilde{G}(s)$, is

$$\tilde{G}(s)e^{\jmath\omega T}H_{nc} = G(s)e^{-\jmath\omega T}e^{\jmath\omega T}H_{nc}(s) = G(s)H_{nc}(s) \tag{3.20}$$

which has the correct phase. When the noncausal compensator with lead is approximated, the phase lead in the approximation cancels out the phase lag in the actual plant.

Care must be taken in the general impedance derivation. The general impedance match is

$$H_{nc} = \frac{1}{G_d(s)^*} \tag{3.21}$$

where $G_d(s)$ is the dereverberated mobility of the positive real plant $G(s)$, *not* the actual plant $\tilde{G}(s)$. If the reverberant data includes the time delay, the dereverberated model must be created in such a manner that the time delay does not appear. Fortunately, in the case of the log average, the restriction is simple to implement. Since the time delay appears as a phase perturbation only, the log average should be created by minimizing only the magnitude error.

Note that the technique forces an approximation step, even if the exact impedance match is causal. A rational Pade approximation to the time delay can be created. A single-pole approximation is

$$e^{-\jmath\omega T} \approx -\frac{s-2/T}{s+2/T} \tag{3.22}$$

which is stable but nonminimum phase. The actual plant model is

$$\tilde{G}(s) \approx G(s)\left(-\frac{s-2/T}{s+2/T}\right) \tag{3.23}$$

and the noncausal compensator for the nonpositive real system, which includes a phase lead, is

$$-\frac{s+2/T}{s-2/T}H_{nc} \tag{3.24}$$

The phase lead therefore consists of right half-plane (RHP) dynamics. By the same arguments that the noncausal compensator is stable but noncausal, the phase lead,

and therefore the augmented impedance match, is noncausal. Thus a causal approximation step will be required. The most straightforward approximation is the weighted curve fit shown in Section 2.1.3.

3.2 Noncollocation

The fundamental assumption made to derive the local controllers of the previous section is the collocation of the sensor and actuator. Stability robustness follows from collocation and duality, as a result of the positive real response of the system through the control hardware. Performance robustness results from ensuring that the closed loop system extracts power over a broad frequency range. However, it can be necessary to use a *nearly collocated* sensor and actuator in some applications. Nearly collocated refers to the separation of the sensor and actuator being comparable to the dimension of each. For example, in applications with embedded piezoelectrics, the piezos must be displaced from one another to avoid near-field interaction from swamping the measurement with feedforward of the actuator signal. The physical spacing is such that it is still reasonable to consider the influence of the control on local power. However, the control transfer function is no longer necessarily positive real. Effects such as missing or nonminimum phase zeros will appear [27].

The local models derived above are no longer sufficient to capture the behavior of the control location. Global characteristics of the system, such as boundary conditions, will effect the control transfer function. It is necessary to use a global model of the system for control design. A secondary benefit to the use of a global model is the wealth of tools available for design and analysis. The $\mathcal{H}_2$ design techniques of Section 2.3.2 are ideally suited.

Power Observer Interpretation It is stated above that nearly collocated sensors and actuators can be used to influence power. Due to the noncollocation, the product of the sensed and actuated quantity is no longer power. However, the near collocation allows the conception of the compensator as composed of an estimator of

the appropriate physical variables at the actuated cross-section, as well as the dynamic compensator which acts to remove power. Since the physical measurement variables at the sensed cross-section are related to the power dual variables at the control cross-section by a small and presumably relatively homogeneous portion of the structure, such estimation will not require knowledge of the global states of the structure. The estimator is in effect modeling the propagation of information from the actuated cross-section through the structure to the sensor. It is suggested that the estimation is done implicitly in the $\mathcal{H}_2$ designs. No work has been done on explicit formulation of such a physical state estimator.

Chapter 4

AMASS Active Materials Testbed

The Advanced Materials Applications to Space Structures (AMASS) program is an investigation of a number of advanced materials and technologies. The hardware consists of a deployable solar array simulator, gimbal-mounted to an instrumented spacecraft bus. The experiment will investigate techniques for minimizing the spacecraft jitter induced by the array. A metal matrix Solar Array Drive Assembly (SADA) drives the array in two axes of motion, simulating a sun-tracking profile. A passively damped joint and a active composite yoke, actuated with embedded piezoelectrics, are used to control the array. The active control is implemented by four Multi-Chip Module (MCM) microcontrollers attached to the yoke. The active control design is of interest because the disturbance, in the form of the SADA torque, is not measurable. Additionally, the active control must be highly robust to modal frequency shifts. The impedance matching and energy-shunting techniques of Chapter 2 are promising candidates.

4.1 AMASS Flight Experiment

The array simulator flight hardware consists of a deployable solar panel simulator, an active composite yoke with embedded piezoelectric actuation and sensing, a viscoelastically damped joint, and the SADA gimbal (Figure 4.1). The passive joint can be locked out with a caging mechanism. The testbed is bolted to the back of the STEP 3

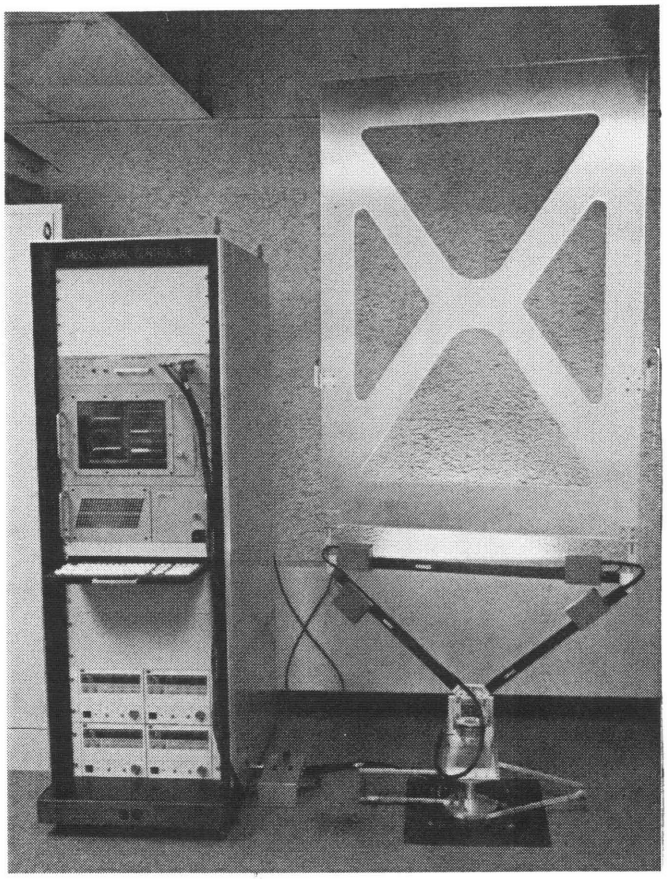

Figure 4.1: The AMASS testbed.

spacecraft, between the functional solar arrays. Four Intel 80196KD microcontrollers implement the active control. The controllers are uploaded from the ground control station. Accelerometers on the array and the spacecraft measure motion induced by the gimbal stepper motor. Spacecraft jitter is measured in four configurations: undamped, passive damping only, active control only, and combined passive damping and active control.

The Intels also operate in two system identification (ID) modes. A sine sweep mode drives the array with a swept frequency sine wave. The microcontroller collects and downloads the Fourier coefficients of the frequency response. A Schroeder mode drives the array with a Schroeder-phased input, which contains equal power at all

frequencies, and collects the time response. Since the sine sweep accumulates the transfer function directly, it produces a much more compact set of data, and requires no post-processing. However, it requires more time to complete than the Schroeder ID.

The active control design is interesting and challenging from a number of perspectives. No accurate model is available prior to the flight. The control design will be based on the on-orbit system ID. A Controlled Structures Interaction (CSI) problem exists due to the coupling which will occur between the AMASS dynamics and the functional arrays. While this problem exists for AMASS since it is not the functional array, an actively damped, functional array could interact with flexible payloads on the bus. The CSI problem is therefore general in scope.

Additionally, the data-collecting ability of the array host restricts the amount of data which can be taken. The system identification consists only of the control channels. The disturbance to performance transfer functions, and cross-coupling between the control and the performance, are unknown. The flight controller must be insensitive to the directionality of the disturbance.

Finally, the desire for stability robustness is high. Locating the source of instability from the ground station would be time-consuming and expensive. In the case of a functional array, an unstable controller could result in failure of the array and loss of the spacecraft. The attributes of stability robustness and insensitivity to disturbance directionality are exactly those of local control, motivating an investigation into the potential applications of energy shunting and impedance matching.

The proposed control design sequence will be presented. A series of designs will be created, and experimentally evaluated on a ground version of the AMASS array. The performance of the compensators will be compared to one another and to standard damping compensators. The stability attributes of each of the compensators will be discussed. Finally, a discussion of the flight control design procedure will be given.

Table 4.1: Identified Modes of the AMASS ground testbed.

Mode	Freq [Hz]	Damping [%]	Modeshape
1	0.9582	1.7218	1^{st} bending
2	5.4960	0.5356	1^{st} torsion
3	9.8558	0.5796	2^{nd} bending
4	20.2347	0.8494	
5	28.5356	0.6842	

4.2 AMASS Ground Testbed

The AMASS ground testbed is the prototype flight hardware. All of the hardware capability is in place. The array can be bolted to an inertial base, or mounted on a gimbal assembly. Prototype Active Control Drive Electronics (ADCE) breadboards are bolted to the active yoke. The ADCEs are controlled via an RS-232 link to the host PC. The host PC controls the ADCE and piezo drive power sources, uploads the controller matrices and scaling factors, and downloads compensator diagnostics parameters. The ADCEs cannot communicate. Control must be implemented via separate single-input, single-output (SISO) compensators, one per ADCE.

An independent data acquisition system is used to measure frequency response and time domain data. The data acquisition system is MacIntosh-based, running LabView software. Stand-alone 6-pole Bessel filters are used for antialiasing. The software does not incorporate any digital filtering. Partially as a result, the antialiasing filter dynamics tend to corrupt the data above about 80% of the test bandwidth, and introduce an approximately linear phase loss at lower frequencies. Data reduction is performed in Matlab.

The first five modal frequencies and shapes are given in Table 4.1. Based on a Finite Element model of the coupled spacecraft and array, the first three modes are the greatest contributors to jitter. The fourth and fifth modes are the most significant modes in the rolloff range. The Intel controller can run an uploadable, 12 state compensator at a sample rate of 250 Hz. The targeted modes are well within the control bandwidth.

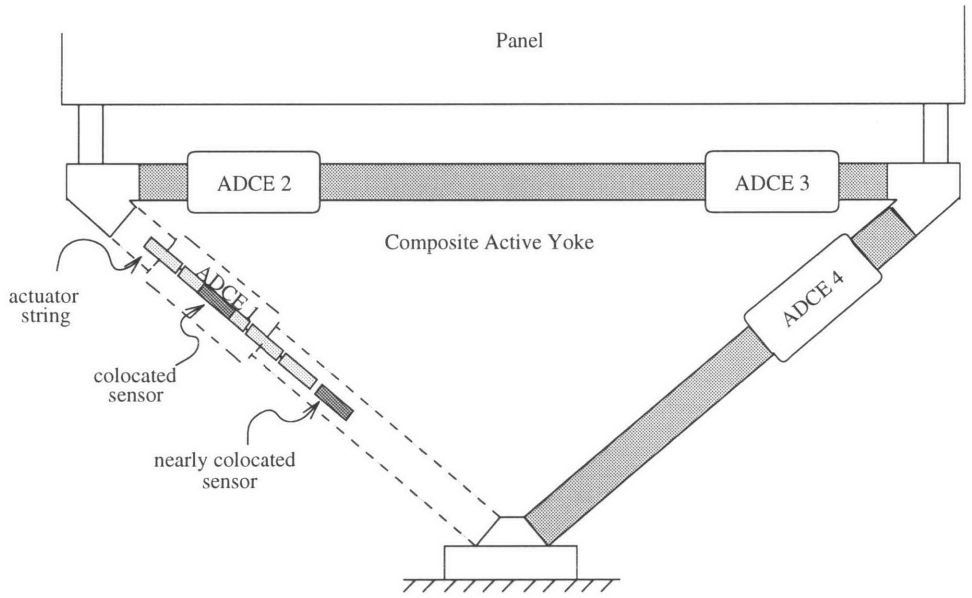

Figure 4.2: ADCE positions on the active yoke. The ADCEs operate independently on embedded piezo actuators and sensors.

4.2.1 Modeling

The AMASS testbed is inherently a multiple-input, multiple-output (MIMO) structure. Each ADCE input is highly observable in the outputs of the other ADCEs. Cross-coupling of the controllers cannot be neglected. The four ADCE drive amps are the inputs. Nominally, there are eight outputs: four nearly collocated sensors , designated as S_{nc_1} to S_{nc_4} and four collocated sensors, designated S_{c_1} to S_{c_4}. These are reduced to four outputs by the weighted summation of the sensor signals. The piezo feedthrough in the collocated sensor is extremely high. The plant modes are nearly unobservable. As a result, only the nearly collocated sensor is used for control.

The plant frequency responses from each actuator to each nearly collocated sensor are shown in Figures 4.3-4.6. The inputs and outputs are numbered according to the ADCE locations. The ADCEs are numbered from 1 to 4, clockwise beginning at the left diagonal (Figure 4.2). First mode is quite observable to ADCEs 1 and 4 (Figure 4.3 and Figure 4.6), on the diagonal members. Third mode is moderately observable, and second mode appears. The cross-member ADCEs have lower modal observability, and second mode is essentially unobservable.

Note that the individual transfer functions of the array though the piezo struts are nonpositive real. In the diagonal strut responses, a zero is missing between second and third modes. The phase drops through 0° at the third mode. The plant transfer function is therefore not positive real.

MIMO frequency response data is used to create a 50-state, 4 input, 4 output evaluation model. The model is created using a unique two step process utilizing a Frequency-domain Observability Range Space Extraction $FORSE$ algorithm to create an initial model [29], and an iterative Log-Least Squares algorithm to reduce and tune the model [30]. The model captures the array response to 100 Hz. A 22-state, 4 input, 4 output design model is created by truncating out the modes of the evaluation model above 60 Hz. The models contain a time delay capturing the 250 Hz sampling rate of the ADCE, with a zero-order hold. The transfer functions through the ADCEs used for control, ADCEs 1 and 4, are plotted against data in Figures 4.7-4.10.

The agreement of the fit to the data for the collocated channels, G_{11} and G_{44}, is excellent. The first discrepancies are noted at about 30 Hz. More error occurs in the cross-transfer functions, G_{14} and G_{41}. However, the agreement to 30 Hz is acceptable.

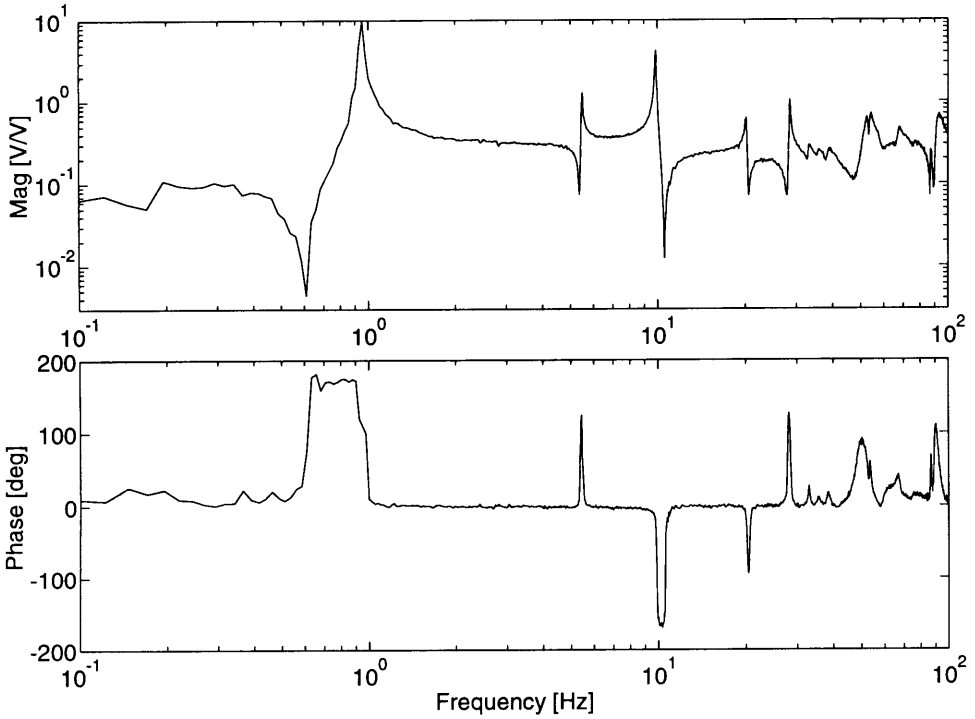

Figure 4.3: G_{11}: Measured response from ADCE 1 drive amp to S_{nc_1}.

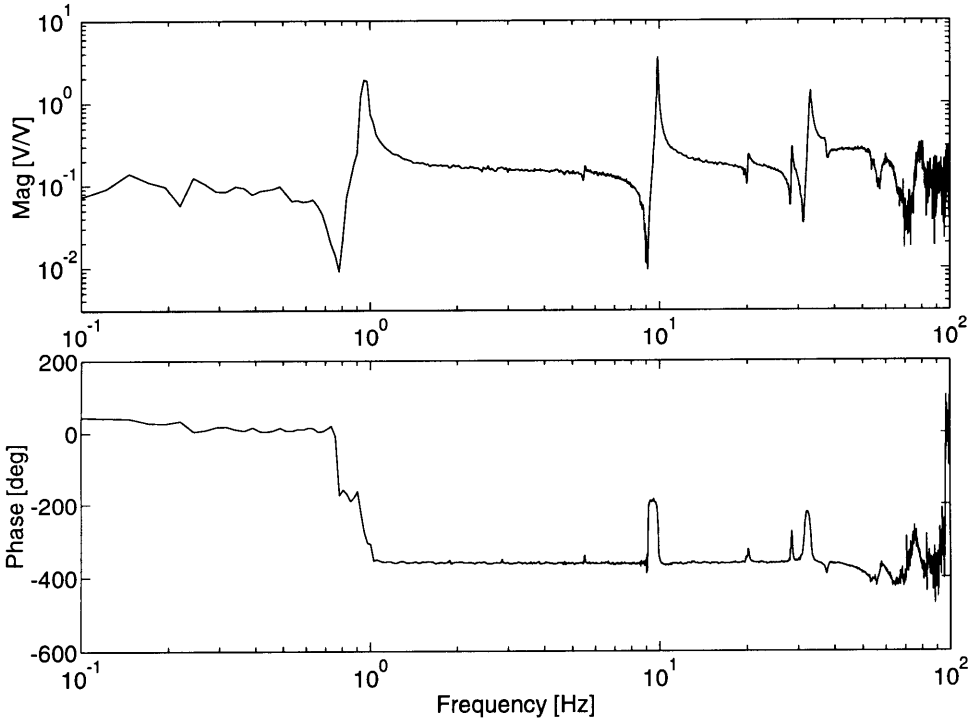

Figure 4.4: G_{22}: Measured response from ADCE 2 drive amp to S_{nc_2}.

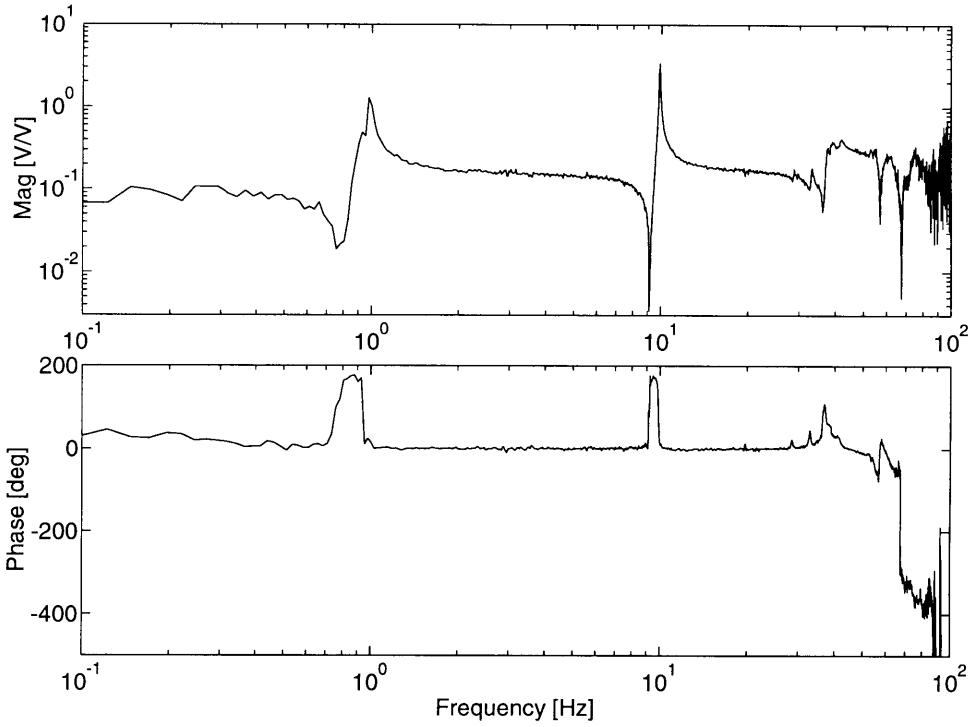

Figure 4.5: G_{33}: Measured response from ADCE 3 drive amp to S_{nc_3}.

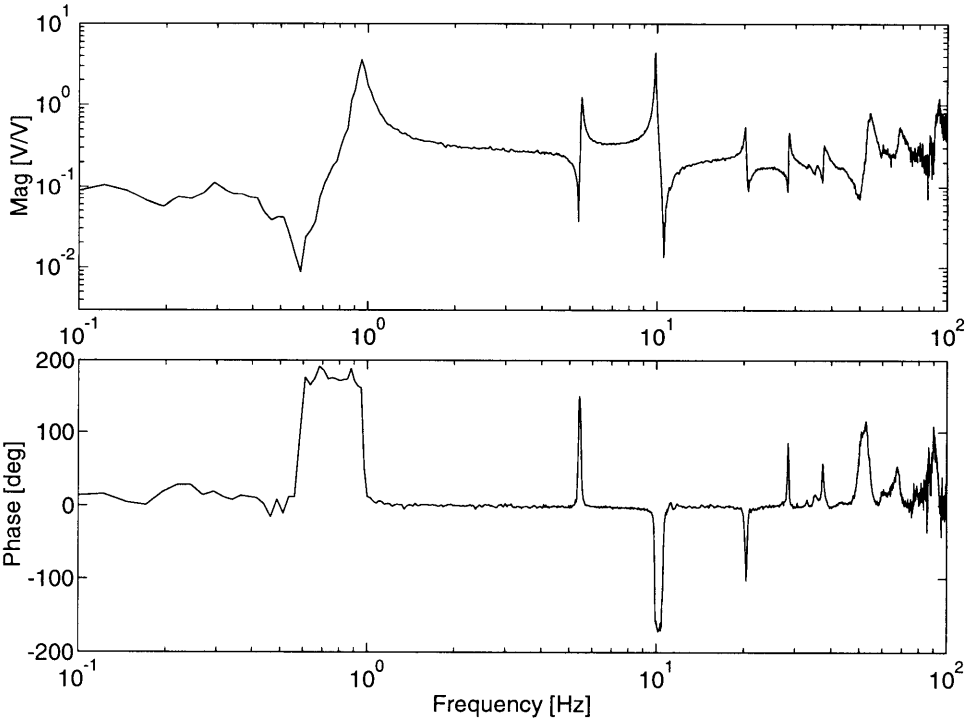

Figure 4.6: G_{44}: Measured response from ADCE 4 drive amp to S_{nc_4}.

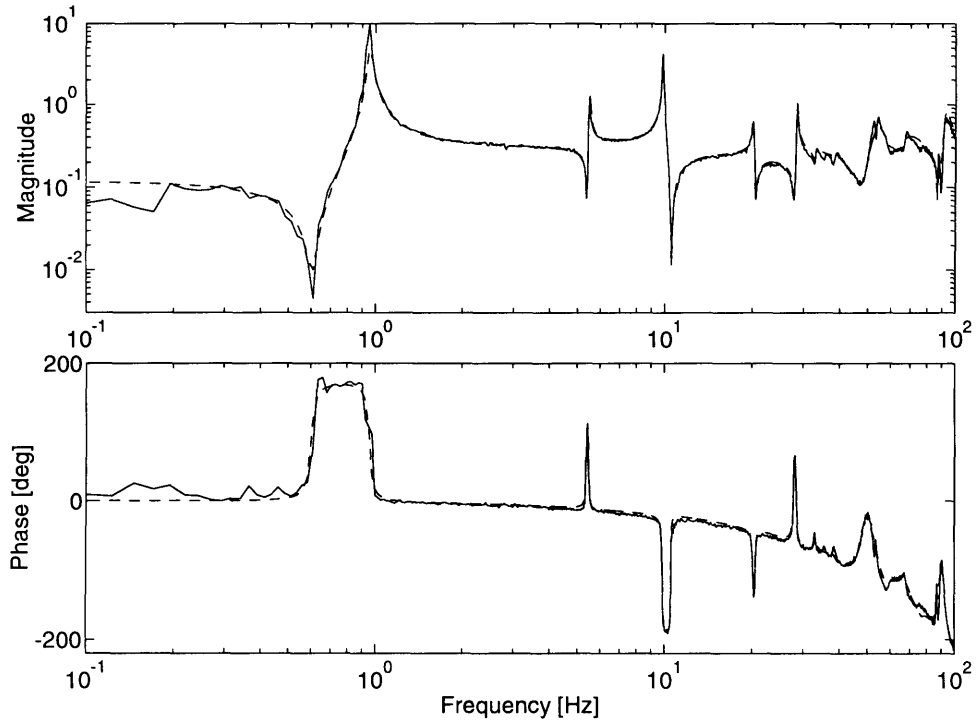

Figure 4.7: G_{11}: measured (solid) and state-space fit (dashed).

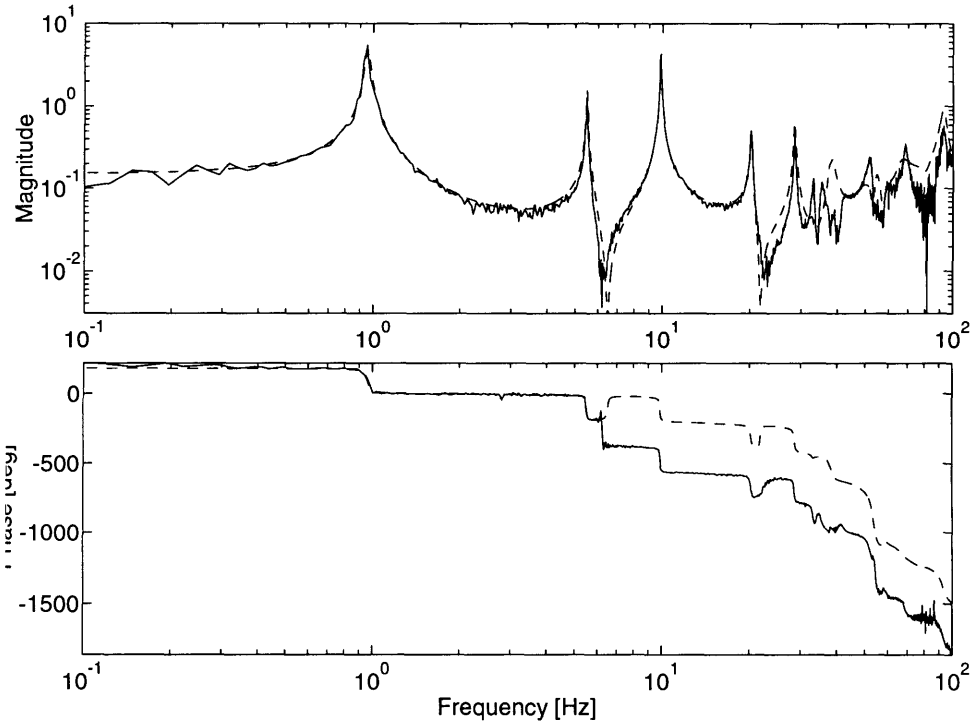

Figure 4.8: G_{14}: measured (solid) and state-space fit (dashed).

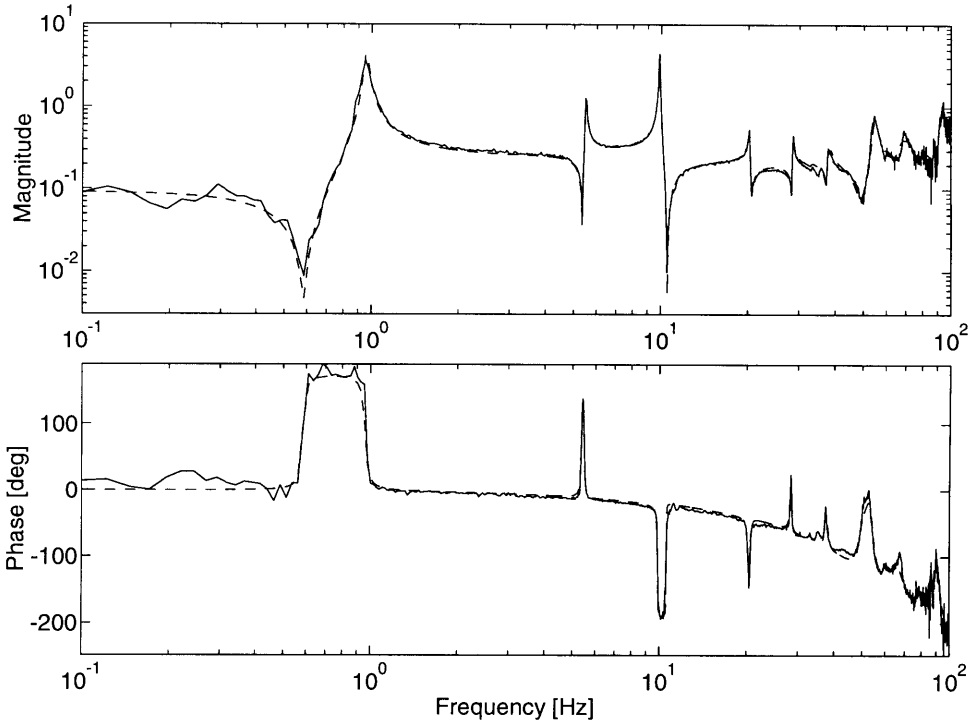

Figure 4.9: G_{44}: measured (solid) and state-space fit (dashed).

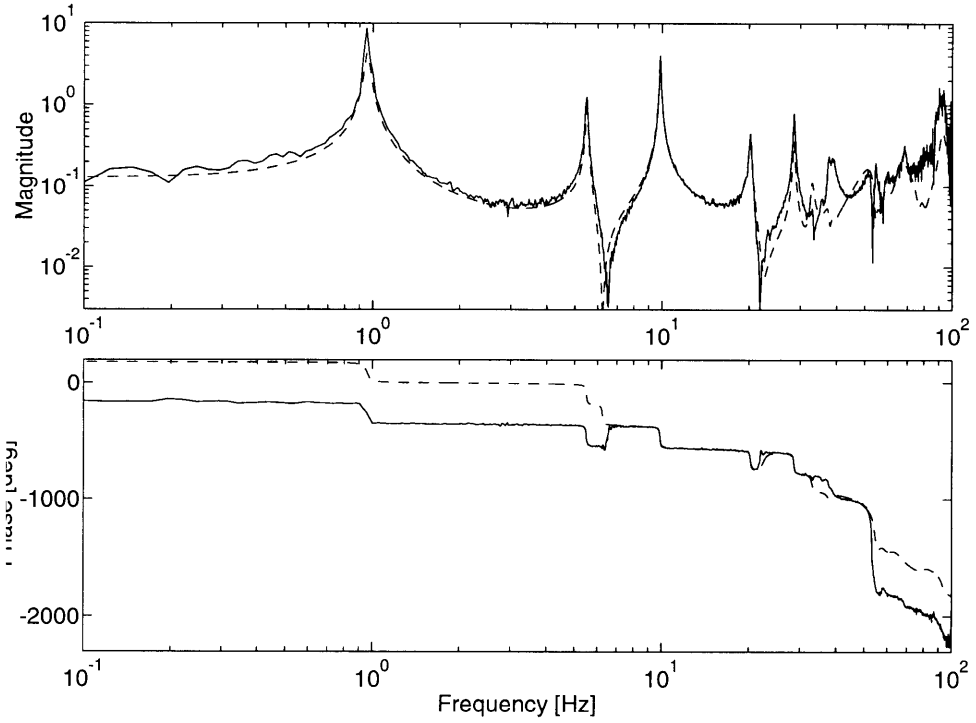

Figure 4.10: G_{41}: measured (solid) and state-space fit (dashed).

4.2.2 Control Objectives

The control objectives of the AMASS ground experiments are determined by the needs of the flight experiment. The objective of the flight experiment is to minimize the jitter induced in the spacecraft. The two drivers of the flight controllers are that the disturbance-to-performance response is not known explicitly, and that the modal frequencies of the structure will change significantly as thermal load varies.

Knowledge of the transfer functions from disturbance to performance (the *performance* transfer functions) would allow the controller to explicitly minimize the effect of the disturbance on the performance. This is a standard $\mathcal{H}_2$ control cost. The $\mathcal{H}_2$ optimal controller may be an impedance match, or an energy shunting compensator, or more likely, a combination. However, since the performance transfer functions cannot be measured, the controller must be designed to give good performance for disturbances which enter anywhere on the structure. The impedance matching controller offers such performance robustness, by damping the closed loop poles. Since the closed loop poles are properties of the system, the closed loop response to any disturbance will be reduced, regardless of where it is introduced.

The first three modes are expected to contribute most to the jitter induced in the spacecraft. The controllers will be designed to introduce damping into the first three plant modes. Since the most lightly damped mode will dominate the closed loop response, the closed loop compensator poles must also be damped. The objective can be stated as maximizing the minimum damping ratios.

Modal frequencies vary due to the changing thermal loads, as the array passes from shadow to sunlight and back. For example, expansion of the gimbal bearings will result in stiffness changes in the gimbal. Modal frequency shifts of up to $\pm 10\%$ are expected. The controller must maintain good performance as the modes shift over the expected range.

The design goal is robust performance for $+10\%$ and -2% shifts in the frequencies of modes 2 and 3. The values are based on the mode shifts between the AMASS ground testbed and the flight hardware. The thermal loads which the flight experiment will experience on-orbit will not be simulated on the ground. The robustness

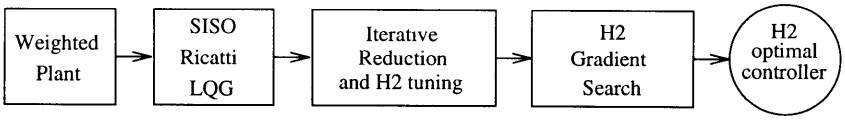

Figure 4.11: The general control design procedure for the AMASS ground testbed.

of the compensators can be experimentally determined by applying them to both testbeds on the ground.

4.2.3 $\mathcal{H}_2$ Control Design Procedure

The requirements on stability and performance robustness suggest the use of a local controller. However, the available sensors preclude the use of the impedance match and energy shunt. The collocated sensors limit performance due to the low observability of the plant modes, and are not used. The plant response is more observable from the nearly collocated sensors. However, the noncollocation results in a missing zero between the second and third modes. Thus the plant transfer function is nonpositive real, and the impedance match and high-gain shunt are not applicable.

The alternative is a global control technique, for example a constrained $\mathcal{H}_2$ technique which combines elements of the state space formulations presented in Section 2.3.2. The six techniques presented are variants of the LQG compensator. Three are derived by constraining the LQG solution: these are the reduced order, positive real, and real-axis compensators. The other approaches modify the model: an alpha-shifted model changes the real parts of the model poles, multimodel design optimizes the same compensator for multiple plants, and modified feedthrough model can be used to improve modal observability for a nondual sensor and actuator. Two constraints can be ruled out: the positive real compensator constraint will not yield any stability guarantees, and the real-pole design will necessarily limit the bandwidth to below the second resonance.

All the LQG variants are numerical, gradient searches. Numerical techniques also can incorporate the SISO compensator limitation imposed by the ADCEs.The SISO controllers can be simultaneously designed on the MIMO model by posing the

problem as a MIMO control design, with a constrained compensator topology. The MIMO controller is block-diagonal, that is, the A_c matrix is nonzero in $n_c \times n_c$ blocks along the diagonal:

$$A_c = \begin{bmatrix} A_{c_1} & 0 & \cdots \\ 0 & A_{c_2} & \\ \vdots & & \end{bmatrix} \tag{4.1}$$

All other entries are zero. Similarly for the B_c and C_c matrices:

$$B_c = \begin{bmatrix} B_{c_1} & 0 & \cdots \\ 0 & B_{c_2} & \\ \vdots & & \end{bmatrix}$$

$$C_c = \begin{bmatrix} C_{c_1} & 0 & \cdots \\ 0 & C_{c_2} & \\ \vdots & & \end{bmatrix} \tag{4.2}$$

Each block of A_c represents one SISO ADCE controller. This topology will be referred to as *block-SISO*. No closed form solution can be found when the block-SISO constraint is imposed, but the constraint can be easily included in a numerical search framework.

Three $\mathcal{H}_2$ control design processes are evaluated. The first is a reduced order LQG design. The α-shifting technique is used to create a compensator with high closed loop damping. Finally, a modified feedthrough compensator is created, in which closed loop damping is increased by making the plant modes more observable to the controller. All of the controllers are stabilized to $+10\%/-2\%$ mode shifts using the Multi-Model technique. The controllers are optimized for a nominal plant, with the measure mode frequencies, a second model with second and third modes shifted up 10%, and a third model in which the same modes are shifted down 2%. In order to robustify the performance, each of the models is weighted the same. Each controller is designed in 3 stages: a full-order, SISO, Riccati initial design, an iterative reduction, and a series of constrained gradient $\mathcal{H}_2$ optimizations (Figure 4.11).

Table 4.2: Design control and sensor noise weights.

Design #	ρ	μ
1	5	0.5
2	0.5	0.05
3	0.05	0.005

A number of design parameters are retained for all three approaches. Three levels of control weight ρ and sensor noise μ are used (Table 4.2). μ is always a factor of 10 below ρ. The compensator which produces the highest closed loop damping at the end of the design process is used. A control weight which penalizes low frequencies is used to force the gain down at low frequencies.

Since the disturbance to performance response of the plant is not available, the inputs and outputs of the uncontrolled ADCEs are used as disturbance inputs and performance outputs, respectively. As pseudo-disturbance sources, they provide a vital function. If the disturbance enters at the control location, the optimal controller attempts to make the control location undisturbable, rather than damping the plant poles.

The initial LQG design and reduction is a method of producing an initial guess for the gradient search methods. The gradient search methods are susceptible to local minima, so the initial guess must be near the optimal. The LQG equations cannot return a block-SISO compensator. The approach taken consists of creating the weighted model (which includes the alpha shifts and feedthrough modification, if necessary). The weighted model will be referred to as the *design model.* A SISO LQG design is found, which is then reduced and put in the block-SISO form.

The initial LQG controller is designed for ADCE 1, with ADCE 4 as the disturbance. The iterative reduction approach uses a combination of Hankel Singular Value (HSV) reduction and direct truncation. HSV reduction removes compensator states with low observability and controllability [31]. Direct truncation simply refers to specifying the states to remove, and is used to remove controller poles outside the

damping bandwidth. After each reduction, the reduced-order controller is tuned to minimize the $\mathcal{H}_2$ output error between the full-order controller and the reduced controller (See Appendix B). The reduction is halted when the controller has 7 states. Six of the states control the three plant modes of interest. The seventh, real mode is intended to allow additional flexibility in placing compensator zeros, in somewhat the manner of a D term.

The resulting controller is no longer optimal. It must be turned into a block-SISO compensator, optimized for the multimodel plant. Generally the controller will not be stable in block-SISO form on the MM plant. The optimization must proceed in steps: a SISO $\mathcal{H}_2$ optimization, a second optimization in which the SISO controller is placed into block-SISO form, and the multimodel optimization.

The block-SISO design incorporates another constraint. The same controller is applied at ADCEs 1 and 4. The reasons are to ease the logistics of uploading the controllers, and to desensitize the controller to zero shifts. Since the array is symmetric, the response from ADCEs 1 and 4 is nearly identical, differing slightly in zero frequencies. The result is a multimodel-like desensitization to zero shifts. For the block-SISO (MIMO) design, ADCEs 1 and 4 are controlled, and ADCEs 2 and 3 are the disturbances.

Each gradient search step must have a stable initial guess. The SISO $\mathcal{H}_2$ design can be stabilized by redoing the truncation step. The multimodel controller can be designed using homotopy, as follows: a multimodel shift is found for which the closed loop is stable. The controller is optimized, generally causing it to be stable for a larger shift. The shift is increased and the design re-optimized. The iteration concludes when the design goal is attained. The most critical step is when the SISO reduced order controller is placed into the block-SISO form. If it is unstable, there is no homotopy step which can be performed. The design must be redone from an earlier stage, possibly the reduced order design. However, for alpha shifted compensators, the first stage, in which the alpha shifting parameters are found, may need to be redone.

The desired stability robustness to shifts in the first three modal frequencies is

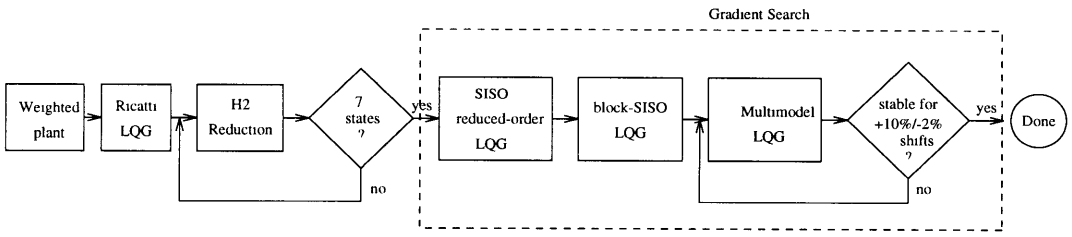

Figure 4.12: Reduced-order LQG control design process.

$\pm 10\%$. The criterion is driven by expected shifts due to varying thermal loads on the flight experiment. Stability and performance robustness to these shifts is implemented using a multimodel (MM) approach (2.3.2). The MM design models are the nominal model, a model with modes 2 and 3 shifted up by $+10\%$, and a third model with the same modes shifted down by -2%. The design model shifts are based on observed differences between the AMASS ground testbed and the flight testbed. The flight testbed modes are 10% higher than the ground testbed modes due to differences in physical dimensions.

Rather than attempt to replicate the thermal loads the flight testbed will see on-orbit, the robustness of the controllers could be evaluated by assessing the performance on both the ground and flight testbeds (the controllers were not tested on the flight hardware since the flight ADCEs were not available). Successful implementation on both sets of hardware will indicate that the control design procedure can achieve the necessary robustness for the flight controllers.

Controllers are evaluated based on closed loop damping (on the true model) and design "cost", that is, the effort required to reach the final design. The poles are grouped according to frequency, into ranges determined by the open loop frequencies. The minimum damping ratio in each group is maximized.

4.3 AMASS Control Designs

4.3.1 LQG

The first control design is reduced-order LQG. The design process is diagrammed in Figure 4.12. For each control weight, a SISO, weighted Riccati LQG controller is designed for ADCE 1. The LQG solutions are 38^{th} order. The LQG controllers are truncated to 7 states, using the iterative truncation and tuning method. The retained states are in the 1 to 10 Hz damping bandwidth. The reduced LQG controllers are re-optimized on the AMASS plant. The SISO controllers are then impinged on the AMASS model in block-SISO topology. All of the compensators are stable initially, allowing the $\mathcal{H}_2$ minimization for the MIMO compensator to proceed.

The final stage is to apply the block-SISO compensator to the multimodel plant. All LQG designs are stable on the design multimodel plant, to $+10\%/-2\%$ shifts in modes 2 and 3. A comparison of the closed loop poles shows that lowering the control weight increases the closed loop damping. The highest-gain compensator, designed with $\rho = 0.05$, achieves the highest closed loop damping. The highest gain LQG compensator is plotted in Figure 4.17, with a solid line. The closed-loop poles are given in Table 4.5.

Lowering the control weight further will eventually lead to diminished performance. If the gain is too high, the closed loop poles are damped onto the real axis and become nonresonant. At this point the compensator is inefficient at removing energy from the system. Since the actuator location has become actively stiffened, a smaller amount of strain energy can enter the active yoke to be damped. Most of the energy remains in the solar panel, which is still undamped.

4.3.2 Alpha-shifted LQG

The alpha-shifting technique creates a design plant for which certain modes are shifted into the right half-plane. The LQG compensator stabilizes these modes, moving them leftward. When the compensator is impinged on the true plant, the plant modes will move leftward, resulting in increased closed loop damping.

The first three modes of AMASS are targeted for damping. At each level of control

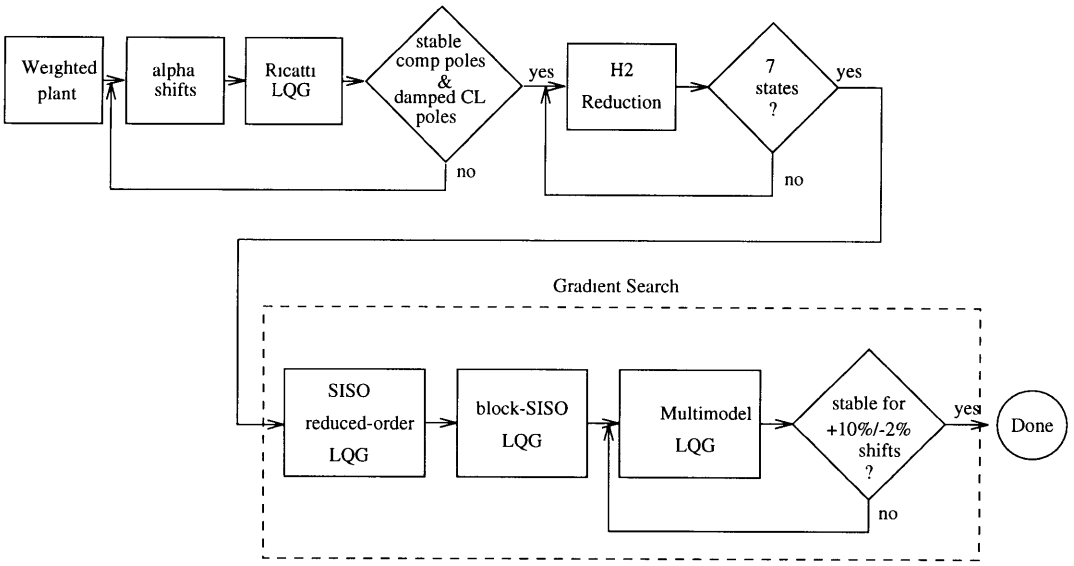

Figure 4.13: The alpha shifted LQG control design process. The design plant is iteratively chosen, then the controller is iteratively reduced and optimized.

weight, the α-shifts are iteratively adjusted to optimize the closed loop damping (Figure 4.13). The iteration involves choosing the design model alpha shifts, solving for the Riccati-based LQG controller on the design plant, then applying the controller to the true plant.

The alpha shifts must be iteratively chosen to create the maximum damping in the closed loop system. Two effects drive the choice the α-shifts. Increasing the α-shift damps the closed loop plant pole, but the closed loop compensator mode can become more lightly damped. An optimal α-shift exists for each value of ρ at which the closed loop plant and compensator mode have the same damping. Second, for poorly observable modes, increasing the α-shift causes the compensator pole to move into the right half plane. It is desirable to have a stable compensator for several reasons. The open loop frequency response of the Intel compensator can be used to scale the state space matrices. Failure of the sensor will make the system unstable, possibly resulting in damage to the array and/or spacecraft.

Table 4.3 shows the alpha shifts which give the best closed loop damping. For decreasing ρ, the design shifts become smaller. The closed loop damping is uniformly better than the LQG controller. To reduce computational overhead, the same alpha

Table 4.3: Alpha shifts for modes 1, 2, and 3.

		ρ=5	ρ=0.5	ρ=0.05
Mode	Open Loop Pole	α-shift	α-shift	α-shift
1	$-0.1037 \pm 6.0194\jmath$	2.2	1.3	0.8
2	$-0.1850 \pm 34.5321\jmath$	0.1	0.2	0.2
3	$-0.3589 \pm 61.9247\jmath$	5	7	5

shifts are used for each step in the design process. Although the performance might be improved by iterating over the alpha shifts at each gradient search, the computational burden would be excessive.

Note that the alpha shifts for each mode are extremely large, indicating that the design plant poles are shifted far into the right half-plane. Decreasing ρ and μ will cause the closed loop poles to go to the stable reflections of the design poles, that is, far into the left half plane. The compensator modes, however, would become unstable.

The 26-state compensators are truncated to 7 states, and re-optimized using the $\mathcal{H}_2$ gradient search. When the resulting controllers are impinged on the two-input, two-output plant in block-SISO architecture, the highest weighted compensator (ρ = 5) is found to be unstable. Only the two lower weighted compensators can be advanced to the next, multimodel stage.

Neither of the two α-shifted compensators is stable for the design multimodel plant. The controllers must be stabilized to the desired $+10\%/-2\%$ shifts using homotopy. Table 4.4 shows the steps which were taken. Neither controller could be stabilized for any negative frequency shift. The lowest weight controller (ρ=0.05) could not be stabilized to the desired +10% shift. In both cases, numerical conditioning problems prevented the search algorithm from converging.

The initial alpha shifted design achieved higher damping as control weight ρ was decreased. The lowest weighted controller introduced the highest closed loop damping. However, after the gradient search procedures were performed, the lowest weighted controller achieved less damping. The initial high performance was achieved at the expense of robustness. To achieve the necessary robustness in the search pro-

Table 4.4: Multimodel homotopy steps taken to stabilize the α-shifted controllers to $+10\%/-2\%$ shifts in mode frequency.

	ρ=5		ρ=0.5		ρ=0.05	
Step	+ shift	- shift	+ shift	- shift	+ shift	- shift
1	-	-	1%	0%	1%	0%
2			3%		2%	
3			5%		3%	
4			7%		4%	
5			8%		5%	
6			9%		6%	
7			10%		7%	

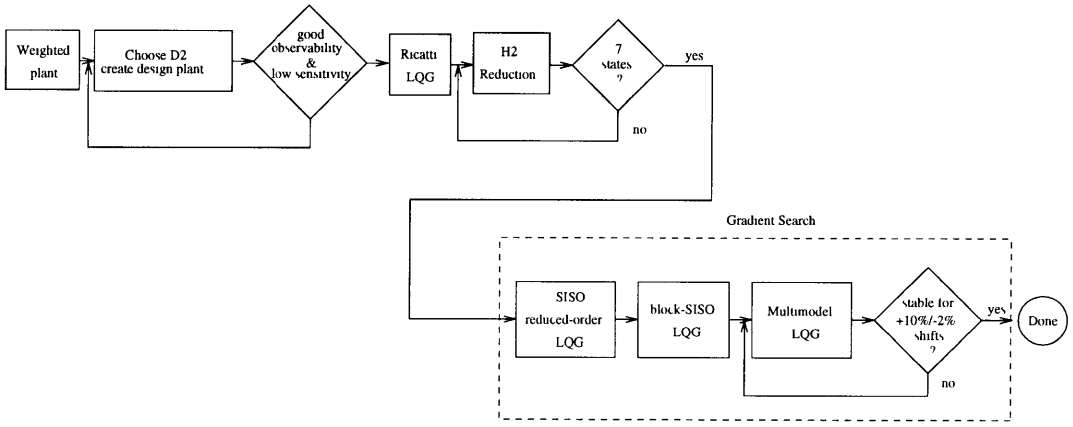

Figure 4.14: The MF compensator control design process. The plant model is modified to increase the observability of plant modes to the controller.

cedure, performance was sacrificed. Since the medium weighted controller ($\rho = 0.5$) achieved higher damping, it was chosen as the compensator to be implemented. The closed loop poles of the final alpha shifted compensator are shown in Table 4.5. Again, the design objective is to maximize the minimum closed loop damping ratios. The alpha shifted compensator creates much higher damping in the first mode than the LQG. The frequency response of the alpha shifted controller is plotted with a dashed line

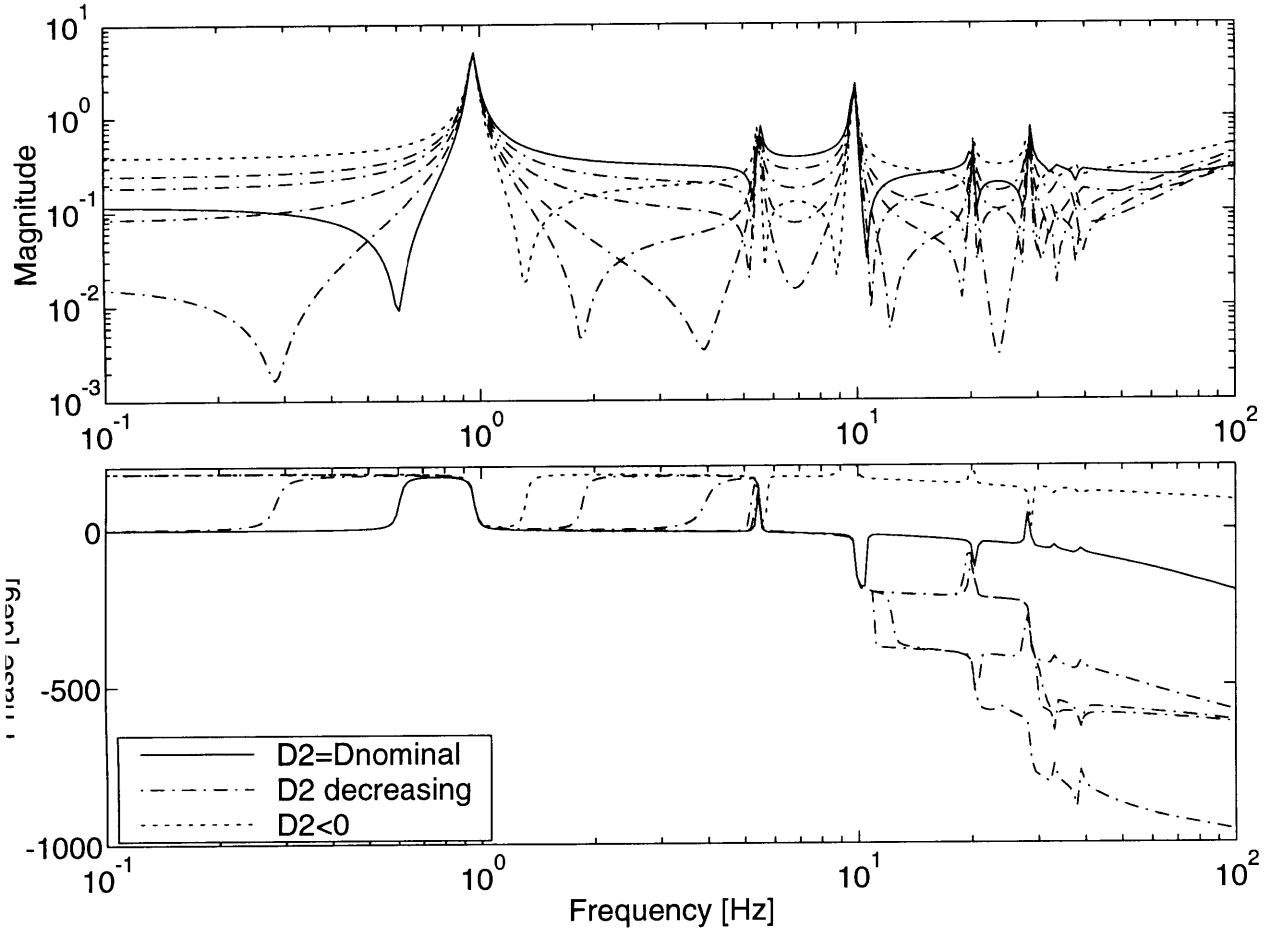

Figure 4.15: Effect of varying feedthrough: The zeros of the plant shift as the D term is varied.

4.3.3 Modified Feedthrough Compensator

The modified feedthrough (MF) compensator of Section 2.3.2 is implemented. A modified model is created by varying the plant model D term, as described in Section 2.3.2. A reduced order LQG design procedure is followed. Finally, the modified D term is folded into the compensator. For the modified compensator, only one control and sensor noise weight is used, for comparison to the highest-gain LQG controller and the alpha shifted controller. The control weighting ρ is 0.05, and sensor noise μ is 0.005.

The design plant model is created by choosing the desired D term, D_2, to maximize the pole/zero separation of the plant response as seen by the ADCE. The filter $\hat{F}(s)$

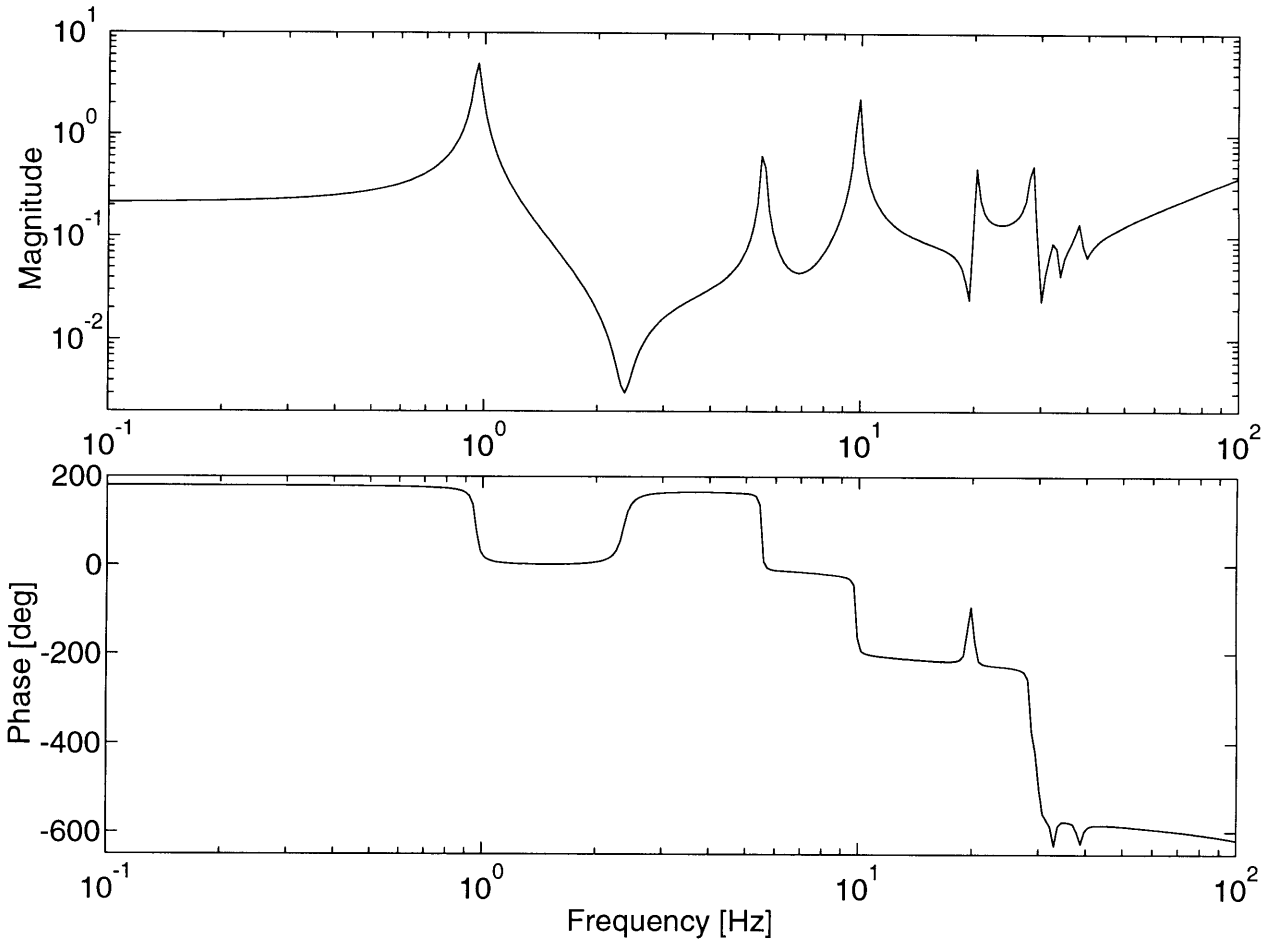

Figure 4.16: The G_{11} transfer function at the chosen design value of D_2, showing the improved modal observability.

must be chosen. Since it must be appended to the controller state vector, a low order filter is desired. A 1-state Pade approximation to the 1 cycle digital time delay is used. The Intels operate at 250 Hz, with a half cycle delay due to the sample and hold, for a total time delay of $\frac{3}{2}\frac{1}{250}$ seconds. The feedthrough of the performance transfer function is also modified, to increase modal observability in the performance.

Choice of the feedthrough term D_2 is motivated by the design to create the power dual sensor to the piezo actuator. The exact value of D_2 which creates the power dual sensor is not known, but it is known to give good pole/zero spacing. The dual is approximated by choosing the feedthrough to improve the pole/zero spacing of the model.

The effect of varying the feedthrough appears as a shift in the zeros. Figure 4.15

shows G_{11} as the D term is varied. The response of the model with nominal feedthrough, $D_2 = D_{nom}$, is the solid line. As feedthrough is decreased, the zeros shift as shown by the dash-dot lines. The first zero moves left to the origin, the second zero moves left to the first mode, and two zeros appear between second and third modes. The lowest feedthrough, shown by the dotted line, has moved the zeros past the optimum.

Ideally, the zeros of the design plant would be exactly between the poles, for maximum observability. In that region, the zero locations are highly sensitive to the D term. As a compromise between sensitivity and modal observability, the zeros are moved part of the way from their initial positions, with a 33% reduction in the feedthrough. The design model is then created from the Pade approximation and the nominal plant. The modified G_{11} response is shown in Figure 4.16. The modified plant rolls up at high frequency, because the Pade approximation is in error above 40 Hz. This does not create a problem, because the controller will roll the loop off.

As a result of the increased modal observability, a sensitized LQG method can be used to create the initial compensator. "Sensitivity- Weighted" LQG, or SWLQG, modifies the LQG cost to decrease sensitivity to particular modes. Details can be found in [22]. For frequency shifts, the SWLQG modification can be parameterized in terms of a scalar β. For the nominal plant, which has poor observability of the second and third modes, increasing β causes the second compensator mode to become unstable. However, for the modified plant, the β factor causes the SWLQG compensator to become more heavily damped, which in turn results in lower sensitivity to mode shifts.

Because the SWLQG formulation is a modification of the Riccati-based LQG controller, it can be solved in closed form for the initial design. The initial design is then reduced to seven states. The seven state compensator is found to be stable when impinged on the block-SISO, multimodel plant. By the use of the feedthrough modification, combined with the SWLQG method, the three steps required to get the reduced order LQG controller into block-SISO, multimodel-stabilized form shown above, have been reduced to a single step.

Lastly, the 1-pole Pade filter is appended to the controller, as in Equation 2.182.

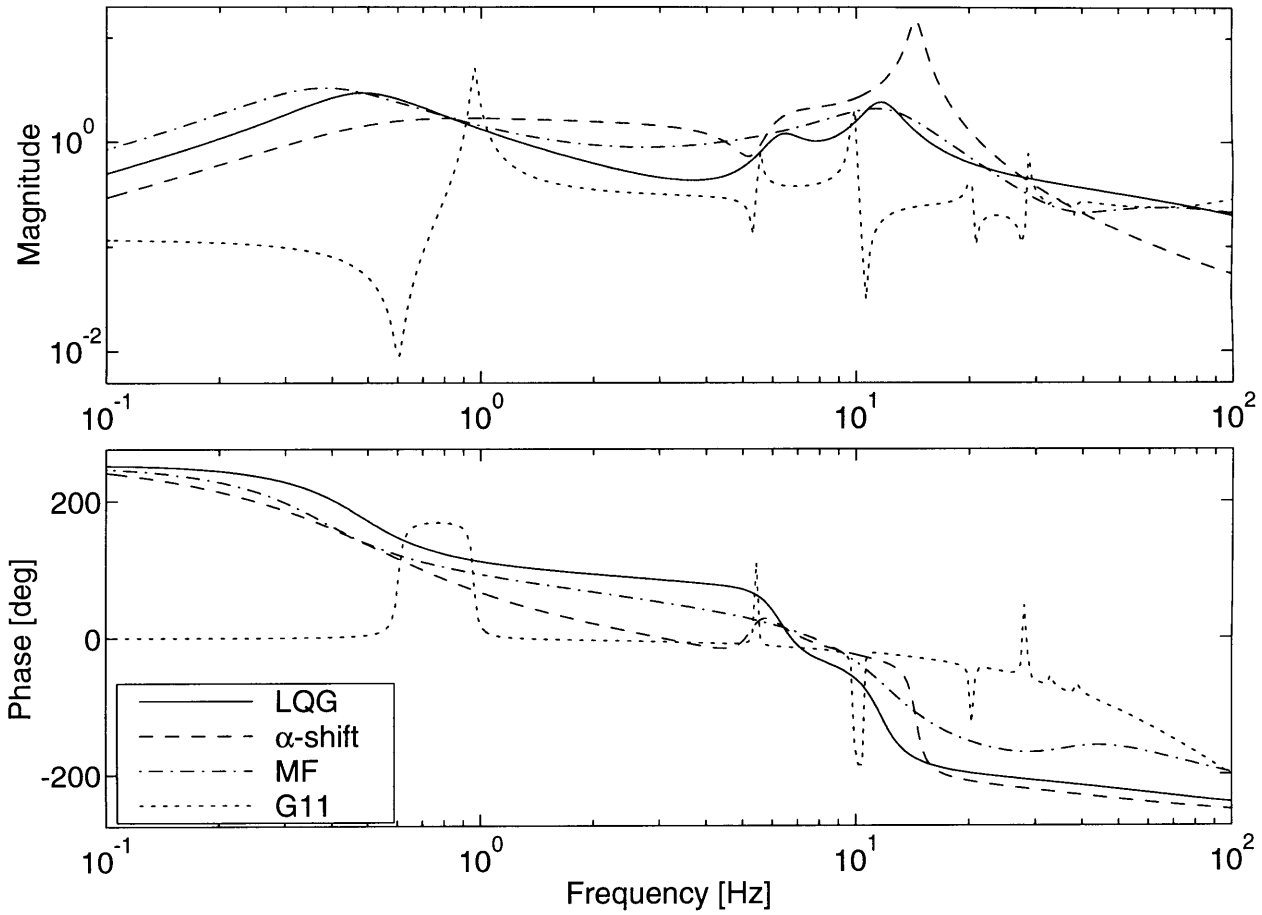

Figure 4.17: AMASS compensator designs: reduced order LQG (solid), alpha-shifted (dashed) and MF (dash-dot), plotted with the open-loop plant response G_{11} (dotted).

The response of the resulting 8-state controller is shown with a dash-dotted line in Figure 4.17. The closed loop poles are given in Table 4.5. For the same ρ, the closed loop damping is higher than the LQG closed loop. It is less than that achieved by the best alpha shifted compensator.

In the next section, the LQG, alpha-shifted LQG, and MF controllers will be analyzed and compared using the measured plant data. The robustness of controllers to frequency shifts in the first three modes will be analyzed using the evaluation model.

Table 4.5: Closed loop poles for the final designs.

	LQG		α-shifted		MF	
Mode	Freq [Hz]	Damping [%]	Freq [Hz]	Damping [%]	Freq [Hz]	Damping [%]
1	0.4948	68.30	0.6328	48.98	0.3988	33.18
	0.5176	21.85	1.6473	52.13	0.4025	89.09
	0.9073	30.44	1.9689	89.52	0.9644	32.05
2	5.5321	1.70	5.5837	01.19	5.6247	1.14
	6.3594	8.50	6.4245	12.24	8.4402	15.45
	6.4112	8.15	6.7012	10.09	8.7800	31.04
3	9.8331	9.38	9.6288	20.88	10.5218	13.00
	10.9405	19.24	13.2982	12.55		
	10.9745	10.04	13.6195	27.15		

4.4 Analytical Evaluation of AMASS Controllers

A useful way to analyze the compensators is to "close the loop" on measured data. Closed loop stability can be assessed using a Nichols chart, a variant of the Nyquist plot. Since the MIMO Nyquist criterion involves a determinant of the MIMO loop transfer function, robustness margins cannot be determined. The closed loop sensitivity can be used look for marginally stable modes, which may be unstable when the controller is implemented on the plant. Finally, the closed loop response can be calculated and compared to the response of the model.

Since the AMASS controllers are designed to give performance and stability robustness to large modal frequency shifts, it is desirable to quantify the achieved robustness. Using the model, the closed loop output covariance of the sensor at ADCE 1 will be found as the first, second, and third modes are independently varied in frequency. The covariance will go to infinity as the closed loop system becomes unstable. The plot of output covariance versus mode shifts is a form of *robustness bucket.* The width of the bucket indicates the range of modes shifts which can be stably accommodated. The "flatness" of the bucket is a measure of how the performance degrades for stable frequency shifts.

4.4.1 Analytical Tools for Assessing Stability and Performance using Data

MIMO Nichols Chart The MIMO Nyquist criterion states that for positive feedback, the closed loop system will be stable if the number of clockwise encirclements of the -1 point by

$$-1 + \det(-I + G(\jmath\omega)K(\jmath\omega)) \tag{4.3}$$

is equal to the number of unstable poles in the open loop plant and compensator. I is the identity matrix, and $G(\jmath\omega)K(\jmath\omega)$ is the MIMO loop transfer function evaluated along the imaginary axis. $G(\jmath\omega)$ is the matrix of plant transfer functions. For the AMASS controllers, GK is a 2×2 matrix (at each frequency) composed of the measured transfer functions:

$$G(\jmath\omega) = \begin{bmatrix} G_{11}(\jmath\omega) & G_{14}(\jmath\omega) \\ G_{41}(\jmath\omega) & G_{44}(\jmath\omega) \end{bmatrix} \tag{4.4}$$

where G_{ij} is the transfer function from input i to output j. The compensator response $K(\jmath\omega)$ is 2×2 and diagonal, due to the uncoupled ADCEs. The diagonal entries are identical due to the single-compensator implementation:

$$K(\jmath\omega) = \begin{bmatrix} k(\jmath\omega) & 0 \\ 0 & k(\jmath\omega) \end{bmatrix} \tag{4.5}$$

The transfer function $k(\jmath\omega)$ is the SISO response of one ADCE controller, evaluated at all the frequencies in the data frequency vector. The data vectors are cycled through point by point, creating the plant and compensator matrices and calculating Equation 4.3 at each data point.

The MIMO Nyquist criterion is used by plotting the real part of Equation 4.3 versus the imaginary part at all frequencies. Since the number of open loop unstable poles is zero, there must be no encirclements of the -1 point. For a structural system with many lightly damped poles, the Nyquist plot can become difficult to decipher.

An alternative is the Nichols chart, which consists of the logarithmic magnitude of Equation 4.3 plotted against the phase. The critical point -1 is represented by those

points with unity magnitude and $-180° + 360°n$ phase, where n is an integer. Using the Nichols chart, stability can thus be inferred directly from the data. However, since the quantity plotted is found from a determinant, which is a highly nonlinear operation, stability margins cannot be inferred. The Nichols plot is only useful in predicting stability.

Closed Loop Sensitivity The closed loop sensitivity $S(j\omega)$ provides one measure of stability robustness. The sensitivity is given by

$$S(j\omega) = (I + GK)^{-1} \tag{4.6}$$

and have been used to assess the effect of disturbances on the mean-square tracking error [3]. The *singular values* (SVs) of the sensitivity can also be used to spot potentially unstable modes.

Modes which are nominally stable, but are on the verge of instability, will be lightly damped. The maximum sensitivity SV will increase sharply at that frequency. Thus spikiness in the sensitivity SVs is an indicator that closed loop modes may be near the $j\omega$ axis, without showing which side. It is generally useful to compare the sensitivity on the data to the sensitivity of the closed loop on the model. If the spikes appear in the model, the measured SVs may be showing the effects of noise. Otherwise, the spike may arise from a discrepancy between the actual plant and the model, and the closed loop may be unstable.

Closed Loop Frequency Response Compensator performance can be assessed from the data by forming the closed loop response from the plant and compensator transfer function matrices. The closed loop response is

$$G_{cl}(j\omega) = (I + GK)^{-1} G \tag{4.7}$$

There is a danger in using the closed loop response to judge the AMASS controllers. Pole/zero cancellations can reduce the closed loop response without increasing the system damping. Instead, the response using data is compared to the response of the closed loop model. If the responses are similar, the closed loop system are inferred to be similar to the poles of the model, which are known to be well damped.

Robustness Bucket The mode shifts for which each compensator is stable are found. The robustness bucket for the first mode shift is calculated by shifting the first mode of the plant model slightly, impinging the compensator, and solving for the closed loop output covariance of ADCE 1. The mode shift is increased and the process repeated until the covariance becomes infinite, indicating an unstable closed loop. The process is repeated for the second and third modes. When the covariance is plotted for the shifted mode frequency, the plot takes the form of a "bucket". The width of the bucket indicates the percentage mode shifts which can be stably accommodated by the compensator. The flatness of the buckets indicates the performance robustness.

4.4.2 LQG analysis

The analytical examination of the controllers is first performed for the LQG controller. The MIMO Nichols chart for the LQG controller is shown in Figure 4.18. The vertical dotted lines are lines of $-180° + 360°n$ phase, and the horizontal line indicates a magnitude of 1. The magnitude of the response is below 1 at all phase crossings, indicating the closed loop will be stable.

The closed loop sensitivity maximum and minimum SVs are plotted in Figure 4.19, obtained from the data and the model. The features of concern are the spikes. The most prominent spike is at 0.9 Hz. Such spikes can result from noise in the data, or can be indicative of lightly damped closed loop modes. Sensitivities of greater than 10 indicate a high probability of instability on the physical plant. The singular values on the data are much lower, and all but the 0.9 Hz match the model closely. It can be concluded, based on the information provided by the Nichols and sensitivity plot, that the LQG controller will be stable on the experimental structure.

The closed loop response of the structure, through ADCE 1, is plotted for the model and the data in Figure 4.20. The predicted response on the data matches the model closely. The compensator should achieve approximately the same damping on the testbed as on the model.

The robustness buckets are plotted in Figure 4.21. The y axis is covariance of the output of ADCE 1. The x axis is the frequency of the shifted mode. The nominal

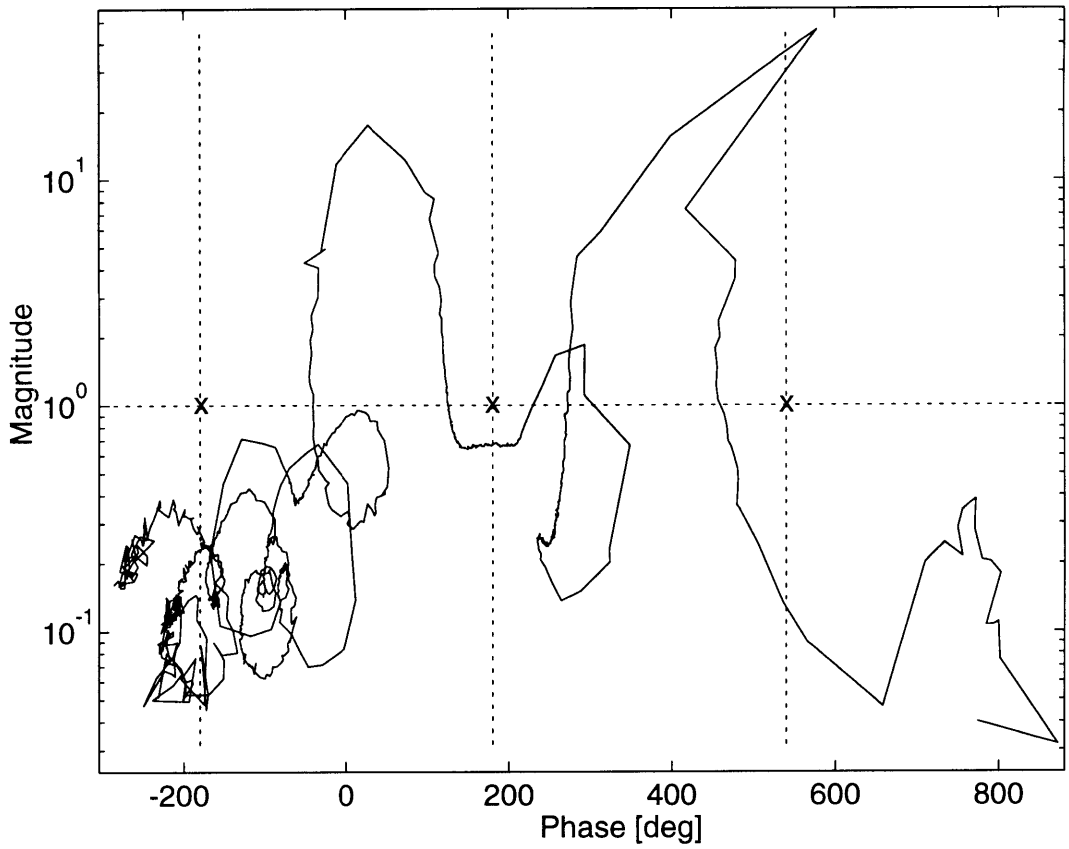

Figure 4.18: Nichols plot of the LQG compensator: The plot must pass below the critical points, marked by "x"s.

mode frequencies are marked with vertical dotted lines. As each mode is shifted, the other modes are fixed at their nominal frequencies. The gray shaded areas represent a $\pm 10\%$ shift in the nominal frequency. The width of the bucket is the stability range of the compensator. The LQG controller is stable to first mode shifts of -37% and at least $+300\%$ (the covariance was only checked for $\pm 300\%$ shifts). Second mode shifts of at least -300% and $+23\%$ are stable, and third mode shifts of -30% and at least $+100\%$ are stable. The increase in covariance at 20 Hz be be stable, or the system may be unstable for a narrow range of mode shifts. Since the analysis calculates the covariance for a discrete set of frequency shifts, two finite covariance points may bracket a frequency at which that mode causes the closed loop system to be unstable.

Note that the closed loop system remains stable even when the second mode is

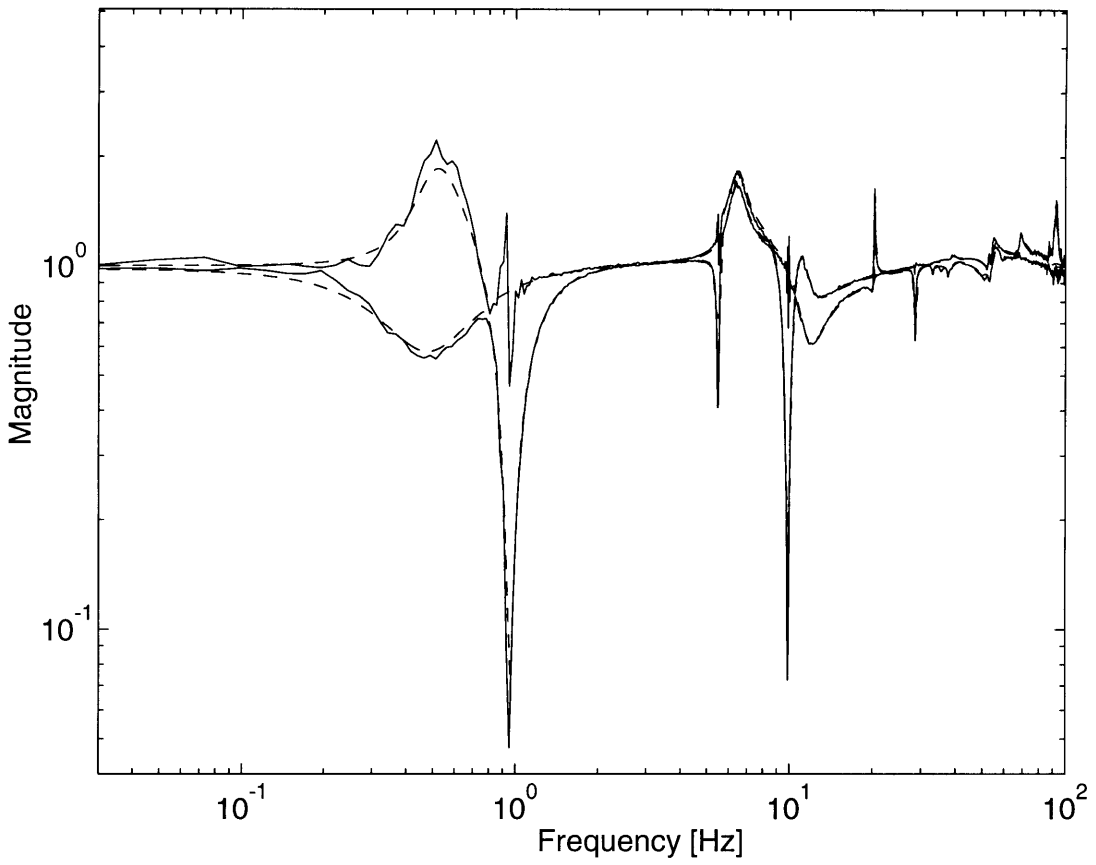

Figure 4.19: LQG compensator sensitivity singular values, calculated from the data (solid) and the model (dashed).

shifted below the first mode. This is because the modes have the same sign residue. There will always be a zero between them, so the phase will remain bounded. The third mode can be increased indefinitely because the loop is gain stable. The most important source of instability is when the second mode increases, or the third decreases. This region is where the plant phase crosses 0°. However, the compensator has easily achieved the design goals for stability robustness to mode shifts, and the relative flatness of the buckets indicates that damping performance is also quite insensitive to plant mode shifts.

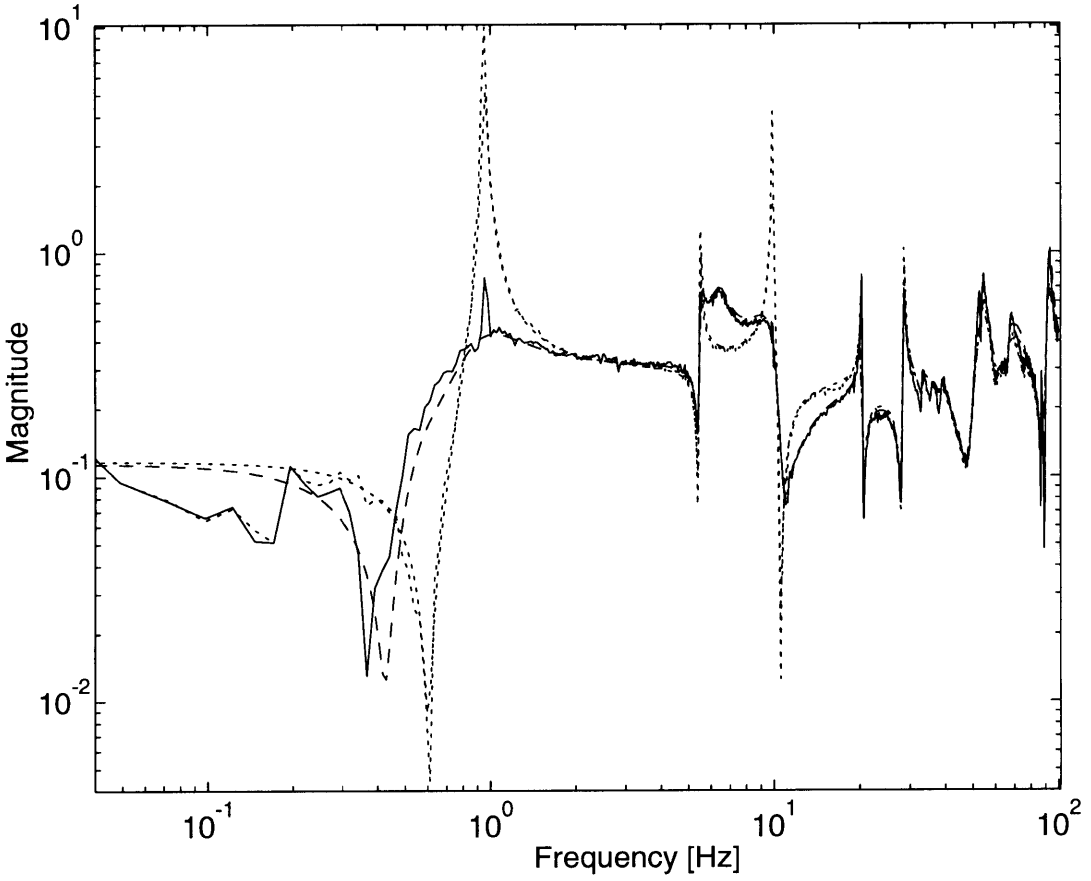

Figure 4.20: The closed loop response for the LQG controller: obtained from data (solid) and the state space model (dashed). The open loop data is also plotted (dotted).

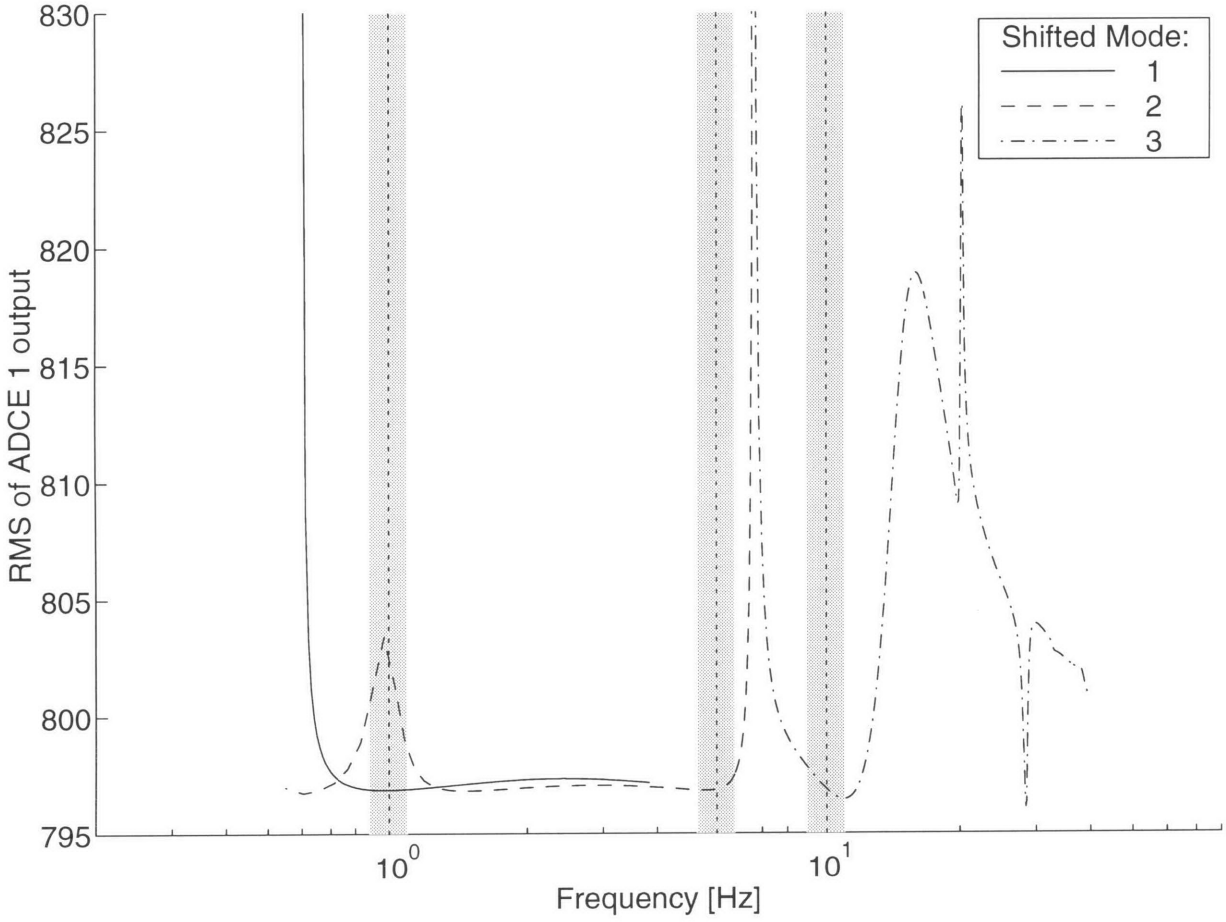

Figure 4.21: The covariance of the output of the ADCE 1 sensor, as modes 1, 2 and 3 are varied. The nominal frequencies are marked by the vertical dotted lines.

4.4.3 Alpha shifted LQG analysis

Next the alpha shifted controller is analyzed. The MIMO Nichols plot for the alpha shifted compensator is shown in Figure 4.22. The critical points at 180° and −180° are approached more closely than by the LQG design. With the proviso that the Nichols plot does not clearly relate to stability margins, one can predict that the alpha shifted compensator will not be as robust to mode shifts. The closer approach is between the second and third mode frequencies, due to the attempt to enforce damping in those modes.

The sensitivity SVs for the alpha shifted compensator are shown in Figure 4.23 for the data (the solid line) and the model (the dashed line). Once again some spikiness is evident near first mode. The spike at 20 Hz is sharper. However, the spike appears in the model singular values also, indicating that the mode has been stabilized. The conclusion can be made that the alpha shifted compensator will be stable when implemented on the testbed.

The closed loop response of the plant, when the alpha shifted compensator is applied, is shown in Figure 4.24. The first three modes are all damped. However, the off-resonance response has been increased. This should not be considered a severe difficulty. The response can be interpreted as an active softening of the array. In open loop, the active yoke is stiffer than the solar panel. Strain energy tends to concentrate in the softer elements. By actively destiffening the yoke, the controller increases the proportion of strain energy in the yoke, thus more energy is available to be damped.

The robustness buckets for the alpha shifted controllers are plotted in Figure 4.25. As before, the nominal modes are shown as vertical, dotted lines, and the desired ±10% shifts are the shaded regions. Clearly the robustness of the alpha shifted model is lower than the LQG model. The closed loop is barely stable for ±10% second mode shifts. The first mode stability range is quite acceptable at −58%, +200%. The third mode is stable for −28%,+50%. The stability robustness is therefore within the design goal, although the second mode is marginal. Subjectively, performance robustness is also lower than the LQG design, based on the curvature of the buckets. A small shift in mode frequency results in a large loss of performance.

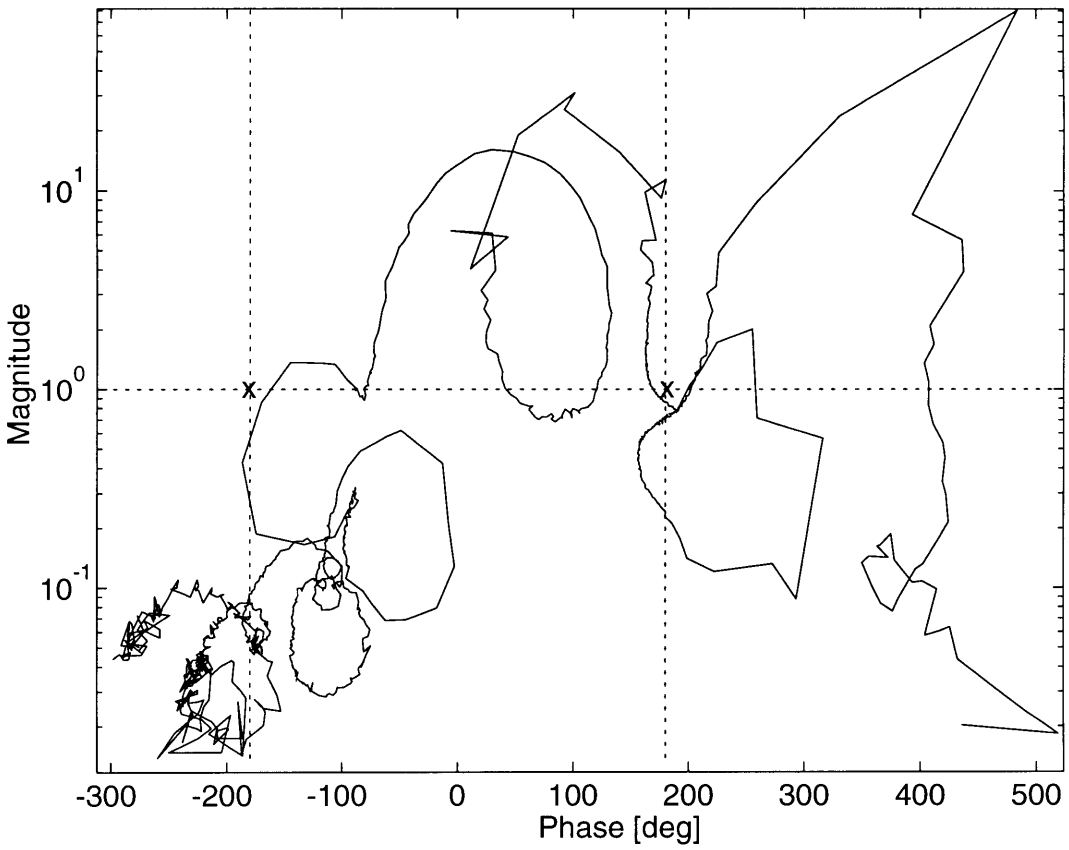

Figure 4.22: Nichols plot of the alpha shifted LQG compensator: The plot must pass below the critical points, marked by "x"s.

The choice between the LQG and alpha shifted LQG is clear if robustness is the only concern. However, a substantial increase in nominal closed loop damping is gained by the decrease in stability and performance robustness. First mode has more than twice the closed loop damping for the alpha shifted design than for the LQG design. If the required stability robustness bounds can be relaxed, the alpha shifted compensator offers clear performance advantages.

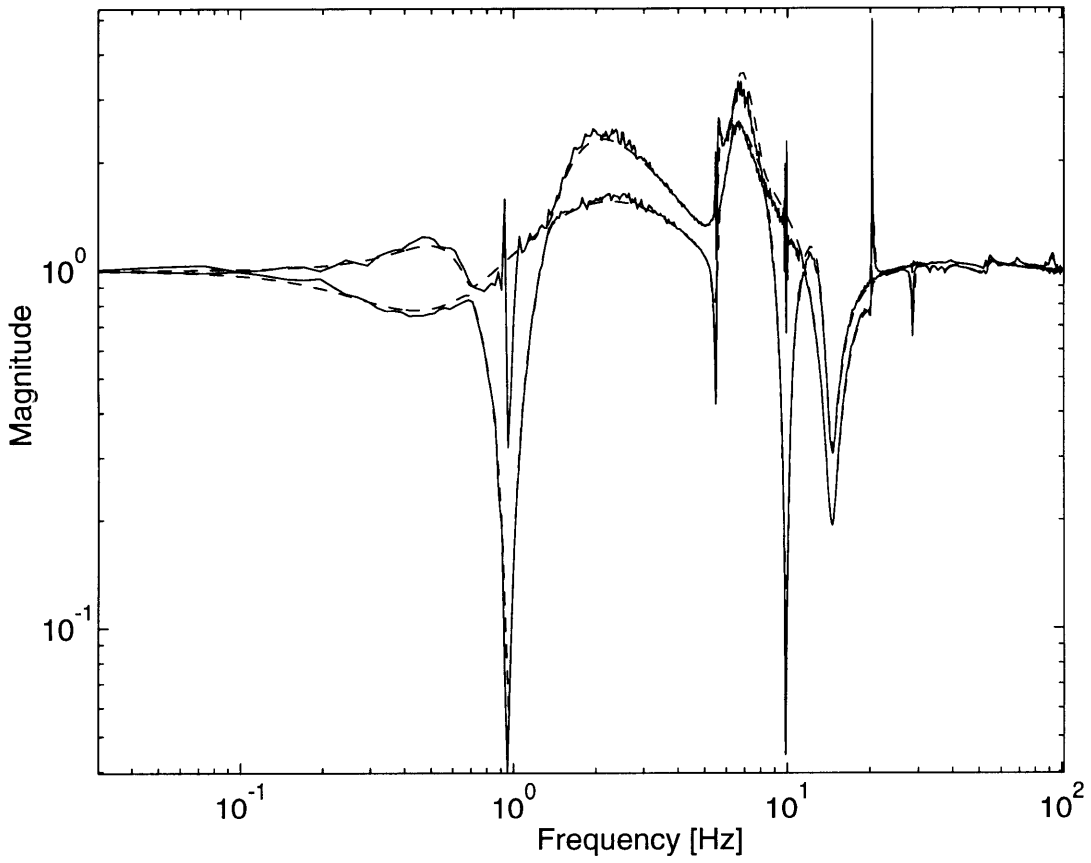

Figure 4.23: alpha shifted LQG compensator sensitivity singular values, calculated from the data (solid) and the model (dashed).

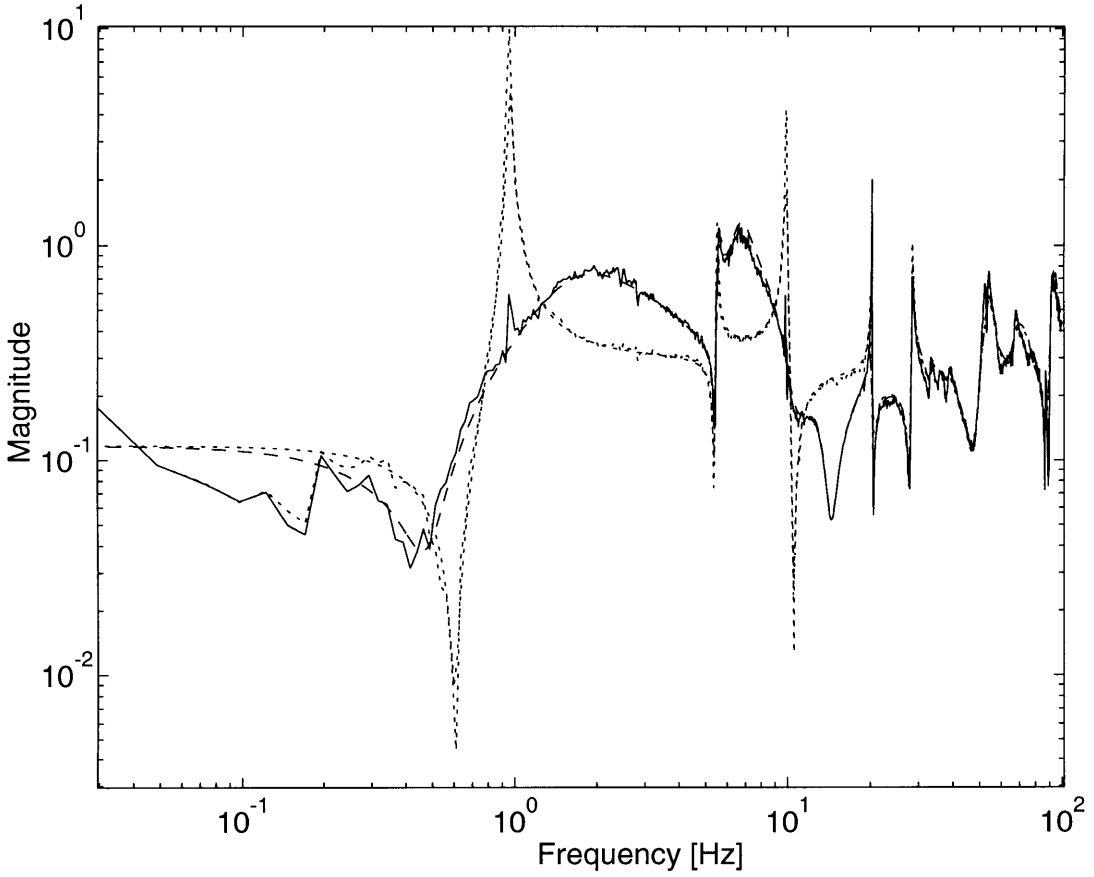

Figure 4.24: The closed loop response for the LQG controller, calculated from data (solid) and the state space model (dashed). The open loop data is also plotted (dotted).

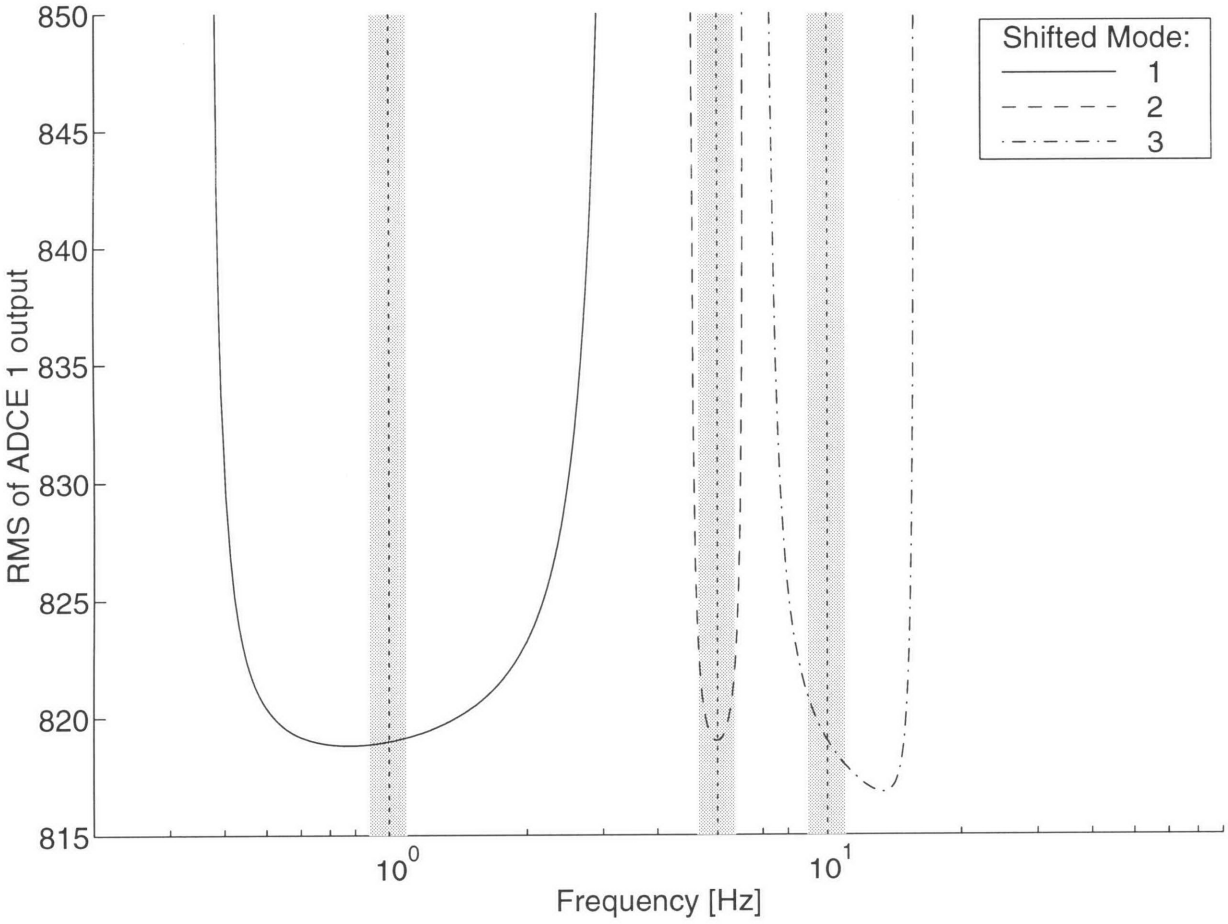

Figure 4.25: The covariance of the output of the ADCE 1 sensor, as modes 1, 2 and 3 are varied. The nominal frequencies are marked by the vertical dotted lines.

4.4.4 Modified Feedthrough Controller analysis

The modified feedthrough controller is now analyzed. The Nichols plot for the MF compensator is given in Figure 4.26. The controller is stable on the data. The proximity to the Nyquist point appears to be greater than the LQG design, but less than the alpha shifted LQG. The Nichols plot rolls off well before the second critical point at $-540°$.

The sensitivity SVs for the D term compensator are plotted in Figure 4.27. The SVs of the data are the solid curve, and the model SVs are dashed lines. Spikes occur at 0.9 Hz and 6 Hz. The spikes at 6 Hz are present in the model. Again, the first mode appears most likely to pose a stability problem when the loop is closed. However, the spike may arise from noise in the data. The MF controller appears to be stable on the structure, based on the Nichols and sensitivity plots.

The closed loop plant response achieved by the modified feedthrough controller is shown in Figure 4.28 for the model and the data. The first and third mode damping appears to be higher than the LQG design. The off-resonance response has not been increased in the manner of the alpha shifted design. The only questionable feature is that second mode seems to be less damped than either the alpha shifted or the LQG designs. However, it is not clear from the transfer function whether the LQG compensator, above, is damping the second mode, or canceling it with a zero. A conclusive assessment of the second mode damping, between the LQG and modified feedthrough compensators, cannot be made from the predicted closed loop response.

The robustness buckets for the modified feedthrough compensator are shown in Figure 4.29. The first three nominal plant modes are marked with vertical dotted lines, and the $\pm 10\%$ frequency ranges are shaded gray. As with the LQG controller, the closed loop system is stable even if first and second modes flip. The closed loop is stable for up to -47% shifts in first mode, and for at least a threefold increase in frequency. Second mode can range between -300% and $+26\%$ without destabilizing the closed loop system. Third mode can vary from -29% to more than $+300\%$. The covariance plots as a function of modal frequency shift are relatively flat, indicating minimal loss in performance for stable mode shifts. Performance robustness is

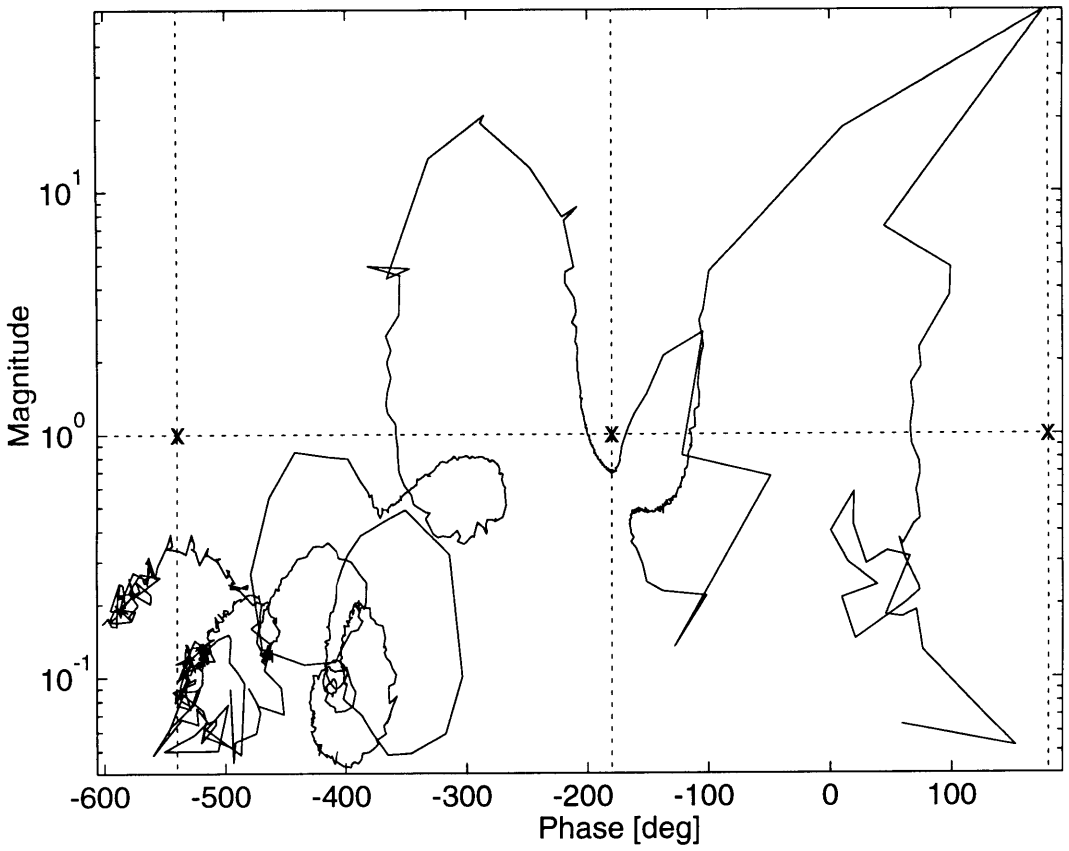

Figure 4.26: Nichols plot of the modified D term compensator: The plot must pass below the critical points, marked by "x"s.

comparable to the LQG design.

The results of experimental implementation of the three control designs will now be presented.

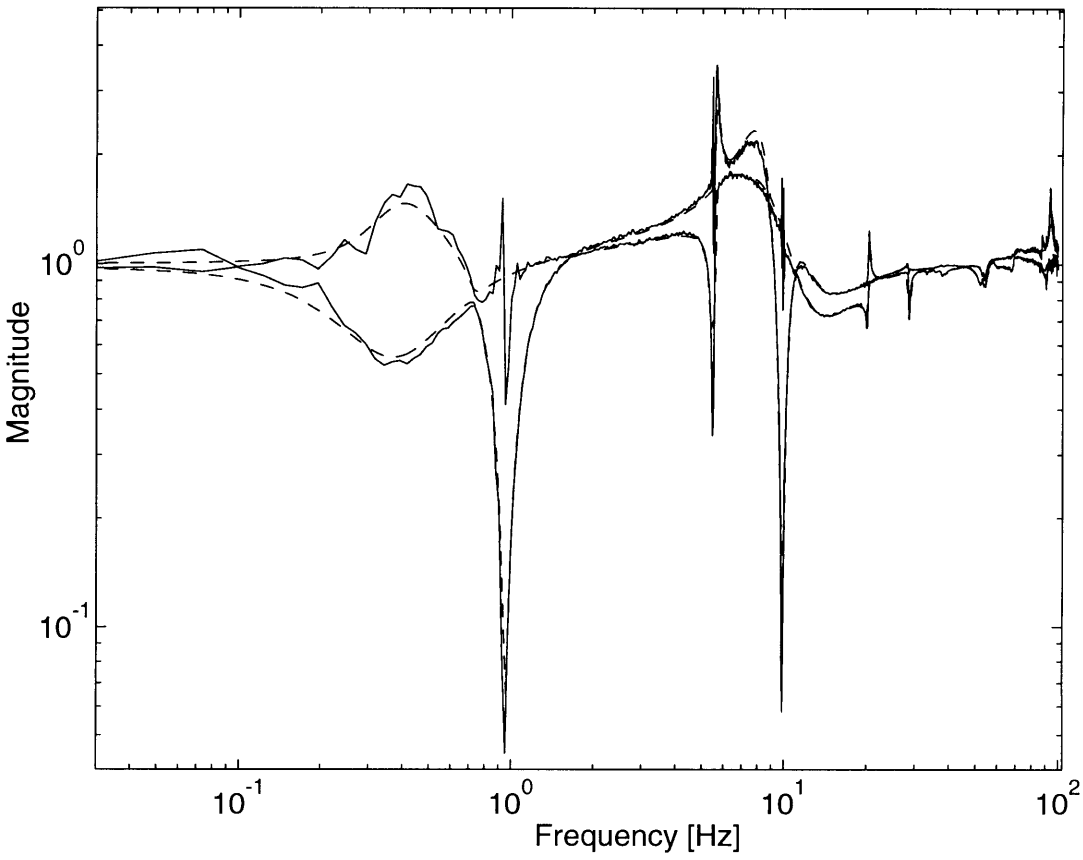

Figure 4.27: MF compensator sensitivity singular values, calculated from the data (solid) and the model (dashed).

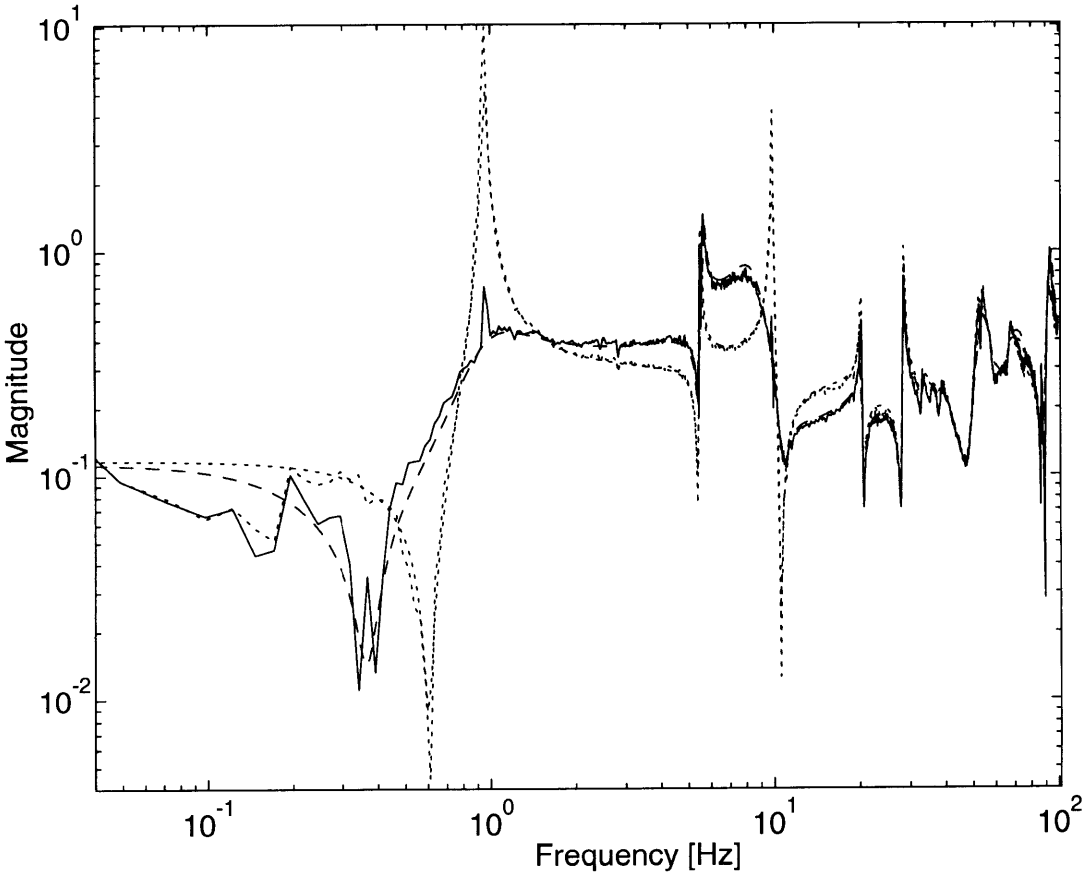

Figure 4.28: The closed loop response for the modified D term controller, calculated from data (solid) and the state space model (dashed). The open loop data is also plotted (dotted).

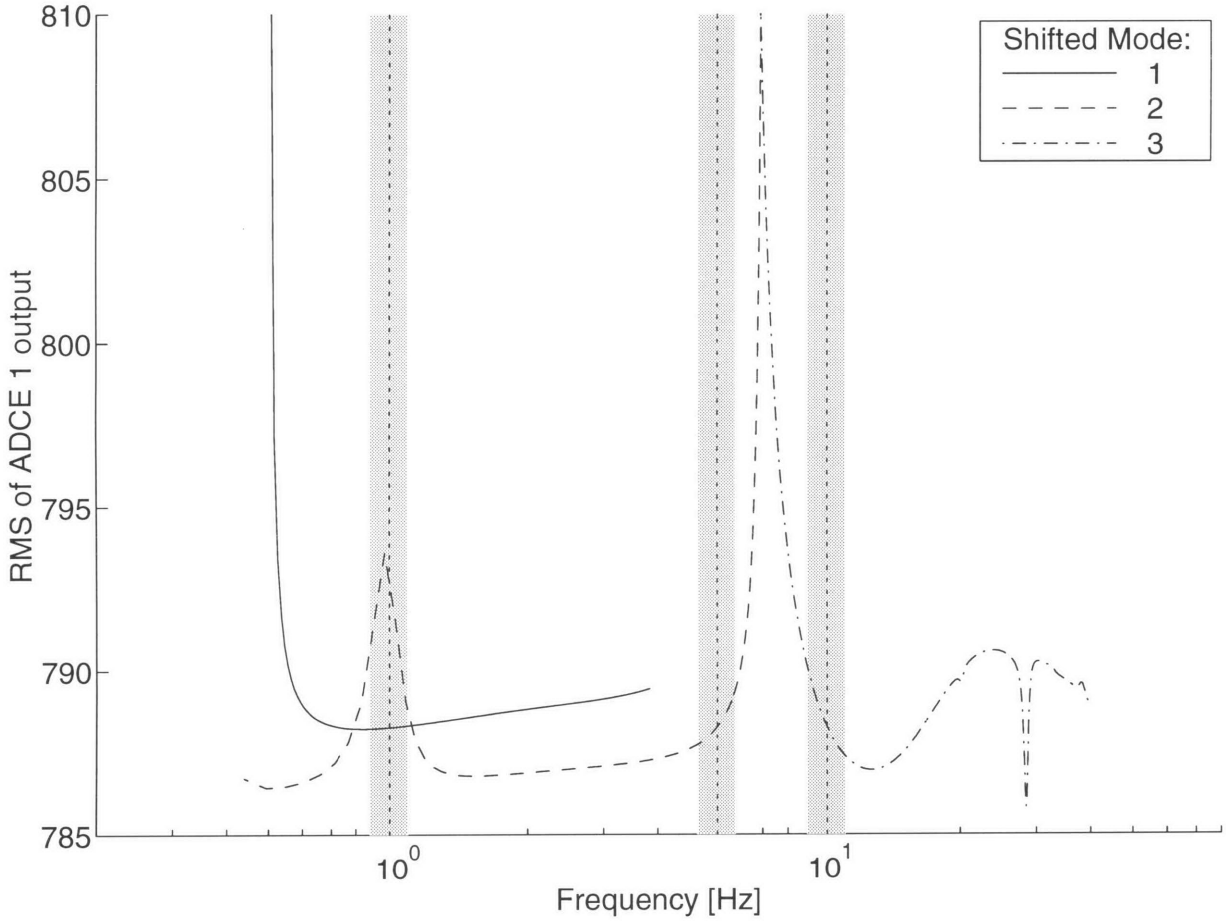

Figure 4.29: The covariance of the output of the ADCE 1 sensor, as modes 1, 2 and 3 are varied. The nominal frequencies are marked by the vertical dotted lines.

4.5 Experimental Evaluation of AMASS Controllers

The three state space controllers are implemented on the ground testbed in the cantilevered configuration. Three types of measurements are made. The frequency response of the Intel microcontroller is measured, to ensure that the compensators are being implemented by the ADCEs. Second, the closed loop plant response through the ADCE 1 piezo drive amplifier to nearly collocated sensor is measured, while each compensator is implemented on ADCEs 1 and 4. The results will be compared to the predicted closed loop response. Since the closed loop poles of the model are known, a similar measured closed loop response will indicate that the closed loop poles of the structure are in approximately the same locations. Finally, time domain impact tests are conducted. The flight experiment is intended to minimize jitter induced by a series of step commands. The actual objective is to minimize a transient condition, while the $\mathcal{H}_2$ design methodologies presented above minimize a steady state motion. Hence the impact tests will result in a more representative comparison of the controllers.

4.5.1 Measured Compensator Frequency Response

Measurement of the compensator response is done by feeding a white noise into the nearly collocated sensor A/D port, and measuring the filtered D/A output while the Intel runs the state space controllers. The white noise amplitude is set to be the same as the sensor signal amplitude when the plant is driven open loop. The matrix scaling parameter β is adjusted for this input amplitude (see Section C). Since the closed loop system will be more highly damped, this is a conservative scaling. In open loop, a 1 volt RMS white noise input produces about a 1 volt RMS sensor output.

The continuous controllers are implemented on the Intel by discretizing them to run at 250 Hz, placing them in real modal form, then finding their integer representations, A^*,B^*,C^*, and D^*. The matrix divisor element, α, is chosen to be 32,000. Table 4.6 shows the errors in the Intel pole locations, compared to the continuous pole locations. The discrete poles are the eigenvalues of $\frac{A^*}{\alpha}$, which have been mapped

Table 4.6: Continuous and discrete pole frequencies for the compensator poles, showing the effects of compensator discretization and roundoff error.

LQG			α-shifted LQG			Mod. Feedthrough LQG		
Cont's Hz	Discrete Hz	Error %	Cont's Hz	Discrete Hz	Error %	Cont's Hz	Discrete Hz	Error %
0.484	0.484	0.222	0.537	0.539	0.701	0.378	0.380	0.664
6.309	6.297	0.199	5.803	5.798	0.077	9.8993	9.956	0.577
11.643	11.5638	0.704	6.140	6.155	0.238	12.118	12.043	0.767
58.247	74.243	27.463	14.461	14.301	1.106	47.713	46.451	11.419
						123.372	139.091	113.2315

into the continuous domain using the relation $z = e^{sT}$, where T is the sample frequency. The error is a combined result of the warping effect of the continuous to discrete transformation, and the roundoff of the integer representation. The greatest errors are in the high frequency poles, where warping is the dominant source of error. Within the control bandwidth, the largest error is slightly over 1%.

The compensators are uploaded to ADCE 1, and a 1 volt signal is used to drive the ADCE. For the LQG, alpha shifted, and modified feedthrough compensators, βs of 10, 7.5, and 10, respectively, are found to yield good compensator frequencies responses. The measured compensator responses are plotted against the continuous compensators in Figures 4.30-4.32. Since the measured compensators include a full cycle time delay due to the digital implementation, the continuous compensators are also plotted with the expected phase loss of $\frac{3}{2}\frac{1}{250}\frac{180^\circ}{\pi}\omega$.

The LQG controller implementation is quite accurate (Figure 4.30). The largest magnitude discrepancies occur at low frequency. The discrete first pole appears to be at slightly above 5 Hz, rather than 4.84 Hz. A low frequency ID confirmed that the effect is not due merely to a lack of low-frequency excitation, or to having too few frequency points in that range. Since the first mode to be damped occurs at 0.9 Hz, where the magnitude has recovered, the error should not be significant.

The measured phase exhibits more loss than expected, on the order of 10° at 10 Hz. The effect is partially due to the antialiasing filters in the data acquisition

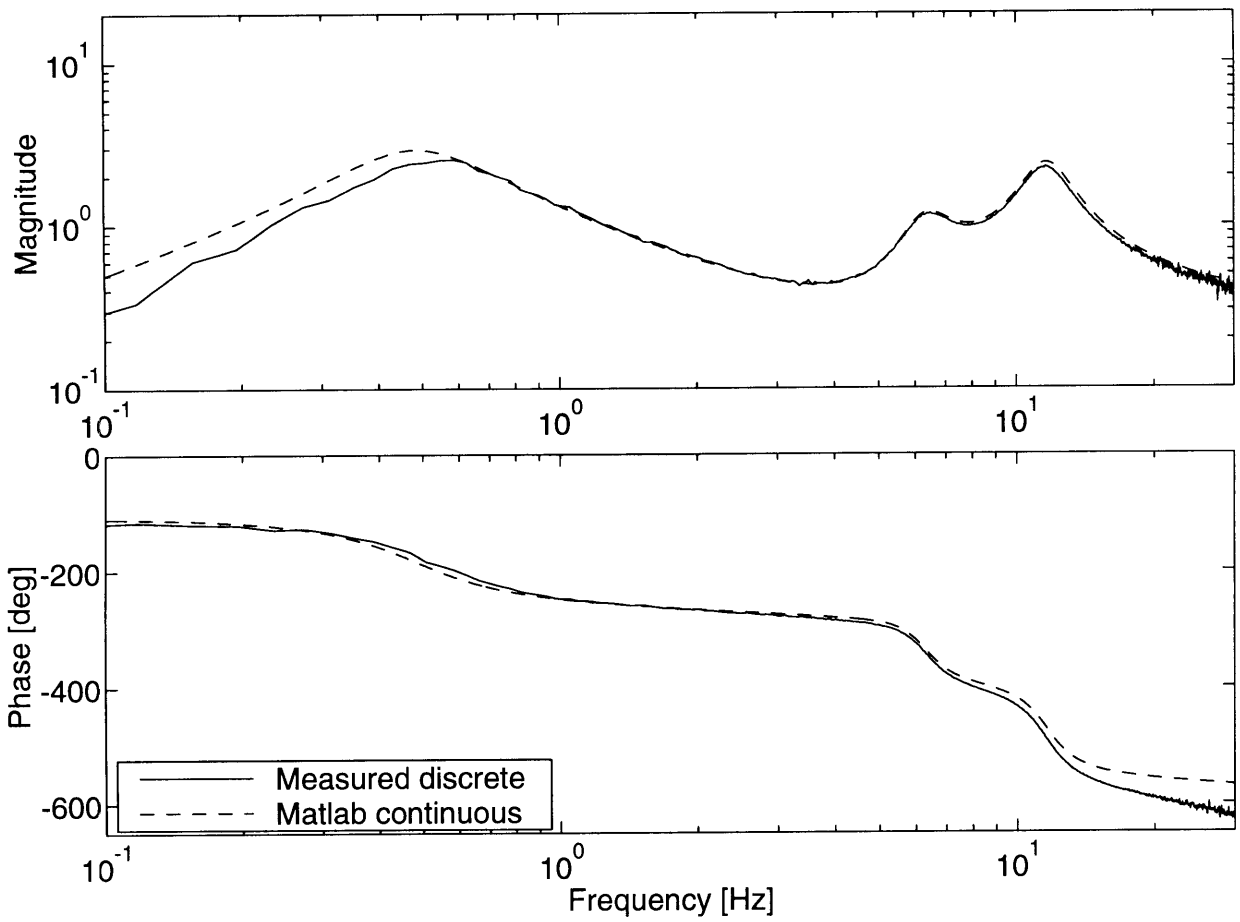

Figure 4.30: Discrete LQG compensator measured through the ADCE (solid), plotted against the continuous compensator with predicted time delay (dashed).

hardware, and is not representative of the actual compensator response. However, the additional phase loss is greater than the measured loss of the filters. Possibly the weighted filter which combines the Intel D/A outputs is the source.

The alpha shifted compensator is plotted in Figure 4.31. The low frequencies are again slightly in error. The most significant error occurs in the third compensator pole. The Intel discrete pole error is only 1%. The discrepancy between the measured and continuous compensators in Figure 4.31 is not due to the discretization or to roundoff. It is possible that due to the light damping in the 14 Hz mode, the B_c/C_c scaling is sensitive. The output is software-limited. A white noise signal which drives the other compensator states enough to get good signal to noise may overdrive the

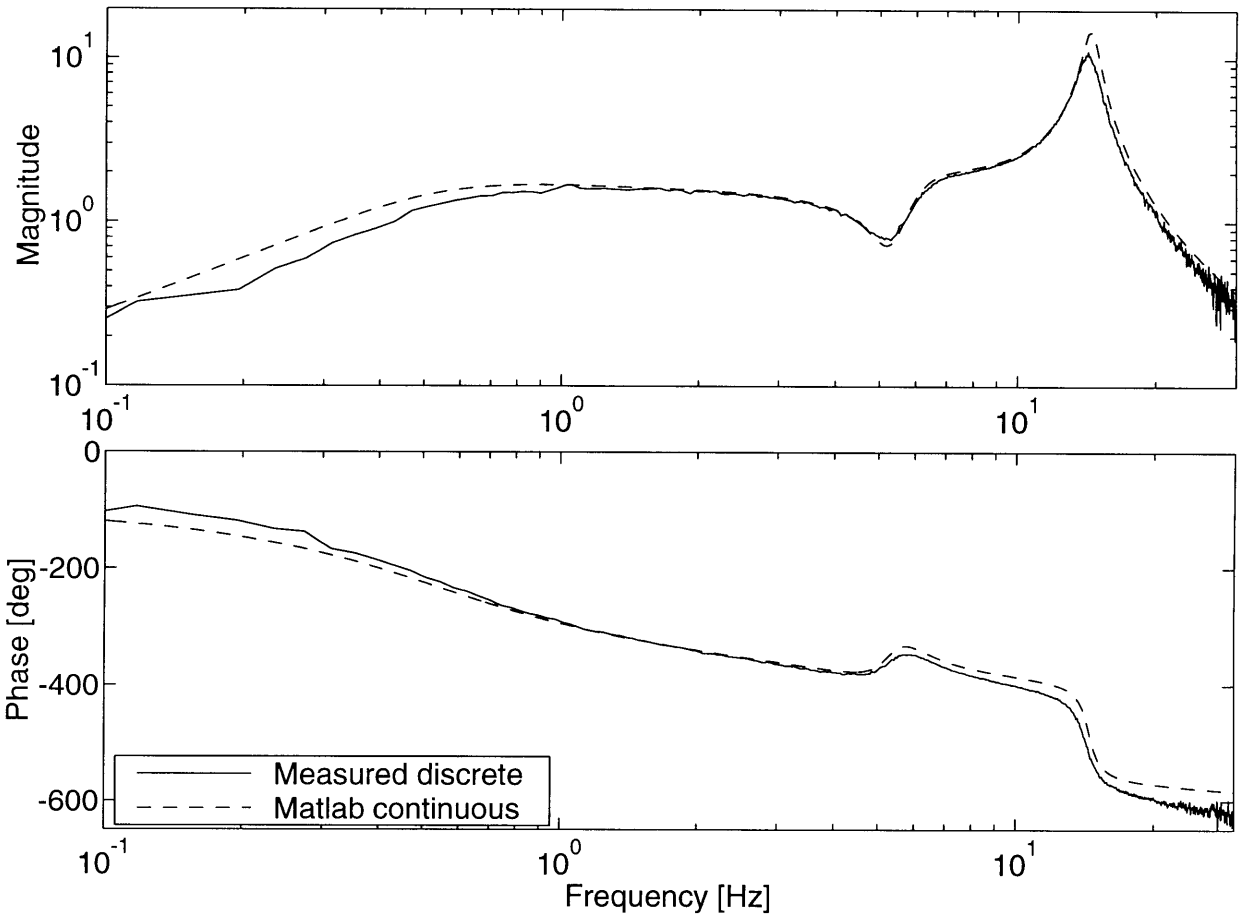

Figure 4.31: Discrete alpha shifted LQG compensator measured through the ADCE (solid), plotted against the continuous compensator with predicted time delay (dashed).

14 Hz mode. It may not overflow, but the output can be clipped. The result would be apparently increased damping at that mode, and no effect would appear at other frequencies.

The modified feedthrough controller is plotted in Figure 4.32. Again a low frequency error is noted. The occurrence of the same error in all three responses suggests that the microcontroller is somehow at fault. The ADCE implementation also shows some error at the higher frequencies around 10 Hz. However, the response is very close.

As a side note, the Intel has been used to implement compensators with poles which have lighter damping than the controllers above. The frequency response er-

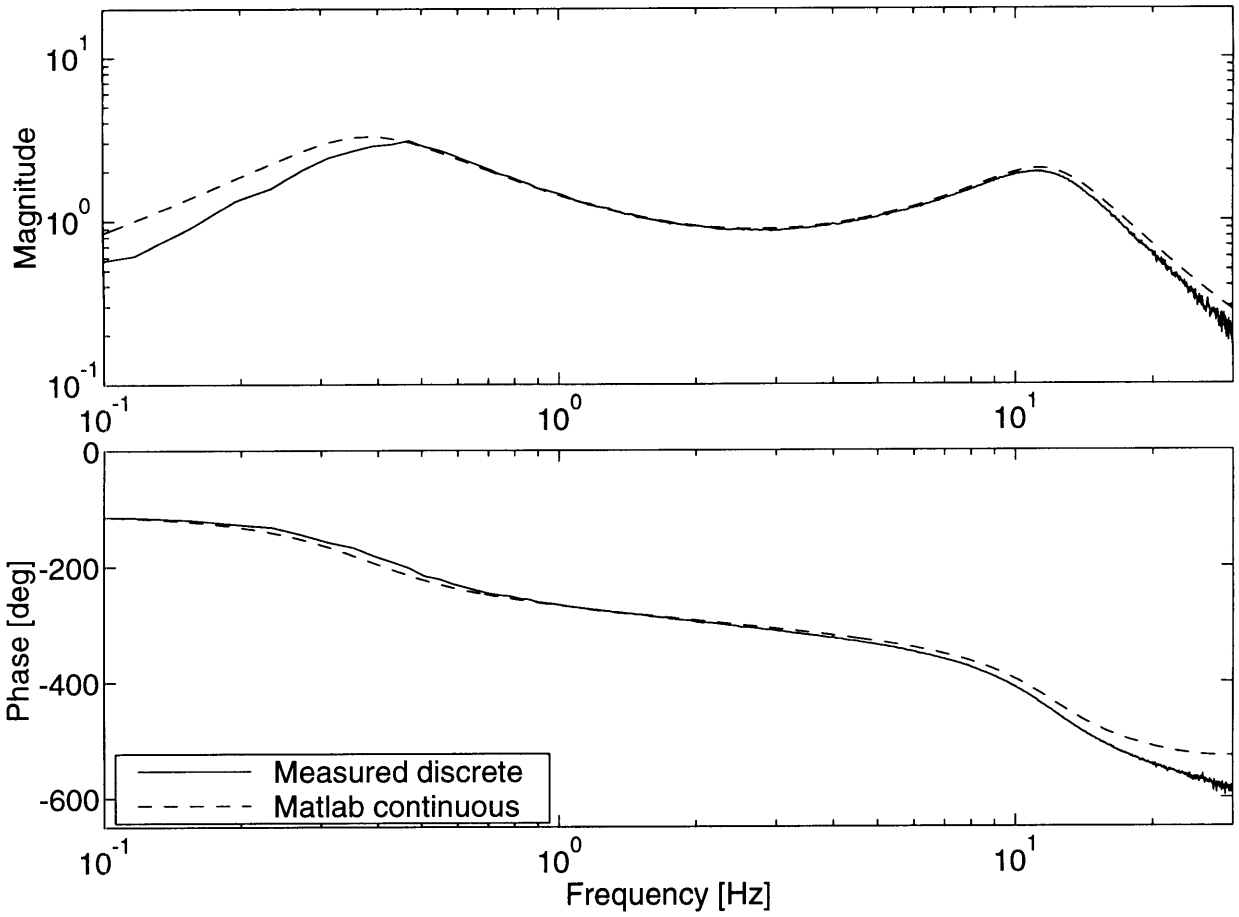

Figure 4.32: Discrete modified feedthrough compensator measured through the ADCE (solid), plotted against the continuous compensator with predicted time delay (dashed).

rors were no greater, leading to the conclusion that lightly damped compensator poles are not themselves causes of error, and do not necessarily need to be avoided. However, lightly damped poles can increase the stability problems caused by the Intel implementation errors.

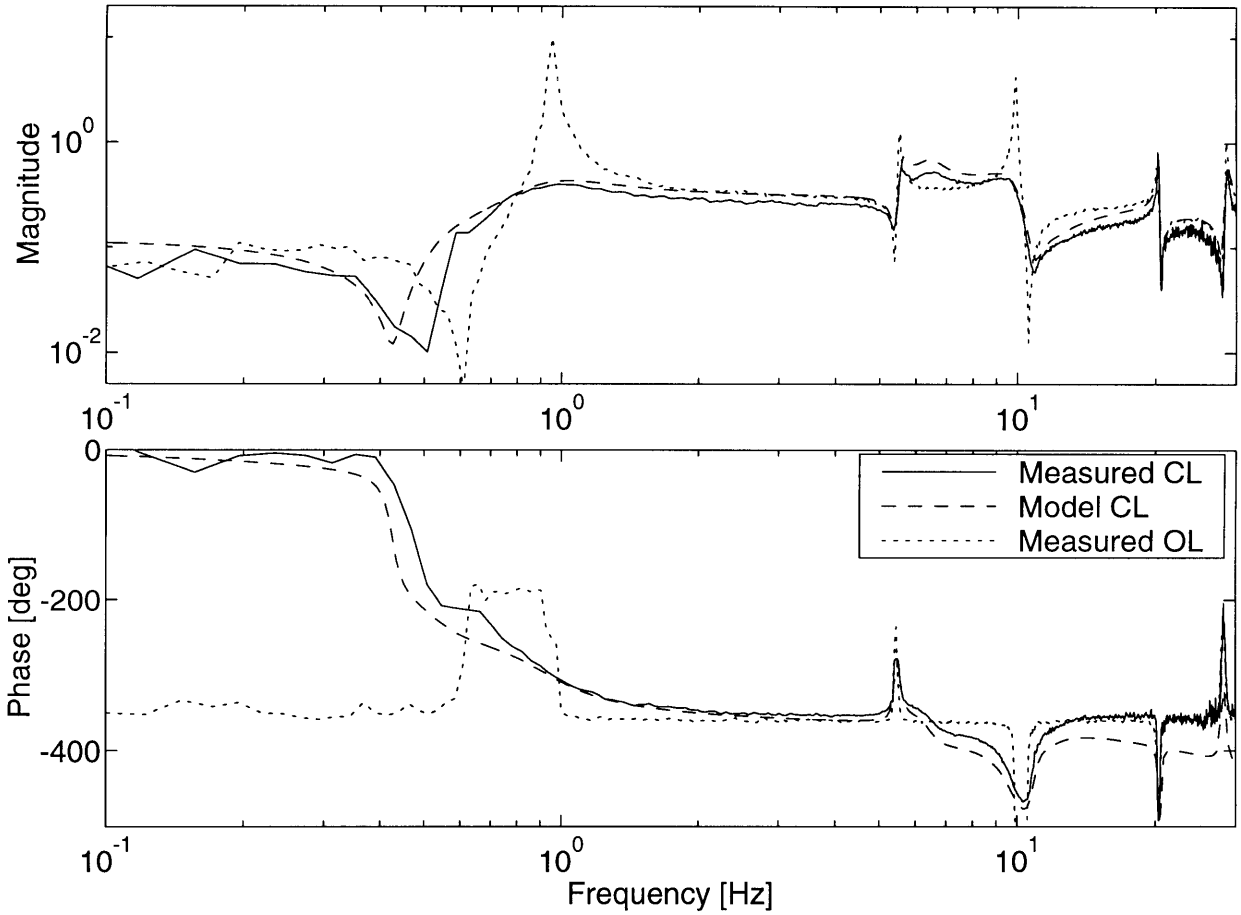

Figure 4.33: Closed loop frequency response through ADCE 1, measured (solid) and modeled (dashed), with the LQG controller closed at ADCEs 1 and 4.

4.5.2 Measured Closed Loop Frequency Response

The three controllers are uploaded to ADCEs 1 and 4. ADCE 1 is driven with an additive white noise, and the ADCE 1 nearly collocated sensor is measured. The resulting closed loop responses are shown in Figures 4.33-4.35. Also plotted is the response of the closed loop state space model.

The measured LQG closed loop response is shown with the closed loop model response in Figure 4.33. The measured response is the solid line. The model response is the dashed line. The open loop is plotted for reference with a dotted line. The experimental data actually shows a lower average response than the model response. From arguments made previously, this does not indicate that the achieved damping

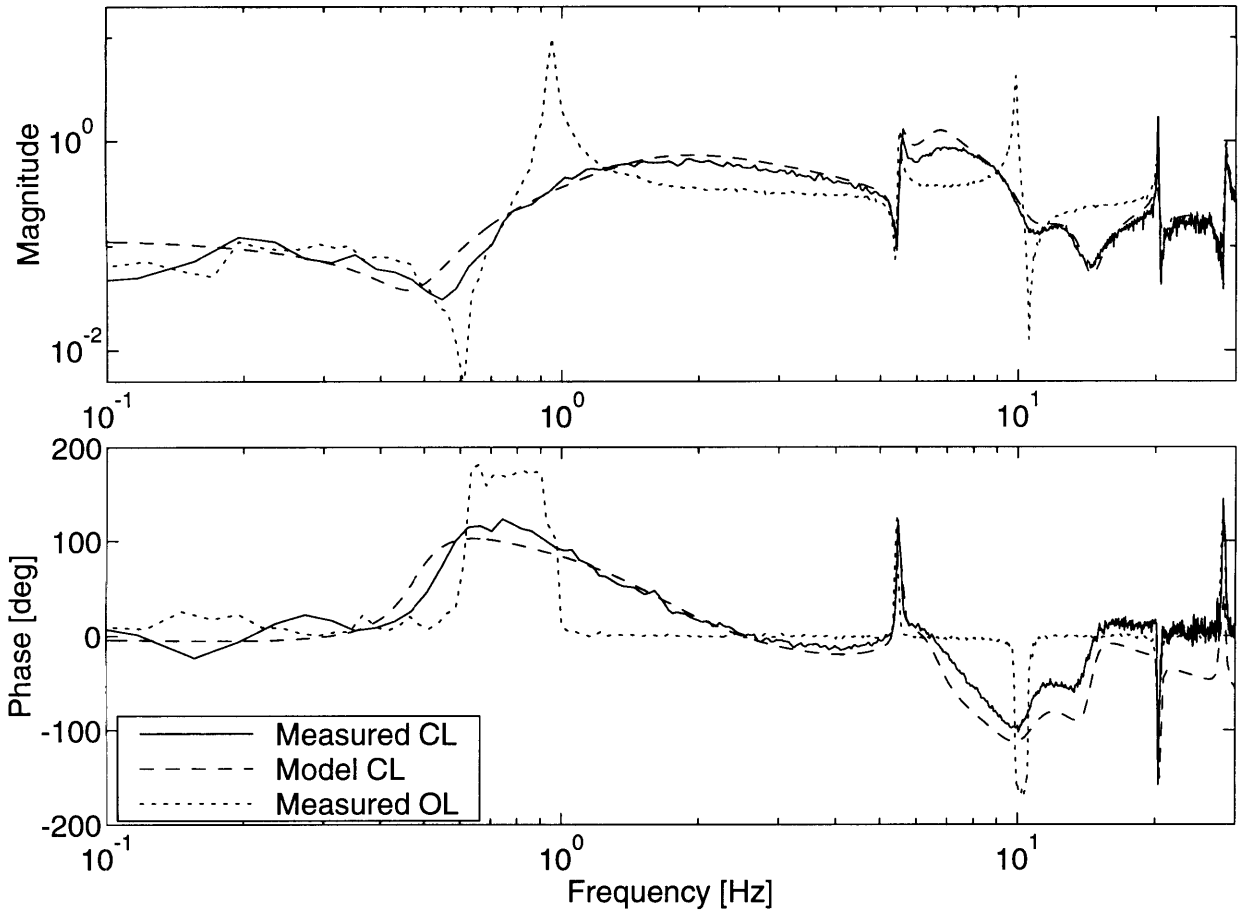

Figure 4.34: Closed loop frequency response through ADCE 1, measured (solid) and modeled (dashed), with the α-shifted LQG controller closed at ADCEs 1 and 4.

is better than the damping in the model. However, the similarity of the responses indicates that the poles of the experimental structure are in approximately the same locations as the model poles. Since the damping of the model is known, the damping in the testbed can be inferred. Note that the spike which appeared in all of the sensitivity plots appears to have been due to noise in the data. None of the three compensators show any lightly damped response at or near the first mode frequency.

The experimental alpha shifted LQG closed loop is shown in Figure 4.34. The measured data is the solid line, the closed loop model response is plotted with a dashed line, and the measured open loop is shown with a dotted line. Again some minor discrepancies are present between the model and the data. In this case, the

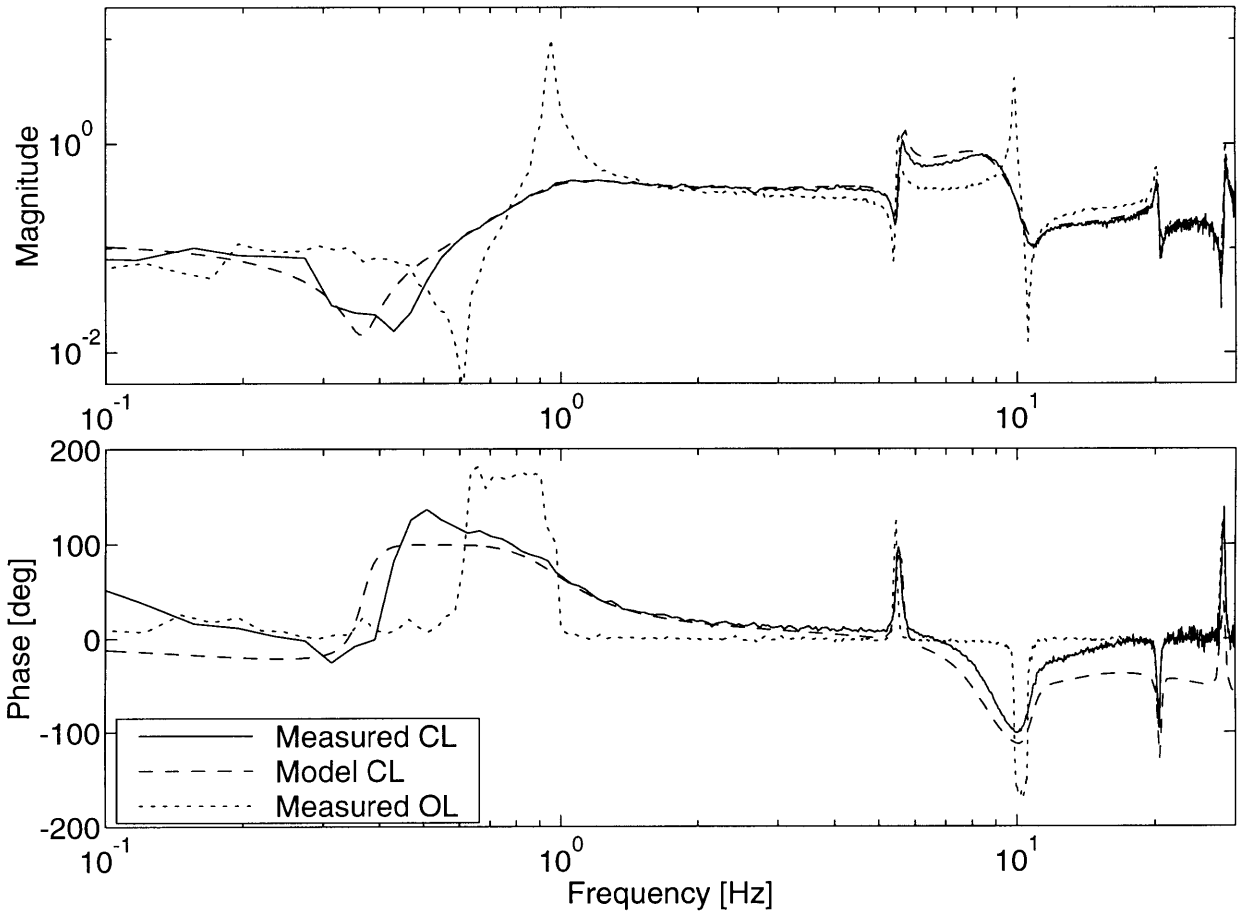

Figure 4.35: Closed loop frequency response through ADCE 1, measured (solid) and modeled (dashed), with the modified feedthrough controller closed at ADCEs 1 and 4.

increased off-resonance response of the closed loop is associated in the model with increased modal damping. The lower magnitude of the measured data may indicate the achieved closed loop damping is less than the closed loop model damping.

The measured closed loop response achieved by the modified D term compensator is plotted in Figure 4.35. Once again the average measured response is lower than the response of the model. The first mode appears to be slightly less damped than the model first mode. The response at the third mode agrees closely between the measured and modeled responses. The measured closed loop second mode response appears to be significantly lower than the model second mode. This potentially indicates some cancellation-type effect which does not translate to improved disturbance attenuation

for other disturbances.

A series of time domain tests are performed, to examine the performance when the plant is subjected to disturbances which were not modeled in the control process. This type of test will tend to emphasize the damping ability of the controllers.

4.5.3 Measured Closed Loop Impact Tests

A series of impact tests are performed to assess the modal damping of the closed loop structure. Time domain testing captures the transient performance which will be important to the flight experiment. Three tests are conducted for each of the controllers, and on the open loop plant. Each test consists of a sharp impact at some location on the structure. Sensor data from the ADCEs is used to measure the number of cycles over which the induced motion dies out.

The magnitude of the impact scales the maximum sensor output. The number of cycles needed to damp the array is independent of the force, so the impact force was not measured. The data is compared by normalizing it by the first positive peak amplitude. The impact was delivered by rapping the array sharply with the finger tips, thus the impact is not a pure impulse. However, the force should have gone to zero by the first positive peak. Three locations were selected to deliver the force to, in order to excite the first, second, and third modes independently.

The impact locations are shown in Figure 4.36. First mode is the first bending mode of the array. The first mode impact point is in the vertical plane of symmetry, three-quarters of the way up the panel. Second mode is the torsion mode. The impact point is at the edge of the array, low to the base to minimize the excitation of bending modes. The third mode is the second in-plane bending mode. The impact point is on the vertical line of symmetry, on the lower face of the array simulator panel.

Array motion is measured using the nearly collocated sensors on the diagonal members, on ADCEs 1 and 4. The sensor signals are fed through a pair of antialiasing filters, and into the data acquisition computer. The computer is configured in a time capture mode. When the input voltage exceeds a preset trigger voltage, the computer collects a block of data. There is a finite trigger delay, partially proportional to the

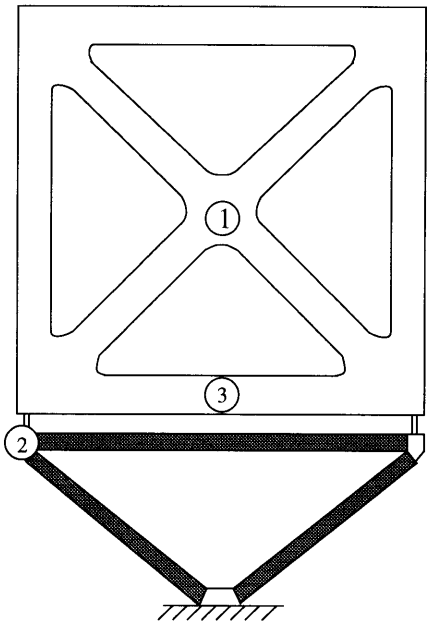

Figure 4.36: The impact locations on the AMASS array: (1) first bending mode , (2) first torsion mode, (3) second bending.

sample frequency, and partly a fixed length delay before the computer can begin to store data. The sensor data from each sensor is stored separately. It can be averaged to partially remove the response of other modes. In-plane bending modes produce sensor outputs which are in phase. By averaging the two signals, torsional motions can be subtracted out of the data. Torsion data is filtered by subtracting the sensor signals to remove the contribution of in-plane modes.

The sample rate for each mode was chosen to give at least 10 samples per mode. The number of points taken at each frequency was chosen to capture at least 10 cycles. The first mode data consists of 1000 samples taken at a sample rate of 20 Hz. The measurement is the sum of the sensor signals, to cancel out torsional motions. Only the first 20 seconds of data will be shown, since the controllers uniformly damp the first mode in three or fewer cycles. For the second mode, 300 samples were taken at 80 Hz. The excitation tended to create more output from the more lightly damped, higher modes. The signals are differenced to measure torsion. The third mode data consists of 600 points taken at 400 Hz.

The FFTs of the three open loop measurements are shown in Figure 4.37. The

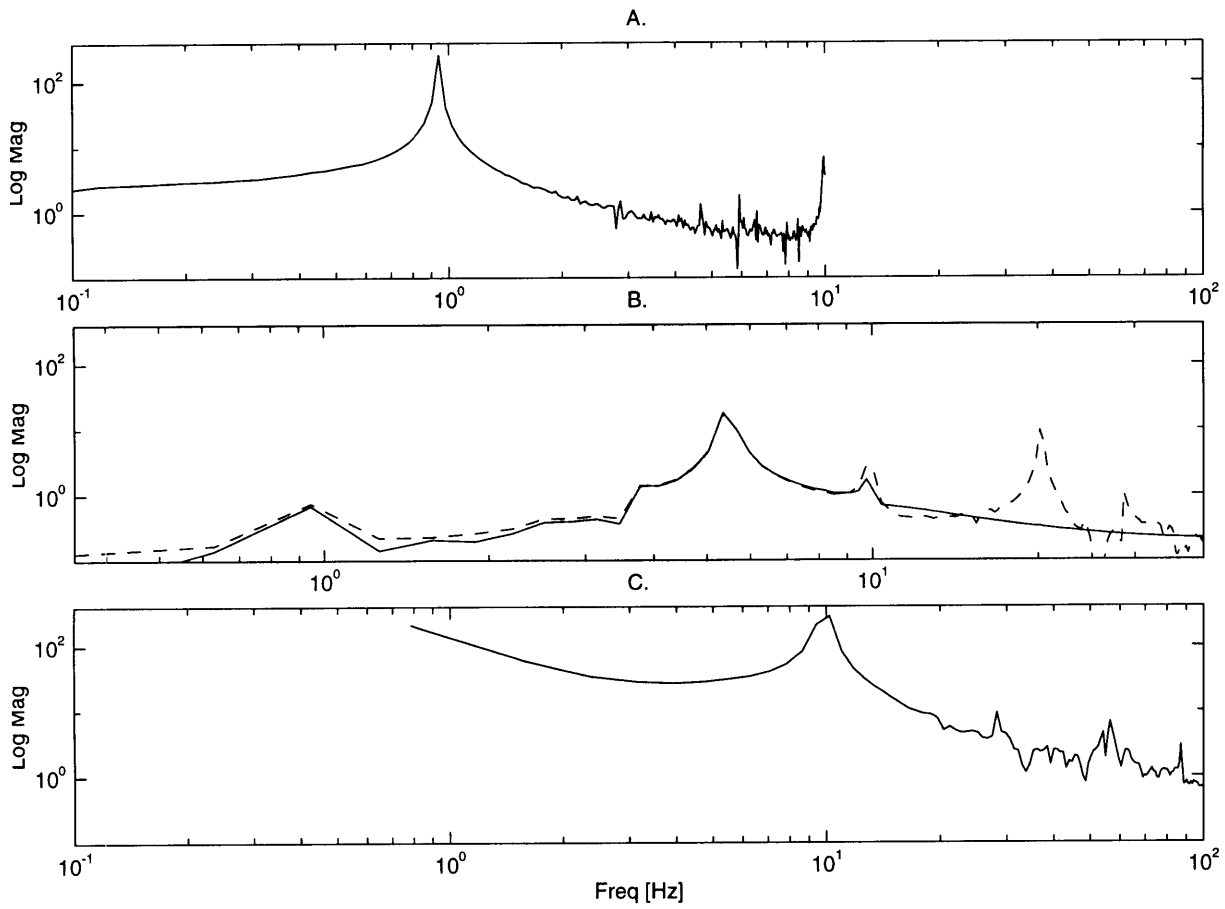

Figure 4.37: FFTs of the tome domain data. A) 1^{st} mode excitation, averaged sensors. B) 2^{nd} mode excitation, differenced sensors. Shown is the postprocessed, filtered data (solid) against the unfiltered (dashed). C) 3^{rd} mode excitation, averaged sensors.

upper and lower plots give the FFTs of the raw open loop data, for impacts at the mode 1 and 3 impact locations, respectively. The sensor data has been averaged to remove the appearance of torsion modes. The FFTs show that the excitations for these modes were very clean. The first mode is exclusively excited. The third mode impact point also excites first mode, however, the signals are easy to discriminate in the time domain data. Unfortunately, the second mode impact test creates motion in several modes, of comparable magnitude to the second mode. It is nearly impossible to pick out the second mode contribution.

The time domain data can be post-processed with a digital filter. Using a 4-pole

discrete time Butterworth filter, the data sequence can be filtered once in the forward direction. The filtered data is then reversed and filtered again. The final filtered signal has zero phase distortion and an effective 8 pole filter. The cutoff frequency is 10 Hz. The center plot shows the FFT of the filtered second mode data (solid) plotted against the FFT of the unfiltered data (dashed). The 10 Hz response has been reduced, and the higher contributions completely eliminated. The desired 5.5 Hz response is unattenuated. Note that the filtered time data will show the effects of initial conditions near the start and end times. Since the filter and the plant are linear systems, the damping of the system will not be distorted by the filtering. Since all three signals to be compared are filtered, the filtering process does not effect the validity of the conclusions.

The closed loop ringdown data are shown in Figures 4.38-4.40. The first mode damping is uniformly good. The second mode damping is fairly low. The third mode response is damped by all three controllers, although not as heavily as the first mode.

The alpha shifted compensator produces the quickest ringdown of first mode, in about one and a half cycles. Surprisingly the MM compensator damps the first mode better than the MF compensator. However, the MM controller response does not completely settle until about 4 seconds have passed. The modified feedthrough controller response seems to settle in about 3.5 seconds.

The second mode is damped best by the LQG multimodel controller, although the damping is too light to show the number of cycles to damp. The alpha-shifted and modified feedthrough controller achieve about the same performance. The damping in the third closed loop mode is about equal for the alpha-shifted and the MF controllers. About six cycles are required to damp the oscillations out. The MM controller requires about seven cycles.

4.6 AMASS Ground Testbed Conclusions

Three $\mathcal{H}_2$optimal control techniques were used to design compensators to actively damp the AMASS ground testbed. The techniques were LQG, alpha shifted LQG,

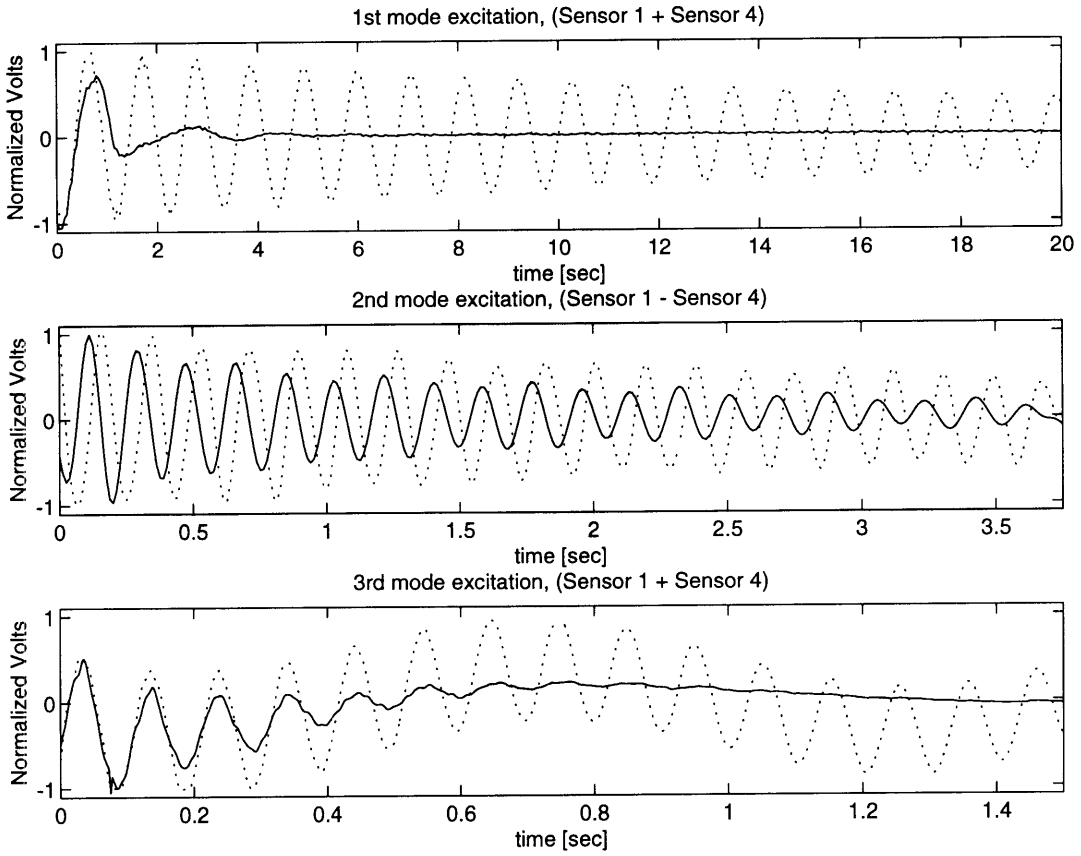

Figure 4.38: LQG compensator: measured ringdown for first, second, and third mode excitations, in closed loop (solid) and open loop (dotted). Second mode has been postprocessed.

and Modified Feedthrough (MF) LQG. All involved a multimodel optimization. The controllers were analytically examined for robustness, and experimentally compared to determine which gave the highest performance. The objectives, determined from the AMASS flight experiment, were to design controllers which gave high damping in the first three modes, and were stable to $+10\%$ and -10% mode shifts in the same modes. Additionally, complexity of the design process is a factor.

The AMASS controllers were designed to be stable for $+10\%$ and -2% mode shifts. These values were based on the differences in mode frequencies in the ground and flight testbeds. It was desired to confirm the robustness of the designs to mode frequencies experimentally. Unfortunately the flight hardware was not complete at

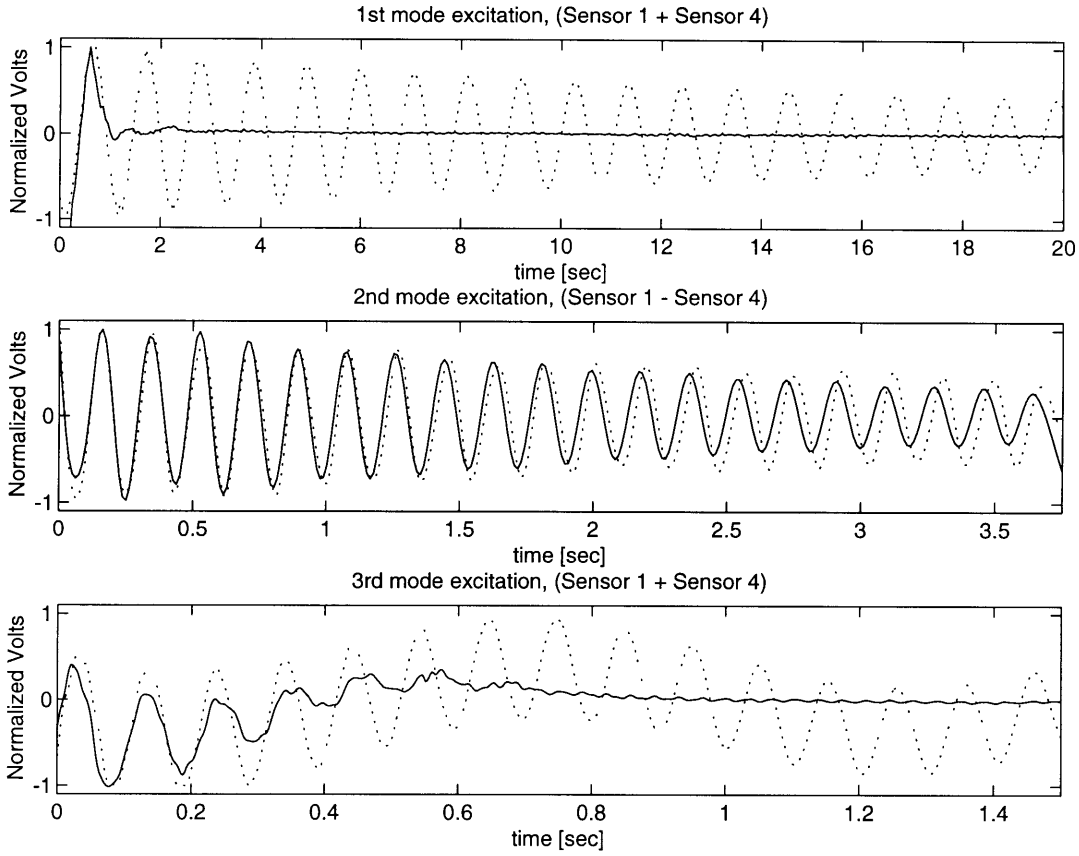

Figure 4.39: alpha shifted LQG compensator: measured ringdown for first, second, and third mode excitations, in closed loop (solid) and open loop (dotted). Second mode has been postprocessed.

the time the experiments were performed. However, the robustness analysis showed that all the control design procedures were stable to $+10\%$ and -10% mode shifts. The alpha shifted compensator is the only marginal design, for the second mode shift. Therefore the control design processes all should be capable of giving the same degree of stability robustness to the flight controllers.

Performance robustness was found, analytically, to be markedly better for the LQG and MF compensators. While the alpha shifted compensator gives better damping to the nominal plant, performance degrades rapidly as the modes shift. Additionally, the design process for the alpha shifted compensator begins with an iteration to determine a set of alpha shifts. The iteration involves a Riccati LQG solution at

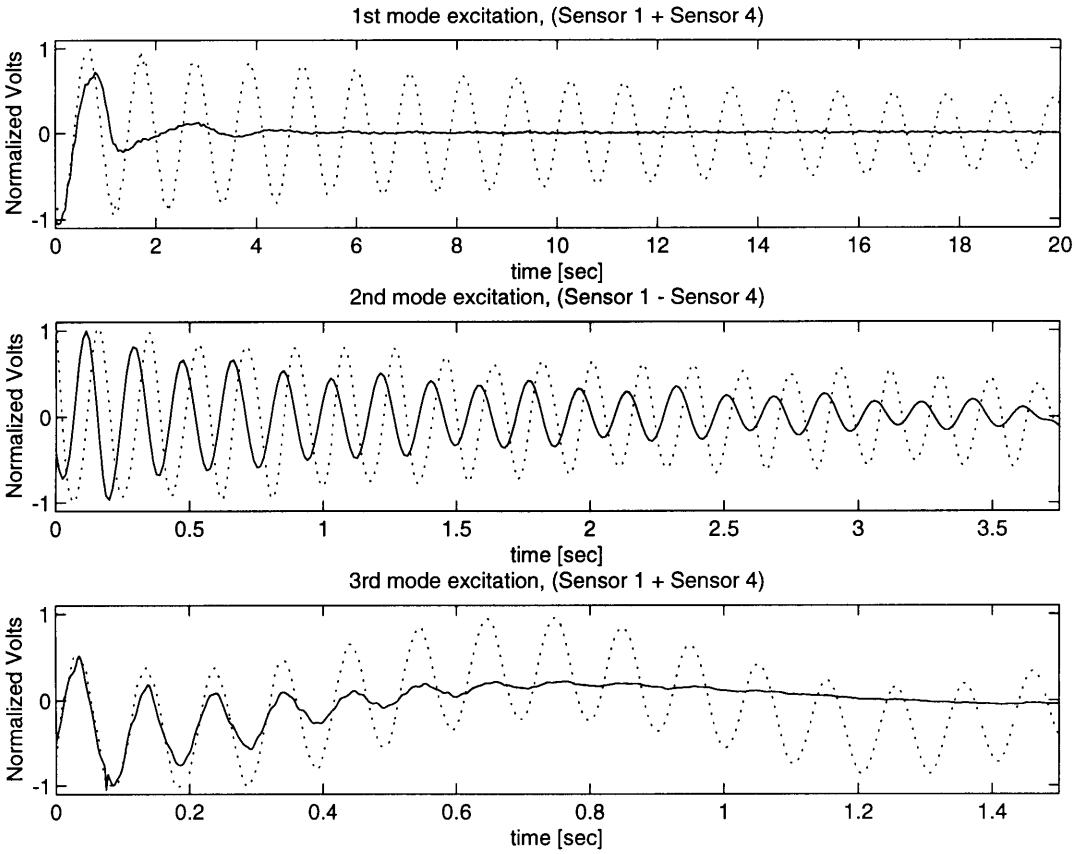

Figure 4.40: MF compensator: measured ringdown for first mode excitation, in closed loop (solid) and open loop (dotted). Second mode has been postprocessed.

each step. The computational cost is high, and many steps are needed because of the highly nonlinear interaction of mode shifts with the closed loop poles, and the necessity of a stable compensator.

The MF compensator also requires a design model to be iteratively chosen. However, the iteration does not require a Riccati solution. Only a single parameter, D_2, is varied, and the desired behavior of the plant is very clearly related to the variation of D_2. Hence the creation of the design model is a minor task, generally quicker than the choice of control and performance weights. The MF compensator process is the same order of difficulty as the LQG design.

The alpha shifted compensator achieved the highest first mode damping, and

damped third mode well. Performance of the LQG and MF controllers on the AMASS ground testbed was found to be more similar than the analysis suggested. Based on analytical tests, the modified feedthrough controller was expected to give better performance on the structure. It is suggested that the experimental performance of the MF designs was less than predicted because nonlinearities in the piezoelectric actuators were not accounted for.

However, both the LQG and MF controllers achieved acceptable damping in the first and third modes. None of the compensators damped second mode well, although some damping was evident.

Based on the robustness tests of the previous section, the alpha shifted model is most likely a poor choice for the flight controller. The modified feedthrough controller requires only slight additional effort, for some improvement in the predicted response. No robustness on the plant model is sacrificed. If the performance of the MF controller on the testbed can be increased to its predicted level, the flight controller will have similar performance to the alpha shifted controller for a large increase in robustness.

Chapter 5

Conclusions

The purpose of this thesis has been to examine the implementation of local controllers. Local control techniques which control the flow of power through the controlled location were examined. Specifically, impedance matching was shown to be the optimal method to damp a structure. The energy shunting approach was shown to be the optimal local controller formulation for zeroing transmissibility through the controlled location. Their ability to guarantee stability and a certain level of performance make them ideal for structural control. Further, any local controller can be described as a combination of impedance matching and energy shunting.

The derivation of local control for structures was then extended to structures which are not positive real, to capture effects which will be present in many physical systems. Two representative effects, time delay and noncollocation, are examined.

Time delay, which can result from a digital implementation, is considered in terms of its effect on the stability and on the performance of the local controllers. Stability in the presence of time delay is found to place constraints on the rolloff of the controller. For the desired bandwidth of control, certain time delays cannot be accommodated. The local controller in the presence of time delay is found by incorporating the inverse of the time delay into the optimal impedance match, and approximating the augmented controller. The result is compared to the creation of a positive real design model from the actual, nonpositive real plant.

Noncollocation removes a fundamental property of the local controllers, that the

actuator and sensor together control power. If the requirement is not met, the impedance matching and energy shunting techniques are not applicable. This follows from conceptual reasons, since the quantity being controlled is no longer power. Also, the local model is no longer accurate. As an alternative, the global attributes of the impedance match and energy shunt are examined, and a number of state space techniques which capture these attributes are enumerated. Three of these are experimentally investigated on the AMASS solar array simulator.

The experimentally implemented techniques are reduced order multimodel design, alpha-shifting, and a modified feedthrough compensation scheme. The alpha-shifting adds damping to the closed loop modes. First mode damping of 48% on the analytical mode is achieved. The MF design increases the modal observability of the design model, which increases the damping in the predicted closed loop modes from 22% to 32% in the first mode, and from 9% to 13% in the third. Second mode damping is limited to less than 1.5% in all controllers, by a combination of low observability and the need to transition the loop phase through -180° between second and third modes. However, this represents a factor of 3 improvement over open loop second mode damping.

The experimental results confirm that the alpha-shifted compensator achieves the highest damping. However, analytical results indicate a lack of robustness. The MF controller achieves approximately the same level of damping on the testbed as the MM compensator. The inability of the MF controller to achieve the predicted levels of damping is suggested to result from the failure to account for nonlinearities in the piezoelectric actuator.

Future Work. A number of research paths have been opened up by the work in this thesis. The highest potential advantage could be gained by stating the local control objectives in terms of a global, state space model. The state space $\mathcal{H}_2$ techniques used on the AMASS structure are not related directly to the local power costs. State space formulations whose minimizing solutions are the impedance match and energy shunt are desired.

A second potential area of research is the modified feedthrough control design. Two questions must be researched. First, the motivation for the design is to create the correct power dual sensor for the given actuator. The connection between the MF formulation and power dual sensor must be made explicit (this may also lead to connections with the simultaneous sensing and actuation of [14]). Second, modifications to counter the effect of piezoelectric nonlinearities must be incorporated.

A final question concerns the noncollocation of the sensor and actuator. It was suggested in Section 3.2 that an impedance matching compensator could be derived for a nearly collocated sensor and actuator by designing an observer which would estimate the velocity at the actuator location based on the velocity at the sensor location. Such a physical state estimator would enable an impedance match to be designed.

References

[1] Hyde, J. M., *Multiple Mode Vibration Supression in Controlled Flexible Systems*, Master's thesis, Department of Mechanical Engineering, M.I.T., Cambridge, MA, May 1991.

[2] Ogata, K., *Modern Control Engineering*, Prentice-Hall, 1990.

[3] Kwakernaak and Sivan, *Linear Optimal Control Systems*, Wiley-Interscience, 1972.

[4] Maciejowski, J. M., *Multivariable Feedback Design*, Addison-Wesley, Wokingham, England, 1989.

[5] Francis, B. A., *A Course in $\mathcal{H}_\infty$ Control Theory*, Springer-Verlag, 1987.

[6] Junkins, J. L., *Mechanics and Control of Space Structures*, AIAA, Washington, D. C., 1990.

[7] von Flotow, A. H., "The Acoustic Limit of Structural Dynamics," in *Large Space Structures: Dynamics and Control* (Atluri and Amos, eds.), pp. 213–238, Springer-Verlag, 1988.

[8] Anderson, B. D. O., "A Simplified Viewpoint of Hyperstability," *IEEE Trans. Automatic Control*, Vol. AC–13, No. 3, June 1968, pp. 292–294.

[9] Chen, G.-S., B. J. Lurie, and B. K. Wada, "Bridge Feedback for Active Damping Augmentation," *Proceedings, AIAA Dynamics Specialist Conference*, Long Beach, CA, Apr. 1990, pp. 502–510.

[10] Fanson, J. L., C.-C. Chu, B. J. Lurie, and R. S. Smith, "Damping and Structural Control of the JPL Phase 0 Testbed Structure," *Journal of Intelligent Material Systems and Structures*, Vol. 2, July 1991, pp. 281–300.

[11] Miller, D. W., *Modelling and Active Modification of Wave Scattering in Structural Networks*, Ph.D. thesis, Department of Aeronautics and Astronautics, M.I.T., 1988. (Space Systems Laboratory Report #12–88).

[12] MacMartin, D. G., *A Stochastic Approach to Broadband Control of Parametrically Uncertain Structures*, Ph.D. thesis, Department of Aeronautics and Astronautics, M.I.T., Cambridge, MA, June 1992.

[13] Skudrzyk, E., "The Mean-value Method of Predicting the Dynamic Response of Complex Vibrators," *Journal of the Acoustical Society of America*, Vol. 67, No. 4, Apr. 1980, pp. 1105–1135.

[14] Spangler, R., *Broadband Control of Structural Vibration Using Simultaneous Sensing and Actuation with Nonlinear Piezoelectric Elements*, Ph.D. thesis, Department of Aeronautics and Astronautics, M.I.T., Cambridge, MA, Feb. 1994.

[15] von Flotow, A. H., "Disturbance Propagation in Structural Networks," *Journal of Sound and Vibration*, Vol. 106, No. 3, 1987, pp. 433–450.

[16] MacMartin, D. G., *An $\mathcal{H}_\infty$ Power Flow Approach to Control of Uncertain Structures*, Master's thesis, Department of Aeronautics and Astronautics, M.I.T., Cambridge, MA, Feb. 1990.

[17] Sun, C., B. Kim, and J. Bogdanoff, "Derivation of Equivalent Simple Models for Beam and Plate–Like Structures in Dynamic Analysis," in *Proceedings of the 22^{nd} AIAA/ASME/ASCE/AHS Structures, Structural Dynamics, and Materials Conference*, 1981, pp. 523–532. Paper No. 81-0624.

[18] Hodges, C. H. and J. Woodhouse, "Theories of Noise and Vibration Transmission in Complex Structures," *Reports on Progress in Physics*, Vol. 49, 1986, pp. 107–170.

[19] Carlson, G. E. and C. A. Halijak, "Approximation of Fractional Capacitors $(1/s)^{1/n}$ by a Regular Newton Process," *IEEE Transactions on Circuit Theory*, Vol. 11, June 1964, pp. 210–213.

[20] Ashkenazi, A. and A. E. Bryson Jr., "Control Logic for Parameter Insensitivity and Disturbance Attenuation," *AIAA Journal of Guidance, Control, and Dynamics*, Vol. 5, No. 4, July 1982, pp. 383–388.

[21] Anderson, B. D. O. and J. B. Moore, *Linear Optimal Control*, Prentice-Hall, New Jersey, 1971.

[22] Grocott, S. C. O., *Comparison of Control Techniques for Robust Performance on Uncertain Structural Systems*, Master's thesis, Massachusetts Institute of Technology, Jan. 1994.

[23] Grace, A., *Matlab Optimization Toolbox*, MathWorks, 1992.

[24] MacMartin, D. G., S. R. Hall, and D. Mustafa, "On a Cost Functional for $\mathcal{H}_2/\mathcal{H}_\infty$ Minimization," *Proceedings, IEEE Conference on Decision and Control*, Honolulu, HI, Dec. 1990, pp. 1010–1012.

[25] Grocott, S. C. O., D. G. MacMartin, and D. W. Miller, "Experimental Implementation of a Multiple Model Technique for Robust Control of the MACE Test Article," *Proceedings, Third International Conference on Adaptive Structures*, San Diego, CA, Nov. 1992.

[26] Crawley, E. F. and J. de Luis, "Use of Piezoelectric Actuators as Elements of Intelligent Structures," *AIAA Journal*, Vol. 25, No. 10, Oct. 1987, pp. 1373–1385.

[27] Fleming, F., *The Effect of Structure, Actuator, and Sensor on the Zeros of Controlled Structures*, Master's thesis, Massachusetts Institute of Technology, 1991. MIT SERC report # 18-90.

[28] Aubrun, J.-N., "Theory of the Control of Structures by Low-Authority Con-

trollers," *AIAA Journal of Guidance and Control*, Vol. 3, No. 5, Sept–Oct 1980, pp. 444–451.

[29] Liu, K., R. Jacques, and D. Miller, "Frequency Domain Structural System Identification by Observability Range Space Extraction," in *Proceedings of the American Control Conference*, 1994.

[30] Jacques, R. and D. Miller, "Multivariable Model Identification from Frequency Response Data," in *Proceedings of the 32nd Conference on Decision and Control*, 1993.

[31] Glover, K., "All Optimal Hankel-norm Approximations of Linear Multi-variable Systems and There $\mathcal{L}_\infty$ Error Bounds," *International Journal of Control*, Vol. 39, 1984, pp. 1115–1193.

[32] Franklin, G. F., J. D. Powell, and M. L. Workman, *Digital Control of Dynamic Systems*, Addison-Wesley, 1990.

Appendix A

Global Wave Model

A global wave model of an arbitrarily complex waveguide-like structure can be constructed from the wave coordinate junction description, Equation 2.8, and the transmission matrix Equation 2.11. Consider Figure A.1, a truss structure composed of M separate members, intersecting at N junctions. The structure is separated into its component members, and the junctions are identified. At each junction n, $n = 1..N$, a set of incoming and outgoing wave modes $\begin{bmatrix} w_{i_n} \\ w_{o_n} \end{bmatrix}$ are defined. Using the boundary conditions at each junction n, the scattering matrices $S(\omega)_n$ and $\Psi(\omega)_n$ for each junction are found. The member transmission matrices ξ_m, $m = 1..M$, are determined (ξ_m is the transmission matrix from one end of member m to the other).

A vector of global wave mode amplitudes is defined by stacking the individual junction wave mode amplitudes together:

$$W = \begin{bmatrix} W_i \\ W_o \end{bmatrix} = \begin{bmatrix} w_{i_1} \\ w_{i_2} \\ \vdots \\ w_{o_1} \\ w_{o_2} \\ \vdots \end{bmatrix} \tag{A.1}$$

where the numerical subscripts indicate the junctions at which the wave amplitudes are described. The incoming wave modes at each junction are related to the out-

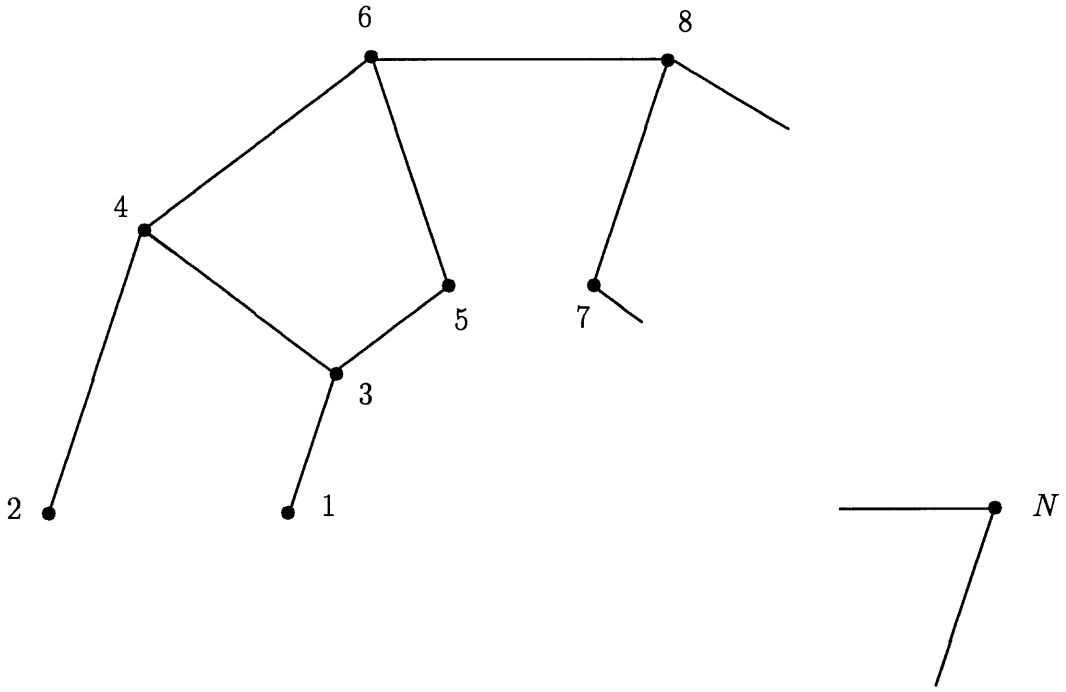

Figure A.1: Truss structure

going waves at the other junctions by $W_i = \xi_{glob} W_o$. The matrix ξ_{glob} is created by assembling the individual member ξs, eg.

$$W_i = \begin{bmatrix} w_{i_1} \\ w_{i_2} \\ w_{i_3} \\ \vdots \end{bmatrix} = \begin{bmatrix} 0 & \xi_{2-1} & \xi_{3-1} & \cdots \\ \xi_{1-2} & 0 & 0 & \\ \xi_{1-3} 0 & 0 & & \\ \vdots & & & \end{bmatrix} \begin{bmatrix} w_{o_1} \\ w_{o_2} \\ w_{o_3} \\ \vdots \end{bmatrix} \tag{A.2}$$

Similarly, global scattering and generation matrices can be assembled from the individual junction scattering and generation matrices, such that $W_{o_{glob}} = S_{glob} W_{i_{glob}} + \Psi_{glob} Q_{glob}$. The resulting global model can be combined such that:

$$\begin{bmatrix} W_i \\ W_o \end{bmatrix} = \begin{bmatrix} \underline{0} & \xi_{glob} \\ S_{glob} & \underline{0} \end{bmatrix} \begin{bmatrix} W_i \\ W_o \end{bmatrix} + \begin{bmatrix} \underline{0} \\ \Psi_{glob} \end{bmatrix} Q \tag{A.3}$$

With a specified forcing condition Q_{glob}, this equation can be solved at each frequency

for W:

$$W = \left(I - \begin{bmatrix} \underline{0} & \xi_{glob} \\ S_{glob} & \underline{0} \end{bmatrix} \right)^{-1} \Psi_{glob} Q_{glob} \tag{A.4}$$

where I is the appropriately sized identity matrix, and W, ξ_{glob}, S_{glob}, and Ψ_{glob} are functions of frequency.

The transformation matrix Y can be used to transform the wave mode amplitudes back into physical coordinates:

$$\begin{bmatrix} U \\ F \end{bmatrix} = \begin{bmatrix} u_1 \\ \vdots \\ u_N \\ f_1 \\ \vdots \\ f_N \end{bmatrix} = Y_{glob}(\omega) W(\omega) \tag{A.5}$$

where Y_{glob} is assembled from the individual junction transformations:

$$Y_{glob} = \begin{bmatrix} Y_{ui_1} & \underline{0} & \cdots & Y_{uo_2} & \underline{0} & \cdots \\ \underline{0} & Y_{ui_2} & & \underline{0} & Y_{uo_2} & \\ \vdots & & \ddots & \vdots & & \ddots \\ Y_{fi_1} & \underline{0} & \cdots & Y_{fo_2} & \underline{0} & \cdots \\ \underline{0} & Y_{fi_2} & & \underline{0} & Y_{fo_2} & \\ \vdots & & \ddots & \vdots & & \ddots \end{bmatrix} \tag{A.6}$$

For example, by setting

$$Q(\omega) = \begin{bmatrix} f_1(\omega) \\ \vdots \\ f_n(\omega) \\ \vdots \\ f_N(\omega) \end{bmatrix} = \begin{bmatrix} 0 \\ \vdots \\ 1 \\ \vdots \\ 0 \end{bmatrix} \tag{A.7}$$

f_n is modeled as a white noise input. By solving Equation A.4 at a vector of frequencies ω, and converting to physical coordinates, a transfer function from force f_n to physical displacements u_n at the junction can be calculated. The power of the

wave model is that it is an exact solution to the governing PDE of the structure, unlike a finite element model, for example, which is only accurate for a certain number of modes. The main drawbacks to the wave model are that tools for constructing complicated models are not widely available (in contrast to finite elements), and that connections to state space representations are not readily made.

Appendix B

Reduction and $\mathcal{H}_2$ Tuning

The iterative reduction and tuning of the AMASS control design (Section 4.2.3) uses two reduction schemes to remove undesired dynamics from the state space controller. The reduction schemes are *balanced reduction* and direct truncation. Balanced reduction places the controller into a form whose states have equal controllability and observability. The controllability and observability is captured in the Hankel Singular Values (HSVs) of the balanced system. States with small HSVs have a small effect on the output, and can be removed with a small impact on the response of the system [31]. The technique is typically used for model truncation. Optimal reduction involves capturing the effect of the truncated poles in a D term. Since the controller is restricted to have no feedthrough, the reduction is a suboptimal method.

Direct truncation refers to selecting specific compensator poles to remove, for example based on frequency. ordering the controller into a block-diagonal form. States which are outside the bandwidth of control are eliminated. Each reduction changes the frequency response of the controller. In order to ensure that the response of the reduced controller captures the important features of the full-order controller, the tuning is performed to minimize the output error between the full-order and the reduced controller. The tuning is performed after each reduction.

The tuning step is performed using a gradient search process. At an intermediate stage in the reduction process, stage i, the reduced order controller is

$$\dot{x}_r = A_{r_i} x_r + B_{r_i} y$$

$$u_r = C_{r_i} x_r \tag{B.1}$$

The reduced order controller has been created in i steps from the n_c order initial compensator, whose dynamics are

$$\begin{aligned} \dot{x}_c &= A_c x_c + B_c y \\ u &= C_c x_c \end{aligned} \tag{B.2}$$

In the reduction step performed to create the i^{th} reduced order controller, above, from the $(i-1)^{th}$ controller, states are removed from the latter system. The truncated states may be above the control bandwidth, or within it. Removing states within the bandwidth tends to introduce larger errors in frequency response than removing states from outside the bandwidth.

The i^{th} system is tuned using a gradient search minimization technique to reduce the error in response of the reduced system (Equation B.1) to the full order system (Equation B.2). The cost to be reduced is the RMS error of the reduced response:

$$J = E\left\{(u - u_r)^2\right\} \tag{B.3}$$

Minimizing this cost will reduce the $\mathcal{H}_2$ error between the reduced order controller response and the full order controller response. In the frequency domain, the technique attempts to match the transfer function of the n_c order controller as closely as possible with the transfer function of the n_{r_i} order controller.

The reduced order controller which minimizes the cost in Equation B.3 cannot be solved in closed form. Instead, a gradient search procedure, similar to the $\mathcal{H}_2$ control design methods of Section 2.3.2 is carried out. An augmented state space system is created, whose output is the error $e = u - u_r$:

$$\begin{aligned} \begin{bmatrix} \dot{x}_c \\ \dot{x}_r \end{bmatrix} &= \begin{bmatrix} A_c & 0 \\ 0 & A_{r_i} \end{bmatrix} \begin{bmatrix} x_c \\ x_r \end{bmatrix} + \begin{bmatrix} B_c \\ B_{r_i} \end{bmatrix} y \\ e &= \begin{bmatrix} C_c & -C_{r_i} \end{bmatrix} \begin{bmatrix} x_c \\ x_r \end{bmatrix} \end{aligned} \tag{B.4}$$

which is written in simplified notation by defining a state vector $\tilde{x} = \begin{bmatrix} x_c \\ x_r \end{bmatrix}$. The state dynamics are

$$\begin{aligned} \dot{\tilde{x}} &= \tilde{A}\tilde{x} + \tilde{B}y \\ z &= \tilde{C}\tilde{x} \end{aligned} \tag{B.5}$$

The closed loop covariance of the error system Equation B.4 is Q, where

$$\tilde{A}Q + Q\tilde{A}^T + \tilde{B}\tilde{B}^T = 0 \tag{B.6}$$

Q is symmetric and positive definite. The cost J can be written in terms of Q:

$$J = tr\left\{\tilde{C}^T\tilde{C}Q\right\} \tag{B.7}$$

At the optimum,

$$P\tilde{A} + \tilde{A}^T P + \tilde{C}^T\tilde{C} = 0 \tag{B.8}$$

P is also symmetric and positive definite.

Adjoining Equation B.6 to the cost with the Lagrange multiplier P,

$$J = tr\left\{\tilde{C}^T\tilde{C}Q + P\left(\tilde{A}Q + Q\tilde{A}^T + \tilde{B}\tilde{B}^T\right)\right\} \tag{B.9}$$

The gradient of the augmented cost Equation B.9 with respect to the reduced order compensator matrices A_{r_i},B_{r_i},and C_{r_i} is found. Partitioning P, Q, and (PQ) into $n_c \times n_c$,$n_c \times n_{r_i}$,$n_{r_i} \times n_c$, and $n_{r_i} \times n_{r_i}$ elements,

$$P = \begin{bmatrix} P_1 & P_2 \\ P_2^T & P_3 \end{bmatrix}, Q = \begin{bmatrix} Q_1 & Q_2 \\ Q_2^T & Q_3 \end{bmatrix} \tag{B.10}$$

Since P and Q are symmetric.

The gradients are

$$\frac{\partial J}{\partial A_{r_i}} = 2(PQ)_{22} \tag{B.11}$$

$$\frac{\partial J}{\partial B_{r_i}} = 2(P\tilde{B})_2 \tag{B.12}$$

$$\frac{\partial J}{\partial C_{r_i}} = -2(\tilde{C}Q)_2 \tag{B.13}$$

$$\tag{B.14}$$

$(PQ)_{22}$, is the $n_{r_i} \times n_{r_i}$,block of the matrix product PQ. $(P\tilde{B})_2$ is the lower $n_{r_i} \times 1$ portion of $P\tilde{B}$:

$$P\tilde{B} = \begin{bmatrix} P_1 & P_2 \\ P_2^T & P_3 \end{bmatrix} \begin{bmatrix} B_c \\ B_{r_i} \end{bmatrix} = \begin{bmatrix} P_1 B_c + P_2 B_{r_i} \\ P_2^T B_c + P_3 B_{r_i} \end{bmatrix} \tag{B.15}$$

Similarly for $\tilde{C}Q$:

$$\tilde{C}Q = \begin{bmatrix} C_c & -C_{r_i} \end{bmatrix} \begin{bmatrix} Q_1 & Q_2 \\ Q_2^T & Q_3 \end{bmatrix} = \begin{bmatrix} C_c Q_1 - C_{r_i} Q_2^T \\ C_c Q_2 - C_{r_i} Q_3 \end{bmatrix} \tag{B.16}$$

The cost in Equation B.9 was minimized using a numerical search technique utilitizing a modified Broyden-Fletcher-Goldfarb-Shanno (BFGS) algorithm. For an overview of numerical optimization techniques,and a discussion of the practical issues involved, see [23].

Appendix C

Controller Implementation

The ADCE package contains the Intel microcontroller as well as analog charge sensors and filters. As noted, each ADCE is wired to a single actuator and sensor. The collocated and nearly collocated sensor signals are conditioned using two charge amplifiers, to produce voltages proportional to strain. The signals are fed into two 10-bit A/D converters which are integral to the microcontroller. The signals are then combined in a weighted sum to create a single measurement. The compensator command signal is converted to a 10-bit output, and sent to two 8-bit D/As. The digital outputs are combined and smoothed by a weighted analog filter, which in turn drives an Apex PA88-based charge amplifier circuit.

The Intel operates in fixed precision. It is capable of 32-bit, integer math operations. State space matrix elements are stored as 16-bit integers and a single 16-bit divisor. As a result a maximum of 4 orders of magnitude between the largest and smallest elements can be attained. Special procedures must be used to scale the controller before it is uploaded. The dynamic states are 16-bit integers. Issues of roundoff error and overflow can arise if the sensor signal is too small or too large. Roundoff error occurs if the states are too small. The signal to noise ratio will be high. Overflow will cause the states to "wrap" to a number with the opposite sign. If overflow occurs often, the compensator response will be poor.

The controller is implemented by splitting the block-SISO compensator into its component $n_c \times n_c$ blocks. The blocks are all identical, as noted above, so the fol-

lowing steps are only done once. The continuous controller is discretized. The Tustin (bilinear) transform is used (for a discussion of the issues associated with digital implementation of continuous controllers, see for example [32]). Note that the discretization introduces a feedthrough (D term) into the compensator matrices.

The discrete-time controller dynamics are represented in state space form as:

$$\begin{aligned} x_{k+1} &= A_c x_k + B_c y_k \\ u_k &= C_c x_k + D_c y_k \end{aligned} \tag{C.1}$$

where the subscript $(.)_k$ refers to the k^{th} time step. There are n_r real states. To minimize calculation overhead, the controller is implemented in "real modal" tridiagonal form. In real modal form, the real poles σ_{r_i} are stored as diagonal entries. Complex poles $\sigma_i \pm \jmath\omega_i$ are stored as 2×2 blocks on the diagonal of A_c:

$$\begin{bmatrix} \vdots \\ x_{r_i} \\ \vdots \\ x_i \\ x_{i+1} \\ \vdots \end{bmatrix}_{k+1} = \begin{bmatrix} \ddots & & & & & \\ & \sigma_{r_1} & & & & \\ & & \ddots & & & \\ & & & \sigma_1 & \omega_1 & \\ & & & -\omega_1 & \sigma_1 & \\ & & & & & \ddots \end{bmatrix} \begin{bmatrix} \vdots \\ x_{r_i} \\ \vdots \\ x_i \\ x_{i+1} \\ \vdots \end{bmatrix}_k + \begin{bmatrix} \vdots \\ b_{r_i} \\ \vdots \\ b_i \\ b_{i+1} \\ \vdots \end{bmatrix} y_k \tag{C.2}$$

All the other entries of A_c are zero. The compensator is placed into real modal form with a two-step transformation which uses the eigenvectors of the A matrix. Denoted in matrix form by V:

$$V^{-1} A V = D \tag{C.3}$$

$$D = \begin{bmatrix} \ddots & & & & & \\ & \sigma_{r_i} & & & & \\ & & \ddots & & & \\ & & & \sigma_1 + \jmath\omega_1 & & \\ & & & & \sigma_1 - \jmath\omega_1 & \\ & & & & & \ddots \end{bmatrix} \tag{C.4}$$

where V and D are sorted so that the first n_r diagonal elements of D are the real poles. A second transformation denoted T converts the diagonalized A_c to real modal

form. Since the first n_r eigenvalues are already real, the first $n_r \times n_r$ block of T is the identity matrix. Each complex mode in D is transformed with a 2×2 block of the form

$$\begin{bmatrix} 1 & -\jmath \\ 1 & \jmath \end{bmatrix} \tag{C.5}$$

so that T is zero except along the diagonal, for the first n_r entries, and in 2×2 blocks corresponding to the complex modes of D, for the rest of the diagonal. T transformation is

$$T = \begin{bmatrix} 1 & & & & & \\ & 1 & & & & \\ & & \ddots & & & \\ & & & 1 & -\jmath & \\ & & & 1 & \jmath & \\ & & & & & \ddots \end{bmatrix} \tag{C.6}$$

The real modal controller controller is

$$\begin{aligned} x_{k+1} &= T^{-1}V^{-1}A_cVTx_k + T^{-1}V^{-1}B_cy_k \\ u_k &= C_cVTx_k + D_cy_k \end{aligned} \tag{C.7}$$

In real modal form, the real state updates involve only 3 operations:

$$x_{i_{k+1}} = \sigma_{r_i}x_{i_k} + b_{i_r}y_k \tag{C.8}$$

Complex states are updated in pairs, in a total of 8 operations:

$$\begin{bmatrix} x_i \\ x_{i+1} \end{bmatrix}_k + 1 = \begin{bmatrix} \sigma_i & \omega_i \\ -\omega_i & \sigma_i \end{bmatrix} \begin{bmatrix} x_i \\ x_{i+1} \end{bmatrix}_k + \begin{bmatrix} b_i \\ b_{i+1} \end{bmatrix} y_k \tag{C.9}$$

As a result, the full state update at each time step is performed in $3n_r + 4(n_c - n_r)$ operations, compared to $n_c^2 + n_c$ for a full matrix A_c. Additionally, the storage requirement for A_c is reduced from n_c^2 to n_c, since each 2×2 block of A_c has only two independent elements, σ_i and ω_i.

Real model storage also simplifies the scaling of the states. The scaling advantage of real modal form results from the independence of each real state and complex state

pair. Each real mode state is driven by the element b_{r_i} of B_c, independent of the rest of the elements. The same state contributes to the output through its own element of C_c. If the sensor signal is large, causing the state to overflow, b_{r_i} can be decreased until the state no longer over flows. c_{r_i} is increased by the same amount, to give the same transfer function. If the sensor signal is small, b_{r_i} is increased and c_{r_i} is decreased. For the complex mode states, the same scaling applies to the corresponding 2 elements of B_c and C_c. Care must be taken, when scaling lightly damped modes, to allow for the amplification of signals near that frequency.

Additional scaling parameters are denoted α,β, and γ. α is the common divisor used to represent A_c,B_c, C_c, and D_c:

$$A_c = \frac{A^*}{\alpha}, B_c = \frac{B^*}{\alpha}, C_c = \frac{C^*}{\alpha}, D_c = \frac{D^*}{\alpha} \tag{C.10}$$

where A_c^*, B_c^*, C_c^*, and D_c^* are integer matrices. α is chosen by fixing the maximum allowable element size. It must be representable with a 16-bit integer. The maximum (in absolute value) element of A_c,B_c,C_c, and D_c is set equal to that value. α can be solved for. The elements of the $()^*$ matrices are the nearest integers to αA_c,αB_c,αC_c, and αD_c.

The choice of α trades off the discretization of the unit circle against the possibility of overflow during the state update and output calculations. Larger αs divide the unit circle into a finer grid, allowing the discrete poles to be placed more accurately. However, as α increases, the size of the elements of the integer matrices A_c^*, B_c^*, C_c^*, and D_c^* increase. The size of the dynamic state vector increases proportionally.

A parameter β is coded which allows the input to be scaled up, scaling the state vector by the same amount. The output is then scaled down by $\frac{1}{\beta}$:

$$\begin{aligned} x_{k+1} &= A_c x_k + B_c(\beta y_k) \\ u_k &= (\frac{1}{\beta} C_c x_k) + D_c y_k \end{aligned} \tag{C.11}$$

The effect is identical to the B_c/C_c scaling above. However, β scales all the states equally. It allows an in situ scaling, for example, for different input levels. To enable

attenuation of the states if necessary, β is stored as a ratio of integers:

$$\beta = \frac{\beta^*}{100} \tag{C.12}$$

β is chosen based on the expected disturbance input. The ADCE software diagnostics download the current states of the Intel, when poled. An input of the correct spectrum and RMS can be fed to the ADCE. β is then chosen by looking at the states directly. None of the states should below 100 often, or above 10,000 often. Alternatively, β can be increased until the ADCE command signal exhibits frequent spiking, indicating overflow within the processor.

Finally, an output gain γ is included to provide a scaling of the output:

$$u = \gamma \left((\frac{1}{\beta} C_c x_k) + D_c y_k \right) \tag{C.13}$$

γ is implemented in integer form as $\frac{\gamma^*}{1000}$. The sign of the compensator can be changed easily by changing the sign of γ. Also, a design flaw in the D/A filter was accounted for using $\gamma = 1350$.

An additional scaling for which γ could be used is to match the signal amplitudes at the A/Ds and the D/As. The signal amplitudes should be matched so that the full bit range of the A/Ds and the D/As are used. Ideally, an analog gain would be included at the output of the D/As. The compensator gain would be scaled (using γ) so that the maximum gain of the compensator is unity. Any signal which does not overload the D/As would propagate through the controller and arrive at the D/As with an amplitude no greater than it had at the D/As. The signal to noise of the discretization in the A/Ds and D/As would then be matched. The analog gain would be scaled up by $\frac{1}{\gamma}$ to give the correct loop gain. The current ADCE does not include an analog gain stage.

The sample frequency of the controller is also variable. On-chip memory limits the maximum compensator size to 12 states. The Intel can run 12 states at 250 Hz. By reducing the number of states, the maximum sample rate can be increased. However, a higher sample rate adversely affects the ability to place the discrete poles. As the sample rate increases, the magnitudes of all the discrete pole locations go to

1. The precision required to differentiate between the poles increases. Since the Intel is limited to 16 bit precision, the pole locations degrade. Additionally. there is no reason to increase the same rate, since the highest mode to be controlled is at 10 Hz, a decade below the 125 Hz Nyquist frequency of the controller running at the design sample rate.